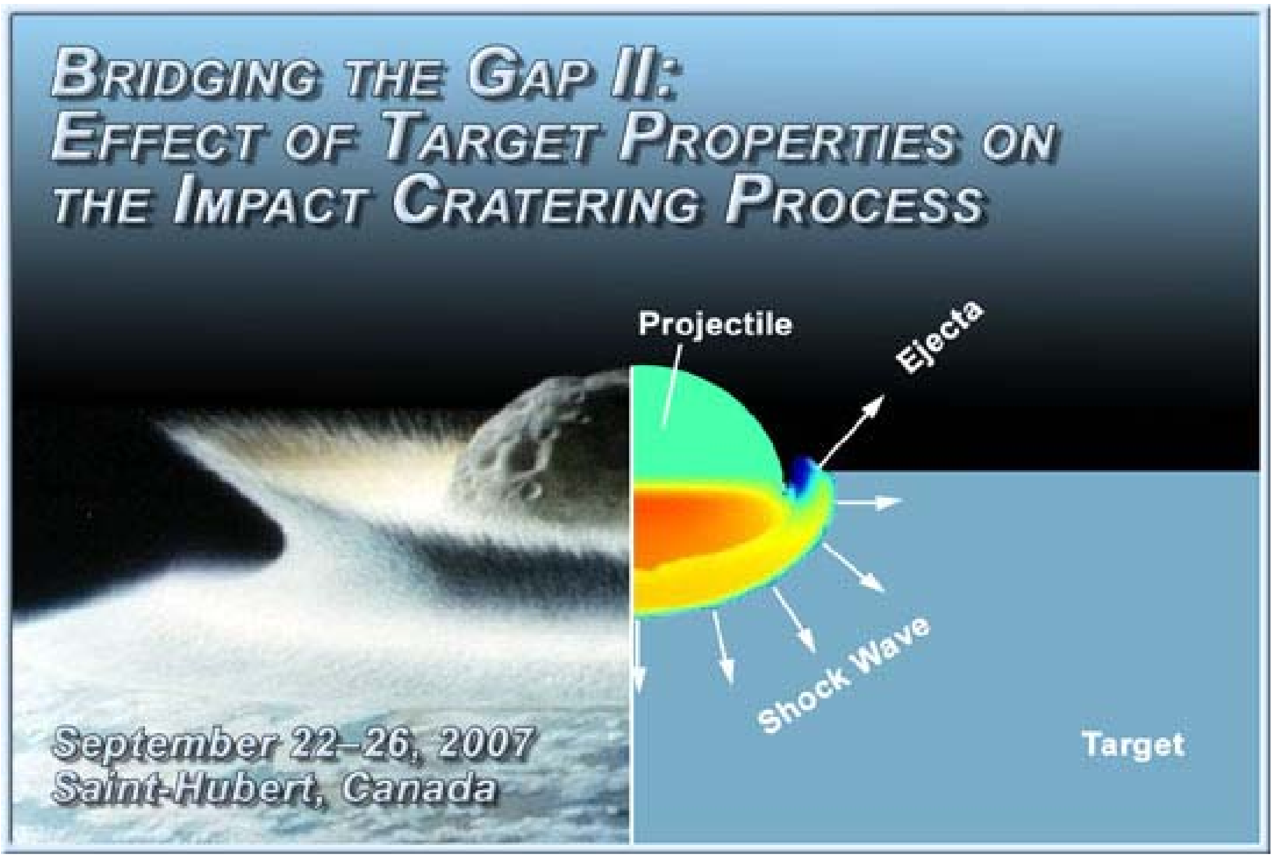

WORKSHOP PROGRAM AND ABSTRACTS

LPI Contribution No. 1360

BRIDGING THE GAP II: EFFECT OF TARGET PROPERTIES ON THE IMPACT CRATERING PROCESS

September 22–26, 2007
Saint-Hubert, Canada

SPONSORS

Canadian Space Agency
Lunar and Planetary Institute
Barringer Crater Company
NASA Planetary Geology and Geophysics Program

CONVENERS

Robert Herrick, *University of Alaska Fairbanks*
Gordon Osinski, *Canadian Space Agency*
Elisabetta Pierazzo, *Planetary Science Institute*

SCIENTIFIC ORGANIZING COMMITTEE

Mark Burchell, *University of Kent*
Gareth Collins, *Imperial College London*
Michael Dence, *Canadian Academy of Science*
Kevin Housen, *Boeing Corporation*
Jay Melosh, *University of Arizona*
John Spray, *University of New Brunswick*

Lunar and Planetary Institute 3600 Bay Area Boulevard Houston TX 77058-1113

LPI Contribution No. 1360

Compiled in 2007 by
LUNAR AND PLANETARY INSTITUTE

The Institute is operated by the Universities Space Research Association under Agreement No. NCC5-679 issued through the Solar System Exploration Division of the National Aeronautics and Space Administration.

Abstracts in this volume may be cited as

Author A. B. (2007) Title of abstract. In *Bridging the Gap II: Effect of Target Properties on the Impact Cratering Process,* p. XX. LPI Contribution No. 1360, Lunar and Planetary Institute, Houston.

This volume is distributed by

ORDER DEPARTMENT
Lunar and Planetary Institute
3600 Bay Area Boulevard
Houston TX 77058-1113, USA
Phone: 281-486-2172
Fax: 281-486-2186
E-mail: order@lpi.usra.edu

Mail orders requestors will be invoiced for the cost of shipping and handling.

ISSN No. 0161-5297

Preface

This volume contains abstracts that have been accepted for presentation at the Bridging the Gap II: Effect of Target Properties on the Impact Cratering Process, September 22–26, 2007, Saint-Hubert, Canada.

Administration and publications support for this meeting were provided by the staff of the Publications and Program Services Department at the Lunar and Planetary Institute.

Contents

Program

Monday, September 24, 2007

WELCOME SESSION
8:30 a.m. Salle I

8:30 a.m. Welcome Address and Introduction

8:40 a.m. Overview Presentation: Impact Cratering Since BG1

INITIAL ENERGY DEPOSITION AND SHOCK WAVE PROPAGATION
9:00 a.m. Salle I

Chairs: M. R. Dence
G. S. Collins

9:00 a.m. Melosh H. J. * [INVITED]
The Contact and Compression Stage of Impact Cratering **[#8060]**

9:30 a.m. Kenkmann T. * [INVITED]
Hypervelocity Collisions of Projectiles and Targets: Shock Wave Propagation in Heterogeneous Rocks Inferred from Microstructures **[#8031]**

10:00 a.m. QUESTIONS

10:10 a.m. BREAK

10:20 a.m. Baldwin E. C. * Milner D. J. Burchell M. J. Crawford I. A.
Shock Wave Propagation and Damage to the Target in Oceanic Impact Events **[#8015]**

10:35 a.m. Milner D. J. * Baldwin E. C. Burchell M. J.
Influence of a Water Layer on the Impact Cratering Process and the Fate of the Projectile **[#8023]**

10:50 a.m. Taylor E. A. * Tsembelis K. Kearsley A. T. Miljkovic K.
Further Development of a Hugoniot for Yorkshire Sandstone **[#8067]**

11:05 a.m. Mohr T. * Reimold W. U. Riller U. Gibson R. L.
Analysis of Small-Scale Pseudotachylitic Breccia Zones from the Central Uplift of the Vredefort Impact Structure, South Africa **[#8018]**

11:20 a.m. Dence M. R. *
An Inconvenient View: Interpreting How Shock-induced Fractures Influence Impact Crater Development **[#8066]**

11:35 a.m. Pierazzo E. * Artemieva N. Asphaug E. Cazamias J. Coker R.
Collins G. S. Crawford D. A. Gisler G. Holsapple K. A. Housen K. R.
Ivanov B. Korycansky D. G. Melosh H. J. Taylor E. A. Turtle E. P. Wünneman K.
The Impact Hydrocode Benchmark and Validation Project: First Benchmark and Validation Tests **[#8038]**

11:50 a.m. DISCUSSION

12:45 p.m. LUNCH

Monday, September 24, 2007

SHOCK MELTING, METAMORPHISM, AND DAMAGE TO THE TARGET
2:00 p.m. Salle I

Chairs: E. Pierazzo
M. J. Burchell

2:00 p.m. Wünnemann K. * Deutsch A. [INVITED]
Impact Metamorphism: On the Width of the Gap Between Observation and Modeling — The Geologist's View vs. the Modelers Assessment I **[#8027]**

2:30 p.m. Deutsch A. * Wünnemann K. [INVITED]
Impact Metamorphism: On the Width of the Gap Between Observation and Modeling — The Geologist's View vs. the Modelers Assessment II **[#8029]**

3:00 p.m. QUESTIONS

3:10 p.m. Schultz P. H. *
Impact Cratering in Soft Sediment Layers **[#8033]**

3:25 p.m. Harris R. S. * Schultz P. H. King P. L.
The Fate of Water in Melts Produced During Natural and Experimental Impacts into Wet, Fine-grained Sedimentary Targets **[#8051]**

3:40 p.m. BREAK

3:50 p.m. Osinski G. R. * Grieve R. A. F. Spray J. G.
Effect of Target Lithology on Impact Melting **[#8044]**

4:05 p.m. Spray J. *
Friction Melting Mechanics: Experimental Evidence Relevant to Impact Cratering **[#8055]**

4:20 p.m. Reimold W. U. * Gibson R. L.
Pseudotachylitic Breccia Development in Impact Structures — Status of Research in the Vredefort Dome (South Africa) and Basis for Process Modeling **[#8011]**

4:35 p.m. Stewart S. T. * Senft L. E.
Frictional Melting and Complex Crater Collapse **[#8021]**

4:50 p.m. Burchell M. J. * Kearsley A. T. Hörz F.
Stardust Craters and Tracks: In Space and in the Laboratory **[#8006]**

5: 05 p.m. DISCUSSION

6:00 p.m. ADJOURN

Tuesday, September 25, 2007

MECHANICS OF COMPLEX CRATER FORMATION
8:30 a.m. Salle I

Chairs: J. G. Spray
K. Wünnemann

8:30 a.m.	Collins G. S. * [INVITED] *The Effect of Target Strength Variations on Complex Crater Formation: Insight from Numerical Modelling* **[#8039]**
9:00 a.m.	McKinnon W. B. * [INVITED] *The Mechanics of Complex Crater and Ringed Basin Formation: Constraints from 30 Years of Planetary Observations* **[#8072]**
9:30 a.m.	QUESTIONS
9:40 a.m.	Elbeshausen D. * Poelchau M. Wünnemann K. Kenkmann T. *Structural Signatures of Oblique Impacts — Insights from Numerical Modeling* **[#8047]**
9:55 a.m.	Morgan J. * Barton P. Christeson G. Gulick S. Collins G. *Asymmetry of the Chicxulub Crater — Is It Produced by Asymmetry in the Target?* **[#8028]**
10:10 a.m.	BREAK
10:20 a.m.	Riller U. * Boutelier D. Cruden A. R. Schrank C. *Kinematic Evolution of the Sudbury Basin Inferred from Scaled Analogue Modelling and Structural Ground Truth* **[#8007]**
10:35 a.m.	Nycz J. C. * Hildebrand A. *Constraining Strength Properties in Martian Surface Layers by Modelling the Peripheral Peak Ring Impact Crater Morphology* **[#8030]**
10:50 a.m.	Boyce J. M. * *Depth and Diameter Relationships of Martian and Terrestrial Planet Complex Impact Craters* **[#8063]**
11:05 a.m.	Senft L. E. * Stewart S. T. *Diagnostic Features from Modeling Impact Cratering in Icy Layered Terrains* **[#8008]**
11:20 a.m.	Bray V. J. * Collins G. S. Morgan J. V. Schenk P. M. *The Effect of Target Properties on Impact Crater Morphology — Comparison of Craters on Icy and Silicate Bodies* **[#8056]**
11:35 a.m.	DISCUSSION
12:45 p.m.	LUNCH

Tuesday, September 25, 2007

PLUME EVOLUTION AND EJECTA EMPLACEMENT (PROXIMAL AND DISTAL)
2:00 p.m. Salle I

Chairs: K. Housen
R. Herrick

2:00 p.m. Artemieva N. * [INVITED]
Impact Plume Numerical Modeling **[#8026]**

2:20 p.m. Anderson J. L. B. * [INVITED]
Experimental Studies of Ejecta Dynamics: Implications for Scaling and Models **[#8043]**

2:40 p.m. Osinski G. R. * [INVITED]
Impact Ejecta Emplacement: Observations from Earth, Moon, and Mars **[#8074]**

3:10 p.m. QUESTIONS

3:20 p.m. Barnouin-Jha O. S. * Cintala M. J. Crawford D. A. Anderson J. L. B.
Yamamoto S. Sugita S.
Effects of Target Properties on the Formation of Laboratory Scale Impact Craters **[#8059]**

3:35 p.m. Collins G. S. * Wünnemann K
The Effect of Porosity and Friction on Ejection Processes: Insight from Numerical Modeling **[#8040]**

3:50 p.m. BREAK

4:00 p.m. Schultz P. H. * Crawford D. A.
Comparing Laboratory and Hydrocode Experiments for Oblique Impacts into Spherical Targets **[#8049]**

4:15 p.m. Richardson J. E. * Melosh H. J.
A Model to Determine Cometary Properties from the Ejecta Plume Behavior Resulting from Deep Impact **[#8017]**

4:30 p.m. Wright S. *
Ejecta Localities of Intermediately Shocked and Shock-melted Impactites in Terrestrial Crater Ejecta and Modeling Constraints on Their Formation and Deposition **[#8061]**

4:45 p.m. Scheider K. C. Cox R. *
Ice-penetrating Impacts: Insights from Hypervelocity Impact Experiments and Galileo Image Mapping of Europa **[#8034]**

5:00 p.m. DISCUSSION

6:00 p.m. ADJOURN

Tuesday, September 25, 2007

POSTERS POPOURRI AND RECEPTION
6:00 p.m. Salle III

Gucsik A.
"Antisymmetric" Shock Wave Distribution at Ries Impact Crater, Germany?: A Micro-Raman Spectroscopical Study of Shocked Zircon **[#8050]**

Ferrière L. Koeberl C. Reimold W. U.
Distribution of Shocked Quartz Grains Along the LB-08A Core Through the Central Uplift of the Bosumtwi Impact Structure, Ghana — Implications for Numerical Models **[#8035]**

Graham R. A.
Pseudo-Liquid (Hugoniot) and Particle-in-Matrix Modeling in Geologic Materials **[#8068]**

Burchell M. J. Robin-Williams R. Foing B. H.
The SMART 1 Impact Event: From the Laboratory to the Moon **[#8005]**

Vishnevsky S. A. Raitala J.
Popigai Impact Fluidizites Derived from the "Wet" Units of Target: Injections of Hot and Mobile Melt + H_2O *Mixtures with Long-living Residual Shock Pressures* **[#8014]**

Öhman T.
The Origin and Tectonic Modification of the Saarijärvi Impact Structure, Northern Finland **[#8019]**

Kohout T. Deutsch A. Pesonen L. J. Hornemann U.
The Magnetic Behavior of Synthetic Magnetite Induced by Shock Recovery Experiments in the Range Between 10 and 45 GPa **[#8036]**

Poelchau M. Elbeshausen D. Kenkmann T. Wünnemann K.
Structural Signatures of Oblique Impacts — Insights from Field Observations **[#8058]**

van der Bogert C. H. Schultz P. H. Spray J. G.
High Strain-Rate Deformation Experiments on Carbonate-Silicate Rocks: Implications for Impact Cratering Processes **[#8062]**

Lorenz R. D. Wood C. A. Lunine J. I. Wall S. D. Lopes R. M. Mitchell K. L.
Paganelli F. Anderson Y. Z. Stofan E. R. Cassini RADAR Team
Titan Impact Craters — Cassini RADAR Results and Insights into Target Properties **[#8024]**

Jahn A. Riller U. Reimold W. U.
From Map to Model — 3D Visualization of the Vredefort Central Uplift, South Africa **[#8002]**

Öhman T. Aittola M. Kostama V.-P. Kallo M. Raitala J.
The Mechanics of Polygonal Impact Crater Formation **[#8020]**

Vishnevsky S. A.
Shiyli Dome, Kazakhstan: Origin of Central Uplift by Elastic Response **[#8013]**

Davison T. Collins G.
Investigating the Effect of Water Depth on Marine Impact Crater Morphology **[#8041]**

Ormö J. Lepinette A. King D. T. Jr. Petruny L. W.
Structure of the Wetumpka Impact Crater: Drill-Core, Field Data, and Numerical Simulation **[#8073]**

Elbeshausen D. Wünnemann K. Collins G. S.
Cratering Mechanisms of Oblique Impacts in Targets of Different Strength — Insights from Numerical Modeling **[#8045]**

Milam K. A.
Petrographic Observations of Central Uplift Formation in Complex Craters **[#8053]**

Lieger D. Riller U. Reimold W. U. Gibson R. L.
Importance of Pseudotachylitic Breccia Zones for Understanding the Formation of Central Uplift Structures: Field Evidence from the Vredefort Dome, South Africa **[#8071]**

Calef F. J. III Herrick R. Sharpton V. L.
Development of a Small Rayed Crater Database for Mars: Initial Results **[#8070]**

Buczkowski D. L. Barnouin-Jha O. S. Weaver A.
Bright-Haloed Craters in Chryse Planitia and Implications for Target Properties **[#8064]**

Meyer C. Reimold U. Wünnemann K. Jébrak M.
The Question of the Evolution of the Ejecta Plume and the Origin of Suevite of the Ries Crater, Germany **[#8037]**

Wittmann A. Kenkmann T.
Indications for Fluidization of the Ries Crater’s Ejecta Blanket **[#8065]**

Thompson T. W. Campbell B. A. Ghent R. R. Hawke B. R.
Differences in the Subsurface Block Distributions Across the Moon’s Southern Highlands **[#8022]**

Chicarro A. F. Dypvik H. Pesonen L. J. Rossi A. P. Krøgli S. O. Zumspregel H.
Automatic Search for New Impact Structures in Fennoscandia **[#8025]**

Byrne C. J.
Effects of Global Target Shape on Impact Cratering **[#8010]**

Wednesday, September 26, 2007

ENVIRONMENTAL CONSEQUENCES OF IMPACT CRATERING
9:00 a.m. Salle I

Chairs: G. R. Osinski
H. J. Melosh

9:00 a.m. Pierazzo E. * [INVITED]
Environmental Effects Associated with Impact Events **[#8048]**

9:30 a.m. Simonson B. * Hassler S. [INVITED]
Environmental Effects of Large Impacts: Was the End-Creataceous Event Typical? **[#8075]**

10:00 a.m. QUESTIONS

10:10 a.m. BREAK

10:30 a.m. Goldin T. J. * Melosh H. J.
Modeling Distal Impact Ejecta Sedimentation: The K/T Boundary Double Layer **[#8057]**

10:45 a.m. Koeberl C. * Ivanov B. A. Goodman J.
Impact Triggering of the Snowball Earth Deglaciation? **[#8003]**

11:00 a.m. Courty M. A. * Deniaux B. Cortese G. Crisci A. Crosta X. Fedoroff M.
Guichard F. Grice K. Greenwood P. Lavigne F. Mermoux M. Smith D. C.
Peucker-Ehrenbrink B. Poitrasson F. Poreda R. Ravizza G. Thiemens M. H. Schärer U.
Shukolyukov A. Walls M. Wassmer P.
Evidence for Transhemispheric Dispersion of an Ejecta Debris-Jet by a High-Velocity Tangential Impact Along the Austral-Indian Ocean at Ca. 4 Kyr BP **[#8032]**

11:15 a.m. DISCUSSION

12:45 p.m. LUNCH

Wednesday, September 26, 2007

INTEGRATED DISCUSSION:
ACHIEVEMENTS SINCE BG1 AND OUTSTANDING PROBLEMS IN IMPACT CRATERING
2:00 p.m. Salle I

Discussion Leaders:
M. J. Burchell
J. G. Spray
G. S. Collins

STARTING QUESTIONS:

1. Where are experiments going next and what should be done?
2. What do modelers need to move forward?
3. What should field observations be focused on?

EXPERIMENTAL STUDIES OF EJECTA DYNAMICS: IMPLICATIONS FOR SCALING AND MODELS.

Jennifer L. B. Anderson, Department of Geoscience, Winona State Univ., Winona, MN (JLAnderson@winona.edu).

Introduction

The formation of an impact crater is a continuum of processes that can be divided conceptually into three stages [1]: the *penetration or compression* stage, during which the projectile transfers its momentum and energy into the target material; the *excavation* stage, in which the target material moves in response to the impact-generated shock, with some material being ejected above the original target surface to be redeposited in the ejecta deposit that surrounds the final crater; and the *modification* stage, after which the transient crater is in its final, pre-erosional form.

In this contribution, I will discuss how the excavation stage of crater growth is studied through laboratory experiments. In particular, I will examine current methods for measuring ejecta dynamics which are well-suited for comparison with numerical models and scaling relationships.

Motivation

In many ways, the laboratory is the optimum setting in which to investigate the excavation stage of crater growth because the initial conditions of the event can be controlled and the excavation of the crater can be observed and recorded in real time as the crater grows. Both the momentum and energy deposition from projectile to target is recorded which is particularly relevant in the case of oblique impacts which are the norm on planetary surfaces [2,3]. An understanding of experimental impacts provides "ground-truth" for numerical models, and a baseline for interpreting the complex ejecta deposits observed in the field. Current scaling relationships are based on data from impact experiments and continue to be modified by new experimental discoveries.

The Evolution of Experimental Techniques

Initial studies of ejecta dynamics in the laboratory simply recorded the ejecta curtain as it moved across the target surface allowing for analysis of ejecta curtain angle, morphometry, and expansion speed for vertical and oblique impacts [e.g., 4]. While these data are vital to understanding ejecta deposition, more detailed measurements of individual ejecta particles in flight would be needed to characterize the subsurface flow-field, transfer of energy and momentum, and to constrain numerical models and scaling relationships.

A series of innovative experiments was performed in which the advancing ejecta curtain was physically dissected into discrete masses of ejecta that were filmed as they traveled along ballistic trajectories [5]. However, the effect of the apparatus used to dissect the curtain on the trajectories was unknown and could have been significant [6].

The first non-invasive technique for observing individual ejecta trajectories (during laboratory-scale explosion events) used a high-intensity light source to illuminate a vertical slice of the ejecta curtain perpendicular to a still camera equipped with a rotary shutter [7]. The resultant photographs showed individual ejecta trajectories as dashed lines.

Ejection-Velocity Measurement System (EVMS) – Two decades later, this photographic method was refined and automated for use at the Vertical Impact Facility at Johnson Space Center [8]. With the EVMS system, a laser sheet is projected vertically through the impact point, perpendicular to the target surface, and parallel to the camera plane. This sheet is strobed at a known rate and illuminates ejecta traveling along ballistic trajectories. By extrapolating the ejecta trajectories back to the target surface it became possible to quantify the ejection position, speed, and angle of a number of individual ejecta particles throughout the majority of crater growth (Figure 1).

Three-Dimensional Particle Image Velocimetry (3D PIV) – The 3D PIV technique commonly used to provide quantitative measurements of fluid flow in wind tunnels was modified for use in impact experiments at the NASA Ames Vertical Gun Range [9,10]. A horizontal laser plane is projected parallel to and a few centimeters above the target surface while two CCD cameras, providing left-eye and right-eye views, look down onto the target surface from above. Each camera takes two images in rapid succession at a preset time after impact and the four resultant images are processed in a way that yields three-dimensional velocity vectors for small groups of ejected particles in all directions around the impact point (Figure 2).

References: [1] Gault DE *et al.* (1968) *Shock Metamorphism*, p. 87-99. [2] Gilbert GK (1893) *Bull. Philos.Soc. Wash.*, p. 241-292. [3] Shoemaker EM (1962) *Phys. & Astron of the Moon*, p. 283-359. [4] Gault DE & Wedekind JA (1978) *PLPSC IX*, p. 3843-3875. [5] Oberbeck VR & Morrison RH (1976) *PLPSC VII*, p. 2983-3005. [6] Housen KR *et al.* (1983) *JGR*, p. 2485-2499. [7] Piekutowski AJ et al. (1977) *Proc. Int. Congr. High-Speed Photog.* p. 177-183. [8] Cintala MJ *et al.* (1999) *Meteoritics*, p. 605-623. [9] Heineck JT *et al.* (2002) *J. Visual.*, p. 233-241. [10] Anderson JLB et al. (2003) *JGR 108*. [11] Maxwell DE (1977) *Impact & Expl. Crat.*, p. 1003-1008.

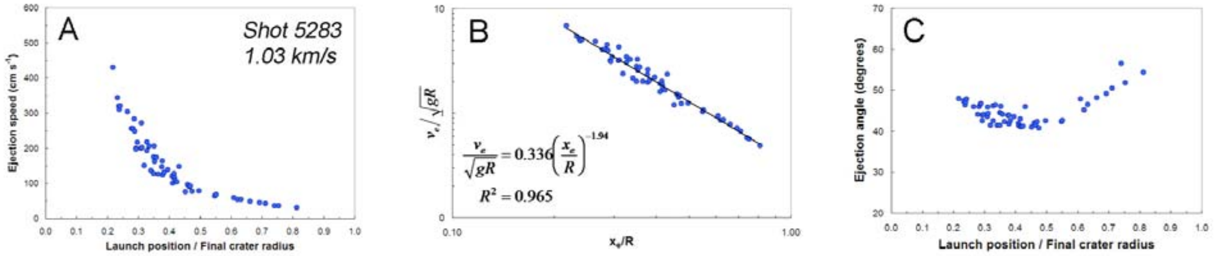

Figure 1: Ejection parameter data obtained using the EVMS system [8] during an impact of a 3.18 mm diameter glass sphere into 0.5-1.0 mm grain size sand at 1.03 km s^{-1} under vacuum conditions. These data are representative of measurements for a range of impact velocities and also for aluminum projectiles. (A) Ejection speed versus scaled crater radius. (B) Scaled ejection speed versus scaled crater radius. The equation represents the fit using standard ejection-speed scaling relationships [6]. (C) Ejection angle versus scaled crater radius. Note the increase in ejection angle during the second half of crater growth.

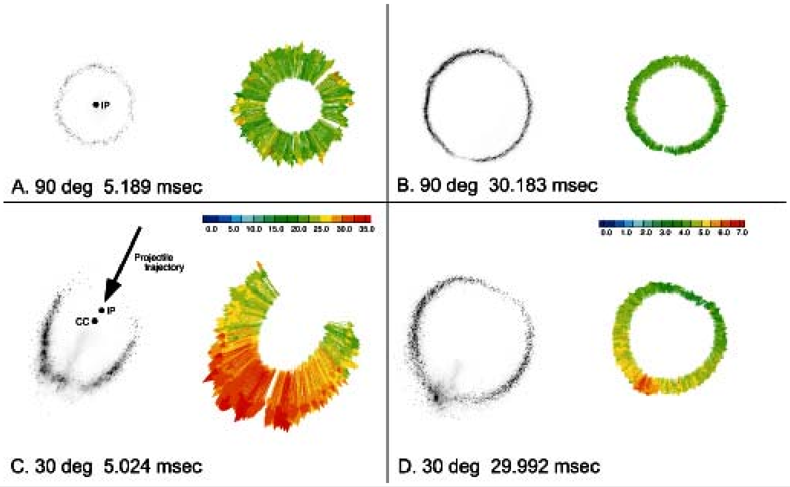

Figure 2: Examples of images and velocity measurements using the 3D PIV system [9,10] during impacts of 6.35 mm diameter aluminum spheres into 0.5 mm grain size sand at velocities near 1.0 km s^{-1} under vacuum conditions. For each pair, the raw image is given on the left and the processed image, showing current ejecta velocities within the laser plane (km s^{-1}), is on the right. (A) and (B) were taken at two different times during vertical impacts with (C) and (D) taken at similar times during 30° impacts. The vertical impacts are azimuthally symmetric while the 30° impacts retain their initial asymmetry as the crater grows.

Implications for Point-Source Scaling

These studies have already yielded intriguing results regarding the excavation stage of impacts. The standard assumption that, while an oblique impact may be asymmetric at early times, it rapidly becomes symmetric and can be approximated as a vertical impact is clearly not the case. Asymmetries in ejection speed and angle during oblique impacts exist up through the first half of crater growth when the majority of material has been excavated from the growing crater [10]. In addition, the subsurface flow-field inferred from the most widely used point-source model, Maxwell's Z Model [11], is not located at a single, stationary point beneath the target surface even for vertical impacts [12,13]. Examining the data using both ejecta-scaling and crater-scaling relationships [6] yields disparate values of the scaling parameter μ for the same series of impacts [14] which may be related to the point-source assumption or potential target material properties [15].

Implications for Numerical Modeling

With the quantitative measurement of ejecta dynamics in the laboratory, the line between experimental observations and numerical models is fading. Direct comparison is now possible between the results obtained from experimental impacts and numerical models performed at experimental scales. A few such studies have already begun [e.g., 16,17,18] but further work is needed. Ideally, numerical models would be able to replicate all of the various observations that are now possible during laboratory experiments. Collaborations could include not only the experiments discussed here, but also those dealing with final crater morphometry, shock-wave propagation [19], crater growth rates [20,21], atmospheric interactions [22], clustered impacts [23], and many more.

References (cont.): [12] Anderson JLB et al. (2004) *Meteoritics*, p. 203-320. [13] Anderson JLB & Schultz PH (2006) *Int. J. Impact Eng.*, p. 35-44. [14] Anderson JLB *et al.* (2007) *LPSC 38*, #2266. [15] Barnouin-Jha OS, this workshop. [16] Wada K *et al.* (2006) *Icarus*, p.528-545. [17] Collins GS & Wunnemann K (2007) *LPSC 38*, #1789. [18] Richardson JE *et al.*, in review. [19] Dahl JD & Schultz PH (2001) *Int. J. Impact Eng.*, p. 145-155. [20] Cintala MJ et al. (2003) *LPSC 34*, #2070. [21] Barnouin-Jha OS *et al.* (1007) *Icarus* p. 506-521. [22] Barnouin-Jha OS & Schultz, PH (1996) *JGR*, p. 21,099-21,115. [23] Schultz PH & Gault DE (1985) *JGR*, p. 3701-3732.

IMPACT PLUME NUMERICAL MODELING. N. Artemieva[1,2] .[1]Institute for Dynamics of Geospheres (Moscow, 119334, Russia, nata_artemeva@rambler.ru), [2]Planetary Science Institute (Tucson, AZ 85719, artemeva@psi.edu).

Introduction: An impact expansion plume is a mixture of vaporized, melted and solid target and projectile material that quickly expands outward from the forming crater from the very early stages of crater formation [1]. The complexity and energy associated with a planetary impact-produced expansion plume cannot be reproduced in low-velocity impact laboratory experiments, with a few exceptions [2]. Attempts to address impact plumes through laser experiments [3-4] are far from the real conditions of natural impact plumes. Numerical simulations are the best approach to investigate the evolution of expansion plumes, but they must be validated by real data.

Specific problems: There are a few serious numerical problems in impact plume modeling: (1) high contrast in densities (from solid material to rarified vapor) and energies (from standard planetary conditions to high-temperature plasma); (2) high expansion velocities; (3) high spatial resolution near a growing crater versus planetary-scaled region to be resolved; (4) a short time of ejection in comparison with a long time of the final ejecta deposition; (5) mixing of vapors versus separation of molten-solid fractions; (6) gas-particles interaction. The plume is a gas-particle mixture, not just a low-density continuum, and should be described using two-phase hydrodynamics [5], which takes into account individual particle characteristics (mass, density, shape) and their collective behavior (momentum and energy exchange with surrounding gas). The plume expansion depends upon both the particle-gas mass ratio and the particle's size frequency distribution (SFD). Solid particles are the product of ejecta fragmentation, molten particles are disrupted melt (tektites) and/or condensates from the vapor (microkrystites). Two-phase SOVA [6] and KFIX-LPL [7-8] are independent models with different particle treatments, but they both describe the physics of phenomena correctly and should produce similar results.

Example 1 - tektites: The modeling approach was satisfactory in the theoretical study of terrestrial tektites - moldavites from the 24-km-diameter Ries crater [9] and Ivory Coast tektites from the Lake Bosumtwi crater [10]. The initial ejection velocities of molten material from the uppermost target layer are high, up to 10 km/s, which is close to the velocity of the expanding plume. As a result, the particles are not subjected to high dynamic pressures that otherwise would disrupt them into a fine dust immediately after ejection. The temperature of the entraining gas is rather high, in the range of 1000-2000 K, so the particles do not cool quickly during the flight, allowing enough time to have them aerodynamically shaped (which is typical for tektites), and to lose volatiles. The total calculated mass of moldavites is near 10 Mt which compares well with the 5 Mt estimated from field observations [11]. An oblique impact (30°-45°) produces a relatively narrow-angle distribution of tektite-type material downrange, in agreement with that observed for the known strewn fields. These asymmetric distributions allow us to speculate about impact angle and impact direction [9-10].

Fig.1 The first 20 s of tektites (in green) ejection from the Ries crater. Gray circle shows the final crater. The projectile strikes along the X-axis.

Example 2 - Chicxulub distal ejecta: In early two-dimensional (2D) hydrocode simulations of impact expansion plumes, the plume expanded vertically as a cylinder above the opening crater: only after reaching the thinner upper atmosphere (well beyond the stratosphere) would it expand horizontally [12]. 2D and 3D simulation of the Chicxulub impact indicate that the expansion plume is initially dominated by water vapor, soon followed by vaporized sedimentary and projectile material, suggesting that much mixing is going on inside the plume during expansion. Recently, we carried out long-term (up to 15 minutes) simulations of the plume expansion created by an oblique impact into a Chicxulub-like target (3 km of sediments, 30 km of crystalline basement, and mantle) [13]. We modeled crater collapse and proximal ejecta deposition, while the high-velocity distal ejecta (i.e., beyond the first 400 km of the atmosphere) was further modeled using a ballistic approach. The simulations covered a range of impact angles (30° to 90°) and projectile size (16 km to 14 km) while keeping the impact velocity at 20 km/s, to maintain a transient cavity size in the range 90-100 km. Results of these simulations indicate that high-velocity, globally distributed ejecta consist exclusively of vaporized/molten projectile material and sediments (Fig. 2). This is in agreement with the understanding that well-known types of high-velocity ejecta (tektites and meteorites from other planets) originate from a very thin surficial layer (probably a few meters for tektites and less than 10%

of the projectile diameter for martian meteorites). Basement ejecta leave the growing crater with velocities well below 4 km/s. Vaporization of ejecta from deep layers is minimal, and does not provide additional ejecta acceleration. Velocity distribution within the plume increases linearly with altitude (in agreement with analytical solutions for plume evolution [14]) with only minor mixing of fast and slow materials at late times (Fig. 2 - right). Large scale (200 km) turbulence does not operate efficiently at the time scale of a few minutes.

The early time mass-velocity distribution from the simulations are in reasonable agreement with observations (a few cm thick layer at distances of 2,000-3,000 km; a few mm world-wide). Molten droplets derived from crystalline basement are deposited within 1,000 km from the crater, consistent with the impact melt found in Haiti and other proximal sites [15]. However, dispersal of basement melt outside this region is unlikely. Even after including non-ballistic transport of very small particles we could not reproduce the massive (850 km^3) worldwide spherule deposits. Shocked quartz grains are a minor fraction of total KT deposits (0.01% of spherules volume –see [13]). They may originate from minor (<1%) contamination of the Upper Cretaceous sediments by sand (or other silica-rich materials) and/or may be transported non-ballistically within a few days after the impact similar to volcanic ash clouds. Deposition of 50 µm spherules through Earth's atmosphere takes a few days (even though ballistic transport occurs within tens of minutes). Current knowledge of the shocked quartz grains size versus distance relationship [16] does not favor any particular hypothesis.

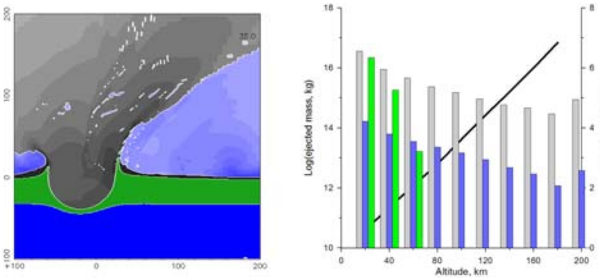

Fig. 2: *Left*: Chicxulub impact plume 35 s after a 45º impact, modeled with SOVA. Gray color shows projectile material and sediments, green - crystalline basement, dark blue - mantle, light blue – atmosphere. *Right*: mass-velocity distribution of different materials with altitude; colors are the same as on the left plate.

Perspectives: A list of plume-ejecta related problems includes: (1) suevite formation and deposition; (2) Australian-Asian tektite strewn field and predictions for the parent crater; (3) rampart craters on Mars; (4) erosion of planetary atmospheres; (5) material exchange between planets; (6) specific chemistry of tektites and KT spinels.

Chemistry: Current approaches allow us to address mainly the "mechanical" component of the complex plume expansion problem; that is, the possibility of non-ballistic transporting particles hundreds and thousands of km away from the parent crater. However, the 3D view of the plume obtained can then be used to model the condensation history of vapor and the recrystallization behavior of melt droplets. If chemical reactions lead to substantial energy re-distribution within the plume, we can take into account this heating (or cooling) in the subsequent set of gas-dynamic iterations. Calculations [17] were not coupled to a realistic dynamic model of plume physics, however, they indicated a highly oxidized plume (due to carbonate and sulfate sediments) that condenses silicate liquid droplets bearing spinel grains of compositions close to those found at the KT boundary.

Bridging the gap: Until recently the results of numerical modeling, based on poorly known initial conditions, could be compared only with old and, hence, not well-preserved geological features. Extension of impact models into volcanology [18] allows us to compare the results of a volcanic direct blast (which is very similar to an impact generated plume in many respects). For example, recorded blast dynamics and fresh geological records at Mt. St-Helens and Bezymianny volcanoes. NASA's Deep Impact experiment [19] opened a new era in impact plume studies, allowing us for the first time to observe an impact plume *in situ* under well-controlled initial conditions.

References: [1] Melosh H.J. (1989) *Impact cratering: A geological Process*, 264 pp. [2] Sugita S. et al. (1998) *JGR 103*, 19427-19441. [3] Mukhin et al. (1989) *Nature 340*, 46-48. [4] Ishibashi K. et al. (2006) *LPS 37*, Abstr. #1721. [5] Valentine G.A. and Wohletz K.H. (1989) *JGR 94*, 1867-1887. [6] Shuvalov V. (1999) *Shock Waves 9*, 381-390. [7] Rivard W.C., Torrey M.D. (1977) *LA-NUREG-6623 NRC-4* [8] Goldin T. J., Melosh H. J. (2007) *LPS 38*, Abstr. #2114. [9] Stöffler D. et al. (2002) *M&PS 37*, 1893-1908. [10] Artemieva et al. (2004) *GGG 5*. [11] Montanari A., Koeberl C.(1999) *Impact stratigraphy: The Italian Record*, 364 pp. [12] Pierazzo E. et al. (1998) *JGR 103*, 28607-28626. [13] Artemieva N. and Morgan J. (2007) *LPS 38*, Abstr. #1543. [14] Zeldovich Y. B. and Raizer Y.P. (1966) *Physics of shock waves and high temperature phenomena.* [15] Smit J. (1999) *Ann. Rev. Earth Planet. Sci. 27*, 75-113. [16] Morgan J. et al. (2006) *EPSL 251*, 264-279. [17] Ebel D.S., Grossman L. (2005) *Geology 33*, 293-296. [18] Artemieva N. (2006) LPS 37, Abstr.#1525. [19] A'Hearn M.F. et al. (2005) *Science 310*, 258-264.

SHOCK WAVE PROPAGATION AND DAMAGE TO THE TARGET IN OCEANIC IMPACT EVENTS.

E. C. Baldwin[1], D. J. Milner[2], M. J. Burchell[2], and I. A. Crawford[1] [1]UCL/Birkbeck Research School of Earth Sciences, University College London, Gower St, London WC1E 6BT. e.baldwin@ucl.ac.uk. [2]Centre of Astrophysics and Planetary Science, University of Kent, Canterbury, Kent, CT2 7NH.

Introduction: Most impact events on the Earth will occur in the oceans and seas that cover more than two-thirds of the Earth's surface. However, of the 170 craters documented, only 15-20 are thought to have formed in a marine environment [1]. The youth of the ocean floor, deep sea sediments and the lack of detailed topographical study of the ocean floor explains, in part, the lack of detected underwater craters. In addition, many impacts may not have left any evidence of a crater, because the water depth to projectile diameter ratio was sufficient to prevent cratering occurring. The only deep sea impact structure detected so far is Eltanin (located in the Bellingshausen Sea) [2], which is characterised by a zone of chaotically mixed sediments, most likely originating from impact-induced turbulent water currents [3]. Present observations do not allow identification of an impact structure on the ocean bottom.

We investigate oceanic impacts in the lab through use of the University of Kent's two-stage light gas gun, to examine the influence of a water layer on the cratering process in the target rock. The lab impacts are modelled using AUTODYN-2D (based at UCL), and we attempt to model the deep ocean impact Eltanin, in terms of the propagation of the shock wave through the water column and the target, the peak pressures endured and the damage inflicted on the basement rock.

Laboratory impacts: Impacts of 1 mm diameter stainless steel projectiles into water layers over 17% porosity saturated and unsaturated sandstone (density = 2.35 g cm^{-3} and 2.18 g cm^{-3} respectively) were conducted at 5 km/s. The depth of the water layers was varied from 0 to 12 mm while all other impact parameters remained constant. A saturated target allowed a greater volume of material to be excavated than an unsaturated target, perhaps an intuitive outcome given that the yield strength of the wet target (43 MPa) was found to be approximately half that of the dry target (90 MPa). See [4] for a full discussion.

For our unsaturated sandstone we find that a projectile diameter to water depth ratio of 1:10 is required to prevent a crater forming on the basement rock, comparable with similar experiments performed by [5] into water layers overlying granite and basalt targets. For our saturated sandstone this ratio is 1:12. Both of our data sets lie within the data range presented by [6], for impacts into sand.

Hydrocode modelling of lab impacts: The impacts into unsaturated sandstone were replicated using the numerical modelling package AUTODYN-2D to provide further insight into the cratering process at this scale (see [7] for a general description of the code]. The Smooth Particle Hydrodynamics (SPH) solver was used for the simulations, with a resolution of 20 SPH particles per projectile diameter. AUTODYN-standard material models were used for stainless steel and water. The sandstone target was defined using the shock equation of state, based on input values derived from [8]. Mechanical properties were drawn from our own experiments, the AUTODYN material library and [9].

Comparison of the crater dimensions and morphology produced in AUTODYN and the lab. AUTODYN allows analysis of material status and assigns tags according to whether the material is hydro, elastic, plastic or has failed. The areas which are indicated as 'bulk fail' are of particular interest as these are likely to delineate the spall region observed in the lab, particularly as the lab targets are held vertically, facilitating the ease at which weakened material can fall from the target. In fact, when we plot the profiles of our craters produced in the lab against the craters produced in AUTODYN as delineated by the failed 'spall' zone, we see a very close match (Fig. 1).

Propagation of the shock wave and peak pressures in the underlying basement rock. The peak pressures experienced in an impact event are directly related to the geological/mineralogical signatures recorded in the target rock. The effects of shock metamorphism begin to occur at ~2 GPa [10]. We record peak pressures down to 0.5 GPa in the underlying sandstone for a water depth to projectile diameter ratio of 1:10 (Table 1). For a water depth of 12 mm, merely a scar is visible on the surface of the lab specimen. The resolution of the numerical model was not sufficient to record any damage to the surface at this water depth, and no pressures were recorded in the target, implying that the basement rock remains essentially unchanged. For water depths of 7.5 - 10 mm, our models reveal that although measurable craters are observed in the basement rock, the projectile itself doesn't reach the target. The crater must therefore be due to the shock wave from the impact that blasts the surface at the water-target interface. This effect is illustrated further in the following section.

Modelling the Eltanin impact: The Eltanin impact was modelled in order to compare with other modelling attempts [1,3] and with direct observations, to further our understanding of the influence of a water layer on the signatures found on the ocean floor. We model the Eltanin impact event in terms of investigating the projectile diameter to water depth ratio, the peak pressures recorded in the basement, and the damage to the basement rock. We build similar models to that of [3], but use SPH to model the impact of a 1 km diameter basalt projectile impacting into a water column of 7 km (this accounts for the fact the impact is likely to have been at 45 degrees through a 5 km deep ocean) at 20km/s. We find that the projectile does not reach the ocean floor, but that the shock wave propagates through the water column and is reflected at the water-rock boundary interface (Fig. 2). The pressures recorded in the basement rock (basalt) peak at almost 3 GPa, sufficient to produce some shock metamorphism effects [10]. We also note that the basement rock is 'dented' by the impact event, to a lateral extent of 24 km and to a depth of 250 m. We are unable to model sedimentation using AUTODYN, but it is possible that this impact scar will subsequently be infilled with sediments due to strong resurges of water at the ocean-target interface. Indeed, zones of chaotically deposited sediments with layers of thickness ranging from 20 to 40 m were recovered from sediment cores, although there is no evidence for a crater [2]. Furthermore, fragments of the projectile were also retrieved, and we also observe that some projectile fragments are dispersed into our simulated ocean, which would presumably be distributed around the impact site if the model was allowed to run for longer.

Conclusions: While the effects of impact cratering into water layers on the target can be investigated efficiently in the lab, an advantage of numerical modelling is that the peak pressures across the target can be mapped in order to compare with observations at natural impact structures. We have demonstrated AUTODYN as a suitable tool to replicate our laboratory impacts, and have applied our models to large planetary impacts. In the lab-scale (5km/s) impacts when the water depth is 7.5 to 10 times the projectile diameter, a measurable depression is formed in the basement rock; modelling reveals this to be due to the impact of the shock wave, and not a direct hit by the projectile. Similarly, for the Eltanin model, the 1 km diameter projectile does not strike the ocean floor if it traverses a 7 km deep column of water at 20 km/s. This observation will vary depending on the impact velocity, projectile mass/diameter and water depth.

Acknowledgements: EB wishes to thank Paul deCarli for discussions on modelling and shock wave physics.

References: [1] Shuvalov V. V. & Trubestkaya I. A. (2001) *Solar System Research* 36, 417-430. [2] Gersonde, R. et al. *Nature 390* 357-363. [3] Wünnemann K. & Lange M. A. (2002) *Deep-Sea Research II 49* 969-981. [4] Baldwin E. C. et al. (2007) accepted for publication *Meteoritics & Planet. Sci*. Feb 2007. [5] Milner D. J. (2007) *Thesis, University of Kent* 236p. [6] Gault D. E & Sonett C. P. (1982) *Geol. Soc. America Spec. Papers 190* 69-92. [7] Hayhurst C. J. & Clegg R. A. (1997) *Int. J. Impact Eng. 20* 337-348. [8] Ahrens T. J. (ed) (1995) *AGU Ref. Shelf 3*. [9] Llama R. D & Vutukuri V. S (1978) *Handbook on Mechanical Properties of Rocks VII* 481p. [10] French B. (1998) *Traces of Catastrophe* 120p.

Water depth, mm	Peak Pressure, GPa
0	85
2.5	17
5	4.5
7.5	1.5
10	0.5
12	/

Table 1. Peak pressures in the target as a function of water column depth for laboratory impacts.

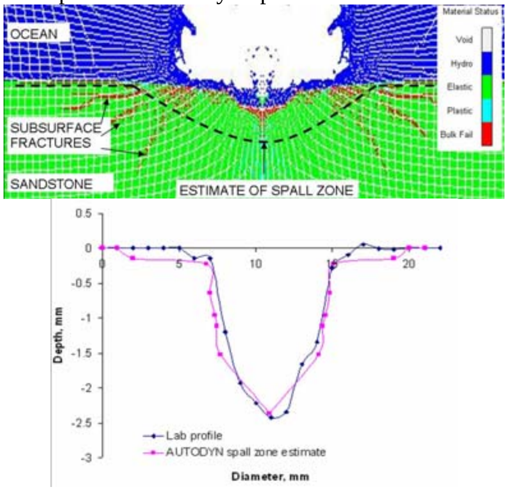

Fig. 1. Output for the impact of a 1 mm stainless steel projectile into 5 mm of water overlying sandstone. Top: AUTODYN material status plot used to delineate spall zone. Bottom: crater profile as determined in the lab compared with profile estimated from the spall zone mapped out above.

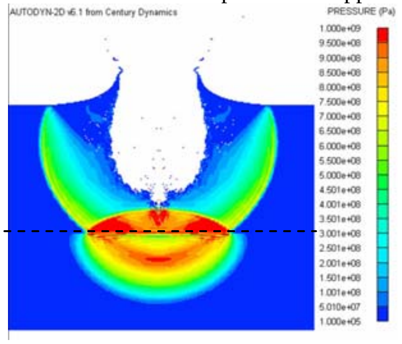

Fig. 2. Pressure contours at 1.77 seconds after impact at the ocean surface. The reflection of the pressure wave occurs at the ocean-target interface (indicated by dotted line).

EFFECTS OF TARGET PROPERTIES ON THE FORMATION OF LABORATORY SCALE IMPACT CRATERS

O.S. Barnouin-Jha[1], *M.J. Cintala*[2], *D.A. Crawford*[3], *J.L.B. Anderson*[4], *S. Yamamoto*[5], and *S. Sugita*[5]. [1]JHUAPL, Laurel, MD; [2]NASA JSC, Houston, TX; [3]Sandia National Labs., Albuquerque, NM; [4]Winona State University, Winona, MN; [5]Dept. of Complexity Science, Univ. of Tokyo, Tokyo, Japan.

Introduction – Nature shows that the shapes of large-scale craters are influenced by various target properties. For example, well-developed systems of fractures often create craters that appear square in outline [1,2], while differences in target strength may be responsible for differences in crater depth to diameter ratios seen on Mars between highland and lowland craters [3,4].

The re-discovery that target properties may play an important role during cratering at broad scales has lead to a suite of laboratory efforts using new non-intrusive measurements techniques [e.g., 5, 6, 7] to systematically assess how some of these properties may be influencing the cratering process. We compare recently acquired datasets [5,6,7,8,9,10], and attempt to assess, or at least constrain what target factors may be responsible for the various observations, always keeping in mind planetary applications.

Background – Prior to the advent of new laser based measurement techniques, where the velocity of ejecta and growth and craters could be accurately measured [e.g., 5, 6, 7], most discussion of the effects of targets on cratering during laboratory experiments primarily assessed crater efficiency [e.g., 11 and reference therein].

Based on such measurements, it was recognized by many [e.g., 11 and references therein] that different types of targets do have different crater efficiency scaling parameters: a wet sand target has lower efficiency than a dry one; an impact into a dry target will generate a smaller crater relative to one in water for the same projectile and velocity.

It was argued that scaling parameters closest to those to water should be used at broad scales because any strength effects of the target should be minor. This reasonable argument also provides the basis for the point source approximation used to justify the widely used crater scaling rules [eg., 11]. This approximation assumes that early time coupling between the projectile and target do not significantly influence the overall cratering process.

An extension of the point source approximation is that a single scaling parameter not only describe cratering efficiency, but also ejection velocities and ejecta-mass distributions [12].

New measurements – In recent years, new experiments [5,6,7,8,9,10] explore how various targets influence the cratering process, and provide new insights on the workings of the crater scaling rules and their applications at broad scales.

In this study, we review results from impacts into granular targets. We consider variations in target porosity, internal friction angle, target grain size, impact velocity and projectile properties. In all cases, we consider only vertical impacts.

Three non-intrusive measurement techniques were used to obtain the data:

(1) A laser sheet technique where the laser is strobed in order to measure the trajectory and velocity of individual ejecta [5]. Crater sizes (for efficiency measurements) are typically measured after impact using a profilometer. Projectile used are either aluminum or glass spheres. The targets used are either coarse sands (0.5-1 mm or 1-3 mm) and uniform 3 mm glass spheres. The impact velocities range from 250m/s to 2.5km/s.

(2) A particle velocity interferometry technique, where two laser sheets allow determining the trajectory and velocity of individual ejecta [6]. Data from a 6mm Al projectile launched at 1km/s in ~0.5 mm rounded sand is used. Crater sizes (for efficiency measurements) are typically measured after impact using a profilometer.

(3) A laser sheet technique where a high speed camera captures crater growth [7,10]. Changes in crater diameter and depth were investigated for impacts by a ~10mm polycarbonate projectile into uniform fine grained glass beads (80m and 220m) and non-uniform angular basaltic sand (<0.5m, 0.5-1mm and 1mm-2mm). Impact velocities considered are low between 80m/s and 350m/s.

Discussion of results

Crater efficiency - Table 1 compares crater efficiency parameters α obtained from measurements of mass displaced by impact. Results indicate that regardless of variations in the coupling between the projectile and target grains, this parameter hardly changes for similar targets. For example, slow impacts into fine grained spheres behave statistically the same as faster projectiles impacting coarse glass spheres. Likewise, all the sand impacts behave nearly the same, despite differences in projectile properties, impact velocities and grain sizes.

Differences in cratering efficiency between the sand and glass beads data can be attributed to differences in their friction angle and porosity. Which factor dominates is difficult to discern, as both typically change in tandem. The coarse sand data do suggest that friction angle effects might be small. The presence of a uniform versus non-uniform grain size distributions in the target may also be important.

Crater growth and ejection velocity – Unlike the consistency seen with crater efficiency, the new laboratory data indicate that scaling parameters describing crater growth and ejection velocities are highly variable, changing with impact velocity, and the size of the projectile and target grains. As an example, impacts by a single glass sphere in a target of comparable spheres can generate a broad range of excavation velocities from near identical launch positions within a crater. Furthermore, in most cases analyzed, the magnitude of α determined from crater growth do not equal α measured from the displaced mass from crater efficiency. Most likely, early coupling geometry between the target and projectile are responsible [5]. Other factors that could contribute include the thickness of shock pulse relative to the target grain size or void space present in the target [5], and friction angle effects [7].

Ejection angle – How ejection angle change with target properties is important for determining the distribution of ejecta emplaced after impact. The new measurements indicate ejection angles first decrease and then increase again during cratering. The cause for these changes may be due to changes in the friction environment throughout cratering, although how this process works exactly remains unclear.

Interior curtain angle – Only the last of three measurements techniques discussed can measure this interior curtain angle (measured at the interior wall of transient craters). Unlike ejection angle, it only decreases as cratering proceeds for the fine glass spheres where such data have been measured. Additional data for sand targets are currently being analyzed to gain further insights on the connection with the ejection angle results.

Crater modification – The dynamic angle of repose appears to dominate when modification ceases. Indeed, when slopes reach 20deg at the crater wall, all motion ceases for the case of the fine glass beads of Table 1. Significant crater modification is observed, with great changes in the transient crater diameter and depth significantly [7]. Additional analyzes in sand and finer glass beads are currently underway to confirm these preliminary results and will be reported.

References – [1] Fulmer, C.V. and W.A. Short, Rock Induration and crater shape, *Icarus* 2, 452, 1963. [2] Shoemaker, E.M., In *The Moon*, eds Middlehurst, B.M. and Kuiper, G.P., Univ. of Chicago Press, Chicago, 301,1963. [3] Pike, R.J., *PLPSC* 11, 2159, 1980. [4] Stewart, S.T. and Valiant, G.J. *MAPS* 41, 1509-1537, 2006. [5] Cintala M.J.,et al., *MAPS* 34, 605, 1998. [6] Anderson J.L.B., et al., *MAPS* 39, 303, 2004. [7] Barnouin-Jha O.S. et al., *Icarus*, 188, 506, 2007. [8] Barnouin-Jha O.S. et al., *LPSC, 36*, 1585, 2005. [9] Anderson J.L.B., et al., *LPSC, 38*, 2266, 2007. [10] Yamamoto S. et al., *LPSC*, 38, 1452, 2007. [11] Holsapple , K., *AREPS*, 21, 333, 1993. [12] Housen K.R., et al., *JGR* 88, 2485, 1983. [13] Yamamoto S. et al., *MAPS*, 183, 215, 2006. [14] Schmidt, R. M., *PLPSC* 11, 2099, 1980. [15] Gault, D. and C. P. Sonnet, *GSA Special Paper 190*, 69, 1982.

Table 1. Preliminary comparison of crater efficiency parameter α from mass displaced by impact.

Target type	Projectile size, *a* (cm)	Grain size, *d* (cm)	Impact Velocity, *U* (km/s)	Porosity, ϕ	Angle of repose*	Scaling parameter, α	Ref.
Coarse glass spheres	0.318 Gl	0.318	0.5-2.5	0.36	26	0.60±0.08	[8]
Fine glass spheres	0.9 Px	0.022	0.08-0.3	0.36	25	0.58±0.05	[7]
Coarse sand	0.476 Al	0.1-0.3	0.9-2.0	0.44	38	0.45±0.01	[5]
Coarse sand	0.318 Gl	0.05-0.1	0.3-1.7	0.44	34	0.45±0.01	[5]
20- 40 Sand	0.635 Al	0.0457	~1.0	0.38	32	0.46	[6]
Ottawa sand	0.318-1.22	~0.01	1.77-7.25	0.33	35	0.51	[14]
Water	0.318-1.22	NA	1.0-3.0	0	0	0.65	[14,15]

* Angle of Repose = Friction angle when cohesion is small (probably true for most of these targets)

DEPTH AND DIAMETER RELATIONSHIPS OF MARTIAN AND TERRESTRIAL PLANET COMPLEX IMPACT CRATERS:

Joseph M. Boyce, Hawaii Institute of Geophysics and Planetology, University of Hawaii, Honolulu, Hawaii, 96822, jboyce@higp.hawaii.edu.

Introduction: The goal of this study is to substantially improve our knowledge of the final, post-formation depth (d_r, average rim height to bottom of the floor) to diameter (D, rim crest to rim crest) function of complex impact craters. The focus of this study is Mars, but preliminary data for complex craters on all terrestrial planets is also discussed. This function is an essential benchmark for studies that utilize crater geometry as their basis.

In previous studies the "fresh crater" d_r/D function for crater populations was often used as a proxy to describe the final, post-crater formation d_r/D function. These studies employed an empirical approach that produced inconsistent results and, at best, yielded only an average fresh crater curve because they fit the curve to a population of fresh impact craters. The total number of fresh craters and their depth range were chosen by each investigator, and as a result varied from investigation to investigation [e.g., 1, 2, 3, 4, 5]. Further complicating the situation, the simple/complex transition can vary broadly from place to place on Mars [1, 3, 4], consequently, the inadvertent inclusion of craters in this transition when calculating the different segments of the curve would affect the slope of their curves. Furthermore, the affects of other processes on the morphology of craters larger than ~ 50 km can also affects crater shape [6].

In this study, the final, post-formation d_r/D function is determined for craters after the end of crater modification (see 19). Only the deepest and morphologically freshest craters (i.e., those with well-developed small-scale primary impact features such as secondary crater fields, or rays, and few superposed craters) are used. Such craters are rare because of the relatively low impact flux of bodies that produce impact craters of the size of complex craters [8], and because the initially steep interior slopes of newly formed craters are rapid reduced by slumping and sliding into the crater. While having the freshest morphology, these craters have probably existed on Mars for, at least, thousands of years with gravity acting on the fractured rock to reduce the initially steep interior slopes.

The d_r and D for 6047 craters (5077 measured from MOLA DEM data utilizing the IMPACT Program of [9] and 970 craters measured from MOLA shot data) found in globally distributed test areas are used in this study. The d_r/D of these craters is plotted in Figure 1 and also includes the craters identified as the deepest, freshest (15) and fresh (87) in this study (binned in geometrically increasing-diameter size bins), and the anomalously deep craters in Isidis and S. Utopia Planitia regions previously identified [3].

Results: The best-fit d_r/D function of the complex craters 12 - 49 km diameter identified in this study as the deepest and freshest complex craters is plotted in Figure 1 (top) and is $d_r = 0.381\ D^{0.52}$ ($r^2 = 0.98$). The high r^2 value suggests little dispersion of these craters from the function, indicating 1) a strong correlation between the two variables, and 2) that other factors, such as target properties or erosion/infilling processes, have had little effect on crater geometry. In addition, the geographic distribution of the deepest, freshest craters, 12 - 49 km diameter is globally random (e.g., the nearest neighbor statistic, R = 1.18 for large pristine crater), but is not for such craters < 12 km diameter [10]. This suggests that target material properties (e.g. strength) have an effect on crater d_r/D for craters < 12 km diameter, but not for ones > 12 km diameter.

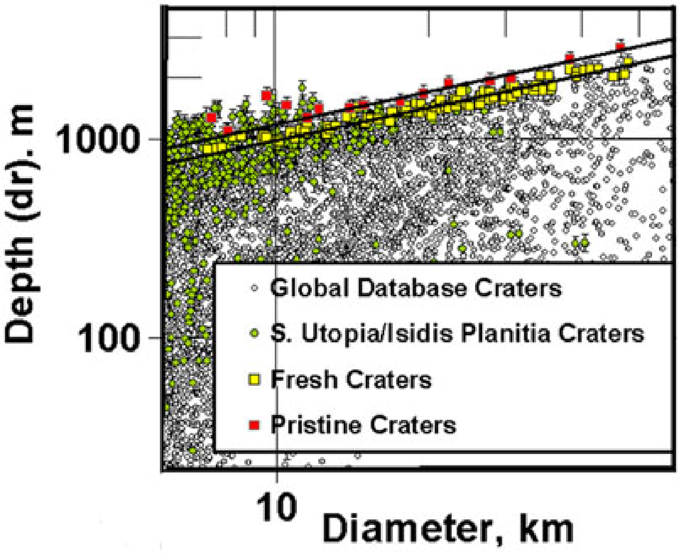

Figure 1. Scatter diagram showing d_r/D of craters in this study, including the deepest, freshest craters (i.e., pristine) (red squares), fresh craters (yellow squares), craters in the S. Utopia and Isidis Planitia region (green triangles) and their measurement error bars, and all other craters (open circles without error bars). Pristine craters average ~ 7 % +/- 3% deeper than the next deepest fresh craters. The best-fit curve is included for the pristine (top) and fresh (bottom) crater d_r/D functions.

For comparison purposes, we have also estimated the global fresh crater d_r/D function using the traditional method of identifying the freshest craters (in this case 4 freshest craters plus the deepest, fresh crater in the same bins as the deepest, fresh craters) in the size range of 12 to 49 km diameter and fitting a best-fit function through them. The best-fit curve for these fresh craters is also plotted in Figure 1 (bottom) and is $d_r = 0.315\ D^{0.52}$ ($r^2 = 0.82$). To further test for consistency, the best-fit fresh crater function and r^2 were also calculated using 1, 2 and 3 of the fresh craters (plus the deepest fresh crater) in each bin. We found that while the constant in the function decreases with number of fresh crater/bin (0.363, 0.356, and 0.333 respectively); the exponent remains nearly content at about 0.52 +/-0.004.

In addition, even though some regions, such as in south Utopia and Isidis Planitia where the simple/complex crater transition has been extended to ~ 11.8 km diameter because of anomalous (strong) target material [4, 5], the best-fit curves for deep, fresh craters above this transition are the same as in other regions (Figure 1).

Discussion and Conclusion: The data provide evidence for one global Martian complex crater d_r/D function. Such a global d_r/D function is suggested by 1) the limited dispersion (i.e., high r^2 value) from a best-fit function of the d_r/D values of the deepest, fresh craters, 2) earlier studies that found no statistically significant correlation of fresh complex crater d_r/D on different terrain types on Mars [1, 7], 3) the similarity in the slopes of the d_r/D function for the deepest, fresh and progressively fresher complex craters suggesting that all these craters are part of the same evolving crater population, and 4) the similarity in all regions of the dr/D curves of the deepest fresh complex craters including regions with anomalous target materials. While these data suggest one global complex crater function, small differences in the d_r/D function from region to region are possible, but they would have to be below the inherent errors of the data and hence undetectable with the available data.

Terrestrial Planets: The approach used for Martian craters has been applied to d_r/D data collected in previous studies for the terrestrial planets [e.g., 11, 12, 13, 14, 15, 16, 17, 18], and new data for the Moon collected in this study and have been used to estimate the simple/complex crater transition for each terrestrial planet. This approach produces results that are more readily inter-comparable (see earlier discussion). These transitions have been plotted against the acceleration of gravity for each of the respective planets in Figure 2 and show a relationship of $D_{transition} = 199\ G^{-0.60}$ ($r^2 = 0.98$).

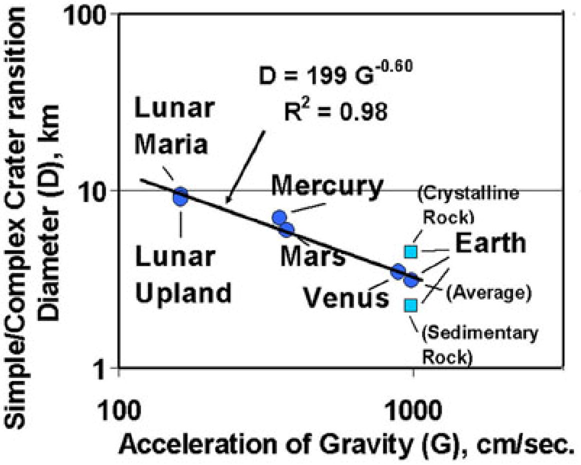

Figure 2. Plot of the relationship between the simple/Complex transition and strength of the gravity of the terrestrial planets.

Reference: [1] Pike, R.J., (1980), Proc. *Lunar and Planet Sci Conf. 11th*, 2159-2190.[2] Garvin, J. B., S. E. H. Sakamoto, J. J. Frawley, and C. Schnetzler (2000), *Icarus*, 144, 329-352. [3] Garvin, J. B., S. E. H., Sakamoto, and J. J. Frawley (2003), *6th Mars conf.*, abstract # 3277.; [4] Boyce, J.M., P. J. Mouginis-Mark, H. Garbeil, and L. Tornabene (2006), *Geophy. Res. Lett.*, L06202, doi.10.1029/ 2005GL024462.; [5] Stewart, S. T., and G. J. Valiant (2005), *Meteor and Planet Sci*., 41, (10), 1509-1537.; [6] Pathare, A. V. D. A. Paige, E. P. Turtle, and W. K. Hartmann, (2002), *Lunar Planet. Sci.*, [CD-ROM], XXXIII, abstract, # 1972.; [7] Pike, R.J., (1977), *In Impact and explosion cratering* (eds. D.J. Roddy, R.O. Pepin, and R.B. Merrill), Pergamon Press, New York, 489-510.; [8] Hartmann, W. K. (2005), *Icarus*, 174, 294-320.; [9] Mouginis-Mark, P.J., H. Garbeil, J.M. Boyce, C.S.E. Ui, and S.M. Baloga (2004),. *J. Geophys. Res. – Planets*, 109, E08006, doi: 10.1029/ 2003JE002147.; [10] Boyce, J.M., and H. Garbeil (2007), *Geophy. Res. Lett.*, submitted.; [11] Wood, C, and Anderson, (1978) *Proc Lunar Plant. Sci Conf.*, P3669-3690; [12] Croft, S., (1978) *Proc Lunar Plant. Sci Conf.*, P. 3711-3735; [13] Pike, R., (1988), In Mercury, (eds.), p 165-273; [15] Grieve R., and G. Shoemaker, (1994), In *Hazards Due to Comets and Asteroids*, ed. T Geherls (Tucson: Univ. Arizona Press), 417-462.; [16] Sharpton, V. I., (1994), In *Large Meteorite Impacts and Planetary Evolution*, eds B.O. Dressler, R. Grieve, and V. I Sharpton, GSA SP-293 (Boulder: GSA), pp. 19-27.; [17] McKinnon, W. B., K. Zahnle, B. Ivonov, and H.J. Melosh (1997), Venus II, U Ariz. Press., (Bouger, Hunten and Phillips Eds.), 969-1014; [18] Herrick R., V. Sharpton, M. malin, S. Lyons, and K. Feely, (1997), In Venus II, U. Ariz. Press., (Bouger, Hunten and Phillips Eds.), 1015-1046.; [19] Melosh H. J., (1989), Oxford press, NY, 245.

THE EFFECT OF TARGET PROPERTIES ON IMPACT CRATER MORPHOLOGY – COMPARISON OF CRATERS ON ICY AND SILICATE BODIES.

V. J. Bray[1] , G. S. Collins[1], J. V. Morgan[1] and P. M. Schenk[2], [1]Earth Science and Engineering Department, Imperial College London, Exhibition Road, London, SW7 2BP, UK, veronica.bray@imperial.ac.uk, [2]Lunar and Planetary Institute, 3600 Bay Area Blvd., Houston, Texas, 77058.

Introduction: The icy Galilean moons of Europa, Ganymede and Callisto display exotic crater morphologies with no obvious analogue to craters on silicate bodies. As the Moon and Galilean satellites have similar gravity, differences in crater morphology are likely due to icy lithospheres being mechanically distinct from rocky bodies. The presence of subsurface liquid layers is also thought to affect crater morphology [1]. As the cratering process is affected by target properties, the study of crater morphology on the icy satellites provides a means for investigating the upper-crustal structure of these bodies.

To understand the effects of layering on crater morphology, the underlying impact process in ice must first be understood. To understand crater formation requires two major elements: sufficient observational data, to inspire formation theories and provide ground truth data, and a means to test these proposed formation processes—numerical models. Craters on Europa are likely to be heavily affected by its sub-surface ocean as it is relatively close to the surface [2]. As Ganymede's ocean is at a greater depth, craters on Ganymede provide better observational data for the investigation of impact into unlayered ice. We present scaling trends of complex crater dimensions drawn from topographic profiles of craters on Ganymede. We compare these trends with those of analogous features in craters on the Moon, and investigate the relationship between these morphological trends and target strength using dynamic modeling.

We collected topographic profiles of 48 craters on both dark and bright terrains of Ganymede from *Galileo* data. Most craters profiled were relatively young so that good comparison could be made with fresh impact craters on the moon and final craters produced by our computer models. Several cross-sectional profiles were taken of each impact crater so that any artifacts introduced as a result of the profiling technique, or features superimposed after impact, could be identified and removed. We then collected measurements from each crater, including crater depths and diameters, heights and widths of central features, and slope angles. When a variance in (e.g.) central peak width between each of the topographic profiles of the same crater was evident, the maximum value was adopted. The variety of scaling trends presented here represent the variation in maximum values.

Comparison of craters on Ganymede and the moon

Rim Slope Angle and Material Strength: The rim slopes of craters on Ganymede are consistently shallower than for lunar craters (Fig. 1a). As the slope angle is a proxy for the effective coefficient of friction of the target, this difference is indicative of the Ganymede surface ice being weaker than the lunar surface. The rim-slope of lunar craters decreases as crater diameter increases from ~29° for craters 10km in diameter to ~14° for 60 km craters [3]; this decrease in slope angle demonstrates an effective weakening of the target material as crater size increases. A similar decrease in slope angle with increasing crater size is evident in Ganymede craters where rim slope decreases from ~24° for a 10 km crater to 17° for 60 km craters. This suggests that the relative amount of material weakening during impact is similar in icy targets.

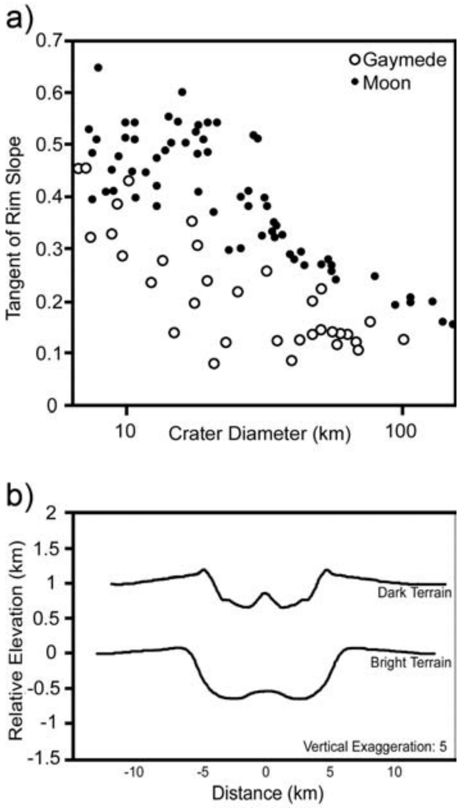

Figure 1:a) Relationship between the tangent of the rim slope for craters on the Moon [3] and Ganymede. b) Topographic profiles across typical central peak craters on Ganymede bright (39N 193W) and dark terrain (13N 200W). The relatively angular peak of the crater in dark terrain is evident. These profiles are averaged about their central point to produce an axially symmetric profile.

Central peak width and slope

Central peak craters on Ganymede have previously been reported up to diameters of 35 km [4]. We have measured 17 central peak craters between 5 and 31 km in diameter and one with a diameter of 50 km. We recorded central peak widths of 1.5 to 17.5 km and found that peak width, W, increased linearly with increasing crater diameter, D: W ≈ 0.30D. This trend is similar to that of lunar central peaks craters (W ≈ 0.22D [5]). Central peaks on the bright terrain of Ganymede appear more rounded than those on dark terrain (Fig. 1b). The slopes of central peaks in dark terrain craters are on average ~4° steeper than those in bright terrain craters. This is consistent with the dark terrain material comprising an ice-rock mix, where the rock component increases the angle of repose relative to that in the pure-ice bright terrain.

Central Pit Craters

On silicate bodies, the morphological class of crater next in size after central peak craters is the peak ring crater. No peak ring craters have yet been observed on Ganymede [6]. Instead, central pit craters replace the peak-ring morphology expected for similar diameter craters on rocky bodies. Pit craters are characterized by terraced rims and flattened floors with a rimmed pit at or near the center (Fig. 2). Although there is no consensus on the formation mechanism for central pits, it as been suggested that they form by a similar mechanism to peak rings in silicate targets, involving the downward and outward collapse of a large central peak [4]. However, it is not clear why such collapse in ice would cause a pit rather than centralized broken massifs as in the lunar crater Copernicus. An alternative, but similar idea is the multiple peak oscillation theory [7] which supposes that the target acts as a Bingham fluid during impact and has the summit pit form by repeated oscillations of the central region of the crater.

The majority of profiles that we collected across craters with summit pits also contained an extra topographic ring feature (Fig. 3) which increases in diameter, Wr, proportionally with increasing crater size: Wr ≈ 0.4D.This value lies between the predicted diameter of central peaks (W ≈ 0.3D) and of peak-rings on the Moon (Wpr ≈ 0.5D [8]). This feature could be caused by oscillations of the crater floor following collapse of the transient cavity, or by collapse and run out of an over-heightened central uplift. In either case, it suggests that the central pit crater morphology forms during the impact event, which provides useful constraints for ongoing models of crater collapse in ice targets.

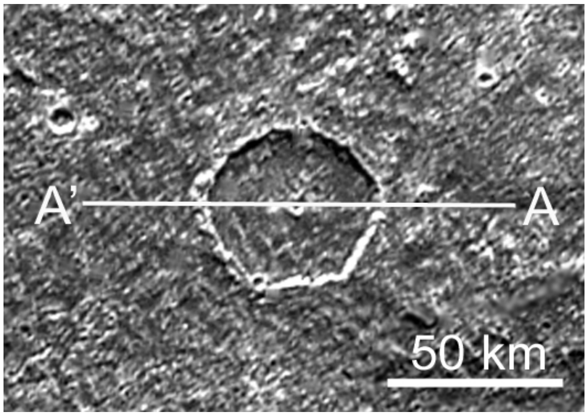

Figure 2: Image of a summit pit crater on dark terrain at 38N 140W (North is right). A possible ring between the summit pit and the crater rim is visible in the southern section of the crater and appears clearly in profile (figure 3).

To investigate the observed differences between central peak crater morphology on the Moon and icy satellites, and the possible formation mechanisms of central pits, we are simulating complex crater collapse in ice using numerical models. We are running suites of models with variable strengths, to determine which sets of parameters produce the best match to central peak craters on Ganymede. Once our strength model is well constrained, we will investigate the progression of larger craters and the effect of fluid layers.

References: [1]Schenk, P. M. (1993), JGR 98, 7475-7498. [2]Schenk, P. M.(2002), Nature, Vol. 417, 419-421. [3]Pike, R. (1977), 489-509 of Impact and Explosion Cratering, Pergamon Press. [4]Passey,Q. and E.Shoemaker (1982), 340–378 of Satellites of Jupiter, UofA Press. [5]Hale,W. and R.Grieve (1982), JGR 87, Suppl.:A65-A76. [6]Croft, S.(1983), LPS XIV, JGR, 88, B71-B89. [7]Melosh, H. J. (1982), JGR 87, 371-380. [8] Wood,C.A. and J.W.Head (1976), Proc. LPS VII, 3629-3651.

Figure 3 (below): Topographic profile of the crater in Fig.2. R marks the crater rims, S denotes the summit surrounding the central pit and black arrows show the intermediate uplift. These uplifted regions were visible in all 4 cross-sectional profiles of the crater indicating that the feature marked with arrows is part of a ring structure. The diameter of the ring in this example is ~24 km, 0.4 times the crater diameter.

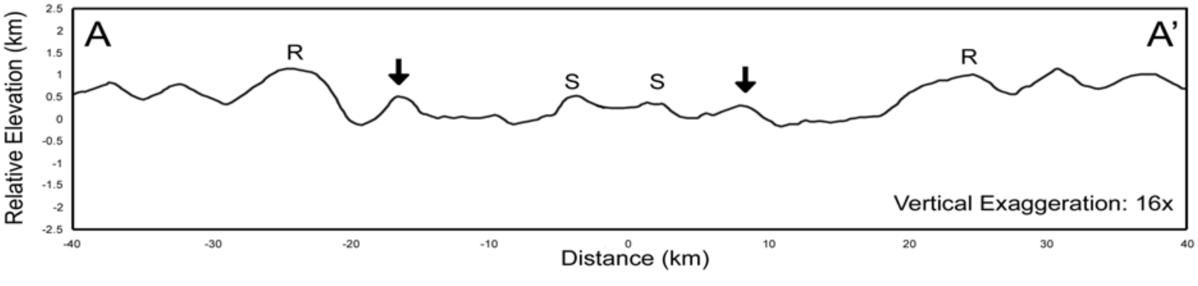

BRIGHT-HALOED CRATERS IN CHRYSE PLANITIA AND IMPLICATIONS FOR TARGET PROPERTIES.

D. L. Buczkowski, O. S. Barnouin-Jha and A. Weaver, Johns Hopkins University Applied Physics Laboratory, Laurel, MD 20723 (debra.buczkowski@jhuapl.edu)

Introduction: We study bright-haloed craters seen in northern Chryse Planitia. We combine imaging data from Mars Odessey, Mars Global Surveyor (MGS) and Viking, and use topographic data from the laser altimeter (MOLA) aboard MGS. We also consider the geological map generated by [1]. The results of this analysis and their implications for the origin of these craters are discussed below.

Bright Haloed Craters: The main defining characteristic of the bright-haloed craters in Chryse Planitia is the presence of a bright debris apron that extends for some distance beyond the crater rim (Fig. 1). Often, the distal edge of these deposits possess a wispy appearance. The bright halos around many of the craters are visible in both the old, low-resolution Viking orbiter visible images and in the more recent 100 m/pixel THEMIS infrared images. Other craters have a distinct bright halo in THEMIS infrared but only a faint halo in visible Viking imagery. All bright-haloed craters in Chryse Planitia are small, ranging in size from approximately 1 to10 km in diameter.

Many of the smaller bright-haloed craters have no other obvious ejecta while the larger bright-haloed craters (>9 km diameter) have interior continuous ejecta that appear fluidized and possess a contiguous rampart surrounding the crater (Fig. 1). All of the craters that have bright halos in both Viking and THEMIS images appear fresh, possessing at THEMIS resolution little or no infill, sharp rims and interior structures. The craters with bright halos only in THEMIS images appear more degraded and perhaps older.

THEMIS images (e.g. Fig. 1) also show that small impacts into the bright-halo materials sometimes excavate dark materials that resemble the surrounding terrain beyond. The sharp contrast between these dark and bright materials essentially produce small "dark" haloed craters.

Topographic Expression: Individual topographic profiles obtained by MOLA indicate that the bright halos are very thin and have little topographic expression. They may be associated with an increase in roughness relative to what is seen beyond the halos, but not typically. They may also possess a small rampart-like feature at their distal ends, but such structures could have existed prior to crater formation and may have simply arrested ejecta flow. It is clear from Figure 2, that a large mound to the north of the crater delineates the edge of the bright apron: no material is deposited beyond it. Such shadowing does not typically occur during ballistic ejecta emplacement [2].

Geologic Setting: Many of the bright-haloed craters are found on the scattered deposits of the Ares Vallis unit (HCa) [1] in Chryse Planitia. HCa is interpreted to be Late Hesperian deposits with with a coarse grained or indurated cap. The halos on these craters tend to be just barely visible in Viking images but are quite prominent in THEMIS.

Six of the haloed craters identified in Chryse Planetia are located in fairly close proximity on a small topographic plateau near its northern boundary (Fig. 3). They are distributed on the Chryse Planitia 3 unit (HCc$_3$), as defined by [1] and are interpreted as Late Hesperian fluvial deposits; HCc$_3$ is coeval or perhaps just stratigraphically above the HCa unit. The halos around these craters are bright in both the Viking and THEMIS images. Three very small craters (>1 km) are found directly to the south of this plateau in the HCa unit; they too are bright in both Viking and THEMIS images.

It should be noted that not all craters present in the HCa and HCc$_3$ units are haloed. However, the unhaloed craters are often degraded in appearance and may be older. Furthermore, while there are large deposits of HCc$_3$ found to the west in Chryse Planitia, no bright-haloed craters are found in this extensive outcrop; whatever factors are responsible for the formation of the halos in this unit, they seem to be limited to the constrained region of the small eastern plateau.

Aeolian processes are responsible for streak deposits on of the south-west side of many craters and other topographic features in Chryse Planitia. These wind-related processes do not seem to affect the bright-halos in any way, as they seem to extend more or less radially around the craters except when obstructed by local topography.

Implications: The bright-haloed craters in Chryse Planitia possess several characteristics:

1) All are located in two geologic units, implying that target properties may be a contributing factor. It is possible that those craters found in the HCc$_3$ unit may have bright halos because of underlying HCa.

2) Freshness of craters suggests that they may have formed in recent times, under similar atmospheric conditons. Fresher looking craters have bright halos in both visible and infrared imagery while older craters have obvious halos only in THEMIS images. This may indicate an evolution in the nature of the halos with time.

3) The halos possess a wispy distal character, suggesting that they are not the result of ballistic deposition. Such wispy deposits are often seen at the distal edge of fine ejecta deposited during laboratory impacts in an atmosphere [Schultz, 1992].

4) Topography delineates the edge of the flow, and confirms that the bright halos are the result of a

ground-hugging flow. Scouring of the target by a shock is probably not the cause of these deposits [4].

5) Some bright halos have been impacted with small craters that have formed dark halos around them. The dark halo material is similar to the surrounding terrain. This indicates that the dark haloed impacts have excavated to the terrain underlying the bright halo deposits.

6) Wind erosion of surrounding terrain but not of the halos implies that the halo material is either very fine or quite coarse. This conclusion is based on wind threshold analysis [e.g. 5] that indicate that extremely fine-grained materials or coarse grains will not be entrained by common winds.

References: [1] Tanaka K.L., Skinner J.A. and Hare T.M. (2005) USGS Sci. Inv. Series Map 2888. [2] Barnouin-Jha O.S. and Buczkowski D.L. (2007) LPSC XXXVIII, abs. 1304. [3] Schultz P.H. (1992) JGR 97, 11623. [4] Wrobel K., Shultz P.H. And Crawford D.A. (1996) Met. Plan. Sci. 41, 1539-1550. [5] Greeley and Iversen (1997)

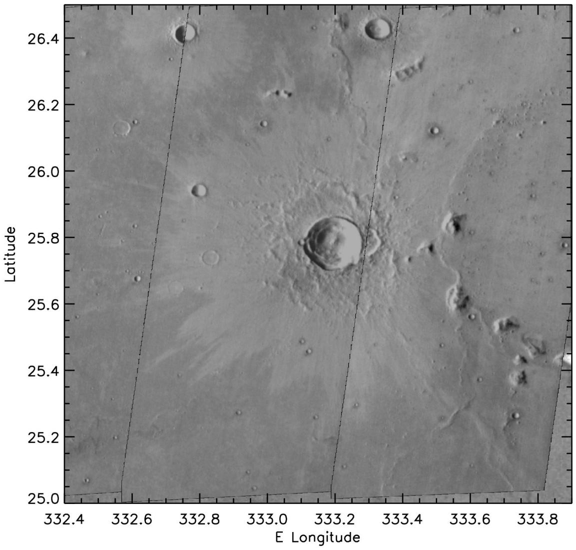

Figure 1. Bright-haloed crater (9.4 km) in Chryse Planitia. A Fluidized ejecta blanket is interior to the halo.

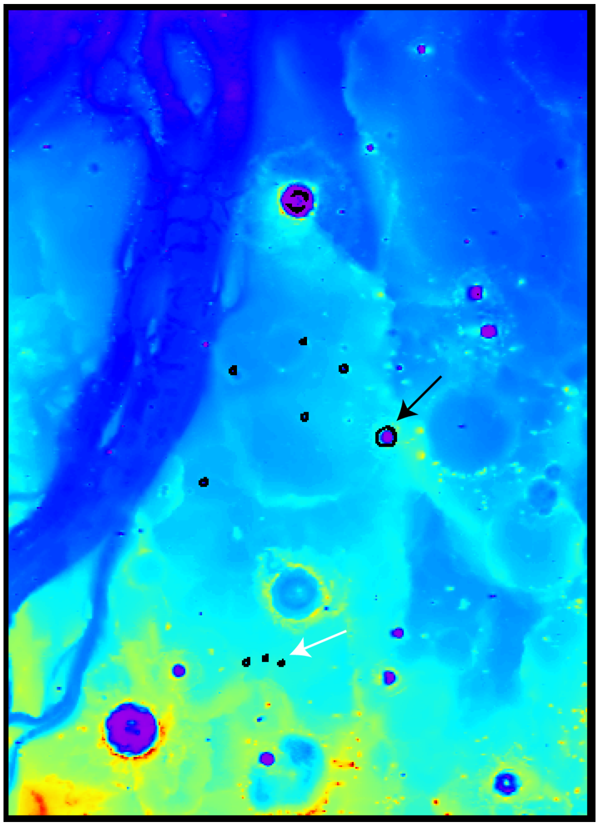

Figure 2. MOLA DTM showing the location of bright-haloed craters (black circles) on a small plateau of the HCc$_3$ unit to the north-east in Chryse Planitia. The plateau has a elevation between that of Chryse Planitia proper to the southwest and the lowland plains to the north. Black arrow points to the crater in figure 1. White arrow points to three bright-haloed craters are in the HCa unit.

STARDUST CRATERS AND TRACKS: IN SPACE AND IN THE LABORATORY. M. J. Burchell[1], A. T. Kearsley[2] and F. Hörz[3]. [1]School of Physical Sciences, Ingram Building, Univ. of Kent, Canterbury, Kent CT2 7NH, UK. M.J.Burchell@kent.ac.uk, [2]Department of Mineralogy, Natural History Museum, London, SW7 5BD, UK. [3]NASA Johnson Space Centre, Houston, Texas, USA.

Introduction: The high speed impacts that cause cratering are simply the result of orbital and in-fall speeds and are not per se limited to large bodies and geological scale events. Hypervelocity impacts (speed greater than ~ 1 km s^{-1}) also occur for small impactors. Use has been made of this for decades to harvest small dust grains in space. In addition, studies of micrometeorite impact craters on lunar samples and laboratory studies of space weathering by micro-impacts have all combined laboratory studies with study of the properties of natural solar system materials.

Recently, the "harvest" collection concept was used by the NASA Stardust mission [1] which flew past comet 81P/Wild-2 in 2004 at an encounter speed of 6.1 km s^{-1} [2], returning dust samples to Earth in 2006 [3]. Stardust sampled the cometary dust both by cratering in aluminium foils and via capture in aerogel [4]. The problem in the subsequent analysis is to determine the pre-impact properties of the dust grains from the observed features in the foil and aerogel (two very different materials, one highly porous). There is a need to understand the impact processes in detail. Although the typical impactor is < 100 um in size, possible insights applicable to large structures may be gained as well, such as the scaling of target and projectile densities or mineralogical and compositional alterations of the projectiles, including selective vaporization.

Some simplifications apply to the Stardust calibrations; the impact speed (6.1 km s^{-1}) and direction (normal or near normal incidence) and the target materials are well known and constant for every impact, and the projectile speed and size regimes are accessible by experiment. For Stardust a large programme of laboratory calibrations was undertaken. This began before the samples were returned and has continued since, informed by the features observed in the data. The method involved direct comparison of observed features with those recreated in the laboratory using two stage light gas guns. Attempts to use numerical modeling of the impacts are still at a preliminary level.

Cratering in Foils: The foil used on the Stardust cometary collector was aluminium Al 1100. It was ~101 μm thick, with exposed area 153 cm^2. Craters were readily observed on the foil after return to Earth (Fig. 1). Due to the resolution in the analysis, these are split into two groups: Large craters are those above 10 μm dia., small craters were those below 5 μm dia. The large craters were located by low resolution optical scans of many strips of foil post flight. The small craters were found via higher resolution SEM work on a small part of the area of a limited number of foils [4].

The initial calibration [5] was made using spherical soda lime glass beads, fired in a series of shots using light gas guns at the Univ. of Kent and NASA. Each shot contained a monodispersive sample of beads, sizes from 10 – 80 μm dia. The results were fairly circular craters (in plane view) with smooth walls and slightly irregular overhanging lips at the crater edges, very similar to Fig. 1.

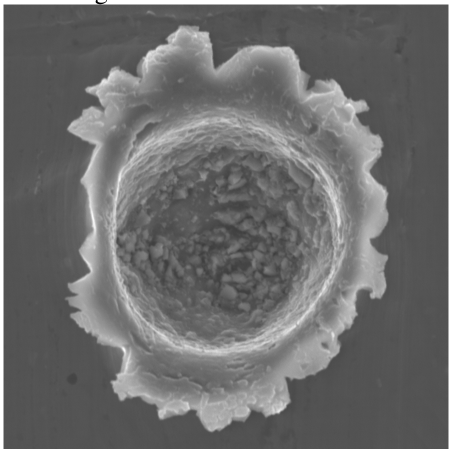

Fig 1. Comet Wild 2 olivine dust grain impact onto Stardust foil C086N,1 at 6.1 kms^{-1}. Crater dia is approx. 50 microns. (Top view)

During the post flight analysis a wide range of crater shapes and wall textures were visible in the Stardust data. Accordingly, more shots were carried out at Kent, varying projectile density and shape [6], mineral composition, etc. The full range of characteristics of the observed Stardust craters can now be reproduced.

Reproducing the full range of crater depth – diameter ratios observed in the Stardust data was informative. For monolithic grains two main features were found to control this parameter: the grain shape (spherical or more elongated along one axis) and density. Spherical projectiles of density similar to the target produced hemispherical craters with lower density produced shallower craters and elongated impactors striking along their main axis produced deeper craters. Combined with residue analysis on the Stardust craters, this helps constrain both projectile density and shape.

A second important group of craters were those with very shallow shapes (small depth / dia. ratio) and multiple pits in the crater floor. One of the 7 large craters in the initial analysis sample meets this description and had 12 internal pits. A simple hypothesis for such an impact feature is that it consisted of 12 discrete grains striking near simultaneously over a region of some 100 or so µm^2. This is incompatible with the observed flux rate, but if a single extended grain with multiple components were to have struck this naively would produce the required crater shape. This suggests a highly porous grain, or a grain with dense (mineral) cores held together in a much lower density and more volatile glue (organic). Traditionally, such a hypothesis is hard to test in a light gas gun facility, as it would collapse during the initial acceleration in the gun. However, two new approaches were applied. First individual mineral grains (size down to less than 10 µm) were glued together using organic glues. Second, pellets of sintered SiO_2 grains [7] (individual grain size 1.5 µm) were used. Both types of projectile (one of widely differing density materials and the other a highly porous material) were sufficiently robust to survive launch in the gun and produced the desired crater shape (shallow crater with multiple pits). It is not necessarily clear which type of impactor made the Stardust craters, or it may have been a combination of both.

Aerogel Tracks: Although hypervelocity impacts are widely held to involve complete disruption of the projectile, this is in fact a misconception. If the target material is porous, the shock pressures on impact are reduced. In the limit, if a highly porous material with relatively thin solids is used, the projectile can tunnel into the target, with relatively minimal alteration or disruption. Aerogel is such a target material, it can be made with densities down to just a few kg m^{-3}. A recent review of the use of aerogel as a cosmic dust collector is given in [8].

For Stardust aerogel data, two calibrations were required. The first was to use soda lime glass beads (as with the foil calibration) to produce a track size vs. impactor size calibration. The second was to use a range of impactor materials to produce the variety of track types observed in the Stardust aerogels. These types were classified into 3 groups (A, B, C) depending on their morphology. Type A were narrow, relatively long tracks with a single grain at their end. Type B had broad initial cavities with one or several narrow tracks emerging underneath, each containing a fragment of a dust grain. Type C tracks had solely a broad cavity with no distinct tracks emerging from them. Associating these classes of tracks with impactor properties was a key feature of the calibration work. The preliminary results are in [4]. Type A tracks were found to be due to well consolidated, homogeneous impactors similar to olivine grains. Type B (example shown in Fig 2) were either non-cohesive impactors with a variety of individual grain sizes and various compositions, or they could have been due to volatile rich impactors which disrupt on impact. Type C were similar to B but with no large discrete components and which disaggregated into sub-micron particles in impact. It appears that radial dispersion of solids played a more prominent role in the formation of these bulbous structures than the liberation and expansion of vapors. .

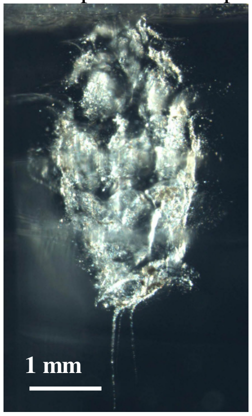

Fig. 2. Example of Type B impact (C092_T1) from Stardust cometary aerogel tray (Level 3 images). Impact direction was from the top. (Side view)

Conclusions: An extensive light gas gun impact programme was carried out to assist in the interpretation of the interpretation of the impact features on the Stardust spacecraft. This was unusual compared to most impact studies in that the size and speed of impact features in space can be directly reproduced in the laboratory. A feature of the work was two greatly dissimilar target materials (one highly porous) yielding very different results from similar impacts. The results successfully reproduce many of the features observed on Stardust. As well as crater and track morphology, studies of laboratory samples has permitted detailed understanding of the amount of the impactors retained at the impact sites and degree of impact processing it has undergone.

References: [1] Brownlee D. E. et al. (2003) *JGR, 108(E10)*, 8111, 1 – 15. [2] Brownlee D. E. et al. (2004) *Science, 304*, 1764 – 1769. [3] Brownlee D. E. et al., (2006) *Science 314*, 1711 – 1716. [4] Hörz F. et al. (2006) *Science 314*, 1717 – 1719. [5] Kearsley et al. (2006) *Meteoritics & Planet. Sci., 41,* 167 – 180. [6] Kearsley et al. (2007) *Meteoritics & Planet. Sci., 42,* 191 – 210. [7] Poppe T (2003) *Icarus, 164*, 139 – 148. [8] Burchell M.J. et al. (2006) *Ann. Rev. Earth. Planet. Sci., 34*, 385 – 418.

Acknowledgements: Kent thanks PPARC for grant support. The authors wish to thank all those who worked on the Stardust post flight analysis.

THE SMART 1 IMPACT EVENT: FROM THE LABORATORY TO THE MOON.

M. J. Burchell[1], R. Robin Williams[1], B.H. Foing[2], and the Smart 1 Impact Campaign Team. [1]School of Physical Sciences, Ingram Building, Univ. of Kent, Canterbury, Kent CT2 7NH, UK. M.J.Burchell@kent.ac.uk. [2]Space Science Dept., ESA – ESTEC, Postbus 229, 2200 AG Noordwijk, The Netherlands.

Introduction: Although the lunar surface is heavily cratered, there has been no well understood, well observed lunar impact event. This ignores the folk law "impacts" such as the Canterbury event of 1178AD, a lunar light flash recorded in contemporary literature and more recently suggested as the possible origin of lunar crater Giordano Bruno [1, 2]. It also ignores the somewhat better founded reports of lunar light flashes of more recent years and the seismic impact data from the Apollo era in-situ lunar seismometers (e.g. [3]). The problem in these latter cases is the lack of knowledge either of the impactor or the resulting crater.

However, the recent demise of the ESA spacecraft Smart 1 in a deliberate impact upon the moon provides a more definite impact event for study. The Smart 1 mission [4 – 6] was deliberately ended by a controlled impact of the 285 kg spacecraft onto the Moon's surface. The impact was at 2 km s^{-1} and at a shallow angle of 1° from the horizontal. The resulting light flash was observed from the Earth [7, 8]. This event offers the opportunity to attempt to explain a well constrained impact event on a rocky body. The crater is as yet still unobserved, but should be within the capability of future lunar orbiters to image. The analysis is thus a blind test of the ability of laboratory experimentation and/or modeling to explain a geological impact event.

Method: The speed of the Smart 1 impact event is within the range of laboratory impacts using guns, but the mass of the spacecraft exceeds the ability of any gun. Therefore laboratory experimentation alone cannot recreate the event (even neglecting the difference in lunar and terrestrial gravity). However, laboratory experiments can be used to gain insight into the processes involved in the impact. Combined with appropriate scaling models, predictions can then be made for the shape and size of the actual (as yet unseen) resulting lunar crater. In addition, there is data on the light flash and associated plume from the impact which were observed from Earth. This should also be included in any detailed explanation of the impact event.

The laboratory experiments were made using a two stage light gas gun at the Univ. of Kent [9]. The target was fine grained sand. This flows under impact into the classic bowl shaped impact crater with a raised rim. Since the Smart 1 impact was at a very shallow angle of incidence, the sand target was adjustable over a range of impact angles (here 1° to 10°). The projectiles were 2.03 mm dia. aluminium spheres. 14 shots were made at a mean speed of (2.08±0.08) km s^{-1}. Four shots were at 1°, four at 2°, four at 5° and two at 10°. The resulting craters were measured and the evolution of crater shape with impact angle was obtained as well as the overall crater sizes. By in-filling the craters after each impact the excavated crater volume was also measured. This has two components, material which flowed into the raised rim walls and that which was ejected by flight. In some impacts the rim walls were pushed back into the crater before in-filling occurred, permitting an estimate of the relative magnitudes of these two effects.

The crater shape (as seen from above) was found to remain circular until angles of incidence of 5° or less were obtained. Then increasing non-circularity was apparent. From 2° and downwards the non-circularity was increasingly due to the emergence from the main crater of secondary craters along the line of flight. Such behaviour had also been previously reported in laboratory experiments [10]. A typical crater at 1° incidence is shown in Fig. 1.

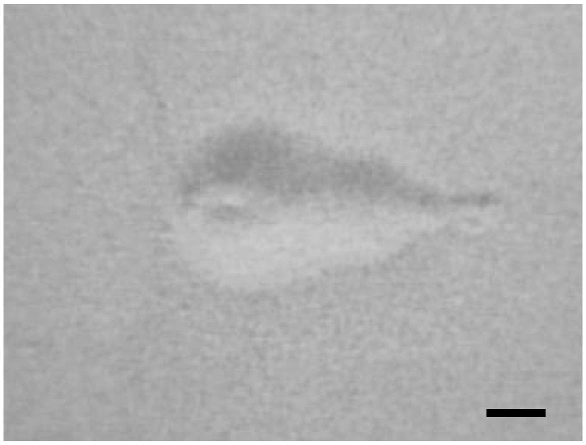

Figure 1. Impact crater in sand in the laboratory at 2 km s^{-1} and 1° incidence (from left). A 1 cm scale bar is shown (bottom right).

The craters were very shallow, with rim wall height approximately 50% of the crater depth (as measured from the original undisturbed surface plane). In these shallow angle impacts the projectile ricocheted from the surface at a very shallow angle. In general this angle was not equal to the angle of incidence; for impacts at 1° the ricochet angle was almost 1°, rising slowly to 2.5° as the impact angle was increased to 10°. Taken at face value this suggests the Smart 1 spacecraft may have bounced off the lunar surface at the initial impact site.

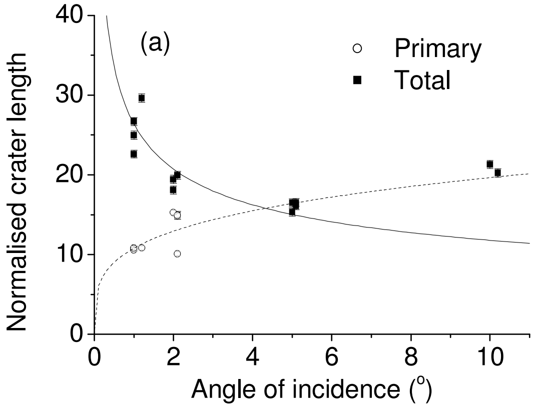

Figure 2. Evolution of crater length with impact angle. Length is shown normalized to projectile diameter.

The behaviour of the crater size and shape vs. impact angle was recorded from the laboratory data. An example is crater length (Fig. 2). In Fig. 2 the primary crater length is estimate at small angles from its general shape and total length is that of the overall impact feature. That total length is controlled at shallow angles by the emergence of other craters attached to the main crater (Fig. 1) is evident. By contrast, crater width is controlled solely by the primary crater (which is always the widest) and continues to decrease even at the shallowest angles.

However, what is of main interest here is the prediction of what the corresponding lunar impact crater will look like. When using scaling relations, there is no single, definite prescription for how to handle highly oblique impacts. Suggestions include replacing the impact speed with its perpendicular component and do not allow for the emergence of multiple impact craters. However, here we have the same angle in the lab and the impact. As a simple approximation we consider this is fixed in the two cases (lab and on the moon) and apply pi scaling to the average laboratory dimensions of the craters at 1° incidence (using total length for the length). Pi scaling (e.g. [11]) adjusts the scaled value for parameters such as crater diameter and excavation volume according to relations linked by power laws. The powers in these relations have to be defined. Here we use the mean values for sand of $\gamma = 0.5$ and β – 0.165 suggested by [11]. The scaling laws also allow for the local gravity aiding extrapolation between the laboratory (Earth) and the Moon. The results suggest that the Smart 1 impact crater on the Moon should be 5.5 m long and 1.9 m wide and depth 0.23 m. The volume of ejected material (after correction for that which flowed into the rim walls) is approximately 2200 kg.

The prediction for the impact light flash and ejecta plume observed on Earth require on-going work. Groups are still producing their estimates of the energy of the flash and the volume of material in the observed plumes.

Conclusions: The Smart 1 impact event has-been simulated in laboratory experiments. Accompanying hydrodynamical computational simulations are awaited. The event was also observed as a light flash and plume of ejecta witnessed from the Earth. Work is underway to tie all these observations into a single account of the impact event. This will necessarily be incomplete, as the crater itself has not yet been observed. However, there is the reasonable expectation that this will be observed in the future. The crater will thus act as a blind test of impact modeling (experimental and computational) and covers both the impact crater and the associated plume of ejecta. To the extent that the lunar regolith is held to be understood based on Apollo era observations, the reasonably well constrained impact represents a good test of our ability to understand impact events. The size scale is still less than the large impacts normally associated with planetary impacts and the spacecraft was an irregular shape not expected to occur naturally, but nevertheless it is one of the few well constrained Solar System impact cratering events known. When finally imaged the results may be similar to the known lunar crater Messier, long held to represent a highly oblique impact e.g. [12].

References: [1] Hartung J. B. (1976) *Meteoritics* 11, 187 – 194. [2] Calame O. and Mulholland J. D. (1978) *Science 199*, 875 – 877. [3] Duennebier F.K., Nakamura Y., Latham G. V. and Dorman H.J. (1976) *Science 192,* 1000 – 1002. [4] Foing B.H. et al. (2001) *Earth, Moon and Planets 85-86*, 523 – 531. [5] Foing B.H. et al. (2003) *Adv. Space. Res. 31*, 2323 – 2333. [6] Foing B.H. et al. (2006) *Adv. Space Res. 37*, 6 – 13. [7] Ehrenfreund P. et al. (2007). *LPSC XXXVIII*, Abstract #2446 [8] Veillet C. and Foing B. (2007) *LPSC XXXVIII*, Abstract #1520. [9] Burchell M.J. et al. (1999) *Meas. Sci. Technol.,101*, 41 – 50. [10] Gault D. E. and Wedekind J.A. (1978) Proc. 9th Lunar and Planetary Science Conf., Pergamon, New York, 3843 – 3875. [11] Melosh H.J. (1989) Impact Cratering: A Geologic Process, OUP pp 245. [12] Ray Hawke B., et al. (2004) *Icarus* **170**, 1 – 16.

EFFECTS OF GLOBAL TARGET SHAPE ON IMPACT CRATERING,

C. J. Byrne, Image Again, charles.byrne@verizon.net

Introduction: The impact cratering process is affected by two aspects of the shape of the target surface: a shape that conforms to the overall geoid and one that varies locally from the geoid. This paper considers the global shape of a spherical target. Two effects are analyzed: the elliptical trajectories of the ejecta (in the absence of an atmosphere) and the variation of depth of the deposited ejecta due to the spherical target.

The determination of the shape of the ejecta depth depends on the radial profile of ejecta velocity. A scalable velocity profile for lunar basins, partly physical and partly empirical, is presented.

Assumptions: The target and its geode are assumed to be approximately spherical and co-centric. The impactor is assumed to arrive at a high angle from the horizontal, so that the impact has nearly circular symmetry. Any atmosphere present in the target is assumed to be negligible, in respect to the size of the impact. The scaling laws for the gravity domain [1] are assumed valid with the radius being measured along an arc of the target surface, following the target's geoid.

Model of impact feature's ejection cavity: The model and scaling rules are taken from reference [1]. An ejection cone is produced at a constant angle φ with the horizontal and a magnitude of velocity $v\ (r)$, from $r = 0$ to the surface intercept radius. The surface intercept radius is at the intercept between the ejection cavity and the estimated target surface, at the inner base of the rim, and is taken to be equivalent to the term "radius of the transient cavity" in [1]. The distinction is made because there has been controversy about whether the radius of the physical transient cavity is greater or smaller than the radius of the excavation cavity.

The volume thrown from an incremental ejection ring per unit of radius is assumed to follow the scaling law [1] out to the surface intercept radius.

Calculation of the deposited depth: The incremental ejecta is thrown from the internal radius r to the deposit radius d = r + R, where R is the range of ejection (see Figure 1). The depth of the ejection field can be found by dividing the incremental volume of ejecta by the ratio of the area of the incremental deposit ring to that of the incremental ejection ring. The relative width of the rings is the derivative of R(r). The circumference of the rings depends on R, as will be described. An allowance may be made for an increase in porosity.

Elliptical trajectory: The equation for the range of an elliptical trajectory (see Figure 1) is [2], [3]:
Where g is the acceleration of gravity at the surface of the target, R_t is the radius of the target, and R is measured along an arc on the target surface. Ejecta from an incremental ring ejected at r is deposited at
$d = r + R$.

$$R = 2R_t \tan^{-1}((v^2 / R_t g)\sin\phi\cos\phi/(1-(v^2 / R_t g)\cos^2\varphi))$$

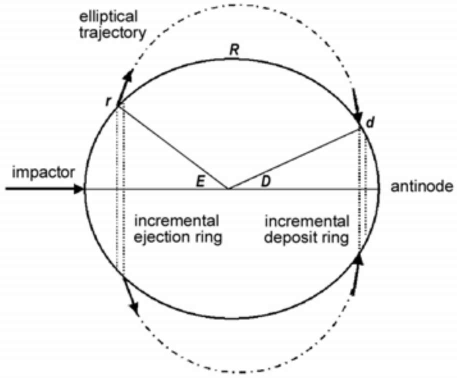

Figure 1: Deposit of ejecta from a large basin on a spherical target. *R* is the range of ejecta thrown out from the incremental ring at *r* and deposited at *d.* Radiii *r* and *d* are measured along arcs of the surface from the point of impact.

Spherical target: On a spherical target the circumference of each incremental ring depends on its radius, measured along the normal to the line between the point of impact and the antinode (see figure 1). The ratio of the circumference of the deposit ring to that of the ejection ring (a factor in the determination of ejecta depth) is the Sin(E)/Sin(D) (see Figure 1). The depth of the ejecta increases as it falls closer to the antinode until it becomes theoretically infinite there, where D = 0. Then it decreases again. In a real case, the chaotic nature of the ejection cone may diffuse the deposit at the antinode, the ejecta that is focussed at a point lands with a large horizontal component of velocity in all directions, and the dynamic angle of repose affects the way the ejecta settles.

For moderate-sized basins, the antinode is in the far field of the ejecta, but in the Near Side Megabasin [5], [8] it lies within the ejecta blanket. Therefore, a very large amount of ejecta gathers there.

Ejection velocity: The profile of ejection velociy as a function of the ejection radius is needed to carry out the range calculations. The scaling laws provide for an exponentially decreasing function of r, but as the rim is approached, this must be modified to bring the ejection velocity to 0. An empirical curve was found that provides a good fit to the ejecta fields of 50 large craters and basins on the Moon (see Fgure 2). An energy-balance equation for the dependence of the magnitude of ejection velocity as a function of the radius [4] provides a good fit to the empirical profile, out to within 7° of the rim.

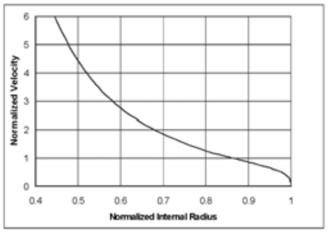

Figure 2: Ejection velocity as a function of radius.

Using a flat-surface target model, this equation, modified by an empirical segment near the rim, provided a scalable [1] radial profile of the ejecta field that was a good match to the radial profiles of 50 large craters and basins of the Moon.

Applications: Using the methods presented above, models of the lunar South Pole-Aitken Basin and the newly identified Near Side Megabasin [5] were produced (Figures 3 and 4).

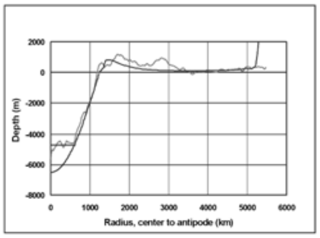

Figure 3: Model (after isostasy) and topographic radial profile of the South Pole-Aitken Basin

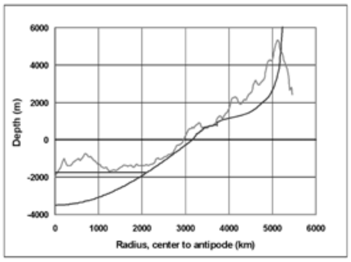

Figure 4: Model (after isostasy) and radial topographic profile of the Near Side Megabasin.

The model of these two giant basins, together with those of the other 50 large craters and basins mentioned above, explain many features of the Moon. In particular, both the topography [6] and crustal thickness [7] data are in good agreement with the model [8], [9] (Figure 5). To reconcile the topographic and crustal thickness data, full isostatic compensation is assumed for the South Pole-Aitken and the Near Side Megabasin.

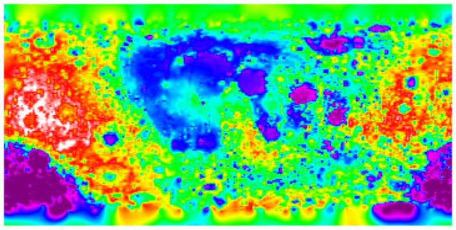

Topography, (Zuber, 2004), Geographic projection

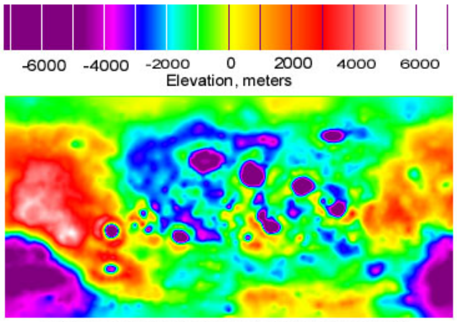

Crustal thickness (Hikida and Wieczorek, 2007)
Pristine Crust 47.5 km, 1/6 Isostasy

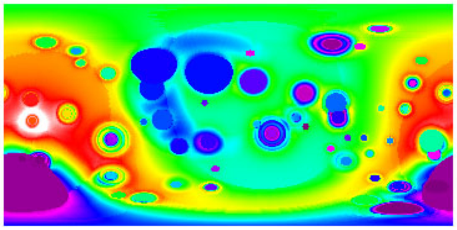

Model, Near Side Megabasin,
South Pole-Aitken Basin, etc. (Byrne, 2006)

Figure 5: A comparison of the composite model with the current topography and the topography implied by crustal thickness data, after isostatic compensation.

References: [1] Housen, K. R., Scmidt, R. M., and Holsapple, K. A. (1983) JGR, Vol. 88, B3. [2] Melosh, H. J. (1989) Oxford University Press, 1989. [3] Ahrens and O'Keefe, (1976), LPSC VII. [4] Richardson, J. E. (2007), LPSC XXXVIII. [5] Byrne, C. .J. (2006), LPSC XXXVII. [6] Zuber, M. T., Smith, D. E., and Neumann, G. A. (2004), http//wufs.wustl.edu/geodata/clem1-gravity-topo-v1/. [7] Hikida, S. H. and Wieczorek, M. A., (2007), LPSC XXXVIII. [8] Byrne, C. J. (2007), A Large Basin on the Near Side of the Moon, paper submitted to Earth, Moon, and Science. [9] Byrne, C. J. (2007), The Far Side of the Moon, book submitted to Springer.

DEVELOPMENT OF A SMALL RAYED CRATER DATABASE FOR MARS: INITIAL RESULTS.

F. J. Calef III[1], R. Herrick[2] and V. L. Sharpton[1,2], [1]Department of Geology and Geophysics, University of Alaska, Fairbanks, AK, 99739, fred@gi.alaska.edu, [2]Geophysical Institute, University of Alaska, Fairbanks, AK, 99739, buck.sharpton@alaska.edu, rherrick@gi.alaska.edu.

Introduction: Subkilometer in diameter rayed craters result from both primary [1, 2] and secondary [3, 4] cratering on Mars. Previous research [5] has identified over 200 images, from a global context, that contain rayed craters in this size range. The goal is to compile a comprehensive and global assessment of their spatial distribution, geomorphology, and target attributes.

This abstract presents the initial results from a data collection of small rayed craters (hereafter, SRC) on Mars, which builds upon previous [5, 6] and [7] current efforts.

Methodology: Using the 227 Mars Orbiter Camera Narrow Angle (MOCNA) images identified with SRC [5], several geometric and geomorphic parameters were extracted from each SRC found. Each imaged was transformed into a Mercator projection centered at the MOCNA centroid to reduce geometric distortion. Linear contrast stretches were calculated on every image to emphasize ejecta patterns.

SRC were selected based upon 1) the existence of ejecta with a contrast distinct from the background (i.e. 'bright' or 'dark'), 2) a diameter less than one kilometer, 3) contained some form of ejecta extended from the primary ejecta blanket, and 4) a crater diameter could be measured that was at minimum five pixels wide. Some SRC were rejected whose ejecta were ambiguous (e.g. rays or ejecta indiscernible), possibly wind modified only (e.g. crater tails), or could be resultant of natural background contrast variation (i.e. all craters have some 'dark' or 'bright' areas around their rims). All measurements are in meters and rounded to the nearest meter or within one pixel width. Crater diameters are measured rim to rim. Minimum and maximum primary ejecta blanket radius was measured from the crater centroid to discern blanket asymmetries. The longest ray of the SRC was estimated. Floor and rim characteristics (e.g. shallow floor or circular rim) were noted. Where ejecta blanket asymmetry indicated low angle impacts, trajectory azimuth was measured in degrees clockwise from North.

Results: From the base set of 227 images, 89 have been processed and 290 SRC found (Figure 1). Crater diameters ranged from 15m to 725m with an average of 71m. Ray lengths fluctuated from 0.2 to 13.4 crater diameters (CD) averaging 3.7. Difference between minimum and maximum primary ejecta blanket widths ranged from nearly circular (0.1 CD) to asymmetric (2.8 CD). Most rayed ejecta was either 'dark' or 'bright' relative to the background surface, though some SRC have bimodal (a 'dark' and 'bright' annulus) and eight had 'neutral' ejecta (i.e. same contrast as the background). Resolution effects limited the recording of floor and rim characteristics to half of the current database. Where observable, craters floors were predominately bowl shaped or shallow with infill, while eleven had irregular floors and three contained central pits. Rims were near equal in ratio between circular and irregular, though ten had discernable elliptical shapes (the primary axis was recorded as the diameter).

Discussion: While the initial SRC measurements and observations are rudimentary, some useful information can be gleaned from the data that is of use to modelers. For example, looking at a bivariate plot of ray length and crater diameter, most SRC are well below 100m in diameter and the majority of rays are only four to six crater diameters in length regardless of the crater diameter (top of Figure 2). If we break out these parameters by ejecta contrast, we begin to see differences. 'Dark' SRC drop off in ray length as their diameter increases (Figure 2, 2nd from top); perhaps these larger, older (?) craters have had their more distal rays removed. 'Bright' SRC are somewhat limited in diameter (~<=75m) and ray length (~<=6 CD) (Figure 2, 3rd from top). 'Bimodal' SRC are also <100m in general, but have a larger range in ray length (Figure 2, bottom).

On Mars, it appears that 'dark' single layered targets have no influence on ray length, while 'bright' single layered targets limit ray length, regardless of crater diameter, from 2 to 6 CD. 'Bimodal', assumed dual-layer, targets may somewhat promote longer rays. Overall, most SRC rays remain below 6 CD.

Future Work: Further examination into the target (e.g. 'dark' basaltic versus 'bright' sulfate/siliceous?) attributes versus ray length and crater diameter may provide limits to modeled impacts in this size range, on Mars. Future work on the database and its parameters could separate secondary and primary impacts yielding limits on both low and high velocity impact events.

References: [1] Malin et al. (2006) *Science, 314,* 1573-1577. [2] Tornabene et al. (2006) *JGR, 111,* 2005JE002600. [3] McEwen et al. (2005) *Icarus*, 176, 351–381. [4] Preblich et al. (2007) *JGR*, 112, 2006JE002817. [5] Calef et al. (2007) *LPSC 38*, #1483. [6]

Calef et al. (2004) *AGU*, abstract #P41A-0890. [7] Calef et al. (2007) Ejecta retention ages on Mars, *in prep*.

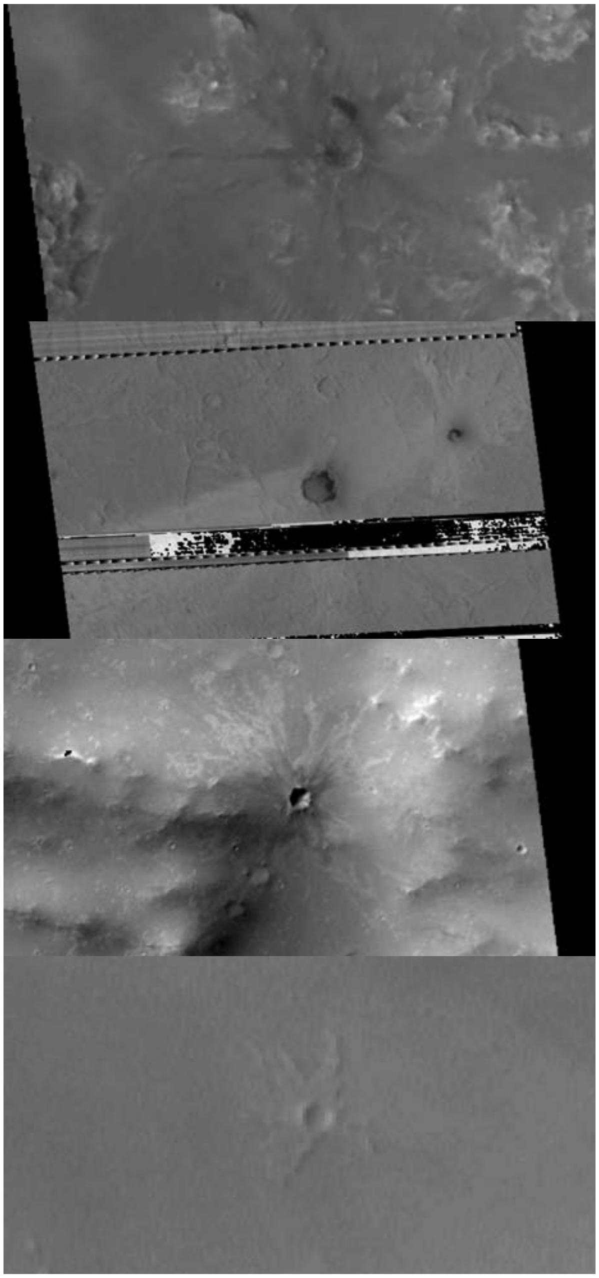

Figure 1: Example of small rayed craters from top to bottom: E110251 (‘dark’ ejecta, crater diam. 46m), E18001385 (‘bright’ ejecta, left: crater diam. 242m and right: 97m, with some wind modification), E0201549 (‘bimodal’ ejecta, crater diam. 152m), and E0400083 (‘neutral’ ejecta, crater diam. 33m). Note rayed ejecta blanket and contrast differences. Top image has evidence of possible impactor from crater, just north of crater rim.

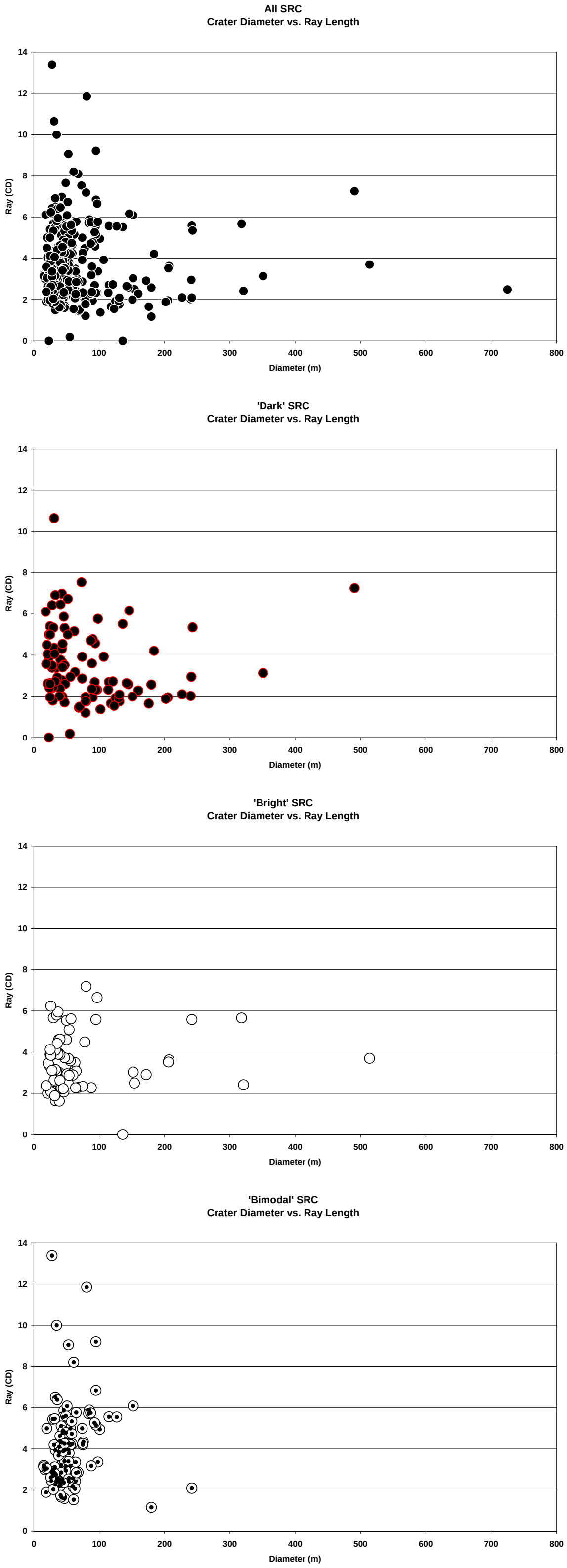

Figure 2: Crater diameter (in meters, x-axis) versus ray length (in crater diameters, CD, y-axis). Ejecta contrast broken out for all, dark, bright, and bimodal SRC, respectively.

AUTOMATIC SEARCH FOR NEW IMPACT STRUCTURES IN FENNOSCANDIA A.F. Chicarro[1] and H. Dypvik[2], L.J. Pesonen[3], A.P. Rossi[1], S.O. Krøgli[2], H. Zumspregel[3], [1]ESA/ESTEC, Scientific Programme, Postbus 299, 2200 AG Noordwijk, The Netherlands (agustin.chicarro@esa.int). [2]Department of Geosciences, University of Oslo, P.O.Box 1047, N-0316 Oslo, Norway. [3]Division of Geophysics, University of Helsinki, P.O. Box 64, FI-00014 Helsinki, Finland.

Summary: This abstract summarizes a new co-operation program on impact crater discovery between the European Space Agency (ESA) and the Universities of Oslo and Helsinki, together with the Geological Surveys of several countries. The main aim is to implement an intelligent search program to identify unrecognized meteorite impact structures in Fennoscandia. The search would be based on applying the mathematical Hough-transform (a tool to recognize circular features) and related pattern recognition algorithms to digital elevation models and geophysical data such as topography, bathymetry, airborne magnetic data, etc. in order to identify new meteorite impact structures which are expected to be of circular shape. This tool has been previously used at ESA/ESTEC in planetary applications [1] and a simplified version is being successfully tested on Norwegian data sets.

Introduction: Impact craters caused by asteroid and comets are an ubiquitous feature in our Solar System [2]. Craters play a key role in understanding the geological and biological evolution of the Earth. Detecting impact craters on Earth is difficult [3], mostly because terrestrial processes (weathering, sedimentation, plate tectonics, etc.) either cover or erase the surface expression of impact structures. Many such structures are in addition covered by younger post-impact sediments, while other impacts have been destroyed by erosion. Currently, about 175 impact structures are recognised on Earth, of which about 20 are localized in Fennoscandia [4]. Of these 11 are found in Finland, 6 in Sweden and 2 in Norway. In Finland, seven out of the eleven impact structures were discovered in the last ten years. The success in finding new impact craters in Fennoscandia in general, and in the Precamrian shield in particular, is mainly due to (i) high-resolution geophysical methods, coupled with drilling of the circular structures, and (ii) detailed petrographic studies of the potential impact-related rocks.

Rationale: The Fennoscandian land surface has been leveled out several times throughout geological history and got its final shape during the last glaciation, ending about 10.000 years ago. Due to this old exposed land surface and to the extended geological and geophysical knowledge of the area, a relatively large number of asteroid and cometary impact craters have been found in the region. Presently about 20 known craters have been recognized as having an impact origin, and in addition some 60 possible impact structures have been suggested. The diameters of the Finnish structures vary from 0.1 to 55 km and the ages from recent to ca. 2.3 Ga [4]. The recognition of impact craters is, however, not equally distributed in the region. A large number of craters have been found in Sweden and Finland, while in Norway only two impact structures have been discovered so far.

Crater Recognition: On Earth, basically all small craters are relatively young, because erosional processes obliterate small (0.5–10 km in diameter) craters after a few million years, causing a severe deficit of such small craters. In terms of cratering rates, there are many craters left to be detected (e.g., [5, 6]). In this context, we address the issue of recognition and detection of impact craters on the Earth by applying processing techniques to Earth observation products, complemented by Digital Elevation Models (DEM), to auto-matically highlight potential targets for future explora-tion.

Objectives: The main objective of this project is first to develop methods helping to identify circular impact structures time- and cost-effectively, and to identify circular structures which will pass some of the pre-established criteria demonstrating that a circular shape has an impact origin. In this project, we will use digital techniques within a Geographical Information System (GIS) framework, in addition to geological and geophysical mapping.

Workflow: The first phase (Figure 1) of the project is to compile existing geoscientific data sets which may disclose unknown impact structures. These data sets are:

- remote sensing imagery
- topographic (digital elevation) data
- lake and sea bathymetric data
- geological data
- ground geophysical data
- airborne geophysical data

The data will be compiled and transformed into digital form enabling their manipulation using various search programs. As outlined above, impact structures have a circular shape due to their formation mechanism, which will be the main diagnostic search item. The second phase of the project deals with organizing the various datasets into digital forms. Most of the Nordic data (topographic and geophysical) already can be obtained in digital form; the rest requires digitizing them with selected interpolation and gridding techniques.

The third phase consists of computer processing of these digital datasets with selected criteria of circularity. The criteria are to be selected in the earliest phase of the project. These analyses will be performed on available satellite imaging, morphological, topographical, geological and geophysical data. We consider this as a large step forward, in particular when planetary analyses could benefit from terrestrial results, in combination with the surface morphology.

Algorithm: Impact craters on the Earth exhibit a much greater degree of variation than impact craters on other planets. Concentrating too heavily on specific crater morphology can be misleading, since similarly sized impact craters on the Earth's surface often exhibit contrasting characteristics. In this context, we have begun characterizing impact craters in a very simple way by using their circularity as their main feature.

Previous ESA-sponsored and -funded studies [1, 7] examine the use of a modified Circular Hough Transform to provide this model. This type of algorithm works best on binary edge-detected (or gradient) images. Where the circular features are not clearly discernable in the original image, edge-detection is unlikely to result in identifiable circles that would fit the simple circle model.

The Radial Consistency algorithm developed by [1] and to be used also in this work models impact craters as having localised rotational symmetry – this replaces the Circular Hough Transform test, that each pixel (x,y) lies on the circle defined by the triple {a,b,r} with the test that the pixel lies within a region of rotational symmetry centred at (a,b). The peaks in the parameter space {a,b} then correspond to the most likely locations of these regions of rotation symmetry in the input image. This allows partially circular features to be picked up, and provides a natural way of fusing the results from multiple data sources [1].

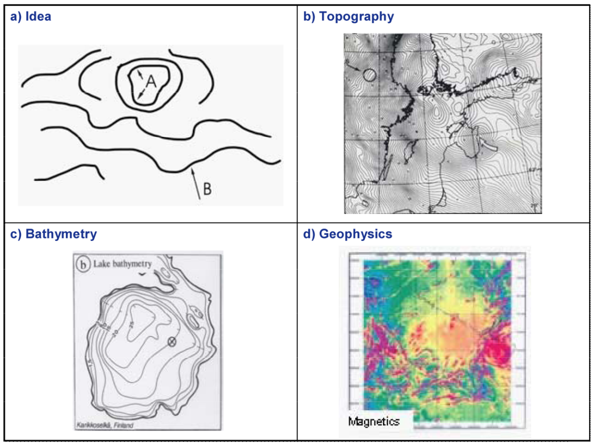

Fig. 1: Multiple datasets, from ground, aerial or satellite observations, which could be used for identifying new crater-like features of impact origin.

Discussion and Conclusions: Early results of this study are encouraging. The use of multiple datasets greatly increases the possibility of circular structure detections with multiple algorithms. Also, the use of data fusion techniques combining multispectral and DEM datasets can aid the detection process. Implementing such a novel computer-based approach to the search of yet to be discovered impact craters in Precambrian shield areas like Fennoscandia could prove quite a useful tool in augmenting the number of confirmed impact structures on Earth. If successful, the approach will be extended to the discovery of new impact structures planetwide.

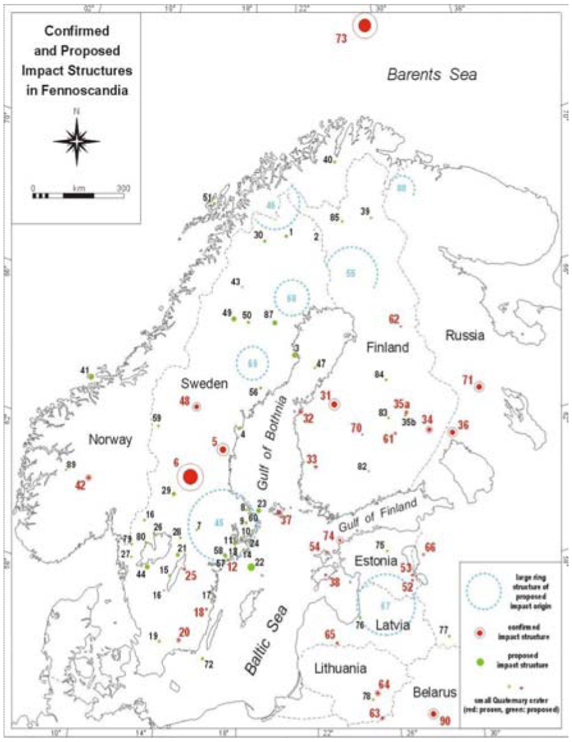

Fig. 2: Confirmed and proposed impact structures in Fennoscandia [4].

References: [1] Earl J., Chicarro A.F. et al. (2005) LPSC XXXVI, Abstract #1319. [2] Grieve R.A.F. and Pesonen L.J. (2006) Earth, Moon, and Planets, Vol. 72, Nos. 1-3, 357-376. [3] Rossi A.P. (2002) LPSC XXXIII, Abstract #1309. [4] Abels A., Plado J. et al. (2002) In: Impacts in Precambrian Shields, Springer Verlag, 1-58. [5] Shoemaker E.M., Wolfe R.E. et al. (1990) In: Global Catastrophes in Earth History (Sharpton V.L. and Ward P.D., eds) GSA-SP 247, 155-170. [6] Trefil J.S., and Raup D.M. (1990) J. Geol., 98, 385-398. [7] Chicarro A.F., Michael G. et al. (2003) ESA Bulletin, No. 114, 68-75.

THE EFFECT OF TARGET STRENGTH VARIATIONS ON COMPLEX CRATER FORMATION: INSIGHT FROM NUMERICAL MODELLING

G. S. Collins, Impacts and Astromaterials Research Centre (IARC), Department of Earth Science and Engineering, Imperial College London, London SW7 2AZ, UK, g.collins@imperial.ac.uk.

Introduction: A phenomenological model for the formation of impact craters in uniform crystalline targets now exists, based on decades of geological, geophysical, experimental and theoretical study [e.g. 1, 2, 3]. An impact excavates a deep, bowl-shaped cavity that subsequently collapses under gravity to form the final crater morphology. Numerical simulations have verified this model, to a large extent, by reproducing the final crater morphology of many large terrestrial craters [e.g. 4, 5], and the size morphology progression of lunar impact craters [6]. Despite the importance of this standard model in a planetary context, many craters in our Solar System do not form in a uniform crystalline target. The majority of the Earth's surface, for example, is covered by sedimentary rocks and or a water layer. Depsite the importance of layering throughout the solar system, very little is known about the effect this has on the cratering process. In this presentation I review recent progress in understanding the effect of target layering on impact crater formation using numerical models.

The effect of target layering on crater formation: The termination of crater growth and the degree and nature of subsequent crater collapse is controlled by gravity and the "strength" of the target material. In this context, strength means the shear strength of the target after it has been processed by the shock wave (fractured, heated, and set in motion) and until the major cratering motions have ceased. It is variations in this dynamic strength within a target that have a profound effect on crater formation. Substantial variations in target strength exist in many contexts in the solar system, due to variations in material and temperature: water and sediment layers on Earth and Mars; brittle and ductile ice or water layers on the icy satellites; regolith layers on asteroids, comets and other airless bodies; and, at the largest scale, crust over mantle on differentiated planets and satellites. Amongst these are some general cases that have been investigated by recent numerical modelling studies:

***Surface water*:** A number of numerical modelling studies demonstrate that the presence of a water layer has two principal effects on impact crater formation [7-13]: (1) to reduce the size of the crater formed on the seafloor, and; (2) to enhance, or modify the late-stage collapse of the crater. For a given size impact, the effect of the water layer can be characterized by the ratio of impactor diameter to water depth [7]. If the water depth is an order of magnitude, or so, bigger than the impactor diameter all the impactor's energy goes towards forming a crater in the water layer, and no crater is formed on the ocean floor. If the water depth is less than about twice the impactor diameter, on the other hand, the final crater is only slightly smaller in size than the corresponding dry-target crater and only minor changes to large-scale crater morphology occur. For intermediate water depths the cratering process is drastically altered. The seafloor is affected by the passage of the shockwave that forms when the impactor strikes the water; by high velocity water resurge flows; and by the temporary removal of the substantial overburden of the water column. The final manifestation of such a seafloor disturbance is yet to be fully quantified by numerical modelling, but is likely to be broader than the equivalent crater had the impact occurred on land, possibly with a larger central uplift.

***Weak over strong*:** Many known terrestrial craters formed in a mixed sedimentary and crystalline target. In several notable cases, impact induced deformation was much enhanced in the sedimentary layer, giving the crater a characteristic "inverted-sombrero" morphology: a broad, shallow outer basin, surrounding a deeper inner basin. Numerical modelling has demonstrated that this type of crater morphology can be reproduced if the sedimentary layer is substantially weaker than the underlying basement (because it is poorly-lithified or water-saturated, for instance; see Figure 1). Simulations of the Mjolnir [8] and Chesapeake Bay [14] impacts, for example, show just this behavior and are in excellent agreement with interpretations of geophysical data from the craters.

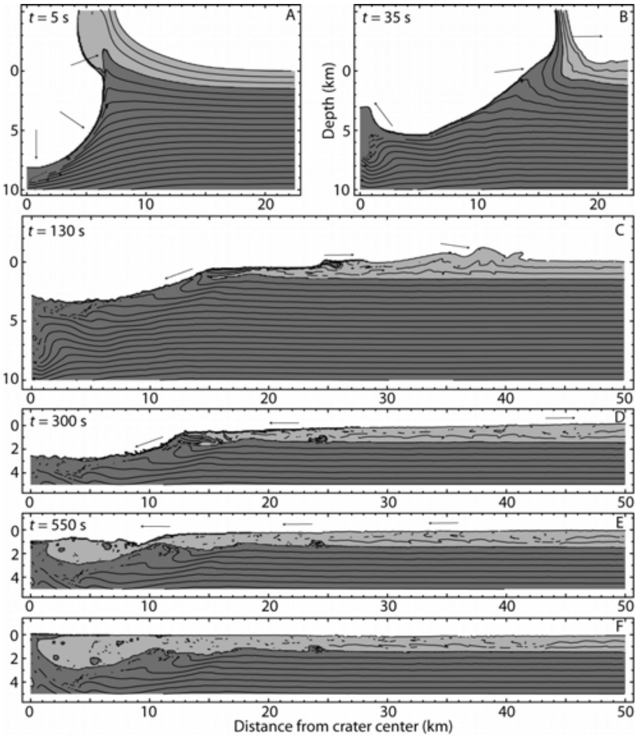

Figure 1. Deformation in a two-layer target (weak above strong) from a numerical simulation of the Chesapeake Bay impact [15]. Dark grey is crystalline basement; light grey is weak sediments). Arrows denote average direction of major motions.

***Strong over stronger*:** In more typical subaerial targets differences in layer strength are less significant than at Cheaspeake Bay, for example. Nevertheless, the presence of sediments can affect the structure of similar size craters if the sediment thickness is different. The Ries and Haughton impact structures, for example, are two craters of similar size (~15-25-km), but with different thicknesses of sediments above the crystalline basement (~0.8 vs ~1.8 km), and quite different interpreted morphology. Preliminary numerical modeling work suggests that the structural differences between Ries and Haughton impact craters are primarily due to the difference in thickness of the sedimentary cover and that the impact energy involved in both was about the same [15,16].

Chicxulub, Vredefort and Sudbury are three larger terrestrial impact craters that, again, differ in structure primarily because of differences in pre-impact target structure. A comprehensive modeling study of all three impacts [17] showed that inclusion of all the important layers—sediment, crust and mantle—each with a common strength model, produces results that are in good agreement with a broad range of available geological data and interpretation based on geophysical data.

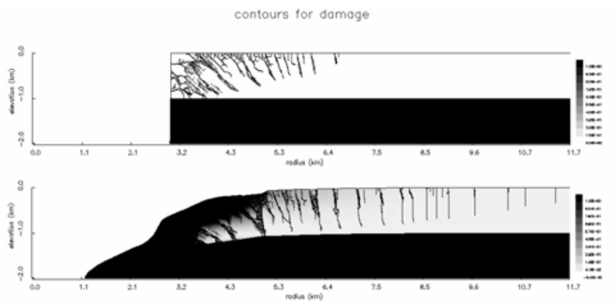

Figure 2: Fracturing in an axisymmetric two-layer cylindrical cavity collapse simulation with a strong, brittle layer over a weak, ductile layer. The shading denotes the amount of damage (black = completely damaged, white = undamaged). From [24].

***Strong over weak*:** Theoretical and numerical modeling of multi-ring craters [18,19] suggests that external ring formation is a consequence of the basal drag exerted on a brittle, elastic surface layer by a weaker, more mobile substrate as it flows inwards to compensate for the absence of mass in the excavated crater. This model has been further constrained for Valhalla-type multi-ring basins, where the rings are closely-spaced, concentric fault-bound graben. The formation of these faults appears to require that the elastic upper layer be thin and that the mobile substrate be confined to a relatively thin layer [20-22]. This rheologic situation occurs on the icy satellites and in rare cases on the Earth. For example, the curious Silverpit "crater", which may be an impact crater, exhibits similar characteristics to Valhalla-type impact basins. It has been suggested that in this case the mobile subsurface layer was caused by the presence of overpressured chalk layers at depth that acted as detachments and expedited inward flow of a thin subsurface layer [23]. Numerical modeling has provided insight into multi-ring cratering. Figure 2 shows results from a simple cylindrical cavity collapse model [24]: the mobile lower layer flows inward causing the elasto-plastic layer above to sag downward. Flexure in the brittle layer causes extensional fractures to form in the upper layer.

Bridging the gap: The presence of strength variations within a target can have a dramatic effect on crater formation. Layering can affect crater size and morphology, and produce craters with multiple concentric rings, the diameter of which may be misleading as a measure of impact size. To best study these craters it is imperative for collaboration between modelers and observers. It is also essential that the dimensions of complex crater features are described explicitly to avoid misinterpretation [25].

The most useful observational data for impact modelling is large-scale: characterization of the pre-impact target (density, porosity, strength, water content); amount of erosion since impact; magnetic, gravity and seismic velocity anomalies; characterization of post-impact target (e.g. shock barometry, temperature estimates, fracture density and spacing, strain measurements) as a function of radial distance from center. There is a need, therefore, for an appropriate method for averaging small (microscopic, or outcrop-scale) measurements over larger regions.

Acknowledgements: I thank Kai Wunnemann, Boris Ivanov and Jay Melosh for their help in developing iSALE. My work on this subject is funded by NERC grant NE/B501871/1.

References: [1] Gault et al, 1968, *in* French B. M. and Short N. M. (Eds), Shock Metapmorphism of Natural Materials, Mono Book Co., Baltimore, pp. 87-99. [2] Grieve et al., 1977, *in* Roddy, D.J., Pepin, R.O., and Merrill, R.B., ed., Impact and explosion cratering: New York, Pergamon Press, p. 791-814. [3] Melosh, H.J., 1989, Oxford University Press. [4] Ivanov B. A. and Deutsch A. 1999. *GSA Special Paper* 339: 389-397. [5] Collins G. S., et al. 2002. *Icarus* 157:24-33. [6] Wünnemann K., and B. A. Ivanov, 2003. Planet. Space Sci., 51 831–845. [7] Shuvalov V. V. 2002. In Impact studies, (Impacts in Precambrian shields), edited by Plado J., and Pesonen L. J. New York: Springer-Verlag. pp. 323-336 [8] Shuvalov V., Dypvik H., and Tsikalas F. 2002. *JGR* 107 E7:1/1-13 [9] Artemieva N. A. and Shuvalov V. V. 2002. *Deep-Sea Res II* 49:959-968. [10] Ormö J., et al., 2002. *JGR* 107 E12:3.1-3.9. [11] Wünnemann K., and Lange M. A. 2002. *Deep-Sea Res.* II 49:969-981. [12] Shuvalov, V. and Dypvik, H. 2004. *MAPS* 39(3):467–479. [13] Davison, T. and Collins, G.S. *MAPS*, in press. [14] Collins and Wünnemann, 2005, Geology, v. 33; no. 12; p. 925–928. [15] Wunnemann, K., et al. 2005, *GSA Special Paper* 384:67-83. [16] Collins, GS and Wunnemann, K., 2007, Lockne 2006, Abs. #4897. [17] Ivanov, B. A., 2005. Solar System Research, 39 (4) [18] Turtle, E.P., (1998) Ph.D. Thesis, University of Arizona. [19] Melosh, H. J. and McKinnon, W. B. (1978) Geophys. Res. Lett. 5, 985-988. [20] McKinnon, W. B. and Melosh, H. J. (1980) Icarus 44, 454-471. [21] Melosh, H. J. (1982) JGR 87, 1880-1890. [22] Allemand, P and Thomas, P. (1999) JGR E 104, 16501-16514. [23] Stewart, S. A. and Allen, P. J. (2002) Nature 418, 520-523. [24] Collins, et al., 2003, 3rd Int. Conf. on Large Meteorite Impacts, Abstr. #4126, LPI, Houston (CD-ROM). [25] Turtle, E.P., et al (2005) *GSA Special Paper*, 384:1-24.

THE EFFECT OF POROSITY AND FRICTION ON EJECTION PROCESSES: INSIGHT FROM NUMERICAL MODELING

G. S. Collins[1] and K. Wünnemann[2], [1]Impacts and Astromaterials Research Centre, Department of Earth Science and Engineering, Imperial College London, London SW7 2AZ, UK (g.collins@imperial.ac.uk), [2]Humboldt-Universität zu Berlin, Museum für Naturkunde, D-10099 Berlin, Germany.

Introduction: The growth of an impact crater is the result of three processes: compaction of pore space, plastic deformation of the target surrounding the crater, and ejection of material from the crater on ballistic trajectories. Quantifying the relative importance of these three processes during crater formation, and how they are affected by target properties, is crucial for understanding the numerous implications of impacts in the solar system. In particular, the amount of material ejected, and the velocity and angle at which this material is expelled, has many ramifications in planetary science. Material ejected at sufficiently high velocity may escape the gravitational field of the target body, which has important consequences for early planetary growth, the collisional evolution of asteroids and the interplanetary transfer of surface material [1]. Moreover, one of the few practical means of shifting the orbit of an asteroid on collision course with Earth is to impact on its surface. The material thrown off the asteroid exerts a thrust in the opposite direction, amplifying the impulse of the impactor itself and helping to change the course of the asteroid [2]. Whether this process can supply sufficient momentum to avoid a catastrophe on Earth depends critically on how efficiently impacts can excavate the material on the surface of asteroids and comets--how much material is ejected and at what speed and angle?

Quantitative experimental studies of ejection dynamics have provided much insight into the relationship between ejection velocity and launch position either indirectly, by tagging target material and locating its post-impact position [3], or directly, by making stroboscopic photographs of grains in ballistic flight [4, 5]. However, the difficulty of measuring the motion of ejecta in such brief, rapid, small-scale events has precluded thorough quantification of the ejection process. In particular, the effects on ejection velocity of target properties, such as porosity and strength, are not well understood due to the practical difficulties of not only measuring ejection velocity, but also constructing targets with a range of porosities and strengths.

Numerical modeling using the Discrete Element Method shows great promise in simulating crater excavation in granular targets [6], particularly in cases where the particles are similar in size to the projectile. However, there has been little continuum modeling of ejection processes, which is more appropriate for hypervelocity impacts into targets where the grain size is a small fraction of the projectile size, primarily because the effects of porous compaction were not properly quantified. In this paper we examine the effect of porosity and friction on crater excavation using the iSALE hydrocode with the epsilon-alpha porous compaction model [7]. iSALE is a multi-material, multi-rheology extension to the continuum hydrocode SALE [8].

Results: In addition to several model validation simulations, which gave good agreement with experimental data [5, 6, 9], we performed over fifty impact simulations spanning a range in target porosity from 0-88% and target friction coefficient from 0-0.75. Our results show that ejection velocity is lower at all launch positions for targets with higher friction (Figure 1). This is because more of the target's kinetic energy is expended as plastic work during excavation in a target with higher friction.

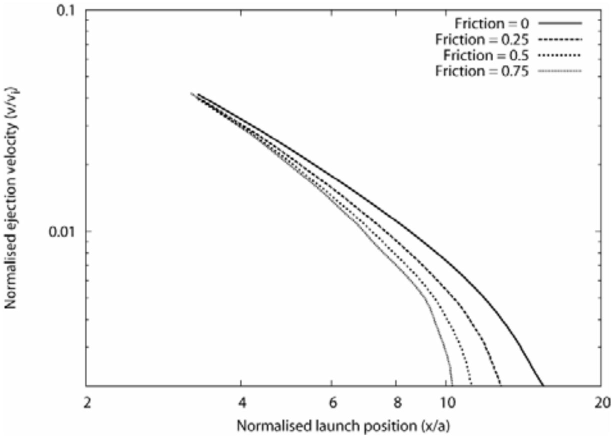

Figure 1: *Normalized ejection velocity as a function of normalized launch position for targets with different friction coefficients (v_i is impact velocity, a is projectile radius).*

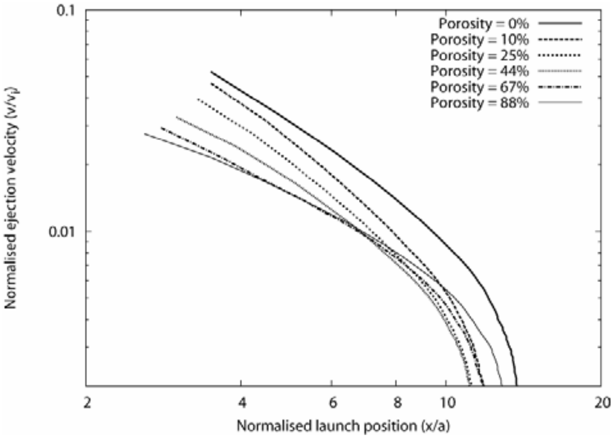

Figure 2: *Normalized ejection velocity as a function of normalized launch position for targets with different porosities.*

The effect of porosity is more complex. As target porosity is increased the target density is reduced, but the attenuation of the shock wave is increased. The effect of increased shock attenuation is to reduce ejection velocity; the effect of reduced density is to increase ejection velocity. In general, shock absorption is the dominant effect and ejection velocity is lower in targets with higher porosity; however, for very high porosity (>50%) the extremely low density of the target becomes important during the late stages of crater growth, and ejection velocities near the crater rim can increase with increasing porosity (Figure 2).

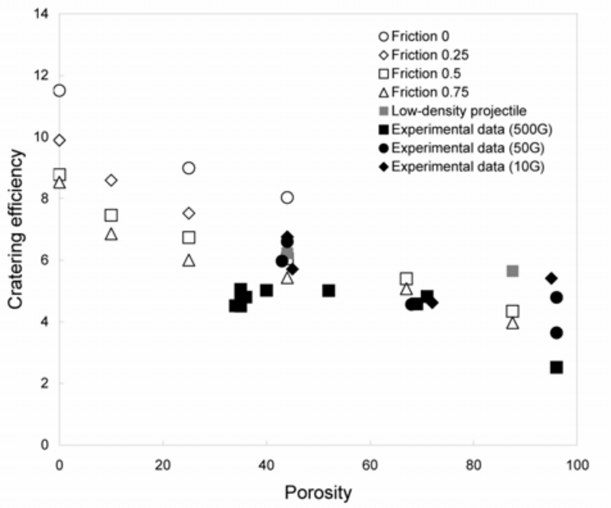

Figure 3: *Cratering efficiency* (π_R) *versus porosity and friction derived from model results.*

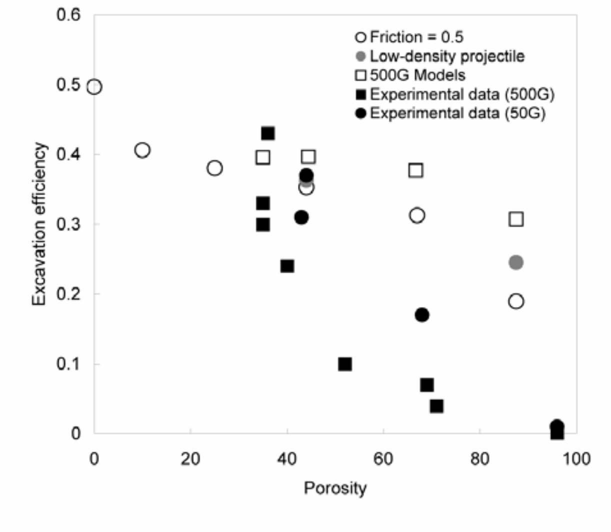

Figure 4: *Excavation efficiency versus porosity*

The competing effects of increased shock attenuation on one hand, and increased compaction and lower density on the other hand, also control the relationship between target porosity and crater size. For low target porosity the effect of shock attenuation dominates; for high porosity the effects of increased compaction and dominate. Consequently, as target porosity increases from 0-25% crater diameter and volume decrease, but for porosities above ~25% crater diameter and volume increase with increasing porosity. Despite this increase in crater size with increasing porosity, cratering efficiency—the mass of material displaced to form the crater relative to the projectile mass—decreases monotonically with increasing porosity, in excellent agreement with experiment (Fig. 3). Excavation efficiency—the volume of material excavated relative to the total volume of the crater—also decreases monotonically with increasing porosity (Fig. 4), although in this case our model results show some disagreement with experiment at very high porosity [9].

Ejecta scaling: The dependence of ejection velocity v (normalized by $\sqrt{gR}$, where g is gravitational acceleration and R is transient crater radius) on normalized launch position (x/R) is qualitatively the same for all porosities and friction coefficients, with trends similar to those shown in Figs. 1 & 2. For $0.3 < x/R < 1.0$ normalized ejection velocity decreases with increasing launch position according to:

$$\frac{v}{\sqrt{gR}} = k\sqrt{\left(\frac{x}{R}\right)^{-2e_x} - \frac{x}{R}}$$

Point-source theory suggests that the exponent e_x can range between 1.5 and 3, and should be ~2.5 for sand, and ~1.8 for water [10]. These theoretical values are supported by some experimental data [e.g. 3, 5] and DEM models [6], but do not agree with other experimental data [4] and our model results. In general, we find that e_x *decreases* with increasing porosity, from ~1.8 at 10% porosity to ~1.2 at 67% porosity. More work, both experimental and numerical modeling, is required to resolve this apparent discrepancy.

Acknowledgements: We thank Boris Ivanov and Jay Melosh for their help in developing iSALE. This work was funded by NERC grant NE/B501871/1 and DFG grant WU 355/5-1.

References: [1] Artemieva N. and Ivanov B. A. (2004) *Icarus 171*, 84—101. [2] Holsapple, K. A., 2004. in: Belton, M., Morgan, T. H., Samarasinha, N., Yeomans, D. K. (Eds.), Mitigation of hazardous comets and asteroids. Cambridge University Press, Cambridge, UK, p. 113. [3] Stöffler D. et al. (1975) *JGR 80*, 4062—4077. [4] Cintala, M. J. et al. (1999) *Meteoritics & Planet. Sci., 34,* 605-623. [5] Anderson, J. L. B., Schultz, P. H., Heineck, J. T., 2004. MAPS 39 (2), 303–320. [6] Wada K. et al. (2006) *Icarus, 180,* 528—545. [7] Wünnemann K. et al. (2006) *Icarus, 180,* 514—527. [8] Amsden A. A. et al. (1980) Los Alamos Report LA-8095. [9] Housen K. R. and Holsapple K. A. (2003) *Icarus, 163,* 102-119. [10] Housen K. R. et al. (1983) *JGR, 88(B3)* 2485-2499.

EVIDENCE FOR TRANSHEMISPHERIC DISPERSION OF AN EJECTA DEBRIS-JET BY A HIGH-VELOCITY TANGENTIAL IMPACT ALONG THE AUSTRAL-INDIAN OCEAN AT 4 KYR BP.

M.-A. Courty[1], B. Deniaux[1], G. Cortese[2], A. Crisci[3], X. Crosta[4], M. Fedoroff[5], F. Guichard[6], K. Grice[7], P. Greenwood[8], F. Lavigne[9], M. Mermoux[10], D. C. Smith[11], B. Peucker-Ehrenbrink[12], F. Poitrasson[13], R. Poreda[14], G. Ravizza[15], M. H. Thiemens[16], U. Schärer[17], A. Shukolyukov[18], M. Walls[19] and P. Wassmer[9]. [1]UMR 5198, CERP 66720 Tautavel, FR, courty@tautavel.univ-perp.fr. [2] Alfred Wegener Inst., Columbusstrasse POB 120161 27515 Bremerhaven. DEU. [3]CMTC, 1260, rue de la piscine - BP 75, 38402 Saint Martin d'Hères FR. [4]UMR-CNRS 5805 EPOC, Av. Facultés, Univ. Bordeaux I, 33405 Talence FR. [5]ENSCP, 11 rue Pierre et Marie Curie, 75231 Paris, FR. [6]CNRS-CEA-UVSQ, Bât. 12, Ave de la terrasse, 91198 Gif/Yvette, FRA. [7]Curtin Univ. Technology, Perth, WA, 6845, AU. [8]University of WA, 35 Stirling Hwy, Crawley, 6009, AU. [9]UMR 8591 , Univ. Paris 1, Meudon, FR. [10]LEPMI-ENSEEG, Univ. Grenoble, 38042 Saint-Martin d'Hères, France. [11]MNHN-minéralogie & CNRS UMR7072 Univ. Paris VI, 61 rue Buffon, 75005 Paris, FRA. [12]Department of Marine Chemistry and Geochemistry,Woods Hole MA , USA. [13]CNRS- UPS- IRD, 14-16, avenue Edouard Belin, 31400 Toulouse, FRA. [14]Dept. of Earth and Environmental Sciences, 227 Hutchison Hall, University of Rochester, Rochester, NY 14627, USA. [15]Dept. of Geology & Geophysics, SOEST, University of Hawaii, Manoa, USA. [16]Chemistry and Biochemistry, Univ. California, San Diego 92093, USA. [17]Geochronologie-Geosciences AZUR, Univ. de Nice-Sophia Antipolis, Parc Valrose 06108 Nice, FRANCE. [18]Scripps Inst. Oceanography, Univ. California, San Diego, USA. [19]Univ. Paris XI, Bât. 510, Orsay, FRA.

Introduction: In the absence of recent analogues and of real-scale experiments, empirical data on young, small impact events are critical for better understanding the complexity of cratering processes on Earth. Even if not severely biased by erosion or weathering, their fingerprints are often ambiguous in contrast to the major impacts. This difficulty is illustrated by our search on the 4 kyr BP impact that has long been confused with a climate or a volcanic event [1]. Coherent evidence for meteoritic materials, shock-melting of marine sediments and sea-water vaporisation now help to elucidate the series of impact-processes in the southern hemisphere and their global effects at 4 kyr BP.

Data processing and analytical methods. The spatial pattern of the 4 kyr BP ejecta emplacement with its two distinctive proximal and distal components has been identified from deep-sea records across the two hemispheres. Its inter-regional to local variability has been investigated by random tests in various continental settings and soil surveys in western Europe, the Middle East, Asia & South America. High resolution stratigraphical records and refined chronology of the 4 kyr BP event have allowed determination of the timing of the ejecta-emplacement and the related effects on seas, coasts, lands, and humans. The microfacies and petrography of the 4 kyr BP signal were thoroughly characterized using optical and environmental electron microscopy techniques (SEM/EDX). The organic and mineral markers were defined using various techniques: XRD, Raman micro-spectrometry, WDS, HRTEM, EELS, GC-IR-MS, isotopes (C, O, S, Pb, Fe, Cr), noble gas measurement.

Results. The 4 kyr BP signal common to all marine and continental archives is defined by a unique suite of exotic micro-debris formed of filaments, flakes, spherules, beads, vesicular glass and angular clasts. It also comprises fist-sized to large debris consisting of layered tektites, pillow-like slabs, highly vesiculated glazed glassy materials and one 10 kg vesicular block of metal-rich basaltic breccia (~3). The coarse end-member is erratically distributed throughout the Mediterranean basin, occurring as linear-shaped small concentrations (~500 m^2) over a burnt soil surface and mixed with carbonised plant material. The vesiculated glazed blocks (VGB) are morphologically similar to previously reported impact-generated glasses debated to trace the proximal dispersion of a cratering event or a large aerial burst [2, 3, 4]. The VGB display a close juxtaposition of flow-textured glass, strongly to weakly heated sedimentary clasts, partly devitrified glass and basaltic microbreccia with vesicles filled by spherules, metallic mounds and fibrous filaments. This phase heterogeneity is similar to the compositional range of the 4 kyr BP micro-debris. The synchronous deposition of the coarse and fine end-members of the 4 kyr BP signal is supported by the increased concentration of micro-debris around glazed blocks at a few metres scale. Their genetic filiation is established from the occurrence within distant sites of similar organic, mineral and metallic markers with unique characteristics. The nearly intact clasts derive from fined-grained and clast-supported unconsolidated materials with sedimentary, volcanic, igneous and metamorphic components. Their marine origin from the southern Austral latitudes is established from the occurrence of an Antarctic micro-faunal assemblage (heated diatoms and radiolarian) in the marine clasts.

Quartz showing pdf, diaplectic transformation and ballen-pattern, and amorphised dropped-shape zircons with structural anomaly provide strong shock metamorphic indicators. They are only encountered in the flow glass domains of the VGB. The transition from intensely fractured quartz grains and partly-amorphised carbonate clasts to the blue flow-glass indicates high pressure shock-dispersion of the fine-grained sediments. The role of a reduced metal-rich carbonaceous phase on shock-melting is suggested by the concentration of CVD-like diamonds associated to hexagonal graphite and hydrocarbons, euhedral iron phosphide (barringerite), iron sulphide and metal blebs (Ni, Cu, Zn, Fe) in the blue flow-glass. The different types of basaltic breccia share in common a complex imbrication of crystallised and glassy phases with common Mg-Cr-Si spinel and various unusual minerals, i.e. silicophosphates, Na-Ca phosphate (buchwaldite). They always contain metal segregation often as spherical blebs, euhedral particles of diamond and graphite, and, volatile-rich hydrocarbons within the crystals and in the interstitial glass. A similar metal/diamond/graphite/hydrocarbon association is also identified in the 4 kyr BP micro-debris as clusters of nano-sized diamonds at the surface and within C-rich vesicular forsterite, as hexagonal graphite, C-rich metallic splash (Fe-Cr, Fe-Cr-Ni, Cr film) at the debris surface, and graphite-associated metallic Fe segregation. Green carbonaceous fibres with chaoite nanoplatelets are always encountered, often coating the micro-debris and vesicles of the coarse ones.

The similar negative ΔO17 anomaly (-0.197 o/oo) obtained in three basaltic breccia from distant regions is completely consistent with either ureilites or carbonaceous chondrites [5]. The high carbon content, the type of diamond and graphite inclusions [6]. and the mass independent fractionation anomaly of the carbon-associated sulphur are in agreement with the ureilite group. The diversity and complexity of the petrographical assemblage of the basaltic breccia (blocks and related small fragments) would designate a heterogenous impact breccia derived from an ureilite-type precursor.

Discussion. The identification of distinctive terrestrial and meteoritic components can be used to interpret the spatial variability of the 4 kyr BP signal with respect to impact processes and ejecta emplacement. The proximal emplacement of the impact-ejecta is defined in the Austral ocean (Adelie Land and Kerguelen Plateau) by the thickest 4 kyr BP signal (7 to 12 m deposits in deep-sea cores). The abundant re-melted meteoritic components, complex grains resulting from shock-melting of the meteoritic and terrestrial components, flow-glass, carbon-injected shocked quartz, and heated marine microfossils (all of local origin with metal splash), provide the characteristics of crater ejecta from an oceanic impact affecting marine sediments on the continental plateau. The range of target materials would match clastic sediments formerly derived from the Antarctic mountains. It synchrony with severe disruption of the north-eastern Kerguelen plateau (up to 50° S) would trace the regional effects of the impact-shock wave. A second type of proximal impact-ejecta seems to correspond to the thinner 4 kyr BP signal in the inter tropical zone (<1 m). Its erratic distribution, abundance of meteoritic components with sea-salt incrustation, metal-splashed planktonic faunal assemblage coming both from Antarctic and subtropical waters, and vitrous carbon (GCF type) with melted marine materials would derive from vaporisation of sea water and of the volatile components of the meteoritic breccia. Its linkage to a unique wild-fire on the Reunion Island and to a giant tsunami along the north-west Sumatra coast would have respectively expressed effects of the fireball and the shock wave generated along coasts by the high velocity propagation of the ejecta along a low-angle impact trajectory. In contrast, the erratic fallout of blocks and dispersed debris throughout the northern hemisphere clearly represent the distal ejecta emplacement. Their preferential occurrence in the northern Mediterranean basin would potentially match the expected concentration of distal ejecta at the antipode [7]. Evidence for splashed ejecta-melt synchronous to thermal effects at the host surface indicate a long distance transport of high-velocity hot fragments of the ureilitic breccia with entrained target materials. The occurrence of marine micro-fossils both derived from antarctic and subtropical waters in vesicles of the blocks support their contact with vaporized sea-water whilst being propelled in the ejecta debris-jet. The comprehensive record of the 4 kyr BP event seems to match a tangential high velocity impact by a highly disrupted and evaporated projectile [8] that possibly produced a series of shallow craters on the continental plateau and lands along its long trajectory. The similar age, location and vesicular glass with CVD-like diamond and probable Mg-Cr-Si spinel [9] suggests a plausible correlation of the 4 kyr BP impact with the Henbuy crater field.

References: [1] M.-A. Courty (2007) *GR* Abstracts 9#10975. [2] P. Schultz et al. (2004) *EPSL 219, 3-4*, 221-238. [3] G.R. Osinski et al. (2007) *EPSL*, *253*, 378-388. [4] J.T. Wasson (2003) *Astrobiology,* 3, 1, 163-179. [5] M. H. Thiemens (2006) *Ann. Rev. Earth & Planet. Sci., 34*, 217-262. [6] Y. Nakamuta and Y. Aoki (2000). *Meteorit. Planet. Sci.*, 35, 487-493. [7] D. Kring and D. Durda (2002) *JGR, 107, E8,* 1029. [8] V.V. Shuvalov (2003) *Meteoritics & Planet. Sci., 38,* (A82), 5149. [9] Y. Ding and D. Veblen (2004) *Am. Min. 89,* 961-968.

INVESTIGATING THE EFFECT OF WATER DEPTH ON MARINE IMPACT CRATER MORPHOLOGY.

Thomas Davison and Gareth Collins, Department of Earth Science and Engineering, South Kensington Campus Imperial College London SW7 2AZ. (thomas.davison@imperial.ac.uk), (g.collins@imperial.ac.uk)

Introduction: 70% of the Earth is covered by the oceans, implying that most meteoroid impacts occur into water-covered targets. However, of the ~170 known or suspected impact structures on the Earth only 15-20 are thought to have formed in a marine environment [1], and the majority of these are now on land. The paucity of marine craters is in part due to the effect of the water layer on inhibiting or altering the cratering process and in part due to the young age of the oceanic crust. Here we quantify the relationship between crater diameter and the ratio between water depth and impactor diameter by numerically simulating oceanic impact events. We then use this relationship to examine the effect of the Earth's oceans on the global crater size-frequency distribution and estimate how many craters we should expect to find on the ocean floor today.

Previous Work: Previous experimental and numerical modeling work has shown that the effect of a water layer on crater formation is most sensitively controlled by the ratio between the water depth and the impactor diameter—referred to hereafter as R [e.g. 2-8]. However, a definitive relationship between final crater diameter and R has not yet been established. By simulating the impact of a 200-m diameter impactor at 15 km s^{-1} into water-covered targets, Shuvalov [3] showed that a shallow water layer ($R < 0.5\text{-}1$) has little effect on the cavity forming in the basement; that for $R > 2$ cavity size is reduced as the impactor is completely decelerated, deformed and disrupted during penetration of the water layer; and that for $R > 4$ no crater occurs on the seafloor. Artemieva and Shuvalov [8] also found from their numerical models that for $R > 4$ a submarine crater is almost nonexistent (for a 1-km diameter impactor with an impact velocity of 20km s^{-1}); however, the marine-impact models of [7] did show significant disturbance of the seafloor for $R = 5$ (using the same impactor size and velocity). Laboratory-scale impact experiments [2] provide further quantitative analysis of the effect of water layer thickness on crater size, albeit at a much smaller scale and lower velocity than typical marine craters. Results from these experiments suggest that craters may form in the target beneath water of depths up to 10-20 times the diameter of the impactor ($R = 10\text{-}20$).

Method: To quantify the relationship between final crater diameter and R we have simulated over 60 marine-target impact events using the iSALE hydrocode. This is a well-established code [7] that has been used to simulate several terrestrial impact events [e.g. 9-11] and develop a generic, quantitative model for the formation of impact craters in crystalline targets [12]. For all simulations the ANEOS equations of state for granite and water were used to represent the seafloor and ocean. Granite was chosen because, unlike basalt, it is has a well-defined EOS and constitutive model, and because the constitutive model parameters for basalt and granite are similar. We used an impact velocity of 15 kms^{-1}, which is an average velocity for impacts on Earth. Density was kept constant at $2700kgm^{-3}$, suitable for a porous stony asteroid and to allow the same material to be used for the impactor and seafloor. The angle of impact in all simulations was perpendicular to the target surface, enforced by the axisymmetric nature of the model.

Three sets of simulations were performed, each with a fixed impactor diameter (L=100m, L=500m and L=1km), to investigate the effect of water layer thickness on crater formation over a range in impactor sizes. The three impactor diameters were chosen to span the range of terrestrial impact events where the effect of a water layer is important, and to keep the maximum water depth investigated within reason. At the lower end, stoney impactors much smaller than 100-m diameter are significantly affected by atmospheric entry (broken up and/or decelerated) and will probably not form a single large impact crater. At the upper end, the maximum depth of the terrestrial oceans (~7 km) implies that a large range in R cannot be achieved for impactors much greater than 1-km diameter. Simulations were run varying the R value between 0 (no water) and 8 (deep water) for each of the different impactor diameters.

Results: Qualitatively, our model results agree well previous work [e.g. 3, 5, 7, 8 13]; we identify three regimes of behaviour (shallow-water, intermediate-water-depth, and deep-water) depending on the ratio of water depth to impactor diameter, R, and whether the impact forms a simple or complex crater.

The deep-water regime occurs for impacts where $R > 8$; in this case, all the impactor's energy goes towards forming a crater in the water layer, and no crater is formed on the ocean floor.

The intermediate-water-depth regime applies only for impacts forming complex craters in the range $3\text{-}4 < R < 6\text{-}8$. In this highly-complex regime the seafloor is affected: by the passage of the shockwave that forms when the impactor strikes the water; by high velocity water resurge flows; and by the temporary removal of the substantial overburden of the water column. Based on our model results, it is unclear what the final manifestation of such seafloor disturbances might be, but it is likely to be broader than the equivalent crater had the impact occurred on land.

The shallow-water regime, which represents all other cases, is characterised by a decrease in crater diameter with increasing R, but little large-scale change in crater morphology.

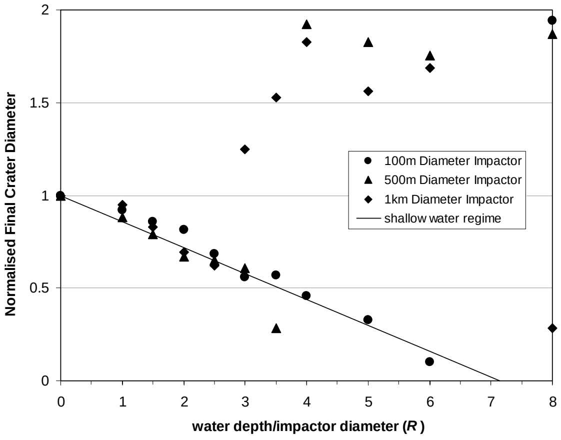

Fig 1: Plot of final crater diameter, normalised by the diameter of the crater formed when no water layer is present, as a function of relative water depth *R* (for impactor diameters of 100-m, 500-m and 1-km). The craters formed within the shallow water regime (see text for further discussion) are well fit by the straight line plotted (Equation 1).

Figure 1 shows our model results of D_N, the ratio of the final crater diameter at a given R to the final crater diameter for R=0 (dry target), as a function of R. Ignoring the data points that correspond to the intermediate water depth regime, a linear regression gives:

$$D_N = 1 - (0.14\pm0.02)R, \quad \text{for } 0 < R < 7. \quad (1)$$

Discussion: Using the quantitative relationship between final crater diameter and the ratio of water depth to impactor diameter (Eq 1), we have calculated expected size-frequency distributions of craters on Earth that for the first time account for the presence of the oceans (Figure 2). The model used makes several necessary simplifications; however, given the uncertainty in estimates of the current terrestrial impactor population, we believe that several important conclusions can be drawn from our model results.

1. The presence of the oceans reduces the number of craters smaller than 1-km in diameter by about two thirds, the number of craters about 30-km in diameter by about one third. For craters larger than ~100-km in diameter the oceans have little effect.
2. More craters of a given size occur in the oceans than on land for craters larger than ~12 km in diameter; at diameters below this more craters of a given size form on land than in the oceans.
3. In the last 100 Ma about 150 impact events formed a 5-20-km diameter impact-related resurge feature, or disturbance on the seafloor, instead of a crater.

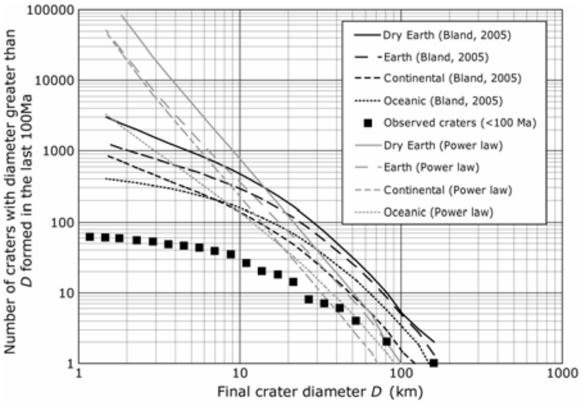

Fig 2: The predicted cumulative size-frequency distribution of craters larger than 1-km in diameter that would form on Earth in a 100 Ma period. Black lines are for results calculated using the impactor population from [14] and grey lines assume a power-law impactor size-frequency distribution derived from observational data. Solid lines represent a 'Dry Earth' case, assuming no oceans are present on the Earth. Wide-dashed lines are for the whole Earth with current ocean coverage. Dashed lines show the craters forming on the continents and dotted lines show those which form in the oceans. For comparison, the observed craters known to have formed in the past 100Ma are also plotted [15].

Acknowledgements: This work would not have been possible without the years of model development behind iSALE, for which we are indebted to Kai Wünnemann, Boris Ivanov and Jay Melosh. GSC was funded by NERC grant NE/B501871/1.

References: [1] Ormö J., and Lindström M. 2000. Geological Magazine 137 1:67-80. [2] Gault D.E. and Sonett C.P. 1982. *GSA Special Paper* 190:69-92. [3] Shuvalov, V. V. (2002) in *Impact Studies, (Impacts in Precambrian Shields)* pp323-336, [4] Shuvalov V., Dypvik H., and Tsikalas F. 2002. *JGR* 107 E7:1/1-13 [5] Shuvalov V. V., and Trubestkaya, I. A. 2002. Solar System Research 36 5:417–430. [6] Ormö J., Shuvalov V. V., and Lindström M. 2002. *JGR* 107 E12:3.1-3.9. [7] Wünnemann, K. & Lange, M. A. (2002) *Deep-Sea Research II* 49, pp 969-981, [8] Artemieva N. A. and Shuvalov V. V. 2002. Deep-Sea Research II 49:959-968. [9] Collins, G. S. & Wünnemann, K. (2005) *Geology* v.33; no.12; pp925-928, [10] Ivanov (2005) *Solar Syst. Res.* 39(5), pp426-456, [11] Wünnemann, K., Morgan, J. V. & Jödicke, H. (2005) in *Large Meteorite Impacts III.* Geol. Soc. Am., Boulder, CO, pp67-83. Special Paper 384, [12] Wünnemann, K. & Ivanov, B. A. (2003) *Planet. Space Sci.* 51, pp831-845 [13] Oberbeck V. R., Marshall J. R., and Aggarwal H. 1993. The Journal of Geology 101:1-19. [14] Bland, P.A. (2005) *Phil. Trans. R. Soc. A* 363, pp2793–2810, [15] Grieve, R. A. F. & Shoemaker, E. M. (1994) in *Hazards due to comets & asteroids*. University of Arizona Press, Tucson. 1300p.

AN INCONVENIENT VIEW: INTERPRETING HOW SHOCK-INDUCED FRACTURES INFLUENCE IMPACT CRATER DEVELOPMENT.

Michael R. Dence, 824 Nesbitt Place, Ottawa, K2C 0K1, Canada, mrdence@magma.ca

Introduction: One of the most interesting outcomes of the first Bridging the Gap workshop was the renewed attention given to the role of fractures in crater development. It was realized early in the study of hypervelocity impact craters that, like omelets, making craters in strong materials requires breakage. Indeed using gravity surveys to measure the volume fractured gave one way of estimating the energy of an impact [1]. However, relatively little attention has since been given to the role fractures play in crater formation as analysis concentrated on shock melting and metamorphism and other manifestations of the early compression phase of impact events. By comparison, fractures are inconveniently difficult to observe and to quantify as a means of gaining insight into the subsequent stages of the crater-forming process.

A critical ingredient has now been provided through the experimental investigation of dynamic tensile fracturing and fragmentation by Ai and Ahrens [2], who measured shock pressures at standard temperature and pressure for the onset of fracturing and for complete fragmentation (brecciation) of two strong crystalline rocks and Coconino sandstone. Their results complement observations [3, 4] that indicate that in crystalline rocks the limit of fragmentation down the axis of natural craters occurs at much higher shock pressures than in the laboratory. Furthermore, from [3], shock pressure at the fragmentation limit (P in GPa) increases regularly with increasing crater size (D in km) as $P = 3.5\ D^{0.5}$. Putting these results together suggests that in strong materials crater size is controlled by dynamic fracturing. This in turn is limited by the intrinsic dynamic tensile strength of the target modulated by the confining pressure of the overburden as the transient cavity grows.

Differences between craters formed in crystalline and sedimentary rock targets: About a third of known terrestrial impact craters are formed in crystalline rocks, the rest entirely in sedimentary rocks or where a thick sequence of sediments overlies a crystalline basement. Crystalline rocks in general are relatively homogeneous whereas sedimentary rocks are commonly heterogeneous, weaker and more porous, with consequent effects on the rapidity of shock pressure attenuation [5], the partition of energy and limits of fragmentation.

Moreover, crystalline rock craters on Earth exhibit a relatively gradual change in form with increasing size from simple through central peak to peak-ring forms, as seen in craters on other rocky planets. This argues for a general similarity in crater mechanics with differences largely due to the effects of gravity. On the other hand, in sedimentary rocks there is an abrupt change from simple crater form exemplified by Barringer crater (1.2km) to a pronounced central peak form as seen in Steinheim and Flynn Creek, each about 3.5km across. Sedimentary rock craters are rarely more than 150m deep while those formed in crystalline rocks may exceed depths of 400-600m. In addition, in complex craters formed in crystalline rocks, the ratio of the amount of uplift to the final crater diameter as estimated from shock metamorphism data is about 1:5 whereas for most craters formed in sedimentary rocks the ratio is 1:8 to 1:10. Such differences argue for the dominant role of a different mechanism in sedimentary than in crystalline rocks an obvious candidate being movement on planes separating strata of contrasting physical properties.

Observations of Fractures in Natural Craters: The relative homogeneity of crystalline rocks makes them the preferred venue for the analysis of the role of fractures in impact crater formation. Beyond the near-field region where high shock pressures result in total melting, rocks that show the standard effects of shock metamorphism bear little evidence of shear deformation. The subsequent release from compression, on the other hand, produces several sets of tensile fractures, best seen in simple craters. These include closely spaced, sub-horizontal fractures and steeply inclined circular fractures. Widely spaced radial fractures may also exist. The remarkable regularity of these fractures in plan and cross-section indicates that the stress field generated by the impact completely dominates the pattern of deformation. Crater structure is generally not strongly influenced by anisotropy of composition or fabric in the target rocks or obliquity of impact except in the far field and in the distribution of ejecta.

Sub-horizontal fractures: These are most clearly observed at the crest of the rim, as exposed at the New Quebec/Pingualuit (3.2km) crater. There they resemble sheet jointing fractures spaced a few centimeters apart that cut the regional gneissosity at high angles. They were apparently sub-horizontal when formed then subsequently tilted during uplift of the rim. The resulting bilaterally symmetric pattern [6] suggests, by analogy with experiments, oblique impact from the southeast. Fractures of this type are inferred to have formed down axis as the initial shock wave was reflected from the trailing edge of the impactor and the free surface. As the transient crater developed they produced fragmentation with the formation of breccia to the limit dictated by the dynamic tensile strength of the target rocks and the confining pressure.

Spheroidal fractures: Drilling at the 3.8km Brent crater has shown that the breccias within this simple crater are bounded by a fracture zone that is circular in plan and conforms to a spherical segment in cross-section [3,4]. It is steeply inclined at the original surface and curves inwards towards the crater center at the base of the breccia lens. Near surface it is expressed as the boundary between breccias filling the crater and the fractured crater wall. At depth it changes into a shear along which sheets of weakly shocked and fractured gneiss from the crater walls slid towards the center. A possible sequence of events is that it was initiated as one of a set of circular tensional fractures generated by release of the initial shock pressure. The excavation of the transient cavity consumes the innermost fractures of the set until the cavity attains its maximum dimensions. The remaining fractures continue to propagate in response to the changing stress field around the cavity. The resulting spheroidal shears allow the cavity walls to slump towards the center of the crater.

Radial fractures: Although radial fractures are generally expected around an impact site there is little direct evidence that they exist. Weak depressions in the rim of the New Quebec crater may be underlain by radial fractures spaced at ~10-15° intervals, that appear not to extend to any great depth or have much influence on the subsequent development of the crater.

Late stage influence of fractures: In simple craters the final crater form would seem to arise from the relative timing of the growth of sub-horizontal and spheroidal fracture systems. Where the spheroidal fractures reach the toe of the crater floor before there is significant upward expansion of the floor of the transient cavity a simple crater results. Any tendency for the center to rise is suppressed by the weight of the thick lens of breccia cascading from the crater walls. The timing is different in larger craters. Expansion of the floor exceeds the rate of propagation of the primary spheroidal shear planes and their point of convergence occurs below the crater floor. As a result the segment above the converging shears is carried upwards to form a central peak and a complex crater is formed. In crystalline rock craters of intermediate size (4 to ~30 km final diameter) the rocks of the central peak are strongly fractured as they converge in the center. In the largest complex craters, this secondary fracturing is dominant towards the margins and the rocks of the central peak are preserved as large blocks with little internal deformation that moved on widely spaced zones of intense shearing lubricated by friction melts.

In craters formed in sedimentary rocks the presence of pre-existing sub-horizontal bedding planes allows movement to take place with relatively limited formation of new fractures. Thus collapse occurs rapidly and relatively completely once a critical size is attained.

Final remarks: To integrate the role of fractures into impact crater models more information on relevant physical properties is needed. This includes a more extensive database of the dynamic tensile strength and related properties of common rocks. In addition, data on the rate of formation and propagation of dynamic fractures is required as well as on the rate at which rocks expand after release from shock compression.

References:

[1] Innes, M.J.S. 1961. *Journal of Geophysical Research*. 66: 2225-2239.
[2] Ai, H.A. and Ahrens, T.J. 2004. *Meteoritics and Planetary Science*. 39: 233-246.
[3] Dence, M.R. 2002. In *Meteorite impacts in Precambrian shields*, J. Plado and L.J. Pesonen, Editors. Springer-Verlag: Berlin. pp. 59-79.
[4] Dence, M.R. 2004. *Meteoritics and Planetary Science*. 39: 267-286.
[5] Cooper, H.F.J. 1977. In *Impact and explosion cratering*, D.J. Roddy, R.O. Pepin, and R.B. Merrill, Editors. Pergamon: New York. pp. 11-44.
[6] Currie, K.L. and Dence, M.R. 1963. *Nature*. 198: 80.

IMPACT METAMORPHISM: ON THE WIDTH OF THE GAP BETWEEN OBSERVATION AND MODELING – THE GEOLOGIST'S VIEW VS. THE MODELERS ASSESSMENT II. A. Deutsch[1], K. Wünnemann[2], [1] Institut für Planetologie, WWU Münster, Wilhelm-Klemm-Str. 10, Münster 48149, Germany, deutsca@uni-muenster.de, [2] Museum für Naturkunde, Humboldt-Universität, Invalidenstraße 43, Berlin 10099, Germany, kai.wuennemann@museum.hu-berlin.de.

Introduction: The investigation of impact metamorphism can be split up in observational data resulting from field studies and laboratory analysis of naturally shocked rocks and minerals, and such accumulated in the investigation of experimentally shocked materials and cratering experiments. The latter allow precise definition of the pre-impact properties, and, depending on the experimental set-up an accurate control of the shock pressure. In rare cases, even peak-shock temperatures have been monitored. Results from shock and cratering experiments and nuclear tests yielded, for example, the basic frame for shock barometry in natural craters and for material parameters under extreme pT conditions. The exceedingly varying results form experimental studies on the shock behavior of carbonates, however, drastically show the importance of the experimental design and of the choice of material subjected to shock (see compilation in [1]). Field data, in contrast, provide the basis for a general 3D picture of impact craters. In constant interaction between field geologists, experimentators, and modelers numerical simulations of impact processes can be refined with the ultimate goal to yield predictions of what can be expected in natural crater structures, and how the observations have to be interpreted [2].

Some topics of interest: In recent years, the above addressed interaction has been increasingly acknowledged in the impact community. Yet still, some authors do not consider the importance of specific target properties in the interpretation of observational data. For example, according to the canonical view decorated planar deformations features (PDFs) represent "altered" or "annealed" glass lamellae; however, their presence in the just 1.07 Ma old Lake Bosumtwi crater, where significant thermal overprint has not been documented, clearly indicate that the H_2O bubles in the PDFs are related to target properties – in this case fluid-rich meta-greywackes [3].

Another problem is the amount of impact melt in craters. In general, the estimated melt volume vs. crater size plot on a well defined regression line for impact structures in crystalline targets [4]. In mixed targets, however, estimates of the volumes of shock - impact melts vary for some craters by orders of magnitudes.

Open problems in observation include the fate of carbonates and sulfates in the shock and post-shock regime, as well as the general shock behavior of soft fluid rich sediments or sedimentary rocks. Some of these problems can be and have been successfully tackled by experimental approaches [3, 5, 6, 7]

Impact-induced melting and vaporization: For thermodynamic reasons, vaporization invariably and melting nearly always The investigation of impact metamorphism can be split up in processes that start to occur during and after unloading from shock.

Shear melting. Rare exeptions in the second case include pseudotachylites with stishovite (Vredefort [8]) and black veins in meteorites with a number of high-pressure minerals, including stishovite, hollandites, akimotoite, and ferro-magnesian silicate titanite (e.g., Zagami [9]). These veins most probably form by shear melting and are quenched in the very beginning of unloading. Experimental proof for this idea was provided by [7] although time constraints (i.e, shock duration of 0.7 μs) prohibited the growth of high-P phases.

The matter is more complex in terrestrial impact structures where several generations of "shear melt veins", so-called pseudotachylites, and clastic matrix breccias occur. In the case of the Sudbury impact structure [10], these pseudotachylite zones and bodies reach a thickness at the 100-m-scale. Their origin by friction exclusively [11] is incompatible with the immeadiate reduction of friction, and thus stress, and seems at odds with the mechanical behavior of the crater foor. Zones of extreme shearing occur in the uplift of the Puchez-Katunki too; there they are manifested in up to 200-m-wide diffuse zones characterized by a high-T mineral assemblage that overgrow shock features. These zones are interpreted as boundaries between differentially uplifted blocks.

Impact melt lithologies – the "normal" case. Melt lithologies, ranging from pure glass, over glass with schlieren (Fig. 1), vacuoles and bubbles, to partially or totally crystallized and/or altered occur in quite different settings in and around impact structures. The size/volume of the melt lithologies range from μm-sized spherules to an estimated volume of 2.5×10^4 km^3 for the differentiated impact melt sheet (SIC) at the Sudbury impact structure [12]. The understanding of their respective formation processes on the level of geological observations (i.e., small scale) is in part still limited and unsatisfactory.

Based on a geochemical analysis of melt lithologies and their precursor rocks from the Popigai impact structure, it was possible for the first time to relate glassy and crystallized distal ejecta to specific source regions in a crater [13]. Using this approach, a current project on different melt lithologies from the Bosumtwi [14] and the Chesapeake impact strucutres [15] is devoted to the issue of the generation of different types of melt, namely tektites, microtektites, fall-back spherules, and melt lithologies in breccias that occur inside and around the crater. Constraining structural properties of impact glasses [16], their precursor lithologies, mixing, and physical conditions during melting and cooling will allow to provide a set of solid input parameters to refine numerical models of impact melt formation which so far consider only the peak shock pressure as criteria for melting (e.g., [17, 18]).

Impact melt sheets – open issues. A new idea in the area of impact melting is the proposed occurrence of carbonatic or carbonate-rich melt lithologies (e.g. [19]). Large scale melting of carbonates at >10 GPa and > 2000K [19] is not supported by the phase diagram for calcite [20]; such pT conditions can only be reached if the sedimentary target material has a large porosity. Melting of carbonate clasts in suevites and impact melt rocks, however, during the post-shock regime seems to occur much more widespread than hitherto assumed [21]. Melting and vaporization of sulfates is of prime interest in the context of the mass extinction at the K-T (Paleogen) boundary [22]. Again, a newly constructed phase diagram [23] indicates that solid (i.e., non-poros $CaSO_4$) hardly will melt in the impact regime as extreme pressures are required for melt. We expect significant progress in the understanding of impact-induced melting of sedimentary rocks by applying numerical models that include porosity into the code [24]. We note in addition that the melt volume resulting in numerical simulations of impact events always exceeds the volume observed in nature.

Another challenging problem in modeling is related to differentiation and cooling of the SIC [12, 25] and large impact melt pools at other terrestrial planets [26]: These melt bodies are topped by thick bodies of breccias (in the case of the SIC > 1700 m of Onaping breccias [10]), acting as insolation which in turn, causes slow cooling of the melt, probably accompanied by differentiation.

Conclusion: The gap between observation in nature and experiments, and modeling becomes increasingly smaller although in some fields, the gap is insurmountable: In nature we see the end product, not the thermodynamic path material takes to reach this stage. In models, we construct simplified cases that can not take into account specific details.

References: [1] Agrinier P. et al. (2001) *GCA 65*, 2615-2633. [2] Wünnemann K. and Deutsch A. (2007) *this vol.* [3] Deutsch A. et al. (2007) *MAPS* 42, 635-654. [4] Cintala M.J. and Grieve R.A.F. (1998) *MAPS. 33*, 889-912. [5] Ivanov B.A. et al. (2002) *GSA Spec. Pap. 356*, 587-594. [6] Langenhorst F. et al. (2002) *Experimental techniques for the simulation of shock metamorphism: A case study on calcite.* High-Pressure Shock Compression of Solids V, Springer, 1-27. [7] Langenhorst F. et al. (2002) *MAPS 37,* 1541-1544. [8] Martini J.E.J. (1991) *EPSL 119,* 2854–300. [9] Langenhorst F. and Poirier J.-P. (2000) *EPSL 184,* 37–55. [10] Deutsch A. et al. (1995) *Geol. Rundschau 84*, 697-709. [11] Spray J.G. and Thompson L.M. (1995) *Nature 373,* 130-132. [12] Ivanov B.A. and Deutsch A. (1999) *GSA Spec. Pap. 339*, 389-397. [13] Kettrup B. et al. (2003) *GCA 67*, 733-750. [14] Luetke S. et al. (2007) *LPS XXXVIII*, Abstract #1682. [15] Deutsch A. and Koeberl C. (2006) *MAPS 41*, 689-703. [16] Langenhorst F. et al. (2005) *GSA meeting Salt Lake City*, Abstr. [17] Artemieva N.A. (2002) *Tektite origin in oblique impacts: numerical modeling of the initial stage.* Impacts in Precambrian Shields (eds. J. Plado and L.J. Pesonen) Springer, 257-276. [18] Melosh H.J. and Artemieva N. (2004) *LPS XXXV*, Abstract #1723. [19] Osinski G.R. and Spray J.G. (2002) *EPSL 194,* 17-29. [20] Ivanov B.A. and Deutsch A. (2002) *Phys. Earth Planet. Interiors 129,* 131-143. [21] Deutsch A. and Langenhorst F. (2007) *GFF, 129,* 155-160. [22] Brett R. (1992) *GCA 56,* 3603-3606. [23] Ivanov B.A. et al. (2004) *LPS XXXV*, Abstract #1489. [24] Wünnemann K. et al. (2006) *Icarus 180*, 514-527. [25] Ariskin A.A. et al. (1999) *GSA Spec. Pap. 339*, 337-387. [26] Ivanov B.A. (2005) *Solar System Res. 39*, 381-409.

Acknowledgements: We appreciate support by German Science Foundation grants De 401/15 and Wu 355/5-1. and stimulating discussions with Natalia Artemieva, Boris Ivanov, Falko Langenhorst, and Jay Melosh.

Figure 1. Micrograph of schlieren-rich glass from a suevite of the ICDP-USGS drillcore Eyreville; Chesapeake impact structure; //nicols.

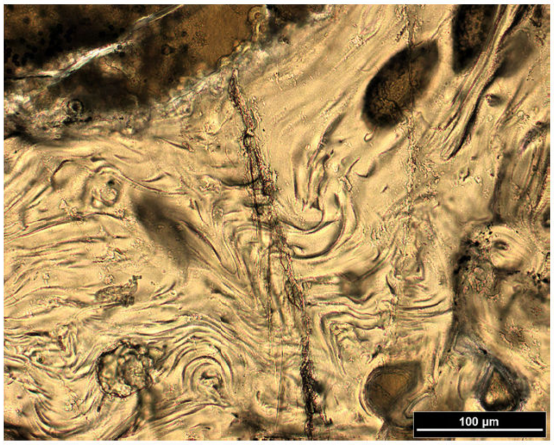

STRUCTURAL SIGNATURES OF OBLIQUE IMPACTS – INSIGHTS FROM NUMERICAL MODELING.

D. Elbeshausen, M. Poelchau, K. Wünnemann and T. Kenkmann, Humboldt-Universität zu Berlin, Museum für Naturkunde, D-10099 Berlin, Germany (dirk.elbeshausen@museum.hu-berlin.de)

Introduction: Meteorites striking the surface vertically are most unlikely [1]. Anyhow, most of our knowledge on the physics of impact processes and especially the crater formation is based on vertical impact experiments. Since oblique laboratory experiments in a velocity range of scientific interest are very costly, numerical studies are a powerful tool to investigate oblique impacts. Using our three-dimensional hydrocode iSALE-3D [2], we are performing extensive parameter studies concerning the influence of the impact angle on those physical processes. Our aim is to extend the validity of existing scaling laws for oblique impacts.

To make the application of such oblique scaling laws feasible for interpreting existing crater structures, identifying the impact angle and direction with those structures is of crucial importance. Here we are presenting some suggestions based on numerical modeling how it might be possible to identify angle and direction of the impactor at real crater structures. With this work we are investigating both the physical processes during an oblique impact and the resulting morphology including the distribution of proximale ejecta.

Trajectory motion model: For a better understanding of crater formation, the change of material motion (trajectories) with the impact angle is very important. Figure 1 shows some trajectories of tracers (massless particles that are placed in the target and follow the material motion) from an oblique impact model (30° measured from target surface).

Our simulations show that the crater rim in uprange direction is degenerated and defined by the so called "forbidden zone" of ejecta distribution (e.g. [3,4,5]). The magnitude of this degeneration is most likely dependend on the impact angle as well as on the impactor's size, friction, strength and other material properties. Identifying this structure at real impact craters is very difficult. Very oblique impacts are also assumed to produce degenerated rim-zones by ricocheting projectile material in downrange direction (e.g. [6]). For those cases it is not clear whether this feature is a result of the forbidden zone or just an effect of ricocheting matter.

Studying the trajectories may provide a better understanding of the general mechanism which leads to the formation of degenerated crater rims. We also found a correlation between the size of the forbidden zone and the impact angle. Since material motion is strongly dependent on the physical properties of both target and projectile material, the influence of friction on the trajectories most likely is important. Therefore we will incorporate a simple strength model (Mohr-Coulomb dry friction) in our simulations to study those influences.

Even though we found some good indicators for the impact angle and direction, identifying such characteristics in nature is much more complicated. We are going to compare our results with some geological studies from impact craters in Australia [Poelchau et al. (this volume)].

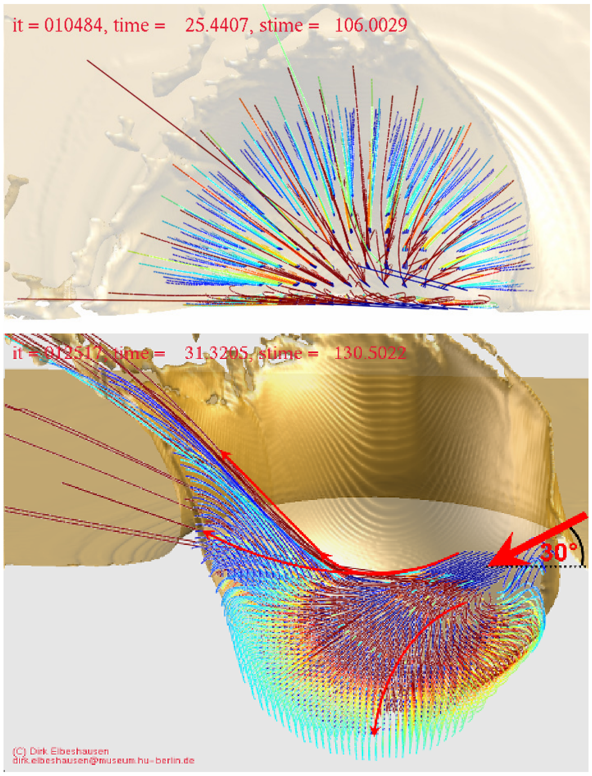

Fig.1: *Visualization of trajectories of an oblique (30°) impact. Trajectories are colorized by the peak shock pressure of the tracer. Tracer particles, which moved less than the projectile diameter are not drawn.*

Top: View from top into the crater (impact direction from right to left)

Bottom: View in a cross-section spaned by the impactors trajectory.

Slope of the crater rim: Although most oblique impacts are leading to circular craters [7], the slope of the crater rim may show local variations due to the impact direction [8].

Here we are trying to find some principles for the slope of the crater rim depending on the impact angle and direction. This is done by both numerical simulations (Fig. 2) and geo-structural studies of impact craters located in Australia [Poelchau et al. (this volume)].

Asymmetry of the central uplift: Fig. 3 shows a snapshot of an oblique impact at the time when the central uplift reaches its maximum extend. A slight asymmetry is observable at this stage for low impact angles. With both numerical modeling and geological observations [Poelchau et al. (this volume)], we want to identify the influence of the impact angle and direction on the morphometry, location [9] and especially the structure of the central uplift.

Conclusion: This is just the beginning of an interdisciplinary study of oblique impacts and the influence of obliquity on the geological structure of the resulting impact craters. Although our numerical study shows some very useful indicators for the impact direction, finding such indicators at real crater structures is much more complicated and might be impossible due to the state of preservation of most terrestrial impact structures. Therefore we tackle the objective to define characteristic indicators for the direction and angle of impact at crater structures by an interdisciplinary approach combining numerical modeling with structural geology [Poelchau et al. (this volume)]. Numerical models provide important information on structural peculiarities of oblique impact craters and what field geologist should in particular pay attention to. Results from field observations can be used by numerical modeling to conduct more detailed studies of the physical processes of oblique impacts. This may be another step forward in understanding oblique impact processes and their crater formation.

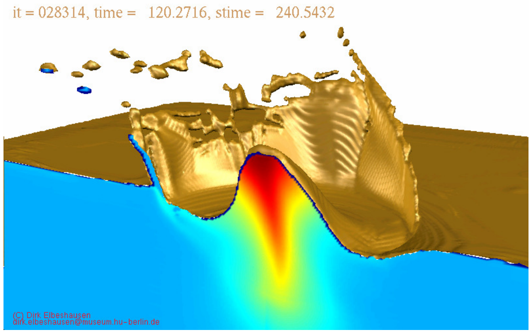

Fig.3: *Snapshot of an impact simulation with 30° impact angle (impact direction from top-right to bottom left). Front face shows temperature.*

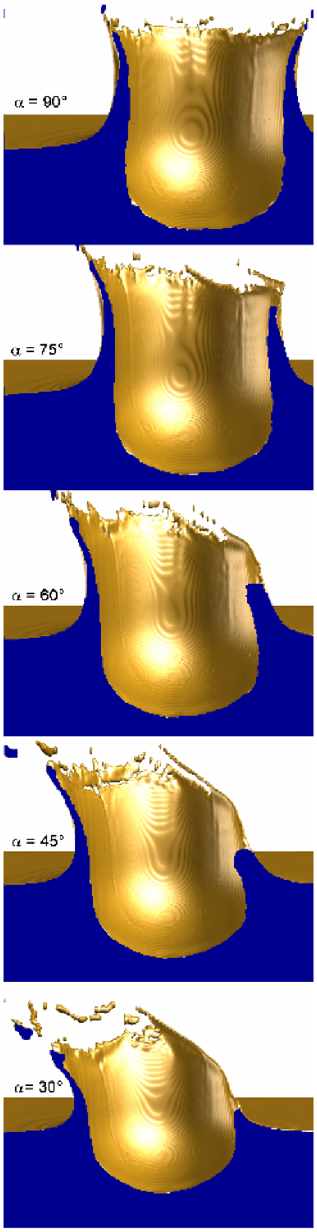

Fig. 2: *Crater shape depending on the impact angle*

Here are shown some crater profiles along the area spaned by the impactor's trajectory. These profiles are taken approx. at the time when the maximum crater volume is reached. The crater centre is moving slightly downrange with the impact angle. Also the angle between the ejecta trajectories (especially in downrange direction) and the target surface is getting lower with decreasing impact angle. The degeneration of the crater rim in uprange direction is stronger for lower impact angles. Surprisingly, the depth of the crater is nearly the same in a range between 90° and 60°. Afterwards, the depth of the crater decreases in a sinusoidal manner. This may be a first indicator for scenarios, where crater formation becomes more and more dependent on the momentum of the projectile [Elbeshausen et al. (this volume)].

Acknowledgements: This work was funded by DFG grant WU 355/5-1.

References: [1] Shoemaker, E. M. (1962) *Physics and Astronomy of the Moon,* 283-359. [2] Elbeshausen, D. (2007) *LPSC XXXVIII*, #1952. [3] Artemieva, N. A. and Ivanov, B. A. (2001), *LPSC XXXII*, #1321. [4] Artemieva, N. A. and Ivanov, B. A. (2004), *Icarus 171*, 84-101. [5] Artemieva, N. and Pierazzo, E. (2003), *Workshop on impact cratering*, #8022. [6] Chappelow, J. E. and Herrick, R. R. (2007) LPSC XXXVIII, #1419. [7] Gault, D. E. and Wedekind, J. A. (1978), *Proc. LPSC IX,* 3843-3875. [8] Poelchau, M. H., Kenkmann, T., Scherler, D. and Quart, S. (2007) *LPSC XXXVIII*, #1698. [9] Shuvalov, V. V. (2003) 3rd Int. Conf. Large Met. Imp. #4130.

CRATERING MECHANISMS OF OBLIQUE IMPACTS IN TARGETS OF DIFFERENT STRENGTH – INSIGHTS FROM NUMERICAL MODELING.

D. Elbeshausen[1] , K. Wünnemann[1] and G. S. Collins[2], [1]Humboldt-Universität zu Berlin, Museum für Naturkunde, D-10099 Berlin, Germany (dirk.elbeshausen@museum.hu-berlin.de) [2]Impacts and Astromaterials Research Centre, Department of Earth Science and Engineering, Imperial College London, London SW7 2AZ, UK

Introduction: Meteorite impact is a fundamental process on all planetary surfaces. Most impacts occur at angles between 30° and 60° (measured from horizontal) [1]. However, most of our knowledge on crater formation is based on vertical impact scenarios. Therefore studying the physics of oblique impacts is of crucial importance. Experimental studies have shown that the impact angle affects crater properties such as depth, diameter, morphology [2,3]. However, most of these experiments are controlled by the strength or friction of the material. In previous modeling studies it was demonstrated that in the initial contact and compression stage of an impact (where the impactor penetrates the target) the strength of the generated shock wave is highly asymmetric in oblique impacts [4,5]. This suggests that the late stage crater formation and collapse is influenced by the impact angle as well. However, both observations and numerical calculations (Fig.1) show a circular morphology of most crater structures, regardless of impact angle.

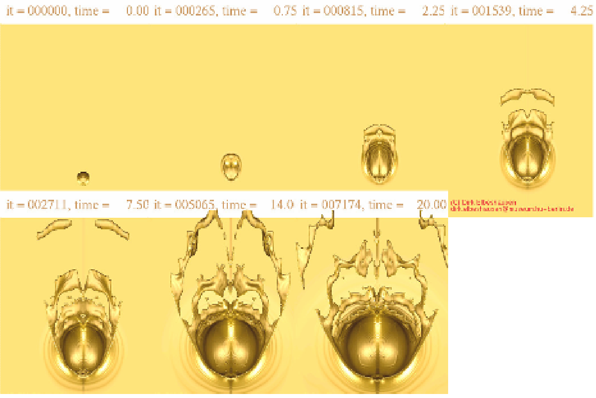

Fig. 1: *Steps of crater formation during an oblique impact (impactor size: 10km, velocity: 20km/s, impact angle: 45°). The initially formed oval crater shades off into a circular morphology.*

One of the most important tasks in analyzing existing impact structures is to link the size of a crater to the energy released during the crater formation. This is essential for estimating the environmental consequences of the impact. Since most of the required scaling laws are valid only for vertical impacts, investigating the influence of the impact angle is of crucial importance. Therefore, we are using our new hydrocode, iSALE-3D, to address following questions: Does a low impact angle change the main cratering mechanism from an energy-driven to an impulse driven scenario? How is the scaling of crater dimensions affected by the angle of impact? And how does strength influences this scaling?

Numerical Results: To answer these questions we performed some scaling analysis using the Pi-Group-Scaling [6]. Point source solutions [7] show a power law dependency between the gravity scaled source size $\pi_2 = 1.61 \cdot g \cdot L / v_i^2$ and the cratering efficiency $\pi_V = V\rho_t/m$ which looks as follows:

$$\pi_V = C_V \cdot \pi_2^{-\gamma}$$

g is gravity, L is the projectile diameter and v_i is the initial impact velocity, ρ_t is the density of the target, m the mass of the projectile and V the volume of the crater. C_V and γ are experimentally derived, material dependend scaling constants. The range of γ is limited between ¾ ("Energy-Scaling", the cratering efficiency is dependent on the impactor's energy only) and 3/7 $\cong$ 0.43 ("Momentum-Scaling", the crater formation is dependent on the impactor's momentum only) [8]. In our calculations we used Earth conditions (g=9.81 m/s^2) and chose a constant impact velocity of 20 km/s which corresponds approximately to the mean impact velocity on Earth of 17 km /s. In order to vary π_2 only the projectile diameter was changed. So far we only performed hydrodynamic calculations but also different strength models will be introduced. We calculated each scenario (π_2) for different impact angles in a range between 30° and 90°. Figure 2 shows the scaled maximum crater volume in a strengthless target as a function of π_2 for different impact angles. For vertical impacts, we obtained a scaling exponent of γ=0.66, which is in good agreement to experimental results of 0.65 (for water saturated sand) [8]. In the vertical case, γ is close to the energy-scaling limit, so impactor's momentum is less important than its energy. For lower impact angles (increasing obliquity) the scaling exponent does not change significantly (fig.3). Since the accuracy of the calculation dependending on the impact angle is not sufficiently known, the slight decrease of the exponent may be over-interpreted. However, even for low impacts (up to 30°) we found high exponents, which suggests that in a strengthless target the cratering efficiency of oblique impacts is also dominated by the impactor energy.

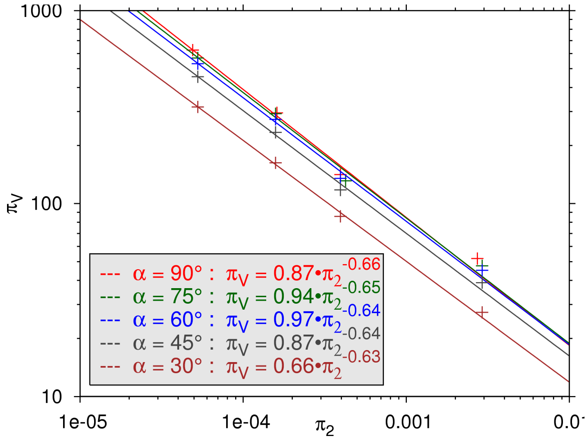

Fig. 2: *Scaling of oblique impact craters.*
The Pi-group-scaling (here: gravity scaled source size π_2 vs. cratering efficiency π_V) applied for multiple oblique impacts. A lower impact angle is resulting in lower crater volumes.

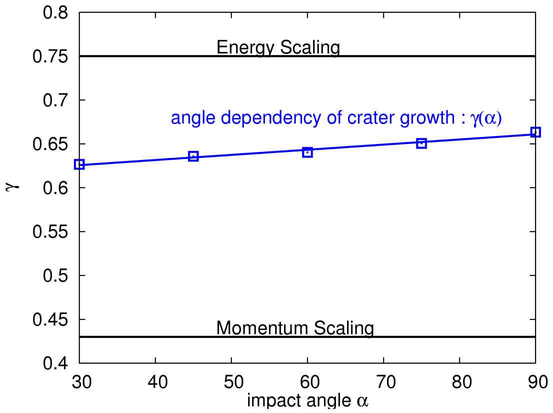

Fig. 3: *Scaling exponent depending on impact angle.*
Since the scaling exponent does not change significantly with the impact angle, also crater formation of oblique impacts (above 30°) is mainly dependend on the impactor's energy.

Conclusion and future studies: These are the first results of a detailed parameter study on crater formation for oblique impacts in the gravity dominated regime (crater size is controlled by gravity where strength plays only a minor role). We found that the main cratering mechanism is based on the impactor's energy. This does not change with increasing obliquity for impact angles in the range 30-90°.

This probably is no longer valid at very low (but also very unlikely) impact angles, which are close to the transition to ricocheting projectiles [3]. At very low angles to the horizontal we expect a rapid decrease of the scaling exponent γ towards the momentum scaling limit. This critical angle probably depends (amongst others) on the projectile size, its velocity and most likely on the strength of the target and projectile material. A numerical study concerning this question is intended.

Acknowledgements: This work was funded by DFG grant WU 355/5-1 and NERC grant NE/B501871/1.

References: [1] Shoemaker, E. M. (1962) *Physics and Astronomy of the Moon,* 283-359. [2] Burchell, M. J. and MacKay, N. G. (1996), J. Geophys. Res. 103(E10): 22761—22774. [3] Gault, D. E. and Wedekind, J. A. (1978), *Proc. LPSC IX,* 3843-3875. [4] Pierazzo, E. and Melosh, H. J. (1999), *Earth planet. Sci. Lett. 165*, 163-176. [5] Pierazzo, E. and Melosh, H. J. (2000), *MAPS 35*, 117-2000. [6] Holsapple, K. A. and Schmidt, R. M. (1982), *JGR 87,3*, 1849-1870. [7] Holsapple, K. A. and Schmidt, R. M. (1987), *JGR 92,7*, 6350-6376. [8] Schmidt, R. M. and Housen, K. R. (1987) *IJIE, 5,* 543-560.

DISTRIBUTION OF SHOCKED QUARTZ GRAINS ALONG THE LB-08A CORE THROUGH THE CENTRAL UPLIFT OF THE BOSUMTWI IMPACT STRUCTURE, GHANA - IMPLICATIONS FOR NUMERICAL MODELS.

L. Ferrière[1], C. Koeberl[1], and W. U. Reimold[2], [1]Department of Geological Sciences, University of Vienna, Althanstrasse 14, A-1090 Vienna, Austria. (ludovic.ferriere@univie.ac.at; christian.koeberl@univie.ac.at). [2]Mineralogy, Museum of Natural History, Humboldt-University, Invalidenstrasse 43, D-10115 Berlin, Germany (uwe.reimold@museum.hu-berlin.de).

Introduction: The 1.07 Myr old, 10.5-km-diameter Bosumtwi structure in Ghana (West Africa) is a very well preserved, complex impact crater with a pronounced rim and a small central uplift [1]. During the 2004 International Continental Scientific Drilling Program (ICDP) at the Bosumtwi impact structure [2], the LB-08A borehole was drilled into the crater fill and the underlying basement at the outer flank of the central uplift [3]. This drill core, recovered between 235.6 and 451.33 m below lake level, consists of (from the top to the bottom) approximately 25 m of polymict, clast-supported lithic breccia intercalated with suevite, which overlies fractured/brecciated basement composed of metasediment (mainly meta-greywacke).

Here, we present the results of a detailed petrographic study of eighteen different meta-greywacke samples from the basement. This work was carried out using an optical microscope and a 4-axis universal stage. It comprised three distinct steps:

1) Detailed modal analysis by point-counting; ~960 grains counted, on average, per thin section.

2) Systematic analysis of the properties of ~500 quartz grains per thin section; e.g., unshocked, shocked (with planar fractures [PFs] and planar deformation features [PDFs]), number of sets, decoration, toasted appearance, etc. (~9000 quartz grains investigated in total).

3) Analysis of the crystallographic orientation of the PDF sets in all PDF-bearing quartz grains per section.

Results and Discussion: The investigated samples show some variation with regard to abundance of major minerals (mostly quartz and feldspar), groundmass (mineral grains with apparent diameter <50 µm) mode, and phyllosilicate minerals; however, these variations are not major and were only determined for reference and in order to investigate possible limitations on interpretation of the final data.

Shocked quartz grains observed in meta-graywacke samples display PFs (usually 1 set) and PDFs (1, 2, or rarely 3 to 4 sets; Fig. 1), some of which are decorated with abundant tiny fluid inclusions. Some of the shocked grains have a "toasted appearance" (see [3] for more information). The relative abundances of quartz grains with decorated planar features and of those with "toasted appearance" indicate a moderate, but significant correlation (R=0.64). Furthermore, this study demonstrates that no correlation exists between the presence of decorated PDFs and fluid content (i.e., LoI) in the samples, which is contrary to a suggestion by [4].

Our work has revealed an obvious decrease of the abundance of shocked quartz grains with increasing depth (see Fig. 2). Surprisingly, the abundance of PDF sets per grain (denoted D) is rather constant with depth, averaging 1.32 ± 0.07 (excluding samples KR8-29-30-31, for which D is between 1.5 and 1.8 - due to the occurrence of PDF with 3 and extremely rarely 4 sets per host grain in these samples from the top of the section; Fig. 2). Those values of D, directly calculated from our systematic analyses, follow the same trend as the values of D determined from U-stage investigations; considering the fact that in the latter case, D values are, on average, 27 ± 8 rel% higher than values directly calculated from systematic analysis. This difference/shift is only due to the fact that some PDFs not visible under horizontal stage examination were observed during U-stage analysis. The systematic shift in the D values permits to confirm that our U-stage measurements seem to be representative of the full thin sections (even though only a restricted part of the section can be investigated using the U-stage).

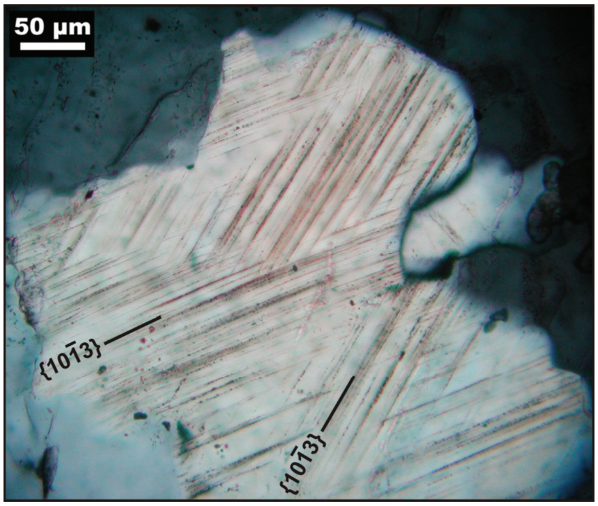

Fig. 1: Microphotograph of a typical shocked quartz grain with 2 symmetrical equivalent sets of PDFs (sample KR8-080, depth = 384.54 m).

The crystallographic orientations of 211 PDF sets in 116 quartz grains were analyzed in four thin sections of meta-graywacke samples (KR8-030, KR8-036, KR8-066, and KR8-101; depths = 272.00, 281.32, 353.95, and 414.28 m, respectively). A large proportion (83 to 91 rel% for the various thin sections) of the poles to PDF planes measured form angles of ~23° (corresponding to the $\omega\{10\bar{1}3\}$) with the c-axis orientation). Only a small proportion of basal PDFs was found (0 to 6 rel% per section) and planes parallel to the $\{10\bar{1}2\}$, $\{10\bar{1}1\}$, $\{10\bar{1}0\}$, $\{11\bar{2}2\}$, $\{11\bar{2}1\}$, $\{11\bar{2}0\}$, $\{51\bar{6}1\}$, and $\{21\bar{3}1\}$ orientations occur (1 to 6 rel% per section). This corresponds to shock stage 3 of [5], moderately shocked, according to observations from other impact craters [summary table in 5], which means that the studied section experienced a range of peak shock pressures up to ~20 GPa [e.g., 5]. Surprisingly, no significant differences of crystallographic orientations of PDF sets in quartz grains have been observed in the four investigated samples (the preliminary observations need to be confirmed with further investigations of other samples).

Conclusions: It is obvious that the observed distribution of shocked quartz grains (Fig. 2) reflects the variation of shock pressure in the uppermost part of the central uplift. However, based on the crystallographic orientations of PDF sets in quartz grains, it is not evident that the shock pressure differs significantly over the about two hundred meters of core investigated. It is not clear why this obvious decrease of PDFs abundance with depth is not clearly associated with significant differences of crystallographic orientations in quartz grains. The amount of shock-wave attenuation in this part of the uplifted target was apparently not strong.

In addition, this study provides an indication of the shock history of the rocks uplifted (and collapsed?) to the actual position of their occurrence. Such data may be useful for modeling of the zone of origin of these rocks in the target prior to crater modification, and provide constraints that need to be taken into account in future numerical modeling of the Bosumtwi structure.

Acknowledgments: This work was supported by the Austrian Science Foundation (FWF), grants P17194-N10 and P18862-N10, and the Austrian Academy of Sciences.

References: [1] Scholz C.A. et al. (2002) *Geology, 30,* 939–942. [2] Koeberl C. et al. (2007) *Meteoritics & Planet. Sci., 42,* 483–511. [3] Ferrière L. et al. (2007) *Meteoritics & Planet. Sci., 42,* 611–633. [4] Deutsch A. et al. (2007) *Meteoritics & Planet. Sci., 42,* 635–654. [5] Stöffler D. and Langenhorst F. (1994) *Meteoritics & Planet. Sci., 29,* 155–181.

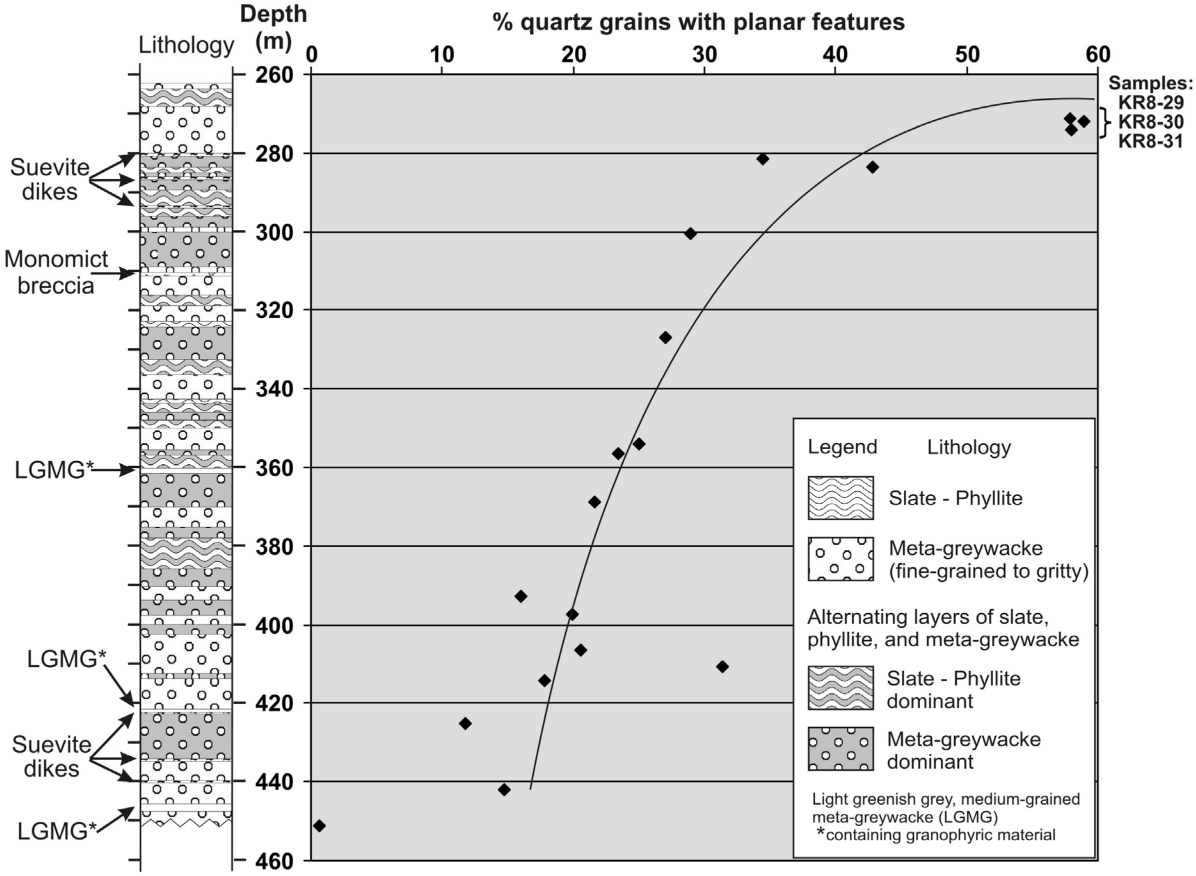

Fig. 2: Detailed lithostratigraphic column of the basement section of core LB-08A with the relative abundance of shocked quartz grains (with planar fractures and planar deformation features) in meta-greywacke samples.

MODELING DISTAL IMPACT EJECTA SEDIMENTATION: THE K/T BOUNDARY DOUBLE LAYER.

T. J. Goldin[1] and H. J. Melosh[2], [1]Department of Geosciences, University of Arizona, Tucson, Arizona 85721 (tgoldin@geo.arizona.edu), [2]Lunar and Planetary Lab, University of Arizona, Tucson, Arizona 85721 (jmelosh@lpl.arizona.edu).

Introduction: Impact ejecta layers not only serve as important marker beds in the stratigraphic record, but also hold information about the impacts that formed them and the environmental consequences of such events. Thus, ejecta deposits are just as important to the field of impact cratering as the crater itself. However, the mechanics of impact ejecta deposition are not well understood for planets with atmospheres, such as Earth, where complex interactions occur between the ejected particles and the surrounding atmosphere. Current models of ejecta emplacement that rely on the fact that material is ejected from craters on ballistic trajectories cannot account for multiple layers of ejecta deposited around some terrestrial craters such as Chicxulub, where a dual ejecta layer is oberved in North American localities. Studying the interactions between Chicxulub impact ejecta and the atmosphere is particularly important for understanding the environmental effects of this catastrophic impact.

Observed Chicxulub Ejecta: The global ejecta layer at the K/T boundary has been linked to the 65-Ma Chicxulub impact off the coast of the Yucatan, Mexico. The distal ejecta layer is found at sites more than 7000 km from the crater and has a fairly constant thickness of 2-3 mm [1]. In general, the distal ejecta layer, the "fireball layer", consists of ~250 µm densely packed spherules with a spherule area density of ~20,000 per square centimeter [2]. The layer is also enriched in Iridium, an impact indicator, which suggests an origin from the impact plume.

At sites of intermediate distance (2000-4000 km) from the crater in continental North America, the Chicxulub impact ejecta consists of two layers: In addition to the ~3 mm-thick upper layer containing the Iridium anomaly and relict spherules, there is a lower, thicker (i.e. ~2 cm-thick in Raton Basin, NM) layer consisting of mainly terrestrial claystone [2]. Despite local thickness variations [3], the average thickness of the lower layer decreases with increasing distance from Chicxulub [2]. It has been suggested that the upper layer is equivalent to the distal fireball layer and the lower layer represents weathered material from the ejecta curtain, but the mechanics of producing two distinct layers is unclear. The dual-layer stratigraphy has led to the argument of a second impact event, but we argue that atmospheric interactions can explain the emplacement of two distinct ejecta layers from a single impact.

Modeling: KFIX-LPL is a version of the KFIX code [4], which has been modified to suit the problem of impact sedimentation. KFIX is based on the original KACHINA code [5]. The finite-difference code models two-dimensional, two-phase fluid flow allowing us to examine the interactions between the atmosphere and ejected particles (spherules). The code can accomodate both stokes and turbulent flow.

Distal Fireball Layer: Starting with the simplest case of impact plume ejecta only, we modeled a simplified distal Chicxulub scenario of the injection of uniform sized (250-µm diameter) spherules into the atmosphere at 8 km/s, at an altidude of 200 km and with a inflow density consistent with the volume of spherules observed in outcrops. The initial mesh approximates the Earth's atmosphere and employs an exponential pressure gradient, constant temperature, and standard gravity of 9.8 m/s^2. Air is modeled using the equation of state of a perfect gas and the spherules are modeled as a simple incompressible fluid with the properties of basaltic glass.

The particles fall through the thin upper atmosphere, pushing the atmosphere downwards until the particles decelerate due to drag and increasing atmospheric pressure. The particles accumulate in dense layers at ~50-km altitude. The deceleration of spherules heats the atmosphere (>700 K) around the particles causing expansion of the atmosphere and creating a sharp boundary between hot dense atmosphere below the spherules and cool thin atmosphere above.

Double Layer: Deposits from the ejecta curtain are expected to extend to the intermediate distances where the double layer is observed. Thus, we employed an initial brief injection of terrestrial ejecta at 4.5 km/s into our model atmosphere in addition to the more prolonged flux of fireball material. The size (500 µm) and total volume of ejecta curtain material injected is again equal to that observed on the ground.

The high flux of ejecta curtain material compresses the atmosphere to below 40 km in altitude. As this brief pulse ends, the atmosphere rebounds upwards and ejecta from the fireball pulse accumulates at a higher level. Thus, the compression of the atmosphere by the terrestrial material alters the structure of the atmosphere causing the fireball material to fall separately and resulting in the deposition of two distinct layers (Fig. 1). Initially, the spherules settle through the atmosphere as individual particles, but as each layer nears the ground, density currents form. The layers are thus deposited more quickly than stokes flow settling would allow. Deposition of the lower terrestrial layer on the ground begins at ~80 minutes and that of the upper fireball layer begins at ~130 minutes.

Instability Formation: It is necessary to confirm that the instabilities produced in our KFIX-LPL simulations are real density currents and not numerical artifacts. Instead of attempting to evaluate the complex conditions of the ejecta models, we instead tested KFIX-LPL by simulating the observational results of a series of tephra fall experiments in water [6]. In these experiments, Carey [6] dropped Pinatubo tephra into a water tank at a mass flux comparable to that measured in nature and observed that the particle settling in the water column is accelerated by the formation of density currents. We modeled these experiments by dropping spherical tephra particles at various mass fluxes into a model mesh with the properties of water and observed instabilities formation. These instabilities were then evaluated using a criterion yielded by the ratio between turbulent instability growth rate and the Stokes velocity of individual particles:

$$B = \frac{\eta}{2a^2}\sqrt{\frac{N\,h}{\rho_0(\rho_p - \rho_0)g}}$$

where η is the viscosity of water, a is the particle radius, N is the particle volume fraction of the particle layer, h is the thickness of the particle layer, ρ_0 is the water density, ρ_p is density of the tephra particles and g is the acceleration of gravity. Large values of B (B>1) favor the formation of density currents and small values (B<1) favor Stokes flow settling.

Instabilities in our tephra fall models all agree with the instability criterion, occurring at B values exceeding 1.0. The modeled tephra layer is more stable than observed in the experiments; instabilities form at B values ranging from 10 to 15 instead of closer to 1. KFIX-LPL cannot accommodate some of the heterogeneities in the experimental setup, such as a range of tephra sizes and shapes, and so it is more difficult to initiate density currents than in nature. However, the models do consistently obey the instability criterion and thus the density currents are real and not numerical.

Summary: Results from KFIX-LPL models suggest that the influx of distal ejecta spherules into the upper atmosphere following the K/T impact event compressed the upper atmosphere, disrupted the normal pressure gradient, and heated the atmosphere at an altitude ~50 km. Such extreme changes to the atmosphere explain the deposition of the impact plume and ejecta curtain material as two distict layers and our models suggest deposition of both layers occurred over a timescale of hours. Density currents, the formation of which we have verified by modeling experiments of tephra fall in water, permit the ejecta to fall through the atmosphere much faster than individual particle settling. The double layer observed in North American localities is *expected* from a single impact at intermediated distances from Chicxulub.

References: [1] Smit, J. et al. (1992) *Proc. Lunar Planet. Sci. Conf.* 22, 87-100. [2] Smit, J. (1999) *Annu. Rev. Earth Planet. Sci.* pp. 27,75-113. [3] Izett, G. A. (1990) *GSA Special Paper* 249, 1-100.[4] Rivard, W.C. & Torrey, M.D. (1977) *Los Alamos National Laboratory Report* LA-NUREG-6623, Los Alamos, 125 pp. [5] Amsden, A.A. and Harlow F.H. (1974) *Los Alamos Scientific Laboratory Report* LA-5680, Los Alamos. [6] Carey, S. (1997*) Geology* 25(9), 839-842.

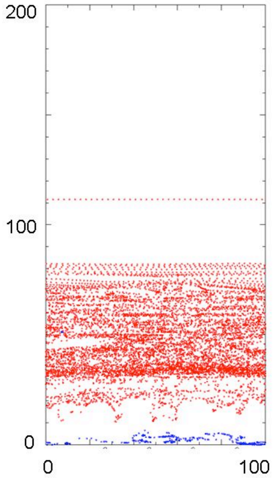

Figure 1. The position of injected spherule tracers after 90 minutes for locations ~2000 km from Chicxulub, where there is both an initial ejecta curtain pulse (blue) and the fireball pulse (red). At 90 minutes, the ejecta curtain material is being deposited to form a lower layer, distinct from the fireball material which will form the upper layer. Note the density currents forming in both types of ejecta as they approach the ground.

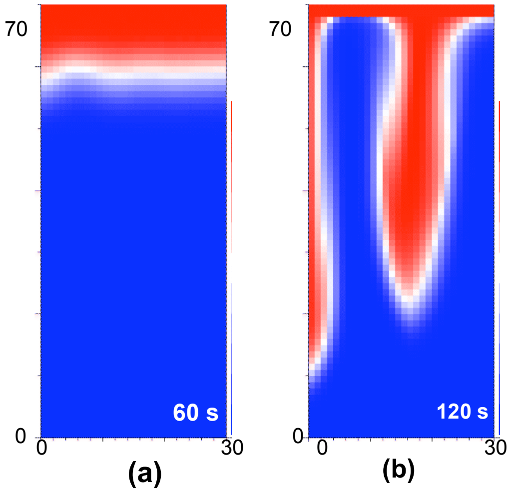

Figure 2. Macroscopic tephra density from model results for 48-µm tephra falling through a 30 x 70 cm^2 tank of water. Warm colors indicate higher densities. (a) Instabilities beginning to form after 1 minute. Tephra volume fraction is ~4% and B=14. (b) Further development of plumes after 2 minutes.

Pseudo-Liquid (Hugoniot) and Particle-in-Matrix Modeling in Geologic Materials.

R. A. Graham, The Tome Group, 608 Cenizo Blvd., Uvalde, Texas 78801. tomecenzo@aol.com

Introduction: Pressure-volume states in solids at elevated temperatures have been determined over the past fifty years with shock-compression loading and sample response measurements. The resulting equations-of-state materials models assume precise control of loading and sample geometry, thermodynamic equilibrium, and homogeneity. Such "Hugoniot" modeling is essentially pseudo-liquid in nature, as known or unknown characteristic solid behaviors are applied to observed liquid-like data and called "strength effects." Development of the field of high-pressure shock-compression science is one of the most outstanding accomplishments of the late 20th Century; it is largely responsible for our present high pressure knowledge of planetary and earth materials. 21st Century shock-compression science is directed toward developing models for quantification of local heterogeneities, a modeling challenge orders-of-magnitude more difficult. I have characterized the modern efforts as "stirring the pseudo-liquid" [1]. Quantification of PDF processes in quartz requires development of a "Particle-in-Matrix Model" that explicitly models local effects at the particle (quartz grain) level and continues stirring of the pseudo-fluid based on PDFs as indicators of local stresses.

Planar Deformation Features in Quartz: Some of the most persistent and thoughtful work in impact metamorphism has been carried out in quartz from impact craters and in laboratory experiments [2,3,4]. The work has moved from PDFs as general indicators of a pressure range to their use in semi-quantitative measures of shock pressure [5]. It is generally agreed that PDF orientations are along selected crystallographic directions and that their orientation with respect to the c-axis and their numbers are a unique result of shock compression. Further, as Robertson [6] has related based on his PDF studies of Bee Bluff samples "*It is apparent that a total comprehension of quartz planar feature development has not been achieved and that attention and that attention should be focussed on porous lithologies*." When fully developed, the particle-in-matrix model will accomplish that goal.

Shock-Compression Science in Quartz: The first shock work on quartz under precise laboratory conditions was begun in the Physical Research Department of Sandia Corporation (National Laboratories) in 1959. The work involved measuring the piezoelectric responses of x-cut quartz under precisely controlled explosive and impact loading [7,8,9]. The startling result obtained showed a state of zero piezoelectric polarization above the Hugoniot-elastic-limit; quartz was transformed to a bulk-state of zero shear-stress. This observation was verified by conventional shock response measurements by Wackerle [10] and Fowles [11]. Observations of optical emission showed linear features oriented at 36 and 26 degrees to the optical axis. Further impact work on impact showed similar linear optical planar features in quartz and in piezoelectric lithum niobate. Grady [12] developed a model of localized deformation along specific crystallographic directions with thermal energies resulting from release of the large shear strains (5 to 10% of shear modulus) under shock compression. In Grady's model temperatures are kept above melt temperature for 100 nsec or so. The present understanding is that we can expect loss of bulk shear stress in strong-solids of low- thermal conductivity. As shown in Davison and Graham [13] the model was tested over a range of materials and found to be characteristic of high-strength, low-conductivity solids. All available shock-compression work supports a model process of localized slip at critical shear stresses.

How Can We Model Local Effects in Quartz? : There is evidence from observations of quartz in impact craters that particle size, morphology and orientation significantly affect PDF formation. It is a relatively straight-forward task to identify the problem conceptually, but a long and detailed study is needed to quantify the processes. Figure 1 shows overall features of the particle-in-matrix conceptual model.

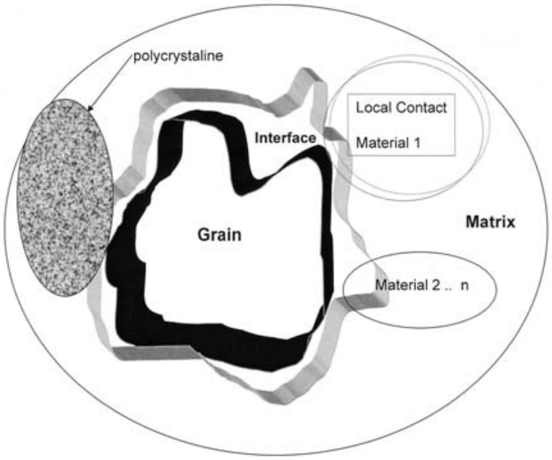

Figure 1. Typical particle-in-matrix modeling configurations to be quantified.

Note that starting from the grain level, each particle morphology is expected to strongly influence local deformation effects. Grains can be expected to have grain boundaries and internal structure. As deformation continues deformation interfaces will develop with local deformation depending upon the mechanical interaction between grain and matrix. In general the matrix may represent local contact or fully-contacting media. The local deformation can be easily shown to be in a shear-deformation space outside those available from macroscopic measurements. Thermal behaviors are directly dependent on the local deformations and thermal properties. Quantification and verification of a specific model requires a persistent, focused effort.

Current Status of Modeling: Over the past ten years significant progress has been made in developing the ability to calculate and quantify local processes in shock-compressed solids. PDF observations provide a defining basis for confirming theory as their presence provides the only capability available today to quantify grain-level effects. Describing the effects require shear stress prediction in the quartz particle. Most advanced modeling work is that of Horie [14,15], Baer [16] Eakins and Thadhani [17], and Dwivedi, et al [18]. Computer codes to incorporate characteristic local effects are in place in both 2-D and 3-D, but confirmation of calculations rests upon measurements at the macroscopic level. It is generally agreed that work is in an early development state.

Interesting Geologic Configurations: Two well-defined particle-matrix configuration are available from Bee Bluff target materials. The Carrizo Sandstone is essentially a highly porous compact of fine sandstone. The limonite present is of negligible strength. Its shock-transformed configuration is a well-bonded quartz compact resulting from melt at particle interactions. The quartz silt in the calcareous Indio siltstone consists of silt of random orientation in calcite particles.

Thus the sandstone is a porous quartz target with contacting local surfaces, a classical modeling problem. In contrast, isolated quartz grains in Bee Bluff Siltstone present a configuration of a hard grain of high strength in a soft, essentially hydrostatic medium, as calcite has low strength and deformed hydrostatically under shock deformation. The siltstone configuration is ideal in that in a hydrostatic deformation mode, all particles experience the same deformation regardless of their original crystallographic orientation. Controlled, precise shock preservation experiments will provide valuable data on the particle-in-matrix model for quartz.

References: [1] Graham, R. A. (2007) Samara Memorial Colloquim , Sandia Labs.
[2] French B. M. (1998) *Traces of Catastrophe, LPI Contribution #954*. [3] Grieve, R. A., Langenhorst, F. and Stöffler, D. (1996) *Meteoritics and Plan. Sci. 31*. 6-36. [4] Stöffler, D. and Langenhorst F. (1994) *Meteoritics 29*, 155-181. [5] Trepmann, C A. and Spray, J. G. (2005) *Geologic Society of America Special Paper #384*, 315-328. [6] Robertson, P. B. (1980) *LPI XI*, 938-940. [7] Neilson, F. W., Benedick, W. B., Brooks, W. P., Graham, R. A. and Anderson, G. W. (1961) in *Les Ondes de Detonation, Paris*, 391-419. [8] Brooks, W. P. (1965) *J. Appl. Phys. 36*, 2788-2790. [9] Graham, R. A. (1979) *J. Phys. Chem. Sol. 83*. 3048-3056. [10] Wackerle, J. (1962) *J. Appl. Phys. 33*, 922-937. [11] Fowles G. R. (1961) *Stanford Research Inst.Report #003-61*. [12] Grady, D. E. (1980) *J. Geo. Res. B2 85*, 913-924. [13] Davison. L. and Graham, R. A. (1979) *Phys. Reports 55*, 255-379. [14] Horie, Y. (2002) *Int. J. Plasticity 18*, 1427-1446. [15] Case, C. and Horie, Y. (2007) *J. Mech. Phys. Solids 55*, 589-614. [16] Baer, M. (2007) in *Encylopedia of Explosives, edited by Y. Horie.* [17] Eakins D. and Thadhani, N. (2007) *J. Appl. Phys.10* 043508. [18] Dwivedi, S.K., Asay, J. R. and Gupta. Y. M (2006) *J. Appl. Phys. 100*, 083509.

"ANTISYMMETRIC" SHOCK WAVE DISTRIBUTION AT RIES IMPACT CRATER, GERMANY?:A MICRO-RAMAN SPECTROSCOPICAL STUDY OF SHOCKED ZIRCON.

A. Gucsik, Max Planck Institute for Chemistry, Department of Geochemistry,. Joh.-J.-Becherweg 27, D-55128 Mainz, Germany (gucsik@mpch-mainz.mpg.de).

Introduction: Zircon is a highly refractory and weathering-resistant mineral that has proven useful as an indicator of shock metamorphism in the study of impact structures and formations that are old, deeply eroded, and metamorphically overprinted (e.g., [1-3]. Zircon has advantages compared to quartz or other shock-metamorphosed rock-forming minerals that have been widely used as impact indicators, but are far less refractory. Furthermore, U-Pb dating of zircon can provide constraints on the ages of impact events or deposition of impact formations (e.g., [4] and references therein).

Effects of high degrees of shock deformation (>10 GPa) in quartz and other rock-forming minerals (e.g., feldspars), such as planar deformation features (PDFs), were first described from shocked granite inclusions in suevite. Additionally, shock metamorphic indicators, such as high-pressure mineral phases (e.g., coesite, stishovite), diaplectic quartz and feldspar glass, and fused quartz glass (lechatelierite) from suevite were also found in impact breccias from the Ries Crater. The Ries crater is the source of the moldavite tektites of the Central European Strewn Field [5,6].

The extent of shock metamorphism in minerals from the impact formations of the Ries impact crater can be classified into six stages (known as 0, I, II, III, IV, and V) that are characterized by various elastic and plastic deformation phenomena as well as isotropization of minerals, the formation of high-pressure phases and the occurrence of mineral or bulk rock melting [5,6].

The purpose of this investigation is to further investigate the capability of Raman spectroscopy to document shock deformation and to determine whether specific Raman effects in the zircon/scheelite-structure can be utilised to determine particular shock pressure stages.

Samples and Experimental Procedures: For this study, zircon samples were used that had been separated from three rock samples: (1) a glass bomb from suevite from the Aumühle site, which had been classified on the basis of shock metamorphic effects as a Stage IV specimen; (2) a biotite gneiss sample from Appetshofen, classified as Stage II, and (3) crystalline rock fragments from a suevitic sample obtained near Seelbronn, the shock stage of which was given as Stage III. These locations are shown in Figure 1. Crystals from these three zircon separates were cut both parallel and perpendicular to the c-axis, for the purpose of Raman spectrometric analysis.

Raman spectra were obtained with a Renishaw RM1000 confocal micro-Raman spectrometer with a 20 mW, 632 nm He-Ne laser excitation system and a thermo-electrically cooled CCD detector. The power of the laser beam on the sample was approximately 3 mW. Spectra were obtained in the range 100-1200 cm^{-1}, with approximately thirty seconds total exposure time. The spectral resolution (apparatus function) was 4 cm^{-1}. Raman spectra were taken from 3 μm^3 sample volume and CL spectra were obtained from approximately 35 x 45 µm areas.

Further details on the samples and methodology can be found in [7].

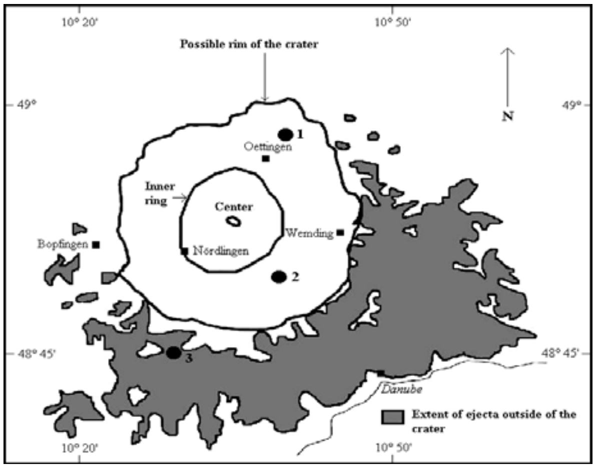

Figure 1. *Locality of the Ries basin in Germany and approximate extent of the Bunte Breccia and suevite breccia. Sample localities are indicated as 1=Aumühle, 2=Appertshofen, 3=Seelbronn. Outline of crater and extent of Bunte Breccia and suevite breccia.* *Scale: the diameter of the possible rim of the crater is approximately 26 km. Map from* [7].

Results and Discussion: The Raman spectra of the naturally shock-deformed zircon samples from the Ries crater (Stage-II: 35-45 GPa, Stage-III: 45-50 GPa, Stage-IV: >50 GPa) cut parallel and perpendicular to their crystallographic c-axes do not exhibit significant differences from each other. The fluorescence background and widths of the Raman bands in all samples are considerably larger than for the experimentally shock-deformed samples, which indicates lower crystallinity with major zoning and defects.

Both Stage-II (35-45 GPa) samples are characterized by five peaks at 224, 356, 439, 974 and 1007 cm^{-1}, indicating zircon-type structure as reidite (Figs. 2a,b). Additionally, a weak peak at 210 cm^{-1} appears in the Raman spectra of the Stage-II (parallel) sample (Fig. 2a). The peak intensities of the (perpendicular) sample are higher than those of the parallel-samples. The peak at 1007 cm^{-1} is relatively strong in the (perpendicular) sample (Fig. 2b).

The Raman spectrum of the Stage-III (45-50 GPa) sample (parallel) shows eleven peaks at 202, 224, 327, 356, 404, 439, 465, 558, 845, 974 and 1007 cm^{-1}, which indicate the presence of the scheelite-type phase among predominant zircon-type material (Fig. 2c). In contrast, the Stage-III perpendicular-sample contains only eight peaks at 202, 214, 224, 356, 404, 439, 974 and 1007 cm^{-1} showing pure zircon-type structure (Fig. 2d). A peak at 1007 cm^{-1} is relatively strong in the perpendicular-sample (Fig. 2d). In general, the fluorescence background in the parallel-sample is considerably higher than in the perpendicular-sample. In both cases, the peak intensities are similar [7,8].

The spectra of the Stage-IV samples (60-80 GPa, parallel- and perpendicular-samples) are characterized by seven peaks at 202, 215, 225, 356, 439, 974 and 1007 cm^{-1}, indicating zircon-type phase [7,8] (Figs. 2e,f). In both cases, a peak at 1007 cm^{-1} is relatively strong. The peak intensities of the perpendicular-sample are higher than those of the parallel-sample (Fig. 2f).

Conclusion: Whilst these three zircon fractions were obtained from three crystalline rock samples from the Ries crater, which, on the basis of the respective variation of shock metamorphic effects had been classified to belong to different shock stages (II-IV), the overall variation of deformation effects noted in this Raman investigation is not compatible with these shock classifications. A highly shocked rock was affected by a heterogeneous shock wave distribution, which causes different shock effects, such as e.g., microdeformations in the mineral content of whole rock. This also a wide range of shock stages in the various minerals that are present in such a rock, including unshocked fragments or clasts to partially or completely melted phases. Consequently, the shock-deformed zircons might be related to the low-shock regime (<30 GPa), and do not represent the same shock stages as indicated by whole-rock petrography indicating the anti-symmetric distribution of shock waves during the Ries impact event. The results show a clear dependence of the Raman properties of zircon with shock pressure, which confirms the possible use of this results in method as a shock indicator.

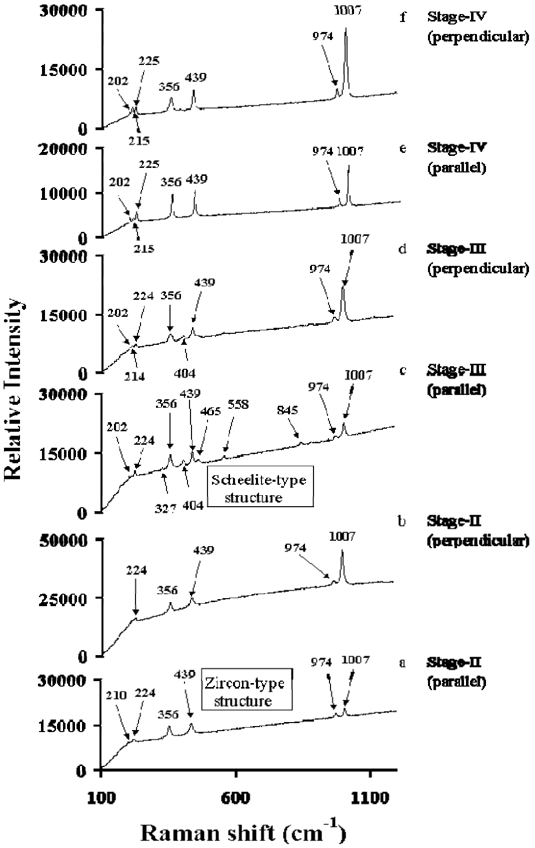

Figure 2. *Raman spectra of shock deformed zircon specimens from the Ries impact crater (Germany). Numbers denote peak positions in [cm^{-1}]. Data from* [7].

References:

[1] Bohor B. et al. (1993) *EPSL, 119,* 419-424. [2] Reimold W.U. et al. (2002) *Eur. J. Mineralogy 14,* 859-868. [3] Wittmann A. et al (2006) *Meteoritics & Planet. Sci., 40,* 1-17. [4] Kamo S.L. et al. (1996) *EPSL, 144,* 369-387. [5] Stöffler D. (1974) *Fortschritte der Mineralogie 49,* 256-298. [6] von Engelhardt W. (1990) *Tectonophysics, 171,* 259-273. [7] Gucsik A. et al. (2004) *In: Dypvik H, Burchell M, Claeys Ph, (Eds,) Cratering in Marine Environments and on Ice, Springer-Verlag, Heidelberg, pp 281-322.* [8] Knittle E. and Williams Q. (1993) *Am. Min. 78,* 245-252. [9] Kolesov B.A. et al. (2001) *Eur. J. Mineralogy 13,* 939-948.

THE FATE OF WATER IN MELTS PRODUCED DURING NATURAL AND EXPERIMENTAL IMPACTS INTO WET, FINE-GRAINED SEDIMENTARY TARGETS.

R. S. Harris[1], P. H. Schultz[1], and P. L. King[2], [1]Department of Geological Sciences, Brown University, Providence, RI 02912 (Scott_Harris@brown.edu), [2]Department of Earth Sciences, University of Western Ontario, London, ON N6A 5B7, Canada.

Introduction: The fate of water is an important consideration in modeling the formation and emplacement of melt ejecta during hypervelocity impacts, especially those that excavate thick successions of porous sedimentary materials [e.g., 1,2]. We have previously reported the occurrence of extremely hydrous glass inclusions (Fig. 1) in 445 ka impact melt breccias from Centinela del Mar, Argentina (UCdM glasses) [3]. Based on electron microprobe (EMP) data, acquired using a Na-decay routine developed by Devine et al. [4], we estimated that water concentrations in some of these glasses are as high as 16 to 24 wt% [3]. These concentrations are comparable to estimates (~10-20 wt%) made by Osinski [5] for hydrous glass clasts in Ries suevites (based on low totals in quantitative SEM/EDS measurements). Textural relationships and cooling fabrics demonstrate that these hydrous glasses could not have resulted from post-impact hydration. The evidence suggests instead that they briefly existed as physically separate, low-viscosity "flows" inside, or attached to, significantly drier melts.

Subsequent observations of similar hydrous melts in six other late Miocene to Recent Pampean impact glass deposits identified by Schultz et al. [6-9] lead us to conclude that they are a common feature of impact melts produced from fine-grained, loosely consolidated sediments. In order to more accurately characterize and quantify the volatiles contained in these melts, we report here the first direct measurements of their water concentrations obtained using three different methods: 1) micro-transmission Fourier Transform infrared spectrometry (μT-FTIR); 2) micro-reflectance FTIR (μR-FTIR); and 3) secondary ion mass spectrometry (SIMS).

We also report the results of hypervelocity impact melting experiments designed to test the plausibility of "trapping" pore water in melts formed from saturated, fine-grained particulate targets.

Natural Hydrous Impact Melts: Although hydrous inclusions occur in all Argentine impact melts, they are particularly abundant in UCdM glasses. They may comprise more than 20-30 vol% of individual melt breccia clasts. The hydrous glasses typically are pale to bright yellow and occur as both irregular patches and distinct flow-like features (Fig. 1).

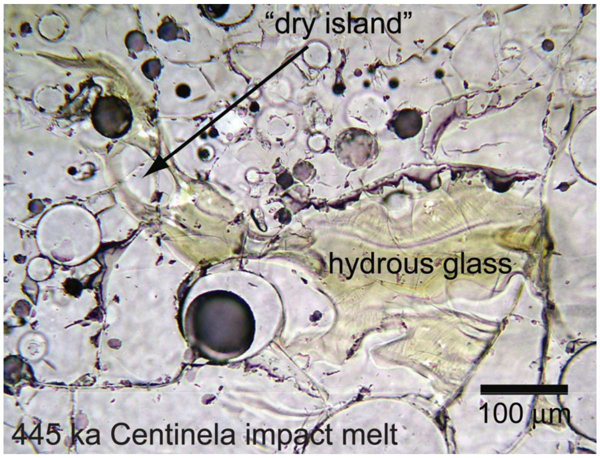

Figure 1. Plane-polarized light (PPL) photomicrograph of a yellowish hydrous glass inclusion in UCdM melt breccia. These melts likely formed during a riverine impact near the present-day village of La Dulce [11]. EMP, μFTIR, and SIMS analyses indicate that water concentrations in the hydrous glasses range between ~3 and 24 wt%. The surrounding colorless glass is essentially anhydrous (<0.1wt% water). Note that the anastomosing, hydrous flow has stranded "islands" of dry glass.

μFTIR analyses were performed using Thermo-Nicolet Nexus 870 and 670 FTIR spectrometers with Continuum microscopes. μT-FTIR data were treated according to King et al. [10]. Because water concentrations in the hydrous glasses are sufficiently high to saturate the detectors at ~3500 cm^{-1}, total water concentrations were calculated by adding [OH$^-$] and [H_2O] determined from absorption spectra at ~4300 cm^{-1} and ~5200 cm^{-1}, respectively. Results ranged from ~3 to 9 wt%. Water concentrations in the surrounding colorless glass were also determined by μT-FTIR and generally are <0.1 wt%. The hydrous inclusions have complex geometries; consequently, the volume of glass measured by μT-FTIR unavoidably includes some percentage of nominally anhydrous glass. Corrections were applied after determining the 3-D shape of some inclusions using SEM/BSE mapping. Recalculated water concentrations approach 15 wt%.

Water concentrations determined from the μR-FTIR technique developed by King et al. [12] range from ~9 to 24 wt%. SIMS measurements, performed using a Cameca IMS 3f ion microprobe, range between ~5 wt% and 18wt%.

From the results of multiple analytical techniques, we have shown that hydrous glass inclusions in UCdM melt breccias contain, at a minimum, between ~3 and 24 wt% water. Petrographic and geochemical observations support the hypothesis that these glasses formed by melting small packets of waterlogged sediment. The packets may have melted as they became entrained in superheated, devolatilized shock melts formed earlier in the formation of the crater. The resulting wet melt inclusions probably failed to degas due to rapid quenching inside the engulfing anhydrous melts. However, it may be possible that some or all of the hydrous inclusions formed directly from shock melting of water-rich sediments. The retention of water may be due to a combination of the high solubility of water in silica-rich melts at high pressure and low diffusion rates for water in silica-rich melts [13] particularly at the high temperatures likely in a shock event. It is notable that the upper limits of water concentrations measured in hydrous impact glasses are consistent with the solubility of water in alumino-silicate melts formed at approximately 1 to 3 GPa (at temperatures >1100ºC) [e.g., 14, 15].

Experimental Hydrous Impact Melts: Pyrex® spheres were fired at 5 km/s into targets composed of water-saturated, very fine-grained fragments of rhyolitic pumice at the NASA/Ames Vertical Gun Range. Melts recovered from these experiments appear to be amalgamations of the impactor and target materials. The alumino-silicate melts contain fluid inclusions (Fig. 2) that are morphologically similar to hydrous glasses in UCdM and other Argentine impact melt breccias. Water concentrations in these inclusions were measured using μR-FTIR. The inclusions— and some regions of the glass where no obvious inclusions are observed— contain at least 8 to 10 wt% water. Most of the glass surrounding the inclusions has water concentrations below the reliability of the μR-FTIR technique (i.e., <1 wt%).

Implications: Our observations of natural and experimental impact glasses show that significant concentrations of water may be preserved in impact melts formed from wet, fine-grained sediments. Our results highlight and extend the point made by Osinski et al. [16] that models of impact processes cannot assume that volatile-rich sediments are simply "degassed and dispersed." We also show that hypervelocity gun experiments can produce reasonable analogs for studying impact melts formed from hydrated sediments. We may be able to examine how volatile behavior in melt ejecta changes for different environmental and impact parameters and how these variations affect the production and dynamics of impact melts.

The concept that hydrous melts commonly are produced by impacts into wet, loessoid sediments has important implications for other sectors of the planetary science community. Impacts into a water/ice-rich regolith, such as we might expect on Mars, should produce hydrous impact melts. Some workers [e.g., 17] have assumed that volcanic and impact melts can be distinguished from one another by the paucity of volatiles in the latter type. That assumption possibly should be reversed. Martian impact melts might at least contain significant water-rich melt inclusions affecting both the spectral properties and alteration products we might observe from such melts. Trapped water will also affect melt rheologies influencing the morphology of melt sheets and melt-rich ejecta deposits.

Finally, if impact melts can trap water from target sediments, it might be possible they could capture volatiles from ice-rich impactors. This is a key question we hope to explore through continued experiments and geochemical investigations of natural hydrous melts.

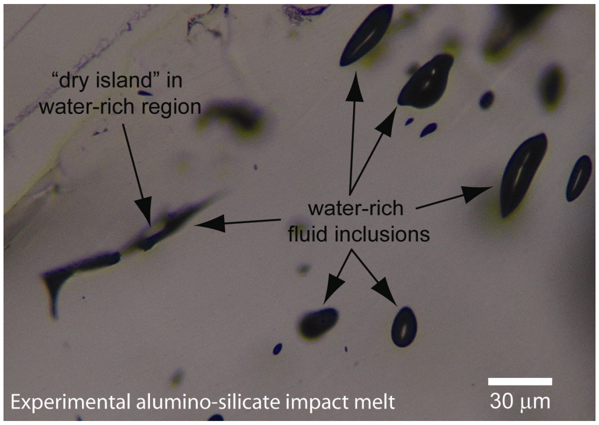

Figure 2. PPL photomicrograph of an experimental melt produced by an impact into water-saturated, fine-grained particulate material. Some target water appears to have been trapped within fluid-rich inclusions. μR-FTIR measurements indicate that these inclusions contain approximately > 8 to 10 wt% water. Note that some inclusions are morphologically very similar to hydrous glass inclusions in natural impact melt breccias (Fig. 1).

References: [1] Kieffer S. W. and Simonds C. H. (1980) *Rev. Geophys. Space Phys., 18*, 143-181. [2] Artemieva N. (2007) *Meteoritics & Planet. Sci., 42,* 883-894. [3] Harris R. S. and Schultz P. H. (2005) *Meteoritics & Planet. Sci., 40,* A63. [4] Devine et al. (1995) *Am. Min., 80,* 319-328. [5] Osinski G. R. (2003) *Meteoritics & Planet. Sci., 38*, 1641-1667. [6] Schultz P. H. et al. (1994) *Geology, 22,* 889-892. [7] Schultz P. H. et al. (1998) *Science, 282,* 2061-2063. [8] Schultz P. H. et al. (2004) *Earth Planet. Sci. Lett., 219,* 221-238. [9] Schultz P. H. et al. (2006) *Meteoritics & Planet. Sci., 41,* 749-771. [10] King P. L. et al. (2004) *Mineral. Assoc. Canada, Short Course Series, 33*, 93-133. [11] Harris R. S. et al. (2007) *XXXVIII,* #2243. [12] King P. L. et al. (2005) *Geochim. Cosmochim, 69,* A744. [13] Zhang Y. and Behrens H. (2000) *Chemical Geology, 169*, 243-262. [14] Paillat O. et al. (1992) *Contr. Miner. Petrol., 112*, 490-500. [15] Bureau H. and Keppler H. (1999) *Earth Planet. Sci. Lett., 165,* 187-196. [16] Osinski et al. (2003) *LPI Contr. No. 1155*, 59. [17] Rieder R. (1997) *Science, 278*, 1771-1774.

Acknowledgements: This work was funded by NASA Grant NNG05G137G. Additional support was provided by the Mary-Hill and Bevan M. French Fund for Impact Geology. EMP analyses were performed at the NSF/Keck Microprobe Facility (Brown Univ.) with the assistance of Joe Devine. SIMS analyses were performed at the NE National Ion Probe Facility (Woods Hole Oceanographic Inst.) with the assistance of Nobu Shimizu. FTIR instruments at the Univ. of Western Ontario and at the NASA/Keck RELAB facility (Brown Univ.) were utilized. We greatly appreciate help from Rachel Klima, Kim Dalby, David Lescinsky, and William Collins.

FROM MAP TO MODEL – 3D VISUALIZATION OF THE VREDEFORT CENTRAL UPLIFT, SOUTH AFRICA.

A. Jahn, U. Riller and W. U. Reimold, Museum fuer Naturkunde Berlin (Invalidenstrasse 43, D-10115 Berlin, Germany, Andreas.Jahn@museum.hu-berlin.de).

Introduction: Structural, petrological and geophysical work [1, 2, 3], as well as numerical modeling [4], have been conducted on the Vredefort impact structure to understand the mechanism of rock deformation during crater modification of large terrestrial impacts. In order to bridge the gap between geological ground truth and dynamic, numerical modeling, we aim to construct a 3D structural model of the impact structure followed by kinematic restoration of deformation that leads to formation and collapse of its central uplift.

The Vredefort Dome is the eroded remnant of a collapsed central uplift of a Paleoproterozoic impact structure[1]. The central part of the Dome, approximately 40 km wide, consists of Archean (>3.0 Ga) granitoids and is surrounded by steeply dipping and overturned sedimentary and volcanic strata of Proterozoic (3.0 - 2.1 Ga) age, known as the collar around the crystalline core. To the north and west, the collar rocks are well exposed and form a series of concentric morphological quartzite ridges and valleys along less resitant shale horizons around the core, whereas to the east and the south, the central uplift is covered by the Phanerozoic Karoo Supergroup.

Methods: Using the software *GOCAD* and *GeoModeller* (Intrepid Geophysics), we attempt to construct a 3D model of the collar rocks. The modell will include the attitude of prominent marker surfaces (sedimentary strata and lithological interfaces) as well as impact-induced discontinuities known from field analysis and geophysical imaging. Exposure of pre-impact rocks is largely limited to the northwestern quadrant of the impact structure and will, thus, constrain the 3D model. The construction of a multi-surface model from this portion of the collar will not only involve marker surfaces but also take into account the volume of lithological groups, e.g. the West Rand Group (Fig. 1), in between major lithological interfaces. As more structural information becomes available from the field and geophysical imaging, the model will consider also the geometry of major discontinuities and local deformation on lithological interfaces.

Following construction of a 3D model, the data set will be imported into *3DMove* (Midland Valley Inc.) to conduct further structural analyses and 3D kinematic restoration. The first step in this procedure will be to eliminate possible effects of post-impact deformation by restoring displacements on post-impact faults, and will result in the geometry of rocks attained upon the end of the modification stage. This model will be used to interpolate the other three quadrants to generate a full circumferential model, on which the "dome inversion tool" of *3DMove* will be applied. Passive back rotation of marker horizons and application of the "volume tracker tool" will allow to estimate the rock volume that was translated during central uplift formation. The tracker tool will also serve to check the plausibility of the kinematic restauration.

Expected results: Although the accuracy of earth models on a crustal scale is often limited, modern geophysical methods will allow to reliably image the deep structure of the Vredefort Dome. The visualization of structural elements as intended in this study will provide new insights into the deep structure of the Vredefort Dome and into the processes associated with crater modification of large terrestrial impacts. In particular, an estimate of the displaced rock volume can provide information on the relative importance of doming and inward-directed mass transport during central uplift formation. The correlation of the moved rock volumes with the current deep structure of the impact structure can also show how much material passed through the core and is today removed by erosion.

References: [1] Reimold W. U. and Gibson R. L. (2006) *Chem. Erde, 66,* 1–35. [2] Lana C. et al. (2006) *S. Afr. J. of Geol., 109,* 265-278. [3] Henkel H. and Reimold W. U. (2002) *J. Appl. Geophys.,* 43–62. [4] Ivanov B. (2005) *Sol. Sys. Res., 39,* 381-409. [5] Bisschoff A. A. and Mayer J. J. (1999), *Council for Geoscience, Pretoria,* Geol. Map 1:50.000.

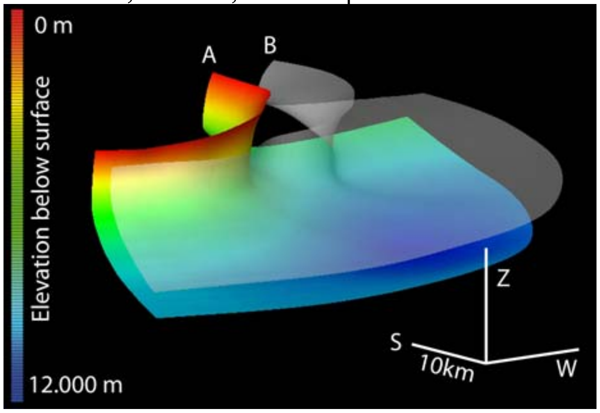

Figure 1: Crude 3D model of the northwestern portion of the Vredefort impact structure inferred from the orientation of strata at surface [3, 5]. The model shows the base (surface A) and top (surface B) of the West Rand Group. View is from northeast.

HYPERVELOCITY COLLISIONS OF PROJECTILES AND TARGETS: SHOCK WAVE PROPAGATION IN HETEROGENEOUS ROCKS INFERRED FROM MICROSTRUCTURES

T. Kenkmann[1], [1]Museum für Naturkunde – Mineralogie, Humboldt-Universität Berlin, Invalidenstrasse 43, 10115 Berlin, Germany, thomas.kenkmann@museum.hu-berlin.de

Introduction: What do we know about the very early stage of impact cratering from the observational point of view? When projectile and target collide, the kinetic energy of the projectile splits up into four components: The internal energies of projectile and target, the residual kinetic energy of the projectile, and the kinetic energy transferred to the target. The fractions of each component depend on the material properties of projectile and target, e.g. the fraction of internal energy increases with increasing compressibility of the material. However, the partitioning between these components is also strongly time dependent and the energy is finally almost completely transferred to the target [1]. The structure of shock waves that are generated at contact planes depends on the rise time to the final peak pressure which is influenced by the dynamic elastic limit and phase transitions. Shock magnitude and propagation velocity are controlled by the projectile and target material and the impact energy. The duration of the shock corresponds to the size of the projectile [2].

Considering large impact craters, rocks involved in the initial contact and compression stage may get completely vaporized upon pressure release from shocks exceeding hundreds of GPa (except for thin spall plates of the rear of the projectile). The vaporized material subsequently may condensate to fine-grained spherules and is disseminated in ejecta plume deposits (suevites). Trace element analysis [3] of these materials suggests that mixing of projectile and target occurs. Jetting by oblique convergence of the projectile-target contact plane is also a very early time phenomenon observed in experiments. It accelerates material to velocities higher than the initial impact speed [4]. Likewise tektite formation is linked to the early cratering [5]. More information on the contact and compression stage is provided from impact events where the entropy increase from shock compression is not sufficient to entirely vaporize or melt the projectile and target at ground zero. Likely candidates to analyse the early shock propagation are (a) shock experiments, (b) meteorites, and (c) small natural impact craters.

Heterogeneities in rocks: Rocks are principally heterogeneous. Any type of interface between different constituents of a rock such as lithological interfaces, voids, fluid inclusions, grain- and phase boundaries are characterized by a discontinuity in density and, hence, shock wave propagation velocity and cause impedance contrasts [6]. Shock impedance is defined as the product of the density of the material times the shock wave velocity in this material. Impedance contrasts disorganize shock waves and lead to shock wave reverberations. This causes the development of localized concentrations of stress, temperature, and deformation, which can ultimately lead to the formation of thin melt veins [7],[8]. The propagating shock wave reverberates on many interfaces and will increase or decrease the pressure stepwise with respect to the first shock wave. After a short time the grains achieve a mean shock state that is often misleadingly called “equilibrium shock state”, e.g. [9],[10]. Shock microstructures used for shock barometry are calibrated against this average pressure. They are in contrast to highly localized shock features like melt veins that can contain high pressure polymorphs, which are sometimes called “disequilibrium shock features”. While they are not suited as pressure gauges to determine the average shock level in projectile or target, they are important for the understanding of shock propagation in different materials. The formation of networks of melt veins in the central portions of impact structures and projectiles is an important energy sink and may leave the rock substantially hotter than predicted from Hugoniot data [11]. The formation and persistence of melt veins produced as a result of rock heterogeneities may be a contributor to the loss of strength on pressure release [11].

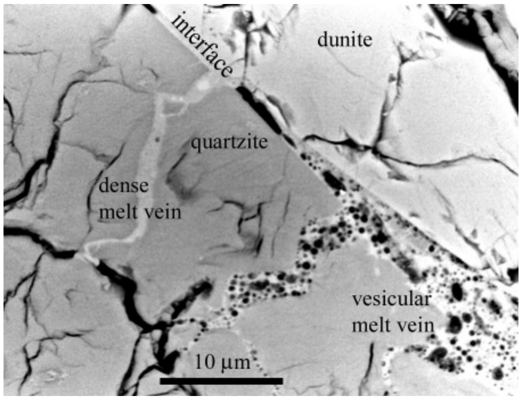

Fig. 1 Experimentally produced dense and vesicular melt vein at the interface between quartzite and dunite [6]

(a) Observation in shock experiments: The shock wave plateau in shock recovery experiments (impedance and reverberation techniques) is always limited to microseconds, which usually prevents the formation of high-pressure phases [12]. Beside the extensive pressure calibration of “equilibrium” shock features by shock experiments, e.g. [12],[13], shock veins were successfully reproduced along lithological interfaces

(Fig. 1)[6], tabular surfaces [8], and within single crystals [14]. Along with the effect of porosity [15] they document the importance of these features for absorbing shock wave energy and for the attenuation of the shock. Formation mechanisms derived from these experiments include shock melting by pressure-temperature excursions (hot spots) plus shear-induced frictional melting. Recently, target and projectiles interpenetration and mixing could be demonstrated experimentally (Fig.2) [16].

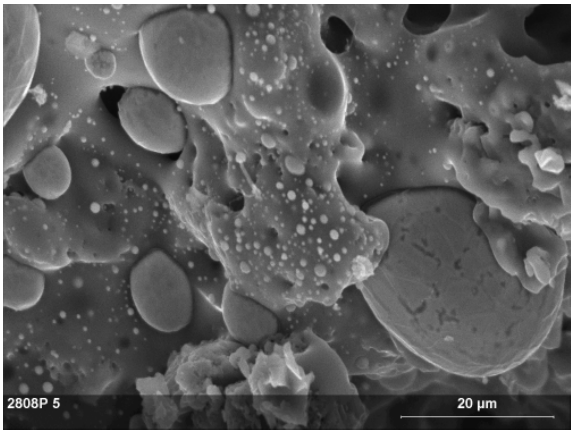

Fig. 2 Surface of a spalled steel projectile after impacting a sandstone target at 5.3 kms^{-1} [16]. The surface is coated by SiO_2 and iron oxide, the bubbles indicate boiling.

(b) Observations in meteorites: Highly shocked meteorites may give some clues to early shock propagation although the observed shock features may result from multiple impacts [10]. The presence of metals in some meteorites lead to impedance contrasts that are substantially higher than those characterizing most terrestrial rocks [9]. Meteorites are often fractured and porous. The strongly different material properties and heterogeneities in meteorites result in shock veins with high pressure silicates [17], melt pockets, melt dikes, and troilite/metal deposits in fractures [9][18]. The effects are most pronounced at metal-silicate and metal-pore space interfaces.

(c) Observation in small natural impact craters: Impact craters can contain residues of the projectile. Their emplacement most likely occurs in a very early stage of the crater forming process. The mechanism by which the emplacement occurs is a matter of debate. It could be emplaced in a vapor phase, as melt droplets or as fine grained solid material. Rocks closest to ground zero undergo the largest amount of strain [11], and frictional heating may contribute to an unknown magnitude to the total heat budget. Like projectiles, rocks located near the point of impact initially contain open pore space that can be filled with volatiles such as water. The strongest impedance contrasts within a rock occur at free surfaces. Open fractures, cleavage planes, or porosity effectively absorb the shock wave energy and heat the target [19]. Consequently, the volume of material shocked during an impact is commonly smaller in porous rocks than in dense rocks as a significant part of energy is used for pore space collapse and localized melting. The depth down to which cavities remain open is inversely proportional to gravity of a planetary body. On Earth, open fractures and pore space may occur down to depths of 1 km and more. Simple impact craters may develop completely within this upper target layer where cavities are present. The larger the impact crater, the less prominent is the effect of open pores or fractures for the cratering process. Interestingly, the simple-to-complex transition of impact craters on Earth (~3-5 km diameter) seems to correlate with depth down to which open cavities may exist. Is the simple-to-complex transition of impact craters even influenced by this critical depth?

Cooperation of observers and modelers: To better understand shock microstructures, more micro- and mesoscale numerical simulations are desired to fully understand their dynamic formation. These micromechanical models may also give valuable input algorithms for macro-scale modeling. Among other aspects observers should try to quantify how much shock energy is absorbed at heterogeneities.

Acknowledgement : I am grateful to the Workshop organizers for their kind invitation. The research was made possible by Deutsche Forschungsgemeinschaft.

References: [1] O´Keefe, J. D., Ahrens, T. J. (1982). GSA SP 190, 103-120. [2] Melosh, H. J. (1989) Impact cratering, 245 p. Oxford. [3] Koeberl, C. (1994) GSA-SP 293, 133-154. [4] Gault, D. E. et al. (1968) in Shock metamorphism of Natural Materials, 87-99. [5] Artemieva, N. A. (2002) in Impacts in Precambrian shields, 257-276, Springer. [6] Kenkmann, T. et al. (2000) MAPS 35, 1275-1290. [7] Kieffer, S. W. (1977) in Impact and Explosion cratering, 751-769. [8] Heider, N. Kenkmann, T. (2003). MAPS, 38, 151-1460. [9] Stöffler, D. et al. (1991) Geochim. Cosmo. Acta, 55, 3845-3867. [10] Stöffler, D., Grieve, R. A. F. (2007) IUGS Subcommission on Metamorphic rocks, Chapter 11, Blackwell. [11] Fiske, P. S. et al. (1995) Science, 270, 281-283. [12] Langenhorst, F., Deutsch, A. (1994) EPSL 125, 407-420. [13] Reimold, W. U., Stöffler, D. (1978) Proc. LPSC, 9, 2805-2824. [14] Langenhorst, F. et al. (2002) MAPS, 37, 1541-1553. [15] Stöffler, D. et al. (1975) JGR, 80, 4062-4077. [16] Kenkmann, T. et al. (2007). LPSC 38,CD-Rom#1831 [17] Sharp et al. (1997) Science, 277, 352-355. [18] Spray, J. G. (1999). Geology, 27, 695-698. [19] Kieffer, S. W. (1971) JGR 76, 5449-5473.

IMPACT TRIGGERING OF THE SNOWBALL EARTH DEGLACIATION? C. Koeberl,[1] B. A. Ivanov[2], and J. Goodman[3]. [1]Center for Earth Sciences, University of Vienna, Althanstrasse 14, Vienna, A-1090, Austria, (christian.koeberl@univie.ac.at), [2]Institute for Dynamics of Geospheres, RAS, 119334, Moscow, Russia, (baivanov@idg.chph.ras.ru), [3]Woods Hole Oceanographic Institution, Woods Hole, MA 02543, USA (jgoodman@whoi.edu).

Introduction: Observational evidence supports the idea that the Precambrian Earth's history has episodes of total ice coverage of the planet (e.g. [1, 2]). The Snowball Earth hypothesis [1] states that the Sturtian (about 710 Ma) and Marinoan glaciations (about 635 Ma) were of global extent and lasted for several million years each. A variation of this hypothesis, called the Slushball Earth, requires milder conditions without substantial equatorial sea ice [3, 4]. The Snowball Earth glaciations would have ended abruptly in a greenhouse environment, whereas the Slushball would have experienced a slower deglaciation. A variety of reasons for initializing global glaciation have been discussed, including decreased solar luminosity [5], a continent breakup [6] and the passage of the Solar System through a molecular cloud [7]. Not only is the cause of a possible glaciation unclear, but the cause and mechanism of deglaciation is also debated (e.g. [8]).

The goal of our study is to investigate if it is conceivable that a large-scale impact event might have triggered the deglaciation. The problem of the climatic effects of large impact events is not clear, as previously a Chicxulub-scale impact was suggested to induce global freezing [9].

Impact Probability: Fig. 1 presents in the cumulative form the terrestrial cratering rate as the global number of craters of a certain diameter would be accumulated globally (impacts into the ocean are presented with an equivalent crater diameter on land).

If one assumes tentatively that the "critical" impacts would only occur late into a "snowball period", the estimated "snowball" phase duration of 4 to 30 Ma [2] results in estimated probable maximum crater diameter of ~70 km. This provides the limit for our estimates.

The scaling laws of impact cratering allow estimating the projectile diameter, provided the impact velocity corresponds to an average asteroidal value of ~18 km/s, which results in asteroid diameters of ~5 to 7 km. This range of projectile size is used for the reconnaissance numerical modeling of impacts.

Numerical Modeling 1: The hydrocode SALEB has been used for our numerical modeling experiments. The hydrocode has the limited ability to compute multi-material problems. Currently SALEB can handle 3 materials, provided that the mixed cells contain only materials #1 and #2, or materials #2 and #3. This fact forces us to use a set of modeling to study the motion of the rock basement, water/ice, and terrestrial atmosphere in a set of trial runs.

Set # 1 includes the modeling of rocky asteroid impact into the layered target: H_2O layer (ocean water and/or ice cover of continents) over the crystalline basement. Equations of state are ANEOS-computed tables for multi-phase H_2O (water, water vapor, and 7 ice phases [10]), granite and dunite [11]. In this set the atmosphere is not represented, so that the model set #1 allows us to estimate the maximum amount of H_2O ejected above a given altitude.

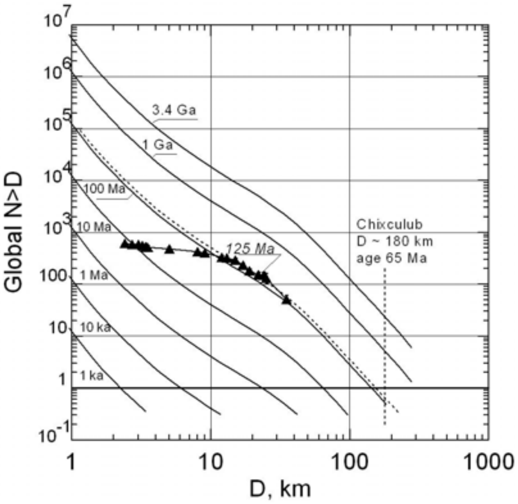

Fig.1. The cumulative global number of impacts, measured in equivalent crater diameter on land, for various time periods. The estimated accuracy is a factor of ~2. During the characteristic time period of 10 Ma a few (3±2) impacts are probable with energy suitable to create a 40 to 50 km crater on land. Black triangles are for dated terrestrial craters [12].

Numerical Modeling 2: To estimate the influence of the atmosphere on the evolution of the H_2O plume we used set #2 of target geometries: air (in the form of an ideal gas) representing the atmosphere above the ice/water layer. In the latter case we are forced to use pure ice target over the rigid bottom, as the atmosphere is described as a separate material and the SALEB code cannot currently handle rock/H_2O/air mixture in a single computational cell

Numerical Modeling 3: The case of a vertical impact is computed using the axisymmetric SALEB code. Qualitative estimates of oblique impacts were done in the planar case.

Preliminary Results: The reconnaissance modeling of the high velocity impact into a "snowball" Earth reveals first estimates of processes and the amount of vaporized water, delivered into the atmosphere and above. In the "modest" case of a 5-km-diameter asteroid impact into an ocean 3 km deep, the mass of water vapor delivered above 20 km reaches 2×10^{15} kg. A larger projectile diameter of 10 km (slightly smaller than the K-T boundary case) increases this estimate about 4 times.

An impact into 800-m-thick ice over a granitic basement produces ~ 4 times less water vapor in the plume (for the case of the 5-km-diameter asteroid).

What follows next in terms of the development of the water vapor in the plume depends on the interaction with the atmosphere. We can approximately model the early plume collapse over the atmosphere (Figs. 2, 3). In the later case our model with the widest spatial boundaries (500 km above the target level and 2000 km from the impact point) results in the pushing out of the upper atmosphere as far as >1000 km outside of the impact location within 400 seconds. The resulting "warm spot" in the atmosphere has a diameter of 2000 km; it initially fills with warm water vapor (which will condense after cooling), and could be a reasonable agent of excitation for a further atmospheric circulation disturbance and cloud formation.

The oblique impact with the most probable impact angle of 45^{o} (modeled here preliminarily only in the planar approximation) demonstrates the same general behavior of evaporated ice/water as for the steam plume in the case of a vertical impact. The unimportance of the projectile wake results in an enhanced forward plume expansion in the upper atmosphere after the oblique impact. However the main outcome of the model is the same: an impact into a water/ice layer uplifts an appreciable amount of initially evaporated H_2O over the top of the terrestrial atmosphere.

Conclusions: In terms of cratering rates, it is statistically plausible that the impact of a ~5 km diameter asteroid occurs during a "snowball period" with a duration of several Myr. Most probably is an impact into the ice-covered ocean. In such a case a vapor plume with a total mass of $n\times10^{15}$ kg will rise up and then collapse over the atmosphere, creating a transient "hot spot". The more indirect consequences may include a global enrichment of the upper atmosphere with water vapors, dust and sea salt particles (in the case of an impact into ocean). Photochemical reactions should be taken into account for a further climatic modeling. At this point our simulations do not allow a conclusion if an impact of a realistic magnitude could cause deglaciation of a Snowball Earth.

References: [1] Hoffman, P.F. et al. (1998) *Science* **281**, 1342-1346 [2] Bodiselitsch, B. et al. (2005) *Science* ***308***, 239-242. [3] Hyde, W.T. et al. (2000) *Nature*, **405**, 425-429. [4] Crowley, T.J. et al. (2001) *Geophys. Res. Lett.* ***28***, 283-286. [5] Crowley, T. J. and Baum, S. K. (1993) *J.Geophys. Res.* **98**, 16723-16732. [6] Donnadieu, Y. et al. (2004) *Nature* **428**, 303-306. [7] Pavlov, A.A. et al. (2005) *Geophys. Res. Let.* ***32***, L 03705. [8] Le Hir, G. et al. (2007) *Comptes Rendus Geosciences* **339**, 274-287. [9] Bendtsen J., and Bjerrum C.J. (2002) Geophys. Res. Lett. **29**, 15,1706. [10] Ivanov B.A. (2005) *36th Lunar Planet. Sci*., Abst. #1232. [11] Pierazzo E. et al. (1997) Icarus **127**, 408–423. [12] Hughes D.W. (2000) *MNRAS* **317**, 429-437.

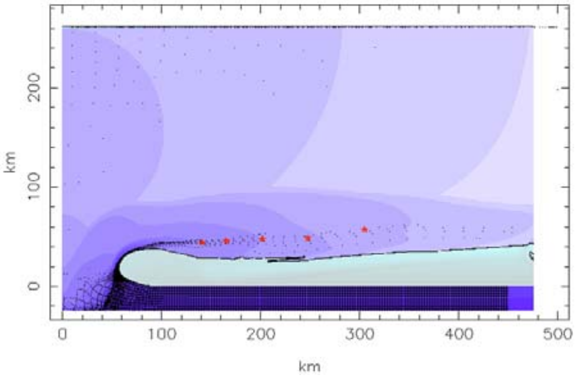

Fig. 2. The snapshot of the H_2O vapor cloud 30 seconds after an impact of a 10-km body into ice. The blue levels logarithmically reflect rarification of expanding vapors. Atmosphere (bluish gray) is trapped under falling and expanding vapors. Red stars show tracers with detailed thermodynamic history recording.

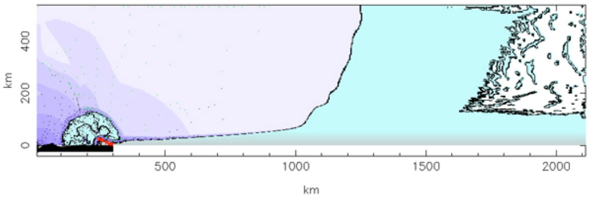

Fig. 3. The same run as in Fig. 2, but 370 seconds after the impact. The vapor cloud expanded to distances > 1000 km from the impact point. The trapped atmosphere at distances of 100 to 300 km has "blown up", what looks like a numerical artifact is caused by incomplete treatment of small volume concentrations in mixed cells. The vapor plume ballistically drops down to the atmosphere, reaching the condensation state at the plume/atmosphere boundary.

THE MAGNETIC BEHAVIOR OF SYNTHETIC MAGNETITE INDUCED BY SHOCK RECOVERY EXPERIMENTS IN THE RANGE BETWEEN 10 AND 45 GPA.

T. Kohout[1], A. Deutsch[2], L.J. Pesonen[1], U. Hornemann[3], [1] Division of Geophysics, Solid Earth Geophysics Lab., University of Helsinki, PO Box 64, FIN-00014 Helsinki, Finland, tomas.kohout@helsinki.fi, Lauri.Pesonen@helsinki.fi,[2] Institut für Planetologie, WWU Münster, Wilhelm-Klemm-Str. 10, Münster 48149, Germany, deutsca@uni-muenster.de, [3] Ernst-Mach-Institut, D-79588 Effringen-Kirchen, Germany, hornemann@emi.fhg.de.

Introduction: Shock-induced changes in magnetic properties of rocks, minerals, and meteorites play an important role in modeling the magnetic anomalies of impact structures (e.g., Vredefort), interpreting the magnetic anomalies of planetary bodies (e.g., Mars) and understanding paleomagnetic data of meteorites. We report results of shock experiments with synthetic fine-grained magnetite (mt) of SD (single domain) to PSD (pseudo-single domain) magnetic behavior. This study complement previous shock experiments on a diabase containing natural PSD-type magnetite [1, 2].

Experimental set-up: Well characterized synthetic mt powder, mixed with Al2O3, was sintered into pellets. The surface-polished disks (Ø 10 mm, h 4 mm) were embedded into an ARMCO steel container, surrounded by an ARMCO momentum trap; details of the set-up are given in [3]. The samples were shocked in series of experiments in the range from nominal pressures of 10 to 45 GPa using high-explosives. Inside the ARMCO container the prevailing magnetic field was ~five times higher than the ambient field. After the shock, the containers cooled down slowly to ambient temperatures. The estimated post-shock T of the samples range from ~ambient T (10 GPa) up to about 1400 K (45 GPa). The given shock pressures correspond to the resp. shock pressure that would be achieved in single crystal quartz using identical experimental parameters (i.e., thickness of the sample, driver, and flyer plates, mass and type of high explosive) [3].

Evaluating pressures actually reached in the experiments requires a model to account for the high porosity of the pellets compacted from the mt powder. Their original density was only 1.7 to 2.3 g_*cm^{-3}; post-shock densities are currently measured (a tricky task due to the small sample size). The high porosity significantly influences the post-shock T. Independent of the fact that p, shock- and post-shock T are insufficiently constrained, the experiments form a well-characterized series of shots at systematically increasing pressure. The driver plate and the sample holder were removed with a lathe. We have monitored cautiously T to avoid re-heating, and hence, a not shock- and/or post-shock change in the magnetic properties of the mt pellets. Surprisingly enough, the sample disks were not friable and could be removed by retaining their shape largely unchanged.

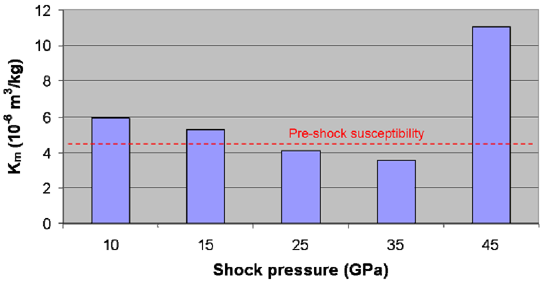

Figure 1. Variation in susceptibility with shock pressure.

Results: *Magnetic Susceptibility*. Tentative results indicate a progressive decrease in susceptibility with increasing shock pressure (Fig. 1). The exception is the 45 GPa sample showing a significant increase of susceptibility, an effect probably related to shock induced changes in mineralogy or to contamination of the sample by melted steel from the container.

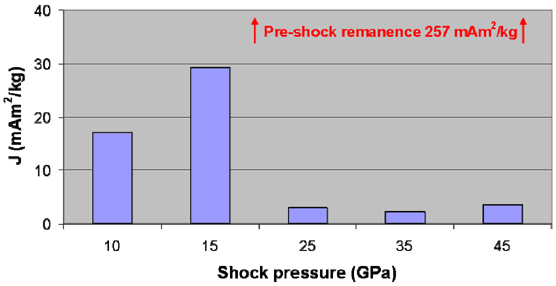

Figure 2. Variation in RM with shock pressure.

Post shock RM (Remanent Magnetization). The samples were given SIRM (Saturation Isothermal Remanent Magnetization) prior the shock. This remanence was significantly reduced due to shock demagnetization. There was more progressive reduction in the remanence observed at higher shock pressures (Fig. 2).

ARM (Anhysteretic Remanent Magnetization) and SIRM (Saturation Isothermal Remanent Magnetization): Analysis of the ARM (50 µT DC field / 100 mT AF field) demagnetization curves of the samples prior to and after the shock reveals a more soft behavior of the shocked samples, probably related to magnetite coarsening due to the shock. The same trend is observed in the case of the SIRM. The overall ARM intensities slightly increased while the overall SIRM intensities slightly decreased as the result of shock (Fig. 4).

References: [2] Langenhorst F. et al. (1999) *LPS XXX*, Abstract# 1241. [1] Pesonen L.J. et al. (1997). *LPS XXVIII*, 1087-1088. [3] Langenhorst F. and Deutsch A. (1994) *EPSL 125*, 407-420.

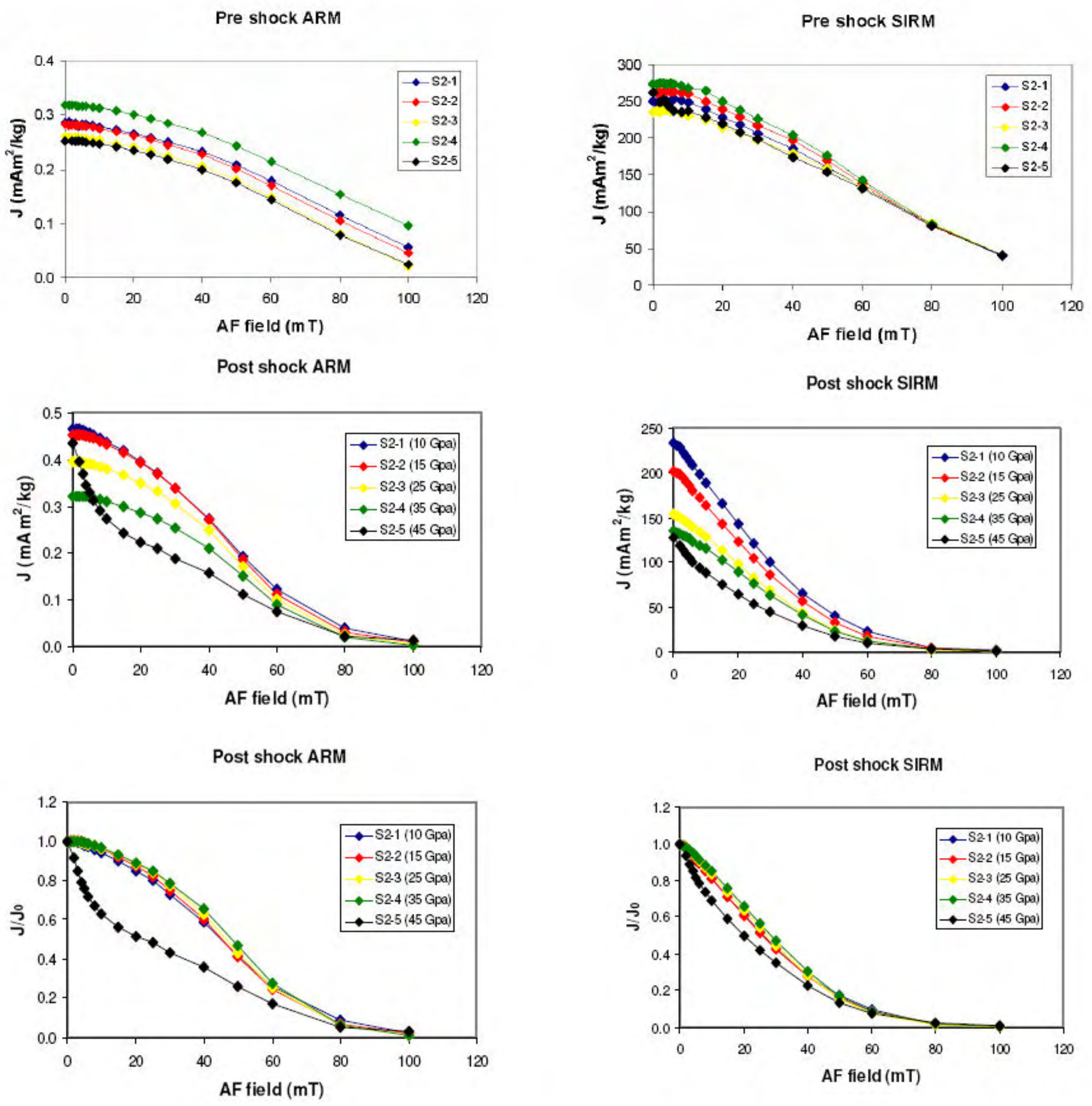

Figure 4. Variation in ARM and SIRM.

Acknowledgements: We thank D. Dunlop and Ö. Özdemir for providing the synthetic magnetite, M. Feldhaus, E. Heikinheimo, U. Heitmann, and S. Hoxha for skilfull technical assistance. Financial support by German Science Foundation grants De 401/15, La 830/4, and Ho 1446/3 is appreciated.

IMPORTANCE OF PSEUDOTACHYLITIC BRECCIA ZONES FOR UNDERSTANDING THE FORMATION OF CENTRAL UPLIFT STRUCTURES: FIELD EVIDENCE FROM THE VREDEFORT DOME, SOUTH AFRICA.

D. Lieger[1], U. Riller[1], W. U. Reimold[1], R. L. Gibson[2], [1]Museum für Naturkunde Berlin, Invalidenstrasse 43, 10115 Berlin, Germany, daniel.lieger@museum.hu-berlin.de, [2]School of Geosciences, University of the Witwatersrand, Private Bag 3, P.O. Wits 2050, Johannesburg, South Africa.

Objectives: Target rocks underlying the central portions of large terrestrial impact craters, such as Sudbury and Vredefort, are characterized by the pervasive presence of pseudotachylitic breccia zones, often up to hundreds of meters in width and many kilometers in length at surface. Uncertainty regarding the origin of prominent breccia zones exists in particular with regard to melt generation (i.e., friction- vs. shock-induced), melt mobility, geometry of zones, fragmentation process and timing of breccia formation with respect to the evolution of central uplift structures. Collectively, this is paramount for assessing the kinematics and mechanics of rock deformation during formation of central uplift structures in large impact structures, a major focus of numerical models. We address these issues with field-based structural analysis of pseudotachylitic breccia bodies in the Vredefort Dome, the central uplift structure of the ca. 2 Ga Vredefort impact structure.

Observations: Our structural analysis focusses on mapping the geometry, orientation, brecciation intensity, and possible indicators of melt flow in pseudotachylitic breccia zones as well as orientation of pre-impact fabrics in the outer core of the Vredefort Dome (made up of Archaean metagranitoid and gneissic rock). The breccia zones range from mm- to cm-wide veins and dm- to m-wide dikes to irregular zones of network breccias tens of meters wide.

Large breccia zones are mostly disposed radially and concentrically with respect to the centre of the Vredefort Dome, often regardless of pre-impact mineral fabric orientation. By contrast, thin pseudotachylitic veins are arranged in multiple sets, orthogonal to each other, whereby one set is often found to be concordant to pre-impact mineral fabrics. Where three-dimensional exposure permitted judgement, such as in quarries, prominent breccia zones approximate planar geometry and were found to be horizontal and vertical.

Brecciation intensity was estimated visually by taking into account breccia zone thickness, fragment-matrix ratios as well as density and shape of fragments. Outcrops characterized by high brecciation intensity seem to connect to radial and concentric zones on the scale of the crystalline core. The trend of these zones coincides with the strike of prominent breccia zones.

The geometry of breccia zone margins indicates that breccia zones are essentially fragment- and melt-filled fractures formed by dilation, i.e., volume increase. This is supported by the fact that strike separation of pre-impact mineral fabrics at the zones is generally less than a few centimetres. Therefore, breccia zones formed as tension gashes or minor hybrid shear faults. Where pseudotachylitic breccia veins overstep each other, their respective tips are curved toward the neighbouring vein, thereby isolating elliptical host rock fragments. This underscores the formation of breccia zones in terms of fracture mechanics known from upper-crustal tectonic regimes. Recognition of the pre-impact fit of marker points across pseudotachylitic veins allowed us to determine the components of maximum dilation vectors at a given outcrop surface. Measurement of the component vectors throughout the outer core of the Vredefort Dome indicates either radial or concentric stretching of material, regardless of breccia zone orientation.

Pre-impact configuration of fragments in large breccia zones and the paucity of fragments that are exotic with respect to the immediate host rock indicates that generally fragments were not transported distances larger than tens of meters. However, this may not apply for the pseudotachylitic matrix, i.e., former melt.

Conclusions: Our field observations indicate that the geometry and distribution of pseudotachylitic breccia zones is rather systematic across the outer core of the Vredefort Dome. In particular, the orientation of prominent zones and components of maximum dilation agrees with a strain field characterized by radial and concentric stretching of rock. Such a strain field is compatible with the terminal stages of central uplift formation inferred from numerical modelling, i.e., gravitational collapse of the central uplift. Thus, transport of melt and its pooling in (low-pressure) dilation zones seems to have been controlled by the overall strain field. By contrast, the geometry of minor sets of pseudotachylite veins and their geometric relationship to pre-impact mineral fabrics may be explained in terms of decompression of rock upon rapid uplift and removal of overburden. The dilational nature of melt-filled dislocations seems to exclude generation of melt by frictional sliding on these dislocations.

TITAN IMPACT CRATERS – CASSINI RADAR RESULTS AND INSIGHTS ON TARGET PROPERTIES

R. D. Lorenz[1], C. A. Wood[2], J. I. Lunine[3], S. D. Wall[4] , R. M. Lopes[4], K. L. Mitchell[4], F. Paganelli[4], Y. Z. Anderson[4], E. R. Stofan[5] and the Cassini RADAR Team [1]Space Department, Johns Hopkins University Applied Physics Laboratory, Laurel, MD 20723. [2]Wheeling Jesuit College, Wheeling, WV 26003 [3]Lunar and Planetary Laboratory, University of Arizona, Tucson, AZ 85721, U.S.A. [4]Jet Propulsion Laboratory, California Institute of Technology, Pasadena, CA 91109, U.S.A.. [5]Proxemy Research, Bowie, MD 20715 rlorenz@lpl.arizona.edu. .

Summary: As Cassini SAR imaging coverage of Titan approaches ~20%, a general picture of Titan's cratering style is emerging: craters are often modified by fluvial and Aeolian processes, so far there is no evidence of viscous relaxation. However, ejecta blankets and rounded rims suggest unusual target properties and atmosphere-ejecta interaction.

Introduction – Crater Density: If Titan were cratered to the same extent as some other Saturnian satellites, it would have >10,000 impact craters [1] with diameter 20km or more (above the atmospheric shielding threshold below which the differential density would decline). However, a striking result even from the earliest Cassini data was the lack of observable craters overall [2,3]. A survey [4] of the first ~10% of Titan's surface imaged by the Synthetic Aperture Radar (SAR) mode of the Cassini RADAR instrument finds that in fact the large-crater (>300km) population may be consistent with other Saturnian satellites (figure 1), but there is a striking dearth of medium-sized impacts (e.g. 30-100km diameter). Indeed, the slope of the cumulative size-frequency distribution is very shallow, much like the Earth, suggesting that similar processes may be responsible for the obliteration of the craters. A crater retention age of several hundred million years (roughly the same as Earth or Venus) appears to be indicated [3,4].

So far only 3 impact structures are securely-enough identified to have IAU-approved names (see figure 2) – we discuss these in turn.

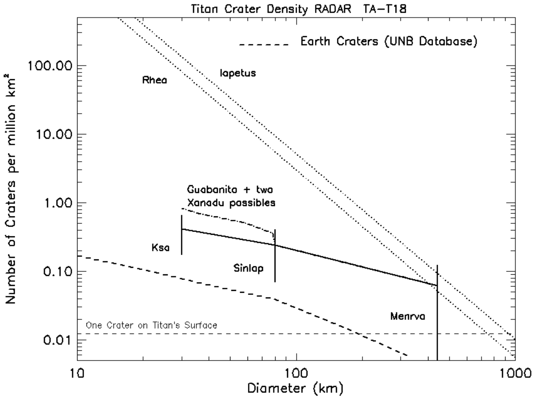

Fig.1 *Titan cumulative size-frequency plot (thick solid line with bars) for TA-T18, compared with Earth and Rhea/Iapetus. Some uncertainty (factor ~2) pertains to a number of structures which may or may not be of impact origin, but even taking these into accout, medium-sized craters are a factor of ~100-1000 depleted from what one would expect.*

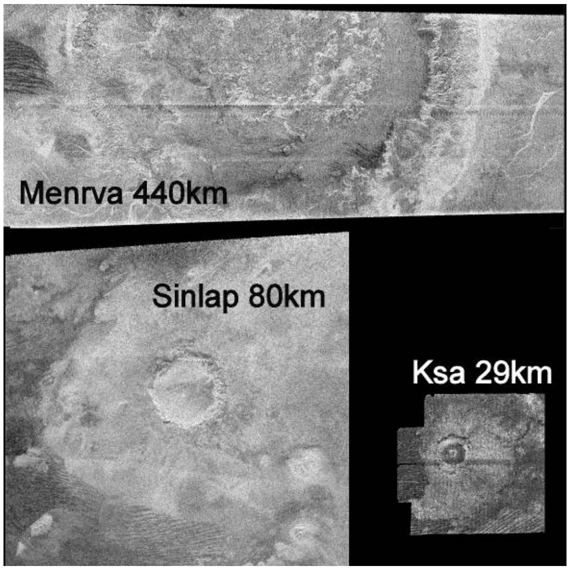

Fig.2 *Montage at same scale (128 pixels/degree) of the three confidently-identified and named impact structures, Menrva, Sinlap and Ksa. . North is up in each case – note the tendency of fluvial channels and Aeolian features to trend eastwards and the better-preserved Eastern rim of Menrva. Near-horizontal stripes across the whole images are radar imaging artifacts. Radar illumination is from above with approximate incidence angles of 21°, 14° and 34° respectively.Menrva – 440km across outer edge.*

Menrva: This impact basin is centered near 87° W, 19° N and had been noted as a dark annular feature in near-IR imaging. RADAR shows the crater morphology clearly. The outermost edge is 450km in diameter, although whether the structure is a true multiring basin is not yet clear. The steep inner wall is bright, exhibiting numerous radial grooves and chutes. The southern and western regions of the floor are relatively bland, suggesting it may have been flooded. The center of the basin appears elevated and is rough-textured, with bright material defining an inner ring about 100 km in diameter. Dark, thin linear streaks seem to seep from the basin's lower wall onto the basin floor. The western rim shows more signs of erosion than the eastern rim. Fluvial features appear to be associated with the basin, but small-scale features in the crater rim and in the central hills are preserved, suggesting that erosion has been rather limited since crater formation. The terrain surrounding the crater and ejecta also are indicative of local geologic processes, e.g., erosion, remobilization of ejecta, or aeolian redistribution. The Cassini RADAR team is presently exploring ways of measuring the topography of Menrva to constrain post-impact modification such as viscous relaxation.

Sinlap : The 80-km crater, at 16° W, 11° N shows no evidence of a raised rim. It appears to be flat-floored – craters on Ganymede of this diameter [5] have domed floors due to viscous relaxation, and central pits, perhaps indicating that their transient cavity came close to a subsurface layer of lower viscosity. There is no indication of such features, nor of a central peak or peak ring, yet the overall impression suggests it was formed by impact. The floor seems flat, similar to some lava-flooded craters on the moon and Mars or to craters with lacustrine deposits on Mars. Making the assumption that the crater wall has the same height and slope around its perimeter, we calculate [6] a slope of 16 +/- 5 deg and a crater depth of 1300 ± 200 m for a depth/diameter ratio of 0.016 ± 0.03. This shallowness may be due to the crater being significantly modified by infilling. The crater is asymmetrically surrounded by a blanket of SAR-bright material biased toward the eastern side : the inner part of this blanket has some radial striation. In places it extends more than two crater radii beyond the rim. While the parabolic shape of the ejecta blanket is similar in shape to the extensive dark, diffuse, parabolic haloes seen around venusian impact craters, we do not detect a similar deposit in this limited view of the crater.

Ksa : The T17 flyby in August 2006 showed a 29km diameter crater named Ksa not far from Menrva. Again, this structure shows the recurring pattern of 'intrusion' of aeolian material from the West. There is a central structure suggestive of a peak ring, and a well-defined but smooth rim. A large and sharp-edged ejecta blanket is reminiscent of the fluidized ejecta around many Martian craters, suggesting a significant influence of the atmosphere in constraining the ejecta plume expansion, and the possibility of surface volatiles.

Suspiciously-Circular Features and other potential impact structures : A number of circular or near-circular features form bright rings in both radar and optical data – many of these may have an impact origin (e.g. figure 3). The dark floors suggest infilling, perhaps by aeolian sediment – in the case of Guabonito, duneforms are evident.

The large leading-face bright region Xanadu appears geologically distinct and has a number of likely (but highly degraded) impact structures. Further study of these, and their implications for the age of Xanadu, are under way.

Radar imaging has revealed polar lakes and seas of liquid hydrocarbons[7], suggesting we may find submarine impact structures [8] (e.g. figure 4).

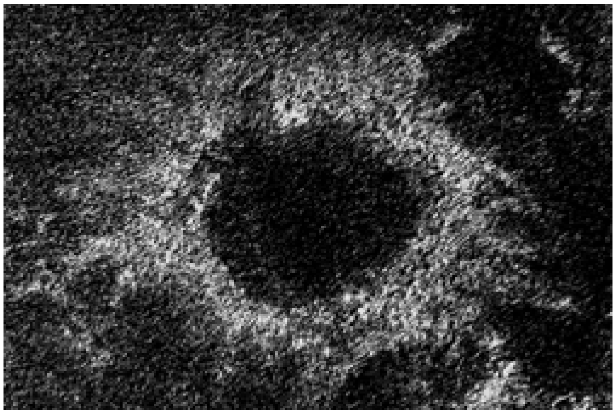

***Fig 3**. Unnamed feature, possibly an oblique impact structure observed on T16 – inner part is 65km across, a typical size for 'suspiciously circular features' on Titan.*

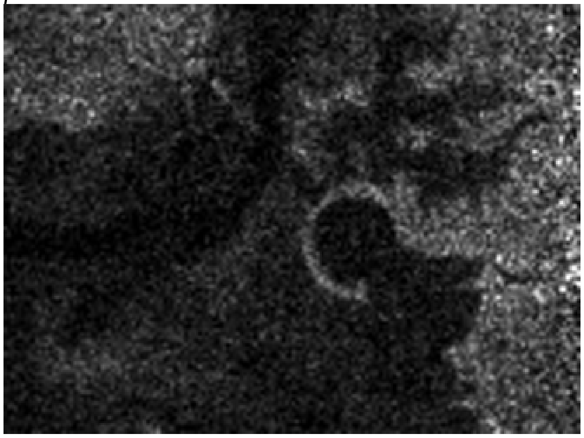

***Fig.4** Unnamed 9km diameter feature, possibly a submerged or previously-submerged crater rim observed on T29. Note nearby river channels.*

Conclusions : Titan's craters are quite distinctive, sometimes having a 'soft' appearance and in many ways are more comparable with craters on the terrestrial planets than on other icy satellites. To generate these morphologies presents a new challenge to modelers and may inform our understanding of Titan's crustal properties. The steep walls of Sinlap contrast with the rounded rims and ejecta patterns seen elsewhere, suggesting possible regional variation in surface properties.

References: [1] Lorenz, R., Planetary and Space Science 45, 1009-1019, 1997 [2] Elachi, C. et al,, Science, 308, 970-974, 2005. [3] Porco, C.C., et al, 2005. Nature 434, 159–168, 2005. [4].Lorenz R. D. et al., Geophys. Res. Lett., 34, L07204, doi:10.1029/2006GL028971, 2007. [5] Schenk, P. (1993), Journal of Geophysical Research 98, 7475-7498 (1993) [6] Elachi, C., et al. (2006), Nature, 441, 709– 713 [7] Stofan et al., (2007) Nature, 441, 61-64 [8] Lorenz, R. Titan - A New World Covered in Submarine pp.185-195, Craters in H. Dypvik, M Burchell and P Claeys (eds) Cratering in Marine Environments and on Ice, Springer, 2004

.

THE MECHANICS OF COMPLEX CRATER AND RINGED BASIN FORMATION: CONSTRAINTS FROM 30 YEARS OF PLANETARY OBSERVATIONS.

William B. McKinnon, Department of Earth and Planetary Sciences and McDonnell Center for the Space Sciences, Washington University, Saint Louis, MO 63130 (mckinnon@wustl.edu).

Introduction: Thirty years ago "bridging the gap" meant bringing the impact and explosion cratering communities together. That highly successful enterprise ushered in many fruitful lines of inquiry, from crater scaling and centrifuge studies [1], to observations of impactor populations [2], to the first model of the *mechanics of complex crater formation* [3]. Complex craters, of course, are seen in a variety of morphological forms across the solar system today, but in the mid-70s the touchstone was the Moon, and the key observations concerned lunar craters with central peaks and rim terraces and those without (complex vs. simple) [4]. Some concepts of the time, such as "elastic" rebound [5] and shallow excavation at large scales (due to target layering or non-proportional growth [e.g., 6]) did not gain acceptance. The concepts that the mechanical properties of the "target" governed the response to impact, and specifically that impacted rock was much weaker than even static rubble [3,7], were not immediately embraced either, but these concepts have proven remarkably durable [8,9]. In elaborated and extended form, the hypothesis of weakening by shock and high bulk strain-rate flow has been adapted to the formation of central peak craters, peak-ring craters (or basins) and multi-ringed basins on the terrestrial planets (including the Moon), and to central peak and pit craters, peak-ring basins, and multiringed basins on the icy satellites of the giant planets [8–11]. Studies of impact morphology in such radically different geological settings (different gravities, different lithologies, ice vs. rock) have proven enlightening.

We now view the "modification stage," as defined by Don Gault, as a continuing part (albeit terminal) of the *late stage* of crater excavation, in which the inertial motion of the crater flow field increasingly responds to some combination of gravity, internal friction, and material viscosity [8–10]. We do not understand precisely how rock (and ice) is weakened during impact, and the major models advanced, acoustic fluidization [12], block oscillation [13], and thermal degradation [14], may or may not embrace the same physics [9].

In the 1970s, observations of lunar crater and basin morphology were augmented by similar data from *Mariner 10* images of Mercury, *Viking Orbiter* images of Mars (late 70s), and a field studies of the few well-preserved terrestrial complex craters [e.g., 15]. Mercury data, though extensively "mined," was limited [16], and measurements and interpretation of martian images are compromised by the active geology of that body [17]. Since that decade major advances have come from 1) the *Voyager* observations of the icy satellites [10], 2) *Magellan* radar images of Venus (especially revealing in terms of peak ring and multiringed basin formation) [18,19], 3) *Galileo* images of impact features on Europa, Ganymede, and Callisto [11], and 4) a resurgence in discovery and geological characterization of complex terrestrial craters and basins (e.g., Chesapeake Bay [20] and Chicxulub [see 21]). Highly capable spacecraft are now operating in martian orbit and on the martian surface (although impact studies are not their focus), and *Cassini* continues its multiyear tour of the Saturn system. High quality images of the midsized icy satellites of Saturn are revealing central peak and peak ring craters there in unprecedented detail (although the dearth of pristine impacts on Titan is disappointing).

In this review I will highlight the advances that have come from 30 years of planetary exploration (including the Earth), and how these have influenced and constrained the development of theories of crater modification. I will also look forward to data to come, from the *Messenger* mission to Mercury, from (proposed) high quality lunar gravity and topography, and from terrestrial field studies of rock that has actually participated in impact flow, where "bridging the gap" between theory and observation may finally occur. The rest of this abstract focuses on fundamentals.

Simple-to-complex transition: Of all the morphological indices that characterize this transition, depth over diameter (d/D) is arguably the most quantifiable and the most significant. Measurements usually follow a power-law form:

$$d \;=\; aD^b \qquad . \qquad (1)$$

For morphologically fresh, simple lunar and mercurian craters, $a = 0.20$ and $b = 1.0$, reflecting their geometric similarity; for lunar complex craters ($d > 15$ km), $b = 0.30$ [4,16]. It was the recognition that complex lunar craters "collapse" (a combination of slumping and uplift) to some limiting depth that led Melosh to argue that a material strength (c) threshold had been exceeded [3]. Fundamental soil mechanics principles then lead to a dimensionless parameter $\rho \;\; d/c$, which must exceed ≈5–7 for uplift or terrace failure to occur in a parabolic crater in rock of density ρ and subject to local gravity g. As is now well known, the value of c implied by a limiting depth of 3 km on the Moon is

~2–3 MPa (extraordinarily low); internal friction must also be very low [8].

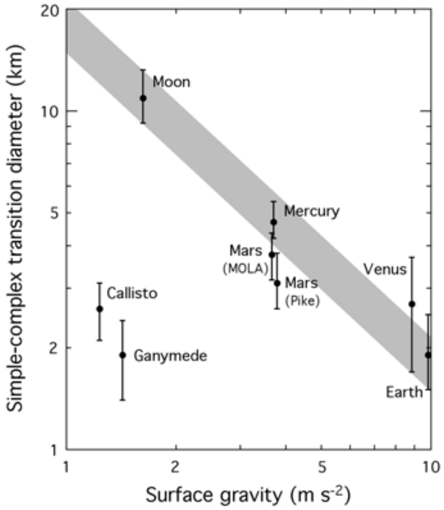

The figure above shows the intersection (including errors) of the *d/D* power-laws for "fresh" simple and complex craters on planets and satellites. Lunar, terrestrial, martian, and mercurian data are from [16]; abundant Mars laser altimeter (MOLA) data confirm the general trends measured by Pike [16,17], but also reveal the morphometry of the most pristine of fresh craters [22] and clear examples of simple craters with *d/D* = 0.2 in specific regions [23], to which the complex crater power-laws in [22] are extended. The terrestrial point should be viewed with caution, as all terrestrial crater rims are eroded to a degree, whereas Venus depths (from floor–rim-crest radar offsets) are only for the freshest, parabola-deposit-bearing craters [24]. There are no simple, bowl-shaped craters on Venus, due to its thick atmosphere [19], so the complex crater power-law is extended to *d/D* = 0.2, and an error of ± 1 km is assumed.

The inverse gravity trend for simple-to-complex transition diameters on the terrestrial planets (gray bar centered on the lunar point) is now much clearer than in the past: the strength measure (*c*) during modification is nearly constant for all five bodies, subject to terrain effects. Mars shows clear morphometric variations for different regions [17,22,23], and has (a) comparatively lower gravity-scaled transition diameter(s) (lower *c*), the simple-complex transition has long been known to occur at smaller diameters for craters formed in sedimentary, as opposed to crystalline, targets on Earth [25], and even the Moon shows a subtle mare/highlands influence on complex crater *d/D* [17].

The nature of Modification-stage strength: No laboratory measurements predict the strength and internal friction required for crater collapse [9]. Even the intuitive dependence of *c* with composition, weaker for sedimentary targets and especially weak for ice-dominated ones, has no obvious basis in rock mechanics (the Ganymede and Callisto points in the figure are based on *Galileo* imagery, and supercede all previous work [11], although details are not yet published).

Thermal weakening [14] would be material dependent, but the influence of temperature at the scales in question does not seem plausible [9]. Code calculations using acoustic fluidization or block oscillation (or simplified versions thereof) have had some success [9,26], but relating these models to geological ground truth remains a major challenge. Post-impact cohesion (*c*) does not depend *explicitly* on impactor properties such as velocity or size, for otherwise there would not be such well-defined *d/D* power laws for complex craters on the Moon and Mercury. Rather, on a given body it depends on crater diameter (or equivalently, the point-source measure of the impactor, the coupling parameter [27]); that is, $b > 0$ for complex craters, often markedly so. This dependence should be degenerate for bodies of similar geology if all lengths gravity-scale. High quality data from *Messenger* will be a test.

References: [1] Schmidt R. M (1977) in *Impact and Explosion Cratering (IEC)* (D.J. Roddy et al., eds), 1261–1278, Pergamon. [2] Shoemaker E. M. (1977) *IEC,* 617–628. [3] Melosh H. J. (1977) *IEC,* 1245–1260. [4] Pike R. J. (1977) *IEC,* 489–509. [5] Ullrich G. W. et al. (1977) *IEC,* 959–982. [6] Settle M. and Head J. W. (1979) *JGR, 84,* 3081–3096. [7] McKinnon W. B. (1978) *Proc. LPS Conf., 9th,* 3965–3973. [8] Melosh H. J. (1989) *Impact Cratering: A Geologic Process,* Oxford. [9] Melosh H. J. and Ivanov B. A. (1999) *AREPS, 27,* 385–415. [10] Chapman C. R. and McKinnon W. B. (1986) in *Satellites* (J.A. Burns and M.S. Matthews, eds.), 492–580, UAP. [11] Schenk P. M. et al. (2004) in *Jupiter: The Planet, Satellites and Magnetosphere* (F. Bagenal et al., eds.), 427–456, CUP. [12] Melosh H. J. (1979) *JGR, 84,* 7513–7520. [13] Ivanov B. A. and Kostuchenko V. N. (1997) *LPS XXVII,* Abstract #1655. [14] O'Keefe J. D. and Ahrens T. J. (1993) *JGR, 93,* 17011–17028. [15] Pohl J. et al. (1977) *IEC*, 343–404. [16] Pike R. J. (1988) in *Mercury* (F. Vilas et al., eds.), 165–273, UAP. [17] Pike R. J. (1980) *Proc. LPS Conf., 11th,* 2159–2189. [18] Alexopoulos J. S. and McKinnon W. B. (1994) in *Large Meteorite Impacts and Planetary Evolution* (B.O. Dressler et al., eds.), 178–198, GSA SP-293. [19] McKinnon W. B. et al. (1997) in *Venus II* (S.W. Bougher et al., eds.), 969–1014, UAP. [20] Poag W. C. (1999) *Chesapeake Invader: Discovering America's Giant Meteorite Crater*, Princeton. [21] Morgan J. V. et al. (1997) *Nature, 390,* 472–476. [22] Boyce J. M. and Garbeil H. (2007) *LPS XXXVIII,* Abstract #1931. [23] Stewart S. T. and Valiant G. J. (2006) *MAPS, 41,* 1509–1537. [24] Sharpton V. L.(1994) in *Large Meteorite Impacts and Planetary Evolution* (B.O. Dressler et al., eds.), 19–27, GSA SP-293. [25] Grieve R. A. F. and Robertson P. B. (1979) *Icarus, 38*, 212–229. [26] Wünnemann K. and Ivanov B. A. (2003) *Icarus, 51*, 831–845. [27] Holsapple K. A. and Schmidt R. M. (1987) *JGR, 92,* 6350–6376.

THE CONTACT AND COMPRESSION STAGE OF IMPACT CRATERING.

H. J. Melosh, Lunar and Planetary, University of Arizona, Tucson, AZ 85721 (jmelosh@lpl.arizona.edu).

Introduction: Impacts at typical planetary encounter velocities, more than a few km/s, are fundamentally different from the low-speed impacts of everyday experience. High-speed impact craters are shallow circular pits whose form is almost independent of the angle of impact, impactor shape or composition. This surprising convergence of form is a consequence of the large amount of energy released in a high-speed impact event, which causes the crater's final size to become much larger than that of the original projectile.

This fact was first appreciated in the early decades of the 20th century by investigators such as E. J. Öpik (1916), H. E. Ives (1919), F. R. Moulton (1922) and A. C. Gifford (1924-1930). Now known as the "impact/explosion analogy", this fundamental insight likens the excavation of an impact crater to an explosion driven by a point source of energy rather than to the familiar indentation of a target by a projectile striking at speeds achievable by human muscular force.

The most distinctive part of this process is the rapid conversion of the kinetic energy of the projectile into heat and motion in the target. This conversion takes place over a period of time roughly equal to the time over which the projectile, moving at velocity v_i with respect to the target, traverses its own diameter L, a period of about L/v_i. During this brief time the projectile slows down, a roughly equal mass of target accelerates, and both are raised to very high pressures and temperatures. The projectile penetrates into the target a distance given approximately by $L\sqrt{\rho_p / \rho_t}$, where the term under the radical is the ratio of projectile density to target density. Having penetrated this far, the high internal energy of the compressed projectile and target asserts itself and the result is a sort of "explosion" driven by the pent-up energy of compression.

Hugoniot Equations: Although the relation between pressure and volume of an ideal gas has been known for several centuries, Boyle's law is a poor approximation to the compression of metal and rocks. P. H. Hugoniot first achieved a correct description of the thermodynamics of shock compression in his 1887 PhD thesis. The three Hugoniot equations relate the thermodynamic properties of material before a sudden, strong compression event to those afterwards using the conservation of mass, energy and momentum. Entropy, however, is not conserved: Sudden (shock) compression events are highly irreversible. Much of the original kinetic energy is converted to heat energy, so that the temperature of shocked material rises sharply and irreversible phase changes may occur.

Equations of State: The Hugoniot relations do not predict a unique relation between pressure and volume valid for all materials. The full relation, in the form of an "equation of state", is a function linking pressure P, density ρ and temperature T (or, equivalently, shock velocity and particle velocity in the compressed material). The Hugoniot equation of state is different for different materials, as well as for different initial states with varying temperature, pressure or porosity. The good news is that the Hugoniot equations of state have been measured for a wide variety of materials in many different initial states and for many different impact velocities. Extensive compilations of available data can be found in the books by Trunin [1] and by Marsh [2]. In addition, there are a number of analytical and semi-analytical equations of state available for theoretical computations of impact processes, some of the best known examples being the Tillotson equation of state [3], the Mie-Gruneisen equation [4] and the computer codes ANEOS [5] and PANDA [6].

The complete thermodynamic path of materials compressed during an impact, followed by adiabatic decompression as the compressed materials rebound, can be computed using modern equations of state. An example for the well-studied material quartz is shown in Figure 1.

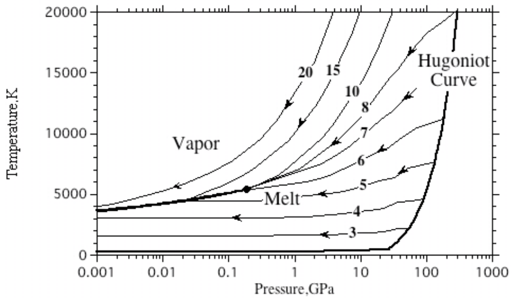

Figure 1: Thermodynamic path of initially dense quartz at room pressure and temperature that is first shock compressed, then released to low pressure during an impact. The numbers on each release curve refer to the maximum particle velocity reached during compression. The particle velocity is approximately half of the impact velocity. Derived from the ANEOS equation of state [7].

Oblique Impacts: The early stages of impact cratering are now relatively well understood for both vertical impacts [8] and oblique impacts [9]. The process of jetting, in which very highly shocked material is ejected from close to the impact site at very high speed, is greatly enhanced in oblique impacts [8]. Once the initial energy is coupled into the target, shock waves radiate outward, irreversibly compressing and accelerating the surrounding material [10]. The subsequent motion, which can be well approximated as an incompressible flow [11], eventually opens the crater. This latter phase, known as the excavation phase, lasts much longer than the initial contact and compression phase. It is characterized by generally subsonic, incompressible, flow [8]. Other speakers will discuss this phase.

Porous Materials: The most recent research into the early phases of shock compression is concerned with modeling the equation of state of complex materials accurately, and consideration of new facets of the material response. One of the most important of these facets is porosity. In general, shock compression of porous material converts much more kinetic energy into heat and thus produces a hotter, more vigorous expansion of the resulting projectile and target material. Figure 2 shows the large differences between the final entropy of Forsterite as a function of initial porosity and shock velocity. Even at low shock velocities, initial porosity in the range of 40% can easily double the final entropy of the shocked material and initiate melting and vaporization at impact velocities that are incapable of causing phase changes in fully dense material.

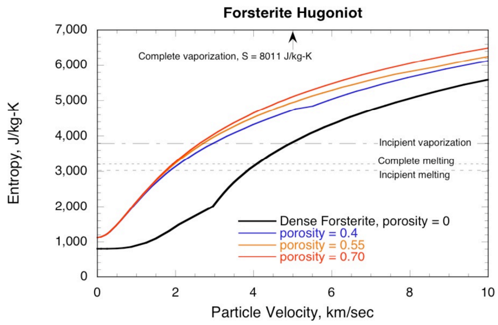

Figure 2. Entropy of magnesian olivine (Forsterite) as a function of initial porosity, derived from the ANEOS equation of state.

Recent advances in numerical methods of modeling porous materials [12] have made it possible to readily simulate impacts into porous targets. Figure 3 shows one such simulation that indicates that, compared to a fully dense target, impacts into porous media not only produce more heat than impacts into dense materials, but the shock wave also attenuates much faster. This type of impact is currently of great interest in the wake of the Deep Impact experiment in which an artificial impact was created on the highly porous comet Tempel 1 [13]. It may also be of importance for impacts onto small, rubble-pile asteroids, of which Itokawa may be our first well-imaged example [14].

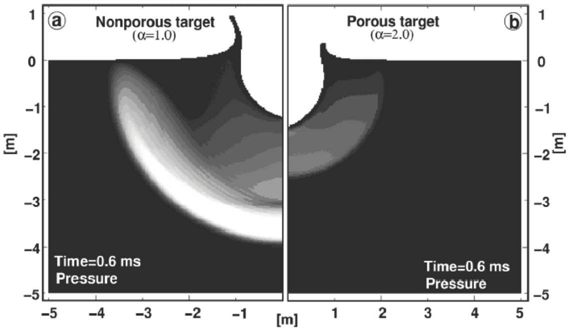

Figure 3: Pressure resulting from a small impact into a dense (left panel) versus a porous (right panel) target [12]. Note the rapid decline of the maximum pressure in the porous target.

References:

[1] Trunin, R.F., Gudarenko, L.F., Zhernokletov, M.V. & Simakov, G.V. *Experimental Data on Shock Compression and Adiabatic Expansion of Condensed Matter* 1-446 (Russian Federal Nuclear Center-VNIIEF, Sarov, 2001).

[2] Marsh, S.P. *LASL Shock Hugoniot Data* (U. of California Press, Berkeley, Los Angeles, London, 1980).

[3] Tillotson, J.H. *Metallic equations of state for hypervelocity impact* (Gen. At., San Diego, Calif., 1962).

[4] Zharkov, V.N. & Kalinin, V.A. *Equations of State for Solids at High Pressures and Temperatures* (Consultants Bureau, New York, 1971) 127pp.

[5] Thompson, S.L. & Lauson, H.S. *Improvements in the CHART D energy flow-hydrodynamic code II: A revised program* (Sandia National Laboratories, Albuquerque, N.M., 1972).

[6] Kerley, G.I. *User's manual for PANDA II: A computer code for calculating equations of state* (Sandia National Laboratory, Albuquerque, 1991).

[7] Melosh, H.J. (2007) *Meteoritics and Planetary Sciences* **in press**.

[8] Melosh, H.J. *Impact Cratering: A Geologic Process* 1-245 (Oxford University Press, New York, 1989).

[9] Pierazzo, E. & Melosh, H.J. (2000) *Annu. Rev. Earth Planet. Sci.* **28**, 141.

[10] Melosh, H.J. (1985) *Icarus* **62**, 339.

[11] Maxwell, D.E. in *Impact and Explosion Cratering* (eds. Roddy, D.J., Pepin, R.O. & Merrill, R.B.) 1003 (Pergamon, New York, 1977).

[12] Wünnemann, K., Collins, G.S. & Melosh, H.J. (2006) *Icarus* **180**, 514.

[13] A'Hearn, M.F., *et al.* (2005) *Science* **310**, 258.

[14] Fujiwara, A., *et al.* (2006) *Science* **312**, 1330.

THE QUESTION OF THE EVOLUTION OF THE EJECTA PLUME AND THE ORIGIN OF SUEVITE OF THE RIES CRATER, GERMANY.

C. Meyer[1], U. Reimold[1]; K. Wünnemann[1], M. Jébrak[2], [1]Museum of Natural History, Humboldt University of Berlin, Germany; email: cornelia.meyer@museum.hu-berlin.de, [2]Université du Québec à Montréal, Canada

Introduction: Hypervelocity impacts of asteroids or comets into solid rock targets lead to instantaneous vaporization, melting and comminution of target rocks in the central excavation cavity. The currently least understood aspect of impact cratering is the process of ejecta plume development and evolution (and related – formation of suevitic breccias). With the current knowledge, a substantial fraction of the central part of the growing impact crater will immediately become engulfed in an upward-rising hemispherical plume that contains a mixture of vaporized, molten, shock metamorphosed, fractured, and unshocked material and expands almost vertically [1]. After collapse of the plume mixed material falls back into the crater, on top of the ballistically emplaced continuous ejecta blanket (deposited within and outside of the crater) forming a hot polymict breccia deposit thought to be represented by the so-called suevite.

We are investigating the suevite of the 14.8 Ma, 24 km wide Ries crater in southern Germany [e.g. 2]. Samples for this work have been obtained from the drill cores “Nördlingen 1973”, 3.5 km laterally from the impact point, with a 300 m thick suevite package; “Wörnitzostheim”, 8 km from the impact point, with a 80 m thick suevite sequence; and “Otting”, outside the crater, 17 km from the impact point, with 9 m of suevite (Fig. 1). Representative core sections have been subjected to digital analysis by a new technique developed by the Université du Québec à Montréal, which will be published in a forthcoming paper.

Observations and results: In the upper 150 m of the suevite sequence in the “Nördlingen 1973” core we found 4 sequences (with increasing width) with increasing particle sizes for rock and mineral clasts with increasing depth (gradation). Below these layers the particle sizes decreases towards the bottom of the suevite sequence. In the “Wörnitzostheim” core, the particle sizes of the rock clasts increases with increasing depth. The “Otting” samples revealed a heterogeneous particle sizes throughout the whole suevite sequence except for the lower two meters where the sizes decreases with depth (Fig. 1).

Melt particles in suevite have so far only been investigated in “Wörnitzostheim” and “Otting” suevite samples. For “Wörnitzostheim” we found an increasing melt content with increasing depth, which is correlated with an increase of average particle size of the melt clasts – corresponding to the size record for the lithic clasts in “Wörnitzostheim” suevite. In the “Otting” suevite, a decrease of the melt content with increasing depth is also correlated with a decrease of average particle size of the melt clasts. The melt particles of both drill cores show an almost horizontal arrangement.

Discussion and further work: Our work attempts to address the questions whether particle size distributions in the suevites are caused by quasi-fluviatile deposition as expected for a lateral, basal transport comparable to a volcanic pyroclastic flow as proposed by [3], or whether it might indicate continuous deposition out of a collapsing ejecta plume (in texture similar to the result of compaction), or deposition through a combination of both processes.

Bearing in mind the results of the investigations of ejecta in the Chixculub crater [3] and based on our present knowledge, it can be suggested that in a first stage of ejecta plume development, the ejecta will be accelerated in a column as it interacts with the atmosphere. A lighter upper part of vaporised, condensed and fine-grained particles rises higher because of its lower density than the atmosphere. These particles fall back at the end of all deposition on top of earlier deposited ejecta and form the fine-grained layer in the uppermost part of the suevite inside the crater [4]. The lower part of coarser-grained rock and melt particles will fall to the ground first and spread outward as a glowing avalanche. First the avalanche has low viscosity and turbulent flow, and might even spill over the crater rim and deposit a heterogeneous suevite as seen in the “Otting” core. After a while the avalanche becomes more viscous due to cooling and fades to a fluent stream, which at first could still flow (e.g., over the inner crater ring at Ries) and forms the graded suevite in the “Wörnitzostheim” core between the inner ring and the crater edge. At an even later more viscous stage, suevite could flow back and forth, perhaps several times, inside the crater to form the graded upper suevite of the “Nördlingen 1973” core in the inner crater.

To resolve these questions and to prove our first model we want to measure now the orientation of melt particles in 3 dimensions to establish the full fabric. In addition, the currently available macroscopic results will be complemented with microscopic image analysis data, and the distribution of particles of different shock stages shall be quantified.

References: [1] Melosh H.J. (1989) *Impact cratering; a geologic process.* [2] (1977) *Geologica Bavarica 75* [3] Salge T. (2006) *PhD-Thesis* [4] Köberl C. et al. (2007) *Meteoritics, 42*, 709-729

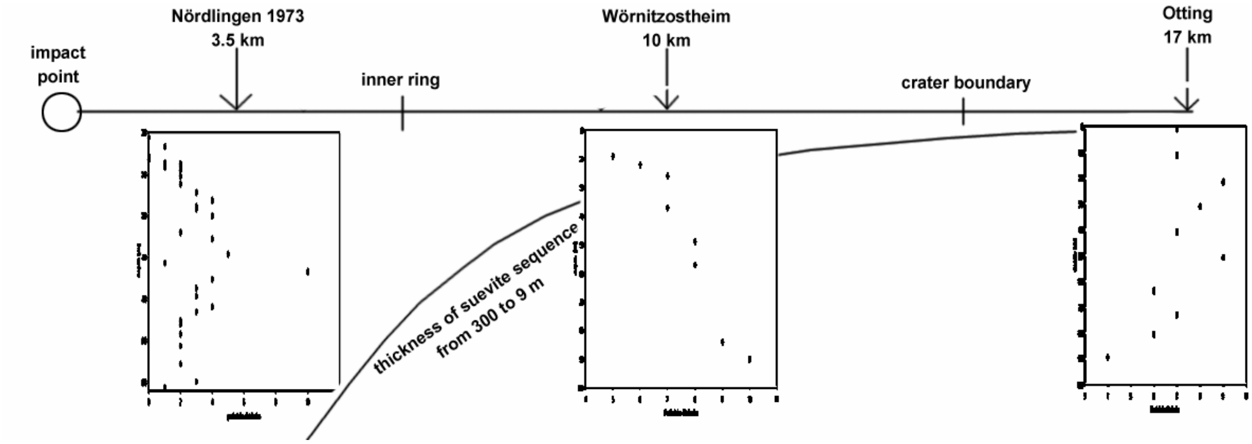

Fig. 1: location of the drill core related to the point of impact, inner ring and crater boundary
The lower line shows the variation of the thickness of the suevit sequence in the drill cores from 300 m at the "Nördlingen 1973" core to 9 m at the "Otting" core.
The diagrams show the particle size distribution of the rock clasts on the x-axis against the depth on the y-axis.

PETROGRAPHIC OBSERVATIONS OF CENTRAL UPLIFT FORMATION IN COMPLEX CRATERS.

K. A. Milam[1], [1]Department of Geological Sciences, Planetary Geology Laboratory, Ohio University, 316 Clippinger Laboratory, Athens, OH 45701, milamk@ohio.edu.

Introduction. Central uplifts in complex impact craters are thought to form during the modification stage of impact by uplift of target strata in the crater floor through a process known as acoustic fluidization [1]. Deformation during the contact/compression stage of impact results in target rock weakening [2], creating potential pathways for subsequent movement of large-blocks of material from depth in craters ~ 3-5 km in diameter [3] on Earth. Target rock from central uplifts shows signs of fracturing, faulting, shock deformation, and even localized melting (pseudotachylites), most of which appear to be related to impact. While central uplifts have been the subject of some study, only limited investigations have begun to uncover the complex petrogenesis that their rocks reveal [4-6]. This information can be useful for modeling target properties such as block size and rock response during central uplift formation in complex craters.

This study has examined the central uplifts from six complex terrestrial impact craters in North America: Flynn Creek, TN (36°17'N 85°40'W; 3.8 km diameter), Kentland, IN (40°45'N 87°4'W), Middlesboro, KY (36°37'N 83°44'W; 6 km), Serpent Mound, OH (39°2'N 83°24'W; 8 km), Sierra Madera, TX (30°36'N 102°55'W) and Wells Creek, TN (36°23'N 87°40'W; 12 km). Shock deformation features and features common to complex craters have been identified and interpreted as being related to crater and central uplift formation. These petrofabrics occur in a predictable petrogenetic sequence that reflect general models for crater formation and provide insight into the behavior of target rocks during and following impact.

Microfractures/Microfaults. All uplifts studiedshow field relationships indicating that large (cm to several hundred meter-sized) blocks of material are uplifted above their normal stratigraphic positions as the result of impact. Many blocks show minimal or no signs of strain, however, many are internally fractured or faulted. Such deformation is occasionally visible in the field or in hand specimen, but most microfractures/microfaults (< 1 mm thickness) are only discernable by microscope. Microfractures and microfaults cut across bedding and other sedimentary features and often occur in primarily parallel and sympathetic sets. It is possible that some microfractures could precede the impact event, but most are distinguished from subsequent (weathering-related) fractures by their lack of extension, termination at block boundaries, and lack of dissolution/precipitation petrofabrics. All microfaults terminate at block boundaries and are responsible for minor offsets (typically < mm's) of target rock strata in major blocks.

Microbreccias. Microfaults often contain silt and clay-sized cataclasis that we term microbreccia (also termed breccia dikes or clastic dikes by others). Petrographic and geochemical analyses (XRD,XRF) indicate that microbreccias are locally-derived. Those from the Middlesboro central uplift even contain shocked quartz fragments [7].

Major faults. Major faults have been observed and mapped in the central uplifts of all craters studied [8-11]. They bound the major blocks and show signifcantly more offset (hundreds of m's) of target strata than do microfaults. Centimeter- to meter-thick faults are typically oriented sub-perpendicular to bedding planes, although fault orientations at other impacts have been shown to be highly variable [12]. These faults are most likely responsible for the amount of stratigraphic uplift (SU) of floor material ($SU=0.086D^{1.03}$) at major impacts [13]. Major faults at Flynn Creek, Kentland, and Middlesboro are sharp and do bear a striking resemblance to microfaults. Some also occur oriented similar to microfaults, suggesting that some microfault surface can become major faults, resulting in larger displacement of target rock strata during central uplift rise and collapse.

Fault Breccias. Major faults at the Middlesboro and Wells Creek impacts contain significant amounts of brecciated material. We use the term fault breccia when referring to breccias generated along major central uplift faults to distinguish these from breccias formed from ejecta. These are similar to those generated by other terrestrial (non-impact) processes and elsewhere along crater floors [4]. Fault breccias are either monomict (Middlesboro, Wells Creek) or polymict (Wells Creek). At Wells Creek, fault breccias contain a wide size range (pebble- to silt-sized) of angular grains. At both locations, many breccias grade from coarse-grained centers to fine-grained outer margins, with some outer margins displaying flow textures. Petrographic, XRD, and XRF analyses of monomict Middlesboro breccias support a local derivation from wall rock material. Similar analyses of Wells Creek polymict fault breccias (referred to as heterogeneous breccias by [11]), indicate host rock mixed with other target lithologies. This is consistent with observed larger displacements along major fault boundaries.

Mechanism of Formation? All of the above features are not unique to impact sites, but can form by other geologic processes. However, at complex craters, these features are particularly concentrated in crater-floors and along central uplifts, while showing a close association with other unambiguous shock features (shocked mineral phases, high pressure phases, melting, and shatter cones). Shatter cones have been found in the central uplifts of all impacts studied here, while shocked quartz has only been detected at Middlesboro [7,14,15] and at Serpent Mound [16].

Cross-Cutting Relationships. While not all of the central uplifts studied have preserved a complete list of the above features, all present features show similar cross-cutting relationships. Sedimentary features (such as bedding, cementation, fossils, and, in the case of Flynn Creek, trace fossils) have been cross-cut and/or offset by microfractures, microfaults, and faults. We interpret the similar appearance and orientations of microfractures and microfaults to suggest that these features were generated contemporaneously and, prior to movement, were essentially the same feature. However, microfaults experienced later movement (when in contact, microfaults offset microfractures). Subsequent (weathering-related) fractures cut across all of these features. Shatter cones cut across sedimentary and diagenetic features at all of the studied craters. Occasionally shatter cones are found in direct contact with microfaults/faults. At Wells Creek some have been cut by faults and fault breccias [11] attesting to displacement of target strata after shatter cone formation. Shatter cone surfaces at Wells Creek have been offset by microfault planes, suggesting that microfault movement occurred following shatter cone formation. Planar fractures (PFs) and planar deformation features (PDFs) in quartz grains from Middlesboro have been cross-cut by faults and microfaults, suggesting that they too preceded fault movement [7].

Petrogenesis. Relationships between sedimentary, diagenetic, deformation, and shock metamorphic fabrics reveals an overall petrogenetic sequence for crater floor target rocks that rise to form central uplifts. This sequence is consistent with the general model of impact crater formation: contact/compression, excavation/ejection, and modification [1] and these observations are consistent with other models proposed for larger impact structures [17,18]. Steps 1-2 are processes involved in pre-impact formation of target rock. Step 3 results from passage of the compressional front of a shock wave, while step 4 represents subsequent decompression, both occurring during the contact/compression stage. Steps 5 and 6 are interpreted to represent rise of the central uplift. Step 5 likely occurs early during the modification stage, immediately followed by major fault movement (step 6). While the sum of offsets from minor faults cannot account for the total stratigraphic uplift in central peaks, major faults are likely responsible and represent the final stages of central uplift formation. Microfaults allow for minor displacements in strained target blocks. Following uplift, weathering processes serve to further modify central uplift morphology.

References: [1] Melosh, H. J., *J. Geophys. Res.*, 84, 7513-7520. [2] O'Keefe, J.D. & T.J. Ahrens (1993) *J. Geophys. Res.*, 98, 17011-17028. [3] Pike, R.J. (1988) In *Mercury*, 165-273, Univ. of AZ Press, Tuscon. [4] Lambert, P. (1981), *Proc. Lunar Planet. Sci.*, 12A, 59-78. [5] Martini, J.E.J. (1991) *Earth & Plan. Sci. Lett*, 103, 285-300. [6] Dressler, B.O. et al. (2001) *LPSC XXXII*, Abs. #1023. [7] Milam, K.A., et al. (2004), *LPSC XXXV*, Abs. #2073. [8] Roddy, D.J. (1968) In *Shock Met. of Nat. Mat.*, Mono Book Corp., 291-322. [9] Englund, K.J. & J.B. Roen (1962) *USGS Prof. Paper 405-E*, E20-E22. [10] Reidel, S.P. (1975) *Ohio Div.Geol. Sur. Rep.of Invest.*, 95, 1975. [11] Wilson, C.W. & R.G. Stearns (1968) *TN Div. of Geol.*, Bull. 68. [12] Kriens et al. (1999) *J. Geophys. Res.*, 104, 18867-18887. [13] Grieve, A.F. & M. Pilkington (1996) *J. Austr. Geol. & Geophysics*, 16, 399-420. [14] Bunch, T.E. (1968) In *Shock Met. Nat. Materials*, Mono Book, 413-432. [15] Carter, N.L. (1968) In *Shock Met. Nat. Mat.*, Mono Book, 453-474. [16] Carlton, R.W. (1998) *Earth & Planet. Sci. Lett.*, 162, 177-185. [17] Martini et al. (1991), *Earth & Planet. Sci. Lett.*, 103, 285-300. [18] Dressler, B. O. & V. L. Sharpton (1997), *Tectonophysics*, 285-311.

Table 1. Petrogenetic sequence for central uplifts

(1) deposition of target rock
(2) lithification/diagenesis
some microfractures generated (?)
(3) production of shatter cones/shocked minerals
(4) microfracture generation
(5) microfault movement/microbreccia generation
(6) fault movement/fault breccia generation
(7) fracturing from exposure/weathering

INFLUENCE OF A WATER LAYER ON THE IMPACT CRATERING PROCESS AND THE FATE OF THE PROJECTILE. D. J. Milner[1], E. C. Baldwin[2] and M. J. Burchell[1] [1]Centre of Astrophysics and Planetary Science, University of Kent, Canterbury, Kent, CT2 7NH djmilner26@hotmail.com, [2] UCL/Birkbeck Research School of Earth Sciences, University College London, Gower St, London WC1E 6BT.

Introduction: The standard model for impact cratering on the Earth currently reflects the case of sub-aerial impact events. This bias towards continental impact cratering is largely explained by the prevalence of sub-aerial craters found on the Earth's surface. Of the 170 documented Earth impact structures, only 33 structures and related deposits are recognized to have formed in a marine environment [1,2,3]. This can be explained by a number of factors such as the finite lifetime of the ocean floor (150-200 million years), a lack of detailed topography of the ocean floor, infilling of the crater with sedimentary layers and extensive crater rim erosion [2]. Currently the Earth's surface is approximately 70% covered by water, with almost 60% representing deep water environments [1]. Assuming this distribution has not greatly changed with time, the majority of impacts on the Earth can be expected to have occurred in marine environments. The standard model of impact cratering should be adjusted to reflect this.

It has previously been shown for marine impacts that at water depths far greater than the projectile diameter, no crater forms on the ocean floor [4,5,6]. The ratio of water depth W_d to projectile diameter P_d required to prevent crater formation is highly dependent upon the target material, with weaker unconsolidated material such as sand requiring a greater water depth to prevent cratering from occurring than a stronger and porous sandstone material [7]. This limit on cratering occurs because the projectile is significantly decelerated during its passage through the water layer, hence the impact energy on collision with the target basement is no longer sufficient to overcome the strength of the target material and produce an excavation flow field. Due to the reduction in impact velocity of the projectile with the basement rock, the shock pressures experienced by the projectile will be decreased and may also influence the chances of projectile survival. We thus investigate the effect the presence of a water layer has on the cratering process and projectile survivability.

Laboratory/numerical simulations: We use the University of Kent's two stage light gas gun [8] in conjunction with AUTODYN-2D computer models (based at University College London) to study the fate of the projectile. Experimental work used 1 mm dia. stainless steel 420 projectiles impacting into varying depth water layers overlying a crystalline basement rock. The projectile diameter and composition, water depth, impact velocity and impact angle were all varied [4]. The surviving projectile fraction was measured.

Simulations of the laboratory scale impacts were performed using AUTODYN-2D. The code has already been used at this scale for impacts on sandstone material underlying a water layer [9]. The Smooth Particle Hydrodynamics (SPH) solver was used for the simulations, with a resolution of 20 SPH particles per projectile diameter. AUTODYN-standard material models were used for stainless steel and water, while the Tillotson equation of state was used for granite, using inputs from [10]. Mechanical properties were derived from [11].

Results: The laboratory experiments demonstrated that a significant amount of the projectile can survive an impact event, the percentage of which is highly dependent upon the water depth, impact angle, impact velocity and projectile density, see Figure 1. As much as ~60% of the projectile can survive. The significant amount of material surviving the impact (compared to impact directly onto rock) illustrates the influence of the water layer. The projectile undergoes a lesser shock on entry into the water, decelerates whilst passing through shallow water depths and then experiences a consequently reduced shock when impacting the basement layer. To consider this further, a study of the velocity change in the water layer is made using the late-stage energy (LE) technique [12,13]. For a 1 mm diameter stainless steel 420 projectile impacting into a 5 mm deep water layer the projectile velocity is reduced from 5.49 km s^{-1} at entry to 1.72 km s^{-1} at the basement layer, and hence a peak shock pressure of approximately 40 GPa would be produced in the projectile during the impact event (reduced from 198 GPa if no water was present). At pressures of less than ~70 GPa the projectile should remain largely unmelted during the impact event [14]. Indeed, in our laboratory impact into a 5 mm deep water layer, 28% of the projectile was found to have survived.

AUTODYN-2D has been utilized to model the laboratory impacts. The impact of a 1 mm diameter stainless steel 420 projectile into a 5 mm deep water layer at 5 km s^{-1} was modelled first; the projectile slowed to 1.2 km s^{-1} by the time it reached the basement, in good agreement with the laboratory data and the LE technique. A peak shock pressure of 17 GPa was produced in the projectile when impacting the target rock (reduced from 222 GPa if no water was present); with a peak shock pressure of 88 GPa when traversing the water layer. The average peak shock pressure experienced across the projectile throughout the entire impact process was 15 GPa. The results of further modeling will be reported at the conference, including more laboratory impacts and larger scale impacts, to suggest the effect of a water layer on the fate of the projectile at a planetary scale.

Planetary scale impacts: It is widely accepted that the majority of the projectile is vaporized during an impact event. The results here, however, imply that in a marine impact there is a significant reduction in shock pressure with corresponding increase in survival of the projectile material. Consider an impact into deep water. The Eltanin impact site is believed to represent the impact of a 1 km diameter asteroid into a 4.7-5 km deep ocean. From examination of deep sea sediment cores taken around the impact site a first order estimate of the overall surviving mass at this site was predicted as 2x10^{12} kg [15,16,17]. This was a controversial prediction, due to the relatively few samples they obtained over such a large area. Based on scaling of results from the laboratory data we predict survival of 1.3x10^{12} kg of meteoritic material [4]. Note that this only indicates the total surviving mass and not the size/distribution of the material.

Conclusions: We have shown that with the presence of a water layer the fate of the projectile is not as simple as in the case of the sub-aerial impact events. A significant amount of material survives a laboratory scale impact event. The effect of impact angle, velocity, varied water depth and projectile density are important, as is the strength of the target material e.g. more material survives a vertical impact into less dense and weaker materials than denser crystalline rock. Utilizing AUTODYN-2D, we have seen that the passage of the projectile through the water layer can be modelled computationally and closely matches the analytical LE calculations.

References: [1] Gersonde, R. el al. (2002) *Deep sea research part 2: Topical studies in oceanography*. 49, 951-957. [2] Dypvik, H. and Jansa. L. F. (2003) *Sedimentary Geology. 161*, 309-337. [3] Allen, P. J. and Stewart, S. A. (2003) *LPS XXXIV*. Abstract #1351. [4] Milner D. J. (2007) *Thesis, University of Kent* 236p. [5] Gault D. E. & Sonett C. P. (1982) *Geol. Soc. America Spec. Papers, 190,* 69-92. [6] Shuvalov, V. V. and Trubestkaya, I. A. (2002) *Solar System Research. 36,* 417-430. [7] Baldwin, E. C. et al. (2007) Accepted for publication in *MAPS* Feb (2007). [8] Burchell M. J. et al. (1999) *Measurement Science and Technology*, *10,* 41-50. [9] Baldwin, E. C. et al. (2007) *Bridging the Gap 2*, submitted abstract. [10] Melosh, H. J. *Impact cratering – A geological process. OUP*. 1989, 245p. [11] Llama R. D & Vutukuri V. S (1978) *Handbook on Mechanical Properties of Rocks VII* 481p. [12] Burchell, M. J. el al. (2001) *Advances in Space Research*. *28*, 1527-1532. [13] Mizutani, H. et al. (1990) *Icarus, 87*, 307-326. [14] Pierazzo, E. Melosh, H. J. (2000c) *Icarus*. *145,* 252-261. [15] Kyte, F. T. and Gersonde, R. (2003) *66th Annual Meteoritical Society Meeting.* Abstract #5225. [16] Kyte, F. T. (2002a) *Deep Sea Research Part I,. 49*, 1029-1047. [17] Kyte, F. T. (2002b) *Deep Sea Research Part II: Topical Studies in Oceanography*, *49*, 1063-1071.

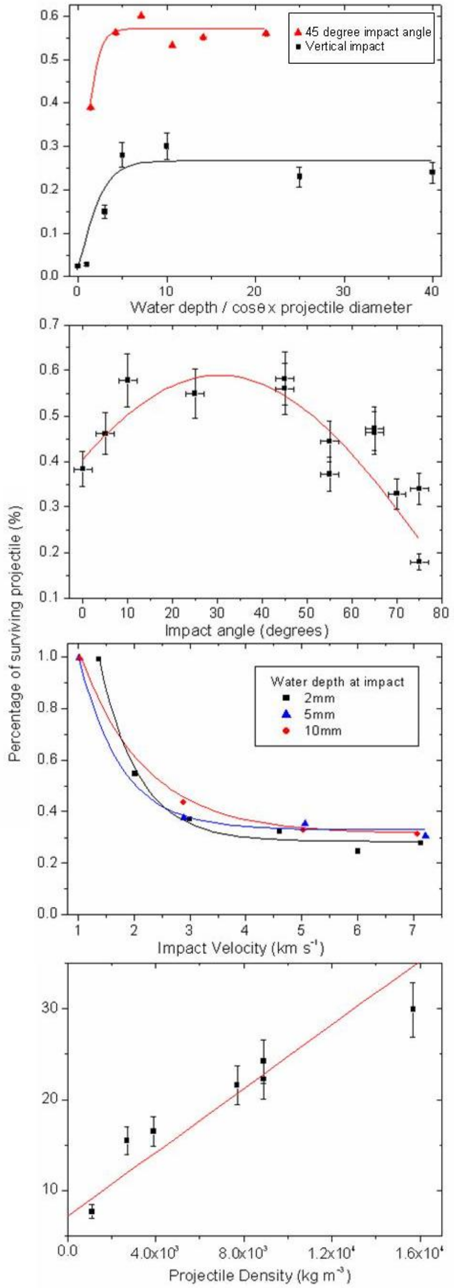

Fig. 1. Change in surviving projectile mass as water depth, impact angle, impact velocity and projectile density are varied.

ANALYSIS OF SMALL-SCALE PSEUDOTACHYLITIC BRECCIA ZONES FROM THE CENTRAL UPLIFT OF THE VREDEFORT IMPACT STRUCTURE, SOUTH AFRICA.

T. Mohr[1,] W. U. Reimold[1], U. Riller[1], R. L. Gibson[2], [1]Humboldt University in Berlin, Invalidenstrasse 43, 10115 Berlin, Germany (Tanja.Mohr@museum.HU-Berlin.de), [2]School of Geosciences, University of the Witwatersrand, Private Bag 3, P.O.Wits 2050, Johannesburg, South Africa (Roger.Gibson@wits.ac.za).

Objectives: Pseudotachylitic breccias represent the most prominent impact-induced deformation structures in the central uplift of the Vredefort Impact Structure [1, 2]. The development of such melt breccias in impact structures has been controversial, with both shock brecciation/melting, decompression melting, and/or friction melting mechanisms having been proposed by various authors (e.g., [3, 4]). Resolving this problem requires detailed field and microscopic structural analysis in order to characterize the nature of different occurrences and identify the exact timing of breccia formation within the rapid and complex impact event. Although field studies have previously been conducted, they have not been adequately related to microscopic studies. In order to bridge this gap, a polished 3 x 1.5 m granite slab [Fig. 1] from a dimension stone quarry in the core of the Vredefort Dome was structurally analysed. This slab provides an ideal opportunity for elucidating the relation between generation of fractures with and without melt, fracture and breccia density, and other geological parameters such as lithology, grain size and mineral fabrics [Fig. 2].

Methods: The geometry and pattern of thin pseudotachylitic breccia veins and microfractures in several portions of the granite slab were examined. In order to analyse the structure of veins on the mesoscopic scale, individual 10 x 10 cm large photos of the polished granite slab were assembled to a mosaic. All veins and fractures were traced on a transparent film and subsequently digitized. Characterization and mapping of microfracture and pseudotachylitic breccia networks with special regard of their orientation, density, and 3D geometry forms the basis for the ongoing structural analysis.

Results: Besides a several dm-wide breccia zone, two types of structures, which cut each other, are macroscopically observed, i.e., generally dark grey to black veinlets of pseudotachylitic breccias and a network of thin reddish-brown microfractures. A penetrative mineral foliation of the granitic host rock seemingly controlled the orientation of segments of the margins (contacts to host rock) of the pseudotachylitic breccias, but not that of the thin red microfractures. Mapping of the microfracture density indicates a decrease in density at a specific angle of 25° from the edge of, and away from the breccia zone. A high fracture density can, in general, be observed between thin pseudotachylitic breccia veins. Close to the breccia zone, red microfractures show a high density with variable orientations. At some distance from the breccia zone, a uniform orientation of microfractures is observed perpendicular to the breccia zone. With decreasing distance from the breccia zone, red microfractures display random orientation. The variation of fracture density seems to depend on the mineralogy of the host rock, which is mainly reflected in the variation of plagioclase and K-feldspar modal abundances of the host granite.

The cross-cutting relationships between the black and red fractures indicate two generations of pseudotachylitic breccias. Thin red microfractures cut and displace pseudotachylitic breccias, but appear not to cut the matrix of the wide breccia zone. The structural observations of the displacements of thin pseudotachylitic breccia veins indicate lateral spreading rather than a compressive regime upon melt breccia emplacement. Reassembling the rock fragments inside the wide breccia zone allowed to reconfigure their respective movement upon opening of the melt zone.

Conclusions: The existence of the breccia zone, as well as the reconstruction of pre-impact fragment configuration of the breccia zone, suggest that dilation played a major role during breccia emplacement. The orientation of dilational, melt-filled fractures will be used to assess the strain field and, thus, the deformation regime, under which the fractures formed. This information is important to infer the cratering stage during which the fracture formed. In this slab, the pre-impact fragmented configuration results in a uniform orientation of red fractures, wich can be observed in the re-established original state of that breccia zone. This indicates that these fractures formed prior to dm-scale pseudotachylitic breccia veins. Pseudotachylitic breccias display lateral strike separations on red microfractures that display en-echelon geometry.

The meso-scale work is followed by detailed microscopic and chemical analyses. Taking all these different analysis aspects into consideration, it may ultimately be possible to delineate different stages of the central uplift formation with the objective of better understanding the mechanics of complex crater formation.

Significance of the study for numerical modelling: Investigating the processes involved in the formation and collapse of central uplift structures, for example leading to intense fracturing, cataclasis, and melting, will provide crucial information with regard to the processes and kinematics involved in the formation of central uplifts of large impact structures. This will allow testing of the acoustic fluidization process. Understanding the genesis of pseudotachylitic breccias is implicit in improving our knowledge about the mechanics of central uplift formation. This study has significant implications for understanding also peudotachylitic breccia formation in meteorites and some lunar rocks (so-called "shock veins"), and the modelling of thermal energy associated with their formation on parent bodies.

References: [1] Dressler, B. O. and Reimold W. U. (2004) Earth-Science Reviews, 67, 1-60. [2] Reimold W. U. and Gibson R. L. (2006) GSA SP 405, 407 pp. [3] Gibson R. L. and Reimold W. U. (2001) The Vredefort impact structure, South Africa, Memoir 92, Council for Geoscience, Pretoria, 110 pp. [4] Gibson R. L. and Reimold W. U. (2005) Shock pressure distribution in the Vredefort impact structure, South Africa. Large Meteorite Impacts III. GSA SP 384, pp. 329-349.

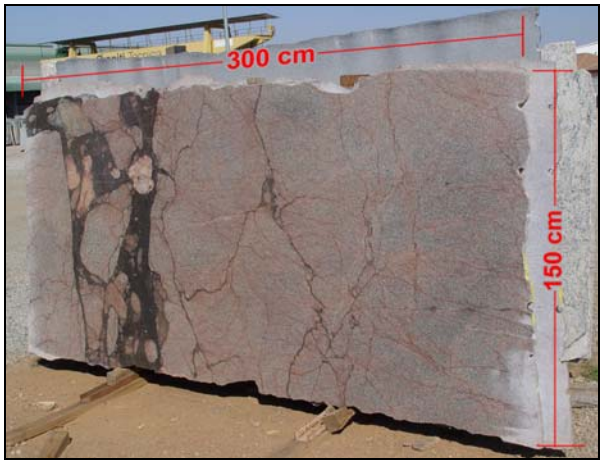

Fig. 1: Polished 3 x 1.5 m granite slab from a dimension stone quarry in the Vredefort Dome.

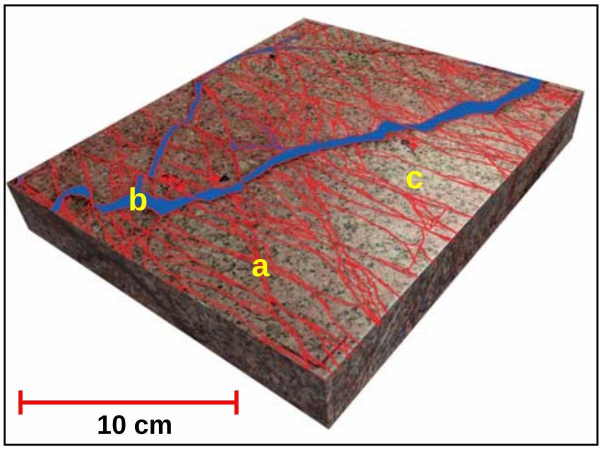

Fig. 2 : Enlarged section of a part of the granite slab. a : network of thin reddish-brown microfractures, b: pseudotachylitic breccia veins, c: granitic host rock.

ASYMMETRY OF THE CHICXULUB CRATER – IS IT PRODUCED BY ASYMMETRY IN THE TARGET?

J. Morgan[1], P. Barton[2], G. Christeson[3], S. Gulick[3], G. Collins[1], [1]Dept. Earth Science and Engineering, Imperial College London, UK, SW7 2AZ, j.morgan@imperial.ac.uk, [2]Dept. Earth Sciences, University of Cambridge, UK, CB3 0EZ, [3]Institute for Geophysics, Austin TX 78758-4445.

Introduction: In 1996 and 2005 we acquired extensive seismic reflection/refraction datasets across the Chicxulub impact crater (Fig. 1). These data reveal that both the crater structure and original target properties vary around the offshore portion of the crater. At this stage, it is not possible to decide whether the azimuthal variation in crater structure is related to: 1) target asymmetry, 2) impact angle or 3) a natural instability in crater formation. However, the correlation between structural asymmetries in the final crater and pre-existing geologic features of the target suggests influence by the target may be significant. Our aim, ultimately, is to test these different hypotheses using 3D dynamic modeling codes that are currently under development.

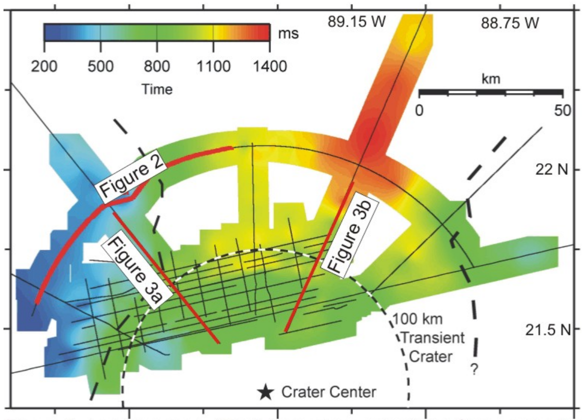

Figure 1. Location map. Black lines show seismic profiles across the offshore half of the Chicxulub crater. Color indicates two-way travel time to K-P boundary. The K-P boundary is relatively deep in the north and northeast, and shallow in the northwest, west, and onshore. The location of figures 2 and 3 are indicated in red.

Target asymmetry: We have imaged the near-surface Cretaceous sediments around the offshore portion of the crater. These data show that the Cretaceous sequence to the north and northeast of the crater is currently 1-1.5 km deeper than the same sequence to the northwest and west (Fig. 2) and also deeper than the Cretaceous sediments onshore, as determined from drill holes. The combined drilling and seismic data suggest that the impact was into shallow water, but that there was a relatively deep, water-filled basin in the north and northeast quadrant [1].

There is also evidence for the Cretaceous section thickening from onshore to offshore and from the east to the west [1, 2], whereas the crustal thickness appears to decrease from west to east [3].

Crater asymmetry: The most striking difference in crater structure imaged by seismic reflection profiles is the cumulative difference in offset on the Cretaceous target sediments across the terrace (megablock) zone. In the northeast the total offset is ~2 km, and in the northwest it is ~6km (Fig. 3) [4]. A second striking difference is the change in character of the crater's peak ring around the crater. It appears that the peak ring is generally broader and flatter in the north and northeast, and narrower and more topographically prominent in the northwest (Fig. 3) [5]. In addition, the innermost Cretaceous sediments are slightly deeper, and lie directly underneath the peak ring in the west and northwest, whereas they are slightly shallower and lie beneath the outer edge of the peak ring in the north and northeast. (Fig. 3).

Onshore, drill holes indicate that the K-P boundary deepens from ~500 m outside the cenote ring to ~1.2 km in the crater center. Reflection profiles to the northwest and east-northeast confirm this deepening of the impact basin. However, to the north and northeast, from the center of the crater outwards, the Tertiary basin gradually increases in depth. There appears to be no crater rim, as such, in this quadrant.

In the central crater, reflections from the Moho indicate that the base of the crust is uplifted by ~2 km [3, 6], and refraction data reveal a high-velocity-zone that is interpreted as central uplift [7]. However the Moho uplift and central uplift are offset from eachother, with the central uplift being southwest of the crater center and the Moho uplift being to the east.

Summary: There is a clear variation in structural features around the crater and variation in the pre-impact target: in the west-northwest the deeper and steeper terrace zone is associated with shallow Cretaceous bathymetry, while in the north and northeast the shallower terrace zone is associated with a deep, water-filled basin at the time of impact. However, it is difficult to know whether asymmetries in pre-impact target and final crater form are linked. Preliminary 2D hydrocode modeling does suggest that a thick versus shallow water and sediment layer could affect crater formation, and the final position of the terrace zone in particular. 3D hydrocodes are now under development [8] and with these codes we will be able to address, for the first time, the effect of asymmetry in the target on final crater form. Future 3D modeling of the formation of the Chicxulub crater will help us distinguish between the effects of both target asymmetry and impact angle on final crater form.

References: [1] Gulick et al. (submitted) Nature Geoscience. [2] Bell et al. (2004) *Meteoritics & Planet. Sci., 92,* 1089-1098. [3] Christeson et al., (2001) *JGR, 106*, 21,751-21,769. [4] McDonald (2007) Master's thesis, UTIG. [5] Mendoza (2007) Master's thesis, UNAM. [6] Christeson et al., (in prep). [7] Morgan et al. (2002) *Tectonophysics, 355*, 217-228. [8] Elbeshausen et al., 2007. LPSC XXXVI, Abstr. #1952

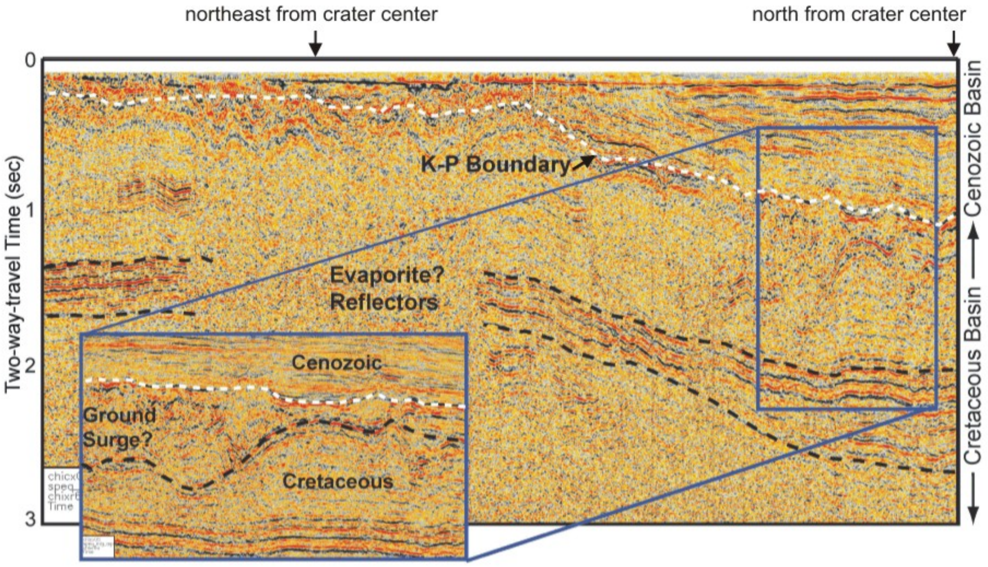

Figure 2. Offshore seismic reflection profile. The Cenozoic basin is unusually deep in the north and northeast quadrant of the crater, and the thickness of the Cretaceous sediments increase in this direction. See Figure 1 for location.

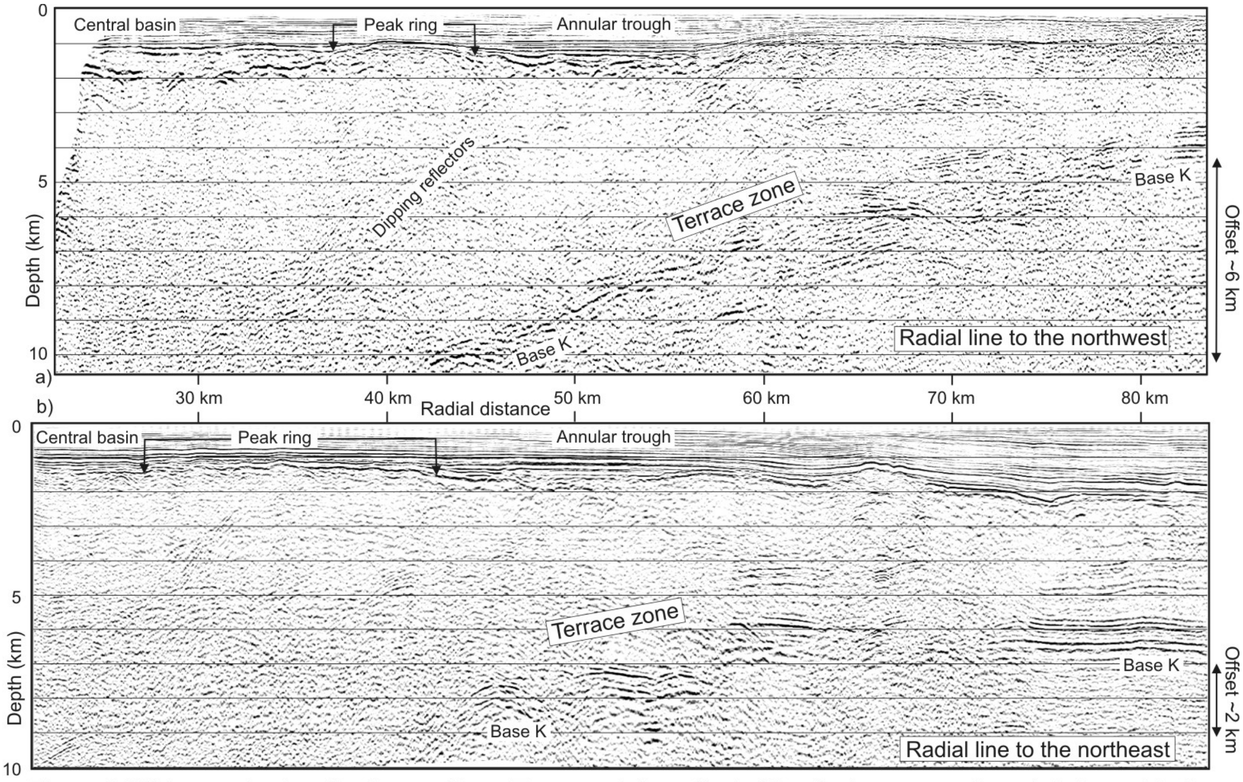

Figure 3 Offshore seismic reflection profiles. The cumulative offset of the Cretaceous sediments is largest in the northwestern quadrant of the crater, and smallest in the northeast. See Fig. 1 for location

CONSTRAINING STRENGTH PROPERTIES IN MARTIAN SURFACE LAYERS BY MODELLING THE PERIPHERAL PEAK RING IMPACT CRATER MORPHOLOGY.

Jason Nycz and Alan Hildebrand, Department of Geology and Geophysics, University of Calgary, 2500 University Drive NW, Calgary, Alberta, Canada. T2N 1N4. jcnycz@ucalgary.ca, ahildebr@ucalgary.ca.

Introduction: Examination of Viking, MOC, MOLA, HRSC, THEMIS, and most recently HiRISE data reveal the presence of impact craters (both simple and complex) that contain a partial or completely collapsed rim. These collapse features have been named Peripheral Peak Rings [1]. PPR occur where an apparent strong near surface layer exists. Albedo and spectral reflectance data establish this near surface layer as basalt, and it is seen in both the rims and the PPR of some impact craters. PPR's are interpreted to form when the crater rim wall, after conventional slumping to form the terraced zone overlying the slumped blocks (in the case of a complex crater), fails thereby detaching large blocks that slide downwards across the terraced zone towards the crater floor. Most recent high-resolution data can better constrain these observations allowing for slope stability modelling which can in turn be used to better understand the strength properties of the upper Martian crust.

Peripheral Peak Ring Formation: PPR are clearly blocks from the crater rim that separated and slid downwards across the terraced zone until stopping near the crater floor (fig 1). PPR can be differentiated from the outermost terrace zone based on morphology. Whereas the slump blocks that form the terraces show downward displacement consistent with normal faulting, PPR undergo displacement that is much more lateral, across the tops of the terraces (in the case of complex craters). This causes the tops of some PPR to be higher in elevation than the resulting crater rim, a phenomenon not seen in terraces. This will result in the somewhat paradoxical situation that subsurface sounding interior and adjacent to the rim would reveal uplifted strata of the structural rim uplift rather than the first down slumped block. Examples of well developed PPR have been observed in simple craters as well (fig 2), and most PPR have shapes that fit back into the depletion zone which once held them.

Why do PPR's form only in some craters, and are relatively common on Mars compared to other planetary surfaces? Geograpically, PPR formation is largely restricted to areas where basalt is present at the surface (e.g., Sinai Planum). This implies that the country rock must have a minimum competency for PPR's to form; an underlying weak layer, such as impact ejecta/regolith or sediments, is needed to facilitate failure of the rim. The final morphology of the PPR (single block, multiple blocks, or a more rubbly appearance) presumably depends on the local rim rock strength.

The restricted geographic distribution of complex craters containing PPR's and their ubiquity in some regions (e.g., the relatively young volcanic terrains) further suggests that local crustal character, such as layering, varies across the Martian surface and influences final crater morphology.

PPR Observations: Evidence of near surface layering is observed in most occurrences of craters having both PPR and available high resolution images of the crater rim (Figs 1, 2). In some of the younger and better preserved craters, similar layering is also seen in their respective PPR. Examination of these layers using THEMIS daytime thermal infra red spectral data shows they have similar spectra to those of Martian basalt [3]. Aside from these layers, the rest of the crater rim and surrounding terrain has spectra consistent with those of Mars' bright regions [4]. Additional work is needed to determine to what extent the spectra of these areas are influenced by dust. However, since many of these craters exist in regions with a low dust composite index [3] and mid range average thermal inertia [4], it is reasonable to conclude that at least some of these craters are in areas with low dust cover, and that the spectral differences seen between the basalt layers and underlying strata are not influenced by thick dust cover.

Strength layering in the near surface: The observed layering in the rims of craters containing PPR's will produce a strength contrast of strong (basalt) over weak (regolith/sediment). Slip line analysis has determined that for a given disruption cavity diameter, the crater state is defined by the cohesion, or yield stress of the rock [5]. The cohesion is a value given for a homogeneous hemispheric half space. Considering the layering required for the formation of the PPR, instead of a single cohesion value for the entire halfspace, a postulated strong (and dense) layer (basalt) overlies weaker strata. At the crater rim, the principal stress is the downward pressure determined by gravity, rock thickness, and density. Once enough basalt is present to allow the critical overburden stress to be reached, wall failure will presumably occur once tension fractures initiated interior to the crater rim generate a slip plane. Lack of confining pressure on the crater wall allows the PPR to detach from the crater rim and slide outward and downward.

Numerical Modelling: Sufficient constraints exist so that the required strength distribution may be modelled. Topographic profiles of Martian PPR craters were obtained from MOLA data and thicknesses of near-surface basalt layers were obtained using HiRise images. Lithology was confirmed with THEMIS spectral data. These geometries were entered into 2-D models with the material properties obtained by using the Hoek-Brown failure criterion [6] and from [7,8]. The models consisted of three layers (ejecta/regolith, basalt, sediment layers/unknown lithologies), and the safety factor for the slopes was determined using both the Morgenstern-Price and Simplified Bishop limit equilibrium methods. Although using published strength properties in the simplified model did not produce a critical slip plane (Safety Factor of 1), models with the basalt in the near subsurface had a significantly lower SF (2-4), than models with the basalt removed (SF 7-35). Models were then run varying such factors as cohesion, friction angle and disturbance factor to obtain the critical failure plane that most closely matched the topography of the observed post failure slopes of crater rims containing PPR. Results show that while it is possible to model observed PPR formation, it was not possible to model failure in any crater rims which did not have a basalt layer relatively close to the surface without using unreasonably weak strength values for the bedrock. This matches very well with the observed distribution of PPR craters on Mars. The modelling constrains the strength properties of the basalt and underlying weaker layer existing in the upper crust.

Implications: Presence of the PPR can be used as an indicator of strength contrast in the near surface of Mars. In addition, crater morphology can be integrated with other remote sensing methods to provide a probe of the Martian crust.

References: [1] Nycz and Hildebrand (2005), LPSC XXXVI Abstract #2167. [2] Melosh, H.J. (1989) Impact Cratering, Oxford Press. [3] Bandfield et al (2000), *Science* 287. [4] Ruff & Christensen (2002), *J. Geophys. Res* 107, E12. [5] Melosh, H.J.(1977) Impact and Explosion Cratering, Pergamon Press. [6] Hoek et al. (2002). *NARMS-TAC Conf* 267-273.[7] Neuffer & Schultz (2006),*J. Qtr Eng Geol & HGeol.* 39. [8] Nahm et al. (2007),LPSC XXVIII Abstract #1976.

Figure 1. HiRise image of northen rim of SAI Crater #5496. 27km diameter, lat 23N, long 208E, Amazonis Planetia. Image resolution is 35cm/pixel. Depth from crater rim to floor is approx 1500m. Crater shows multiple PPR blocks and basalt layering in the crater rim. Area in image is 7.1km wide

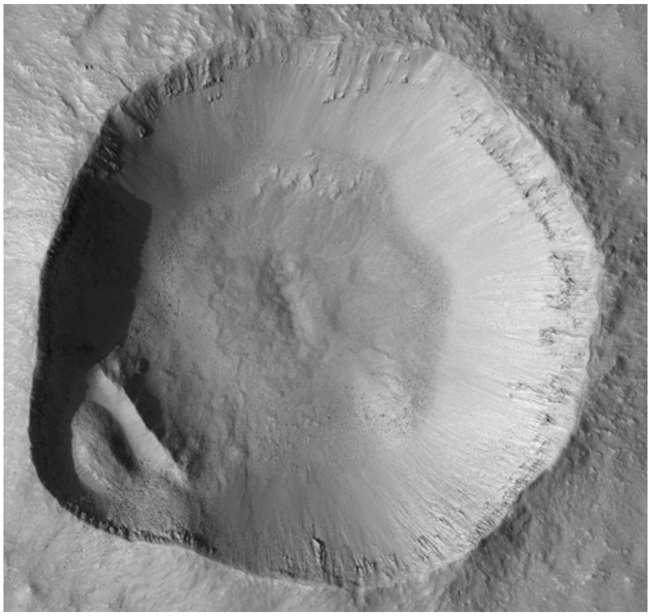

Figure 2. HiRise image of a simple 4km diameter impact crater showing a partial PPR, basalt layering in the rim, and no signs of having undergone gravitational collapse to a complex crater. lat14N, long 123.3E. Resolution is 29cm/pixel. Also of note is the basalt layering seen in the rim is nearest to the surface and appears most massive where the PPR is formed. Both Images courtesy NASA/JPL/University of Arizona.

THE ORIGIN AND TECTONIC MODIFICATION OF THE SAARIJÄRVI IMPACT STRUCTURE, NORTHERN FINLAND.

T. Öhman[1,2], [1]Department of Geosciences, Division of Geology, and [2]Department of Physical Sciences, P.O. Box 3000, FI-90014 University of Oulu, Finland, (teemu.ohman@oulu.fi).

Background: The Saarijärvi structure in Taivalkoski, northern Finland (65°17.4'N, 28°23.3'E) is the northernmost generally accepted impact structure in Europe currently located on dry land, and the only one in the Fennoscandian Shield formed in Archean basement complex. The target consists of Archean gneissose granitic and tonalitic rocks, and three generations of Early Proterozoic metadolerite dykes. Saarijärvi is reasonably well studied, especially given its small size (current D=1.5–2 km) and inconspicuous lake- and bog-filled appearance. This is due the substantial economic interest that was shown to Saarijärvi from the 1800's up to present day. The main economic incentive was the kaolin-bearing Ediacaran and Early Cambrian claystone deposited in the structure. In the late 1990's the structure was also considered a possible kimberlite pipe. As a result, seven drill-cores – three of which extend through the sedimentary rocks to the basement – and a great amount of geophysical data now exist on Saarijärvi. Despite the wealth of data, several aspects of the origin and evolution of the structure are still very poorly constrained.

Indications of impact: The impact origin of Saarijärvi structure was confirmed in 1997, when weakly developed planar deformation features (PDFs) in three orientations in quartz grains from the depth of ~156 m, i.e. from the bottom of the sedimentary sequence, were discovered [1]. In addition, quartz grains display planar fractures (PFs) in multiple orientations, and occasional mosaicism. Later, shatter cones in granitoids and metadolerites were discovered as well. However, the PDFs described so far [1] have been of the "incipient" type [2], and not of the well-documented and totally undisputable type [e.g. 3]. Nevertheless, they are notably different from tectonic deformation lamellae also present in Saarijärvi rocks, and the few measured Miller indices are typical for shocked quartz. Overall, the "big picture" of the Saarijärvi structure leaves very little doubt of the impact origin.

Pre- or post-impact sedimentary sequence? Finnish impact research has recently been slightly enlivened by discussion regarding the pre- or post-impact origin of the mainly Phanerozoic sedimentary rocks currently filling many of the structures [4]. In Saarijärvi, the sedimentary rocks have been interpreted to be post-impact, thus yielding a minimum age of about 600 Ma for the structure [1]. However, there is no real evidence for the post-impact origin. In all of the drill-cores, the sedimentary rocks display variable stratigraphic order, chaotically varying dips of the bedding, as well as slump features. Boulders of basement rocks are present in the middle of the sedimentary sequence in one of the drill cores, as well as in one small outcrop. These observations hint towards a pre-impact origin of the sedimentary rocks, not post-impact. In addition, indications of shock metamorphism, like poorly developed "incipient" PDFs and PFs in quartz grains, are present throughout the sequence. These could be explained as detrital grains deposited long after the impact, but they could also have been deposited immediately after the projectile impacted the sedimentary rocks that were still unconsolidated.

Tectonic modification: The Oulujärvi shear zone is one of the major crustal-scale tectonic features in northern Finland. The Auho fault, which is the main fault in this shear- and fault zone, passes Saarijärvi only about seven kilometers northwest from the structure. More importantly, also on a local scale notable tectonic features are present. The north–south oriented Ölkky lake is situated in a beautiful small gorge immediately north of Saarijärvi. Other similarly oriented fracture valleys are present southwest from Saarijärvi.

One of the curiosities in Saarijärvi is the presence of a central island in such a small and thus presumably simple impact structure. The island is notably elongated in N–S-direction, which is further emphasized by its continuations visible in e.g. apparent resistivity data. The orientation of the island parallels that of the Ölkky lake. Brecciated outcrops in the island consist of metadolerites and granitoids, which display evidence of tectonic deformation (cataclastic veins, slickensides, kink-banded sheet silicates) and hydrothermal alteration, but no signs of shock metamorphism. Also the presence of narrow clinochlore veinlets in the heavily brecciated contact of metadolerite and granitoid implies tectonic deformation. Hence, the island apparently is merely a tectonic block, uplifted well after the impact. Possible other similar but smaller blocks laying somewhat beneath the surface of the sediments may be indicated by minor anomalies in gravity and magnetic data.

The side profile of the Saarijärvi structure, revealed e.g. by the gravity and apparent resistivity data, is notably non-symmetric. The southern side of the structure is deeper, and also the slope of the basin's wall is steeper in the south. Unless an idea of a highly oblique impact is provoked, the whole structure must have been tilted towards south, leading to more severe erosion on the northern side of the structure. Six existing gravity profiles, three of which cross the whole structure including the central island, would make a detailed 3D-gravity modeling of the structure possible, enabling also more robust interpretations of the tectonic modification in Saarijärvi.

The tectonic modification is apparently a relatively late feature in the evolution of the Saarijärvi structure. This is indicated by the fact that especially the clayey part of the sedimentary sequence is strongly fractured obliquely to bedding, often with "polished" slickenside surfaces. Therefore, it seems probable that the major tectonic deformation of the structure took place after the consolidation of the sedimentary sequence, and thus could not have been the main cause for the observed chaotic nature of the sediments now filling the structure. This further implies that the sediments could well have been deposited before the impact. Thus, the probable age for Saarijärvi structure is less than ~520–600 Ma, and not 600–1980 Ma as previously believed.

The breccia problem: A highly interesting aspect in the discussion of pre- or post-impact sedimentation in Finnish impact structures is the question of impact breccias. Even in simple craters a small amount of suevite should be present, with larger quantities of lithic breccia. None can be found in Saarijärvi. The sedimentary rocks lie directly on the basement in all three drill cores that reach the basement. The basement itself is somewhat fractured and weathered, but not brecciated. Hence, it is apparent that no major amounts of breccia are currently present in the northern or central parts of the Saarijärvi structure.

If the justified idea that Saarijärvi is an impact structure is accepted, then a means to dispose of impact breccias is needed. It ought to be kept in mind, that the structure is currently filled with sedimentary rocks that are generally quite soft and easily disintegrated. Yet they have been retained in the depression for the past 600 Ma, surviving e.g. several glaciations, whereas the usually somewhat more coherent impact breccias seem to be totally absent.

Shatter cones and concentric craters: The minimum pressure where shatter cones can be formed is ~2 GPa. Such pressures can be found in the rocks of the crater floor and the central uplift. No true shatter cones have been found in the crater rim or beyond it, because the shock pressure on the rim is about a magnitude lower than required for shatter cone formation. However, in Saarijärvi, shatter cones are found in an area beyond the current depression. The majority of these are in local granitoid boulders that have not moved substantially. Even if they had moved, glacial transport direction indicates that they would have moved towards the center of the structure.

If impact occurs on a stratified target with a weak layer on top of a more rigid one, a concentric crater should form [e.g. 5, 6]. If it is accepted that Saarijärvi area was covered by unconsolidated sedimentary rocks when the impact occurred, Saarijärvi could be a concentric crater. In this model, the current depression filled with sedimentary rocks represents the inner crater, whereas the shatter cones were formed on the floor of the outer crater. If this was the case, then very little erosion has occurred. However, until numerical modeling of a Saarijärvi-sized concentric crater formation is performed, it remains rather speculative if shock pressure in the floor of the outer crater can reach the ~2 GPa required for the shatter cone formation.

Other open questions: Geochemistry of dark cataclastic veinlets in the central island is another problematic issue. The veinlets have elevated nickel contents up to 270 ppm, and Ni/Cr-ratios are several times higher than in typical granites. In fact, they are even slightly higher than chondritic ratios. Although meteoritic contamination is an appealing explanation, hydrothermal leaching and precipitation from the metadolerites, probably occurring in conjunction with the tectonic modification of the structure and the uplift of the central island, is a more plausible one. However, further studies including e.g. platinum group elements of the veinlets, breccias and host rocks should be made before any firm conclusions can be drawn.

Summary and conclusions: The Saarijärvi impact structure is filled with Ediacaran and Early Cambrian sedimentary rocks, now interpreted to be of pre-impact origin. Although the shatter cones are rather crude and in the "wrong" place, PDFs are of the "incipient" type, high Ni/Cr-ratios of cataclastic veinlets inconclusive, and impact breccias lacking, the structure most likely was caused by an impact <520–600 Ma ago. Saarijärvi could have originated as a concentric crater, with the shatter cones now marking the floor of the outer crater. However, modeling of shock pressures in small impacts to layered targets is required to estimate how realistic such a scenario in Saarijärvi actually is.

Acknowledgements: Thanks to the following people for providing data, samples, thought-provoking conversations, and good company on field trips to Saarijärvi: A. Abels, D. Badjukov, S. Elo, J. Kohonen, M. Lehtinen, J. Moilanen, L. J. Pesonen, J. Plado, J. Raitala, P. Tuisku, A. Uutela and S. Vishnevsky. Magnus Ehrnrooth Foundation is thanked for financial support.

References: [1] Pesonen L. J. et al. (1998) *LPS XXIX,* Abstract #1262. [2] French B. M. et al. (2004) *GSA Bull., 116,* 200–218. [3] Stöffler D. and Langenhorst F. (1994) *Meteoritics, 29,* 155–181. [4] Kohonen J. and Vaarma M. (2001) *Geologi, 53,* 111–118. [5] Quaide W. L. and Oberbeck V. R. (1968) *JGR, 73,* 5247–5270. [6] Ormö J. and Lindström M. (2000) *Geol. Mag., 137,* 67–80.

THE MECHANICS OF POLYGONAL IMPACT CRATER FORMATION. T. Öhman[1,2], M. Aittola[2], V.-P. Kostama[2], M. Kallo[2] and J. Raitala[2], [1]Dept. of Geosciences, P.O. Box 3000, FI-90014 University of Oulu, Finland, (teemu.ohman@oulu.fi); [2]Dept. of Physical Sciences, P.O. Box 3000, FI-90014 University of Oulu, Finland.

Introduction: The major significance of crustal structures like faults, joints and fractures or other similar planes of weakness in the target material during the cratering process has been known for decades. This structural control has been confirmed by detailed field studies on a terrestrial crater [e.g. 1, 2], cratering experiments [e.g. 3, 4], and remote sensing studies of craters on various planets (including the Earth), asteroids, icy and rocky moons, and a comet nucleus [see 5 for a review]. Such structures affect the cratering process, and thus also the morphology of the final crater. Hence, information about the structures of the target can be obtained by studying the polygonal crater morphology resulting from an impact into target with some preferred orientations of crustal weakness [e.g. 6, 7].

According to current models, polygonal impact craters' (PICs, defined here as craters with at least two straight rim segments with a clearly discernible angle between them) straight rim segments reflect the orientations of the target differently depending on whether the crater is simple or complex [6]. In simple PICs formed in orthogonally fractured target, straight rim segments should make an angle of ~45º with the fractures. In complex PICs the straight rim segments should parallel the fractures. However, the ground truth data for PICs of simple crater size comes from detailed field studies of only one crater, namely the notably square-shaped Meteor Crater. Hence, it is in order to try to use other approaches to define whether or not it is truly validated to extrapolate ideas based on Meteor Crater to be the general rule of simple crater formation in fractured targets. This is emphasized by impact and explosion experiments [3, 4] that give a much more varied picture of the rim/fracture – relationship than the Meteor Crater. As well-preserved terrestrial craters are extremely few, we have studied impact craters on Mars, Venus, and recently also on the Moon to obtain a better understanding of cratering process in inhomogeneous targets.

Simple and complex PICs' rim strikes: If simple and complex PICs really reflect the target structures differently, the distribution of straight rim segment strikes in the same area should be dissimilar between simple and complex PICs. Continuing our previous work [8], we studied PICs north from the Argyre basin in the southern hemisphere of Mars (10ºW–74ºW, 26ºS–42ºS), using Viking Orbiter MDIM2.0 (Mars mosaicked digital image model) photomosaics (~231 m/px) for all the strike measurements, and the polygonal/non-polygonal classification. However, the simple/complex classification was based on Mars Odyssey THEMIS (thermal emission imaging system) infrared (~100 m/px) and visual channel images (35 m/px). Potential simple craters were pre-selected using 7 km (the average Martian simple/complex transition diameter) as the maximum size. From these craters, the few which showed incipient complex features – mainly enhanced slumping of the rim – were discarded. The remaining 22 polygonal craters were typical Martian simple craters, often with flat floors due to sedimentary infilling. There certainly are some simple craters in the study area larger than 7 km, but their contribution to rim strike distribution is regarded insignificant compared to the substantially larger number of complex craters.

The results of the rim strike studies are intriguing. Instead of the expected differing strike patterns, we could not detect any statistically significant difference between simple and complex craters' rim strike distributions. As previously shown [e.g. 5, 8 and references therein], in a regional study the influence of illumination geometry is insignificant, although it notably affects the apparent polygonality of any single crater. Thus, the similar straight rim segment strike patterns in simple and complex craters can be regarded as real. This contradicts the expectations based on the existing PIC formation models [6].

Size distribution of PICs: If no observational bias occurs, and the formation of PICs favors no particular size range, then the size distributions of polygonal and non-polygonal craters should be similar. We have studied this aspect with data from Argyre region in Mars (10ºW–74ºW, 26ºS–58ºS), from the whole globe of Venus using Magellan SAR-data (synthetic aperture radar images; craters D>12 km, see 9 for details), and from highlands of the Moon (10ºW–40ºE, 10ºN–50ºS; craters D>10 km, at the moment very preliminary data) using photographs from the Consolidated Lunar Atlas. The size distributions of PICs and "normal" craters are somewhat different. It appears that there are "too many" PICs in some size classes compared to the well-defined size distribution of ordinary circular craters. When the sizes are normalized using the average simple/complex transition diameters (D_t=7 km for Mars, modeled D_t=4 km for Venus, and D_t=15 km for the Moon), all the discrepancies in the size distribution curves are roughly at the same D/D_t-ratio: PIC formation appears to "favor" a size range of about $2D_t$ – $5D_t$. Further studies are underway to find out if this truly is a real phenomenon, and not caused by any observational bias. However, at least for Venus the diameter–polygonality -dependence seems quite robust [9]. Also the fact that similar trend can be seen on three different heavenly bodies (although the lunar data is very preliminary) studied with different types of datasets, implies a real preference to a specific size range.

Another PIC formation mechanism? Current models state that in complex PICs, the crater expands preferentially in a direction perpendicular to the strike of fractures, whereas in simple PICs this enhanced expansion takes place in a direction parallel to their strike. This is because simple PICs should form in the excavation stage, when the excavation flow progresses more easily in a direction parallel to the strike of the fractures. Complex PICs, on the other hand, should form in the modification stage, when the rim collapses along normal (listric) faults that utilize the pre-existing planes of weakness [6]. The rim strike data from northern Argyre region is in stark contrast to this idea.

Detailed studies in the few well-preserved terrestrial craters, both simple (e.g. Meteor Crater [1, 2] and Tswaing [10]) and complex (Bosumtwi [11]), clearly indicate the importance of thrusting related to the excavation stage. Therefore it does not seem too far-fetched to think that perhaps this thrusting takes place utilizing pre-existing structures [5]. With this mechanism, straight rim segments would parallel the orientations of regional pre-existing fractures. This mechanism could work in simple PICs, as well as in small and medium sized complex PICs. In larger complex PICs that have gone through more substantial collapse in the modification stage [12], collapse along the pre-existing structures might well be more important mechanism to create polygonality. The suggested size range (small to mid-sized complex craters) of this thrusting model for PIC formation is also approximately the size range where PICs seem to be “too abundant” compared to non-polygonal craters.

The importance of PICs: Polygonal craters are not merely an interesting detail of impact cratering. In addition to increasing our understanding of the most common geologic process in the Solar System, their study has also other benefits. They have been effectively applied in the tectonic studies of various cratered surfaces [reviewed in 5]. Especially useful they are in studying the tectonic history of highly cratered areas with very few other indications of tectonism [7 and references therein]. This aspect is further emphasized by the fact that degradation does not change the strike distribution of straight rim segments [8]. Another aspect favoring their study is that they can be utilized in inferring the general rheological properties of small Solar System bodies: bodies with PICs must have a crust rigid enough for relatively long-lasting fractures to form. As some of these bodies might become an impact hazard, knowing their structure is vital in case there will be a need to try to protect the humankind from their impacts.

Summary and conclusions: Polygonal impact craters, formed by the interaction of pre-existing target structures and the cratering process, are ubiquitous throughout the Solar System. Their current formation models [6] of structurally controlled excavation and slumping predict different straight rim segment strike patterns for simple and complex polygonal craters, respectively. However, we have observed no such difference in simple and complex PICs north from Argyre basin, Mars. Based on our studies of Martian, Venusian and lunar PICs it also appears that there is a preferred size range, where PICs have a higher tendency to form. This size range seems to be roughly around 2–5 times the simple/complex transition diameter. These observations have led us to propose an additional PIC formation mechanism, namely thrusting of the crater rim in the excavation stage utilizing pre-existing planes of weakness. This mechanism would explain the varied results obtained in cratering experiments in fractured targets [3, 4], and it is in concert with observations of major thrusting on the rims of both simple [e.g. 1, 2, 10] and complex [11] terrestrial craters.

Further understanding of PIC formation – complementary to remote sensing and field studies – could be obtained from cratering experiments in fractured targets, including a detailed analysis of pre- and post-impact fractures with respect to the crater rim shape. Another approach would be 3D modeling of the cratering process. Involving relatively small-scale structural discontinuities in the numerical model, however, increases the required computing power substantially.

Acknowledgements: The Space Institute of the University of Oulu is thanked for financial support, and T. Törmänen for helpful discussions.

References: [1] Shoemaker E. (1963) In: Middlehurst B. & Kuiper G. (eds.) *The Moon, meteorites and comets.* Univ. Chicago Press, 301–336. [2] Roddy D. (1978) *Proc. 9th LPSC,* 3891–3930. [3] Gault D. et al. (1968) In: French B. and Short N. (eds.) *Shock metamorphism of natural materials.* Mono Book Corp., 87–99. [4] Fulmer C. and Roberts W. (1963) *Icarus, 2,* 452–465. [5] Öhman T. (2007) unpubl. Lic.Phil. thesis, Univ. Oulu, Finland. [6] Eppler D. et al. (1983) *GSA Bull., 94,* 274–291. [7] Öhman T. et al. (2005) In: Koeberl C. & Henkel H. (eds.) *Impact tectonics.* Springer, 131–160. [8] Öhman T. et al. (2006) *MAPS, 41,* 1163–1173. [9] Aittola M. et al. (2007) *EMP*, accepted. [10] Brandt D. and Reimold W. (1995) *S. Afr. J. Geol., 98,* 287–303. [11] Reimold W. et al. (1998) *Geology, 26,* 543–546. [12] Melosh H. and Ivanov B. (1999) *Ann. Rev. Earth Planet. Sci., 27,* 385–415.

STRUCTURE OF THE WETUMPKA IMPACT CRATER: DRILL-CORE, FIELD DATA, AND NUMERICAL SIMULATION

Jens Ormö[1], Alain Lepinette[1], David T. King, Jr.[2], Lucille W. Petruny[2]. [1]Centro de Astrobiologia, Torrejón de Ardoz, Spain (ormo@inta.es); [2]Geology Office, Auburn University, Auburn, Alabama 36849 USA (kingdat@auburn.edu).

Introduction: Wetumpka is a Late Cretaceous marine-target impact structure in the inner Coastal Plain of Alabama USA [1]. The structure is characterized by a wide, horseshoe-shaped crystalline rim, an interior region of broken and disturbed sedimentary formations, and an extra crater terrain on the south-west composed of structurally disturbed target formations (Fig. 1). The extant crater rim spans 270 degrees of arc and is open on the southwest, the same side as the structurally disturbed terrain just noted. The northwest-southeast diameter of the crystalline rim is approximately 5 km.

Setting: The Wetumpka impact occurred in approximately 30 to 100 m deep marine waters of the Gulf of Mexico, which likely shallowed toward the north where the coeval shoreline was located. In reverse stratigraphic order, the target consisted of marine water; poorly consolidated sediment (comprising 30 m of chalky ooze, 30 m of paralic marine sand, and 60 m of terrestrial clayey sand and gravels, and ultimately, weathered crystalline basement dipping to the southwest with about 10 m per kilometer. This is thought to play a role in the cratering and modification [2].

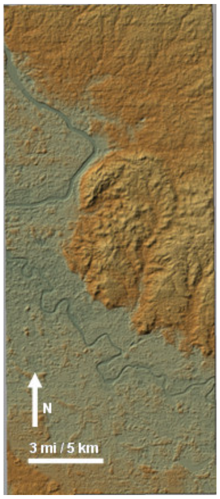

Fig. 1. Setting.

A prerequisite to better understand the processes involved in the formation and modification of the Wetumpka crater is to establish the present erosional level of the crater [2]. The possible existence of basement ejecta at the crystalline rim and its relation with the target sediments within and adjacent to the rim provide crucial information on the erosional level, and thus the size and morphology of the crater. Recently, we performed core drillings at two locations on the crystalline rim [3]. The Eason well on the western rim penetrated 67 m of schist, whereas the Inscoe well on the southeastern rim penetrated 30 m of schistose ejecta resting upon a few meters of schist [3].

In this study we have complemented drill-core and field-based information with a numerical simulation of the cratering event. The simulation has focused on the formation of the rim and its interaction with the resurging seawater.

Method: Numerical modeling is an important tool in the studies of impact cratering, but good material models are required for reliable results [4]. We used iSALE, a multi-material, multi-rheology extension to the SALE (Simplified Arbitrary Lagrangian Eulerian) hydrocode [5] with several improvements [6-10]. In order to describe the response of a rock to stresses, an elastic-plastic rheologic model (RM) is used. The strength model used in this study was first implemented to the code by [7]. It now includes pressure- and temperature-dependent strength, shear failure, strain softening, brittle and ductile deformation [10].

The non-uniform computational grid of the simulations consists of a central cell region around the impact point, where damage is greater, with a regular mesh (horizontal 240 cells, vertical 180 cells) describing half of the damaged zone (axial symmetry). We increased the mesh size progressively outwards from the central cell region with a 1.05 coefficient multiplier for the mesh extension allowing a larger spatial domain to avoid wave reflection problems at the boundaries [nx (radial)=310 cells, ny=460 cells]. The simulation was conducted with a spherical, 396 m diameter granitic projectile (66 cells radius) with an extended cell zone at top of the projectile. Impact velocity is 20km/s.

The thermodynamic state of the material is calculated using the Tillotson EOS [11] as a function of internal energy and density, in our case using granite and wet tuff parameters [12], and ANEOS [13] for water.

The simulated impact was vertical due to limitations of the code. It is, unfortunately, also not possible to use inclined layers in the target, which may be important at Wetumpka [2]. We chose wet tuff to represent the sedimentary part of the target (120 m) as it for the moment is the best available approximation to the low-strength sediments at Wetumpka.

As we are unable to model an impact into a water layer of varied thickness (i.e., 100 m in one end of the damage zone and 30 m in the other) we used an intermediate water depth of 72 m. However, we are currently running simulations with 30 m and 100 m respectively, which then can give information on the rim development on either of the deep-water or shallow-water sides of the crater.

Results and discussion: The two drill cores of the crystalline rim show that basement ejecta is preserved at least on the south-eastern part of the rim, but also that overturned material may exist on the north-western side [3].

The numerical simulation shows how the target water is pushed away from the expanding crater by the shoving-effect of the deposition of the ejecta curtain. This causes a tsunami-like wave travelling away from the crater. When the water comes back to the crater site the elevated rim stands as a wall preventing a resurge into the crater. However, as can be seen in Figures 2 and 3, much of the crater rim consists of material from the poorly consolidated sedimentary target. This provides an unstable foundation for the overturned, more dense basement material. However, the overturned flap formed by denser (i.e., relatively strong) basement material (Figs. 2 and 3) is narrow and the crystalline-blended ejecta is rather thin (Fig 2). In the modeled 75-m target water depth case it is likely that the rim, at least its upper parts, rather soon would collapse and, possibly, open up for a resurge of seawater and megablock slumping of the weakened poorly consolidated sediments outside the crater. This is consistent with the observed opening in the southern part of the rim, the chaotic zone of the extrastructure terrain, and the slumped megablock infill [2]. The forthcoming simulations of 30 m and 100 m water depth options will give further insight in the variations in rim development and hopefully provide answers to the enigma of the yet absent/undiscovered resurge deposits we would expect to find inside the crater.

Conclusions: Drill core and field data show that the erosional level of the Wetumpka crater is not deeper than the polymict ejecta, which is preserved at the rim. Numerical simulation shows, however, that the rim would have a relatively small part developed in the more stable basement rocks. In the upper range of the water depths suggested for the target water sea (i.e. southern side of the crater), collapse of the rim is expected, which likely would open up for extensive slumping of extrastructure sediments as well as resurge of seawater.

References: [1]King, D.T., Jr. et al. (2002) *EPSL 202*, 451-459; [2]King D.T., Jr. et al. (2006) *Met.. Plan. Sci. 41*, 1625-1631; [3]King, D.T., Jr. et al. (2007) LPS XXXVIII, abs. 2178; [4]Pierazzo E. and Collins G. (2003) In *Submarine Craters and Ejecta-Crater Correlation*, 323-340; [5]Amsden A.A. et al. (1980) *Los Alamos National Laboratory Report* LA-8095; [6] Melosh H.J et al. (1992) *J. Geophys. Res.* 97, 14735-*14759*; [7]Ivanov B.A. et al. (1997). *Intl. Jour. Impact Eng. 17*, 375-386; [8]Wünneman K. and Lange M.A. (2002). *Deep-Sea Res. II 49*, 969-981; [9]Wünneman K. and Ivanov B.A. (2003) *Planet. Space Sci. 51*, 831-845; [10]Collins G.S. et al. (2004) *Met. Plan. Sci. 39*, 217-231; [11]Tillotson J.M. (1962) General Atomic Report #GA-3216. San Diego, California: Advanced Research Project Agency, 141p; [12]Allen R.T. (1967) Spec. Nuclear Eff. Lab. - Defense Atomic. Support Agency: DA49-146-XZ-462 16 p; [13]Thompson S. and Lauson H.S. (1972) Sandia National Laboratory, Albuquerque NM 87115, Report SC-RR-71 0714

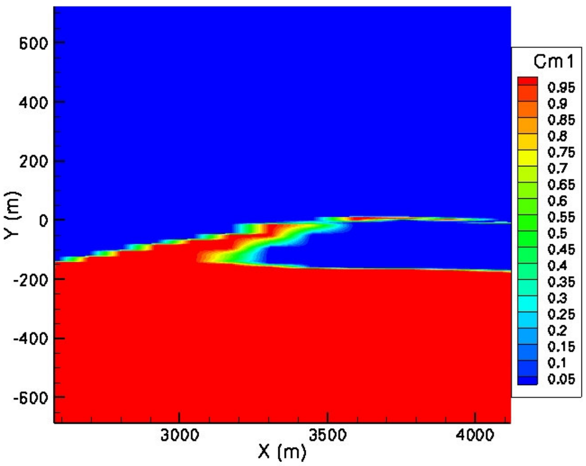

Fig. 2. Relative amount of basement material (granite) at the crater rim (e.g., 0.95 means 95% granite and 5% other material). X-axis shows distance from crater center (to the left).

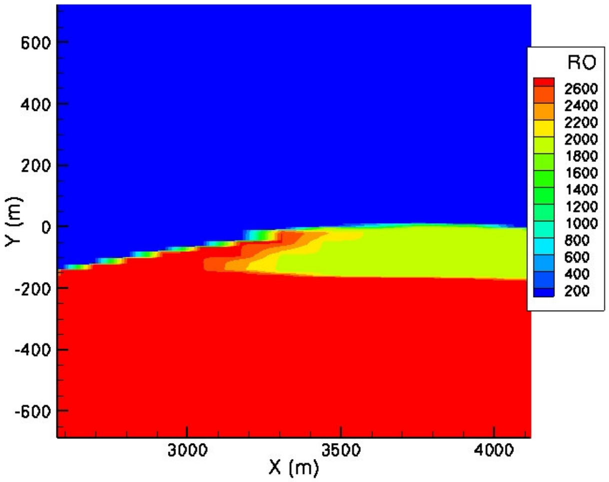

Fig. 3. Density in kg/m^3 of materials in the same frame as in Fig. 2. X-axis shows distance from crater center.

IMPACT EJECTA EMPLACEMENT: OBSERVATIONS FROM EARTH, MOON AND MARS.

G. R. Osinski, Canadian Space Agency, 6767 Route de l'Aeroport, St-Hubert, QC J3Y 8Y9, Canada (osinski@lycos.com).

Introduction: One of the most characteristic, but poorly understood, aspects of meteorite impact events is the generation of ejecta deposits. The lack of understanding is due, in part, to the scarcity of ejecta at the majority of the world's impact structures. Observations of impact ejecta deposits on other planetary bodies provide a complementary data set with which to study the emplacement of impact ejecta; however, ground-truthing is not possible and information is only available about the surface morphology and properties of the ejecta deposits. The aim of this paper is to summarize and discuss observations of impact ejecta deposits from terrestrial, lunar, and martian impact structures and the role of target lithology in their formation.

Proximal versus distal impact ejecta: Proximal impact ejecta deposits are found in the immediate vicinity of an impact crater (<5 crater radii from the point of impact); whereas distal ejecta deposits are found distant from the crater (>5 crater radii) and may be dispersed globally depending on the magnitude of the impact event. It is important to note that for complex impact craters, proximal ejecta deposits do not only occur outside the final crater rim (as in simple impact craters), but also within the collapsed crater rim region (i.e., they occur external to the original transient cavity and up to the outer limit of the continuous ejecta blanket, up to ~5 crater radii from the point of impact).

Proximal impact ejecta: Proximal ejecta deposits are rare on Earth due to post-impact erosional processes, but are common on other planetary bodies. It is generally accepted that proximal ejecta deposits on airless bodies, such as the Moon, are emplaced *via* ballistic sedimentation [1]. In this model, the ballistic emplacement of primary crater-derived ejecta results in secondary cratering and the incorporation of local material (so-called "secondary ejecta"), and considerable modification of the local substrate [1].

Studies of the continuous ejecta blanket (Bunte Breccia) at the Ries impact structure strongly support the importance of ballistic sedimentation during ejecta emplacement on Earth [2]. An important observation is that the Bunte Breccia consists of two main components: (1) primary ejecta excavated from the initial transient crater (~31 vol%; [2]); and (2) local material or "secondary ejecta" (~69 vol%; [2]). The incorporation of large amounts of secondary ejecta clearly indicates that after primary ejecta is initially deposited, it then continues to be transported radially-outwards along the surface.

It is apparent that target lithology plays an important role in the formation of continous ejecta deposits. At the Ries structure, the volatile content and cohesiveness (e.g., resistant limestone bedrock versus unconsolidated clays and sands) of the uppermost target outside the transient cavity governed the maximum radial extent of ground-hugging flow following ballistic deposition [2].

An important observation is that one, or more, layers of ejecta may overlie the continuous ejecta blanket around complex impact structures. This is particularly common on Mars, where so-called double and multiple layered ejecta structures are observed [3]. This is also true for several terrestrial craters, including the Chicxulub (e.g., [4, 5]), Haughton [6], and Ries (e.g., [7]) impact structures. On the Moon, impact melt deposits overlying the continuous ejecta blanket may also be thought of as ejecta deposits [8].

Some of the best-preserved and exposed ejecta deposits occur at the Ries structure, where a series of impact breccias (polymict crystalline breccias), impact melt-bearing breccias (suevites), and impact melt rocks overlie the continuous ejecta blanket (Bunte Breccia) [7]. Early workers suggested that these impactites were deposited subaerially from an ejecta plume [7, 9]. More recently, it has been suggested that the proximal suevites were emplaced as surface flow(s), either comparable to pyroclastic flows (e.g., [10, 11]), or as ground-hugging impact melt-rich flows that were emplaced outwards from the crater center during the final stages of crater formation [12]. This has also been suggested for the impact melt rocks at the Ries [13]. Such a mechanism for the emplacement of this suevite ejecta is consistent with several field observations [12] and the clear temporal hiatus between emplacement of the ballistically-emplaced Bunte Breccia and the overlying suevites/impact melt flow deposits [2], which requires a two-stage ejecta emplacement mode. This is supported by observations made at the Haughton structure, where two layers of proximal ejecta also occur [6]. As at the Ries, the properties of the lower layer (which represents the continuous ejecta blanket) are consistent with emplacement *via* ballistic sedimentation during the excavation stage, with the upper layer being emplaced as ground-hugging flows during the modification stage of crater formation. For the upper layers, target lithology appears to play a fundamental role in determining the amount of melt and vapour generated, which affects the amount of fluidization and flow.

At the larger Chicxulub structure, several layers of ejecta are present, both within and exterior to the final crater rim. Evidence from the Yaxcopoil-1 drill hole suggests complex emplacement mechanisms involving ground surge and ballistic sedimentation; however, the limited thickness of impactites available for study (~90 m) and the evidence for reworking renders it difficult to place these observations in the wider context of impact ejecta emplacement in general [4]. Exterior to the final crater rim, Chicxulub possesses two main types of proximal ejecta deposit [14] (cf., the Haughton and Ries structures): (1) polymict impact breccias up to ~300 m thick, interpreted as the continuous ejecta blanket (cf., Bunte Breccia at the Ries structure); and (2) suevite deposits up to ~150 m thick that overlie the Bunte Breccia-like deposits. Unfortunately, the emplacement mechanism(s) of these impactites has not been addressed in any detail due to poor exposure.

The outer portion of the continuous ejecta blanket has been termed the Albion Formation and comprises a basal spheroid bed and an upper diamictite bed (e.g., [15]), which preserve features such as cross bedding and internal shear planes, indicative of lateral flow outwards from the crater center [15, 16]. Kenkmann and Schönian [16] proposed the following depositional model: following ballistic deposition at <<3 crater radii, ground-hugging flow occurred driven by the water content of the flow itself. At distances of >3.5 crater radii, the incorporation of local clays further fluidized the flow and allowed it to continue moving for greater distances than would have been possible if the substrate was resistant bedrock. Thus, target lithology played a key role in fluidizing the ejecta deposits.

Emplacement of impact ejecta *via* a combination of ballistic sedimentation and ground-hugging flow during different stages of crater formation, is broadly consistent with observations from other planetary bodies. For example, exterior impact melt-rich ejecta flows have been recognized around lunar and venusian impact structures [8, 17, 18]. It is also widely accepted that the layered ejecta deposits of many martian impact craters were emplaced as highly fluidized relatively thin ground-hugging flows [19-21].

Distal impact ejecta: Distal ejecta deposits, collectively termed air fall beds typically comprise two main types: strewn fields of glassy tektites and microtektites, and spherule beds comprising (formerly) glassy impact spherules and fragments of shocked target rocks. Of the four tektite strewn fields, two (the Ivory Coast and Central European fields) have been linked to source craters [22]. In addition, several Phanerozoic to Cenozoic spherule layers have been documented in the rock record [23]. It is typically assumed that distal ejecta gradually settles out from the atmosphere; however, it has also been suggested that distal impact ejecta falling into the atmosphere may clump together into density currents that flow to the ground much more rapidly than might be expected for single particles themselves [24].

Summary: In summary, while many aspects of ejecta emplacement remain unclear, it is apparent that target lithology plays an important role in this aspect of the impact cratering process, for example in constraining the amount of fluidization and surface flow and the amount and properties of entrained impact melt. Further work, however, is required on this subject, including numerical modeling and greater use of planetary datasets for comparative studies.

References: [1] V.R. Oberbeck (1975) *Rev. Geophys. Space Phys., 13*, 337-362. [2] F. Hörz, et al. (1983) *Rev. Geophys. Space Phys., 21*, 1667-1725. [3] N.G. Barlow, et al. (2000) *JGR, 105*, 26733-26738. [4] B.O. Dressler, et al. (2004) *Meteoritics & Planet. Sci., 39*, 857-878. [5] D. Stöffler, et al. (2004) *Meteoritics & Planet. Sci., 39*, 1035-1067. [6] G.R. Osinski, et al. (2005) *Meteoritics & Planetary Science, 40*, 1789–1812. [7] W.v. Engelhardt (1990) *Tectonophys., 171*, 259. [8] B.R. Hawke, et al., Impact melt on lunar crater rims, Impact and Explosion Cratering, Pergamom Press, New York, 1977, p. 815. [9] W.v. Engelhardt, G. Graup (1984) *Geol. Rund., 73*, 447. [10] D. Bringemeier (1994) *Meteoritics & Planet. Sci., 29*, 417. [11] H.E. Newsom, et al. (1986) *JGR, 91*, 239. [12] G.R. Osinski, et al. (2004) *Meteoritics & Planet. Sci., 39*, 1655-1684. [13] G.R. Osinski (2004) *Earth Planet. Sci. Lett., 226*, 529-543. [14] D.A. Kring (2005) *Chemie der Erde, 65*, 1-46. [15] K.O. Pope, et al. (1999) *Earth Planet. Sci. Lett., 170*, 351-364. [16] T. Kenkmann, et al. (2006) *Meteoritics & Planet. Sci., 41*, 1587-1603. [17] M.J. Cintala, R.A.F. Grieve (1998) *Meteoritics & Planet. Sci., 33*, 889-912. [18] R.A.F. Grieve, M.J. Cintala (1995) *Icarus, 114*, 68. [19] M.H. Carr, et al. (1977) *JGR, 82*, 4055-4065. [20] P. Mouginis-Mark (1987) *Icarus, 71*, 268-286. [21] G.R. Osinski (2006) *Meteoritics & Planet. Sci., 41*, 1571-1586. [22] C. Koeberl, in: B.O. Dressler, R.A.F. Grieve, V.L. Sharpton, (Eds), Large Meteorite Impacts and Planetary Evolution, GSA Special Paper 293, Geological Society of America Special Paper 293, Boulder, Colorado, 1994, pp. 133-152. [23] B.M. Simonson, B.J. Glass (2004) *Ann. Rev. Earth Planet. Sci., 32*, 329-361. [24] H.J. Melosh (2004) *Meteoritics & Planet. Sci., 39*, A67.

EFFECT OF TARGET LITHOLOGY ON IMPACT MELTING.

G. R. Osinski[1], R. A. F. Grieve[2], and J. G. Spray[3], [1]Canadian Space Agency, 6767 Route de l'Aeroport, St-Hubert, QC J3Y 8Y9, Canada (osinski@lycos.com), [2]Earth Sciences Sector, Natural Resources Canada, Ottawa, ON K1A OE8, Canada, [3]Planetary and Space Science Centre, Dept. of Geology, University of New Brunswick, 2 Bailey Drive, Fredericton, NB E3B 5A3, Canada.

Introduction: Impact melting is a characteristic feature of hypervelocity impact events on Earth and other planetary bodies. One of the outstanding questions in impact cratering studies is the effect of target properties on impact (or shock) melting and the relative importance and role of impact melting versus decomposition for impacts into sedimentary-bearing target rocks. The aim of this paper is to provide an up-to-date assessment of the effect of target lithology on impact melting, based on studies carried out at several terrestrial impact structures and a review of the existing literature (based on a more detailed review of impact melting, currently *in press* [1]).

Physics of impact melt generation: Numerical modeling of the impact cratering process, together with theoretical calculations and shock experiments, have revealed insights into the generation of impact melt:

1) Shock melting occurs upon decompression [2]. Energy deposited in the target during shock compression remains as heat following decompression; if the shock is strong enough and sufficient heat remains, the released material may be left as a melt or vapor [2].

2) The effect of porosity is such that a large amount of compression and shock heating occurs in porous target rocks [3-5]. The presence of high porosities significantly increases the amount of pressure–volume work in the target rocks resulting from the shock wave, which results in greater amounts of post-shock waste heat, raising temperatures, and generating more melt that non-porous targets. However, the crushing of pore space reduces the overall shock pressures in the target, possibly reducing overall melt volumes.

3) The volumes of target material shocked to pressures sufficient for melting are not significantly different in sedimentary or crystalline rocks [6].

4) Calculations indicate that both wet and dry sedimentary rocks yield greater volumes of melt on impact than crystalline targets [6].

Observed impact melt volumes: Impact melt occurs in two main forms in impactites within impact structures [7, 8]: (i) as coherent impact melt sheets or discrete bodies of impact melt rocks within impact breccias, and (ii) as discrete clasts within impact melt-bearing breccias (impact melt breccias and "suevites").

It is widely reported that the volume of impact melt recognized in predominantly sedimentary and in mixed (sedimentary–crystalline) targets is on the order of two magnitudes less that for crystalline targets in comparably sized impact structures (e.g., the widely cited compilation by Grieve and Cintala [7]. However, when the results of more recent studies are considered, it becomes clear that the volume of impact melt appears to be similar for impacts into different target lithologies (Fig. 1) (e.g., the estimated original melt volume at the 23 km diameter Haughton impact structure (predominantly sedimentary target) of ~22.5 km^3 [9]). This is in accordance with past theoretical calculations [6] and more recent numerical modeling [5] (see above).

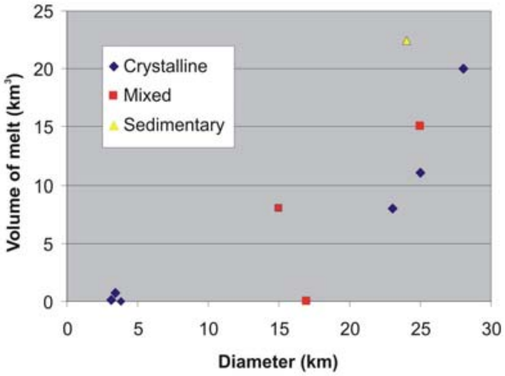

Figure 1. Plot of estimated initial impact melt volume for several terrestrial impact structures up to 28 km in diameter formed in different target lithologies.

It is, however, apparent from Figure 1 that little accurate data is available on melt volumes for terrestrial impact structures and that these estimates are dependant on diameter estimates that may or may not be accurate. Further studies are, therefore, required to refine these melt and diameter estimates.

Recognition of impact melt products: For impacts into predominantly crystalline target rocks, coherent impact melt rocks or 'sheets' are formed. These rocks often display classic igneous features (e.g., columnar jointing) and textures (e.g., glassy or fine-grained crystalline groundmass) (e.g., Fig. 2a). Thus, there has been no questioning of the impact melt origin of these lithologies. In contrast, for impacts into sedimentary-rich target rocks, it has been generally accepted that impact melt rocks are not generated [8], in contradiction of theoretical predictions (see above).

It is suggested that this inconsistency is due to the challenges in recognizing impact melt products derived from sedimentary-rich target rocks, rather than different processes and products during impacts into different target lithologies. For example, at the Haughton structure, distinctive pale gray crater-fill deposits form a discontinuous 54 km^2 layer in the central area of the structure (Fig. 2b). Contrary to previous workers who interpreted these impactites as clastic matrix breccias, or as fragmental breccias [10, 11], recent field, optical and analytical SEM studies reveal that these impactites can be classified as impact melt breccias or clast-rich impact melt rocks according to the terminology of Stöffler and Grieve [12]. Thus, although the products of meteorite impact into volatile-rich target rocks may appear very different from those developed in crystalline targets, it is suggested that these different lithologies are genetically equivalent.

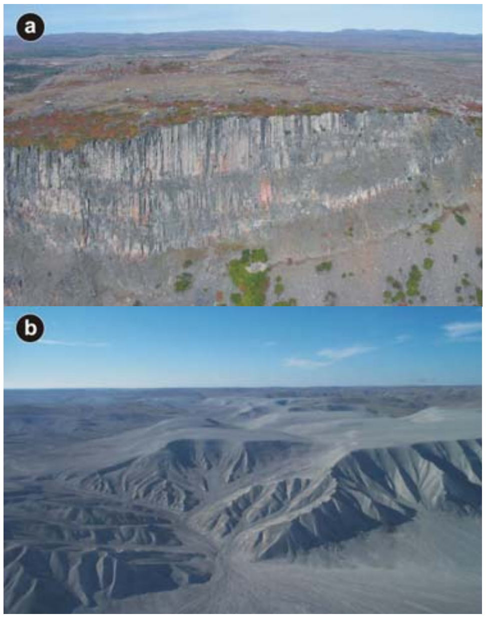

Figure 2. (a) Oblique aerial view of the ~80 m high cliffs of impact melt rock at the Discovery Hill locality, Mistastin impact structure, Labrador. Photograph courtesy of Derek Wilton. (b) Field photograph of the crater-fill impact melt breccias at the Haughton impact structure. The vertical distance to the highest point is 35 m.

Clast content of melt-bearing impactites. One apparent difference between melt-bearing impactites found in craters in different target rocks is the higher clast content of impactites in sedimentary versus crystalline target rocks. For example, the clast content of crater-fill impact melt breccias at Haughton (sedimentary target) is up to ~40–50 vol%, which is higher than in the comparably-sized Mistastin structure (crystalline target) (~20–30 vol% [13]). However, it has been suggested [9] that this can be explained by the effect of mixing ‘wet’ sediments or carbonates into a melt as opposed to dry crystalline rocks: the enthalpies of H_2O-bearing and carbonate systems are so high that a much smaller proportion of admixed sedimentary rocks than of anhydrous crystalline rock is required to quench the melt to subsolidus temperatures [6]. Thus, all other conditions being equal, a lower percentage of sedimentary rocks will be assimilated than crystalline rocks, before a melt is quenched, resulting in higher final clast contents for melts derived from impacts into sedimentary as opposed to crystalline targets.

Melting versus decomposition: The phase relations of $CaCO_3$ suggest that limited decomposition from $CaCO_3$ melt may be possible following decompression [14], although evidence for this has not yet been observed in naturally shocked rocks. For impact into limestones, this absence of evidence may be due, in part, to the recombination of CO_2 and CaO during fast back-reactions [15]. However, studies of naturally shocked rocks also suggest that decomposition is a post-impact contact metamorphic process, which also occurs in igneous rocks [1], governed by the post-impact temperature of the melt–clast mixture (i.e., rapid quenching and/or low post-shock temperatures will inhibit carbonate decomposition).

Summary: Synthesizing observations from terrestrial impact structures with experimental results, computer simulations, and phase relations, it is clear that previous assumptions about the response of sedimentary rocks during impact events are inaccurate. Impact melting appears to be the dominant response of hypervelocity impact into sedimentary rocks. Limited decomposition from the melt phase may be possible following decompression if the melt remains at high temperatures long enough for this to occur. The apparent ‘anomaly’ between the volumes of impact melt generated in sedimentary versus crystalline targets in comparably sized impact structures, therefore, appears to be due to a misinterpretation of the characteristics of impact melts derived from sedimentary rocks.

References: [1] Osinski G. R. et al., (Forthcoming) in: K.R. Evans, et al., (Eds), The Sedimentary Record of Meteorite Impacts, GSA Special Publication, in press. [2] Melosh H. J. (1989) Impact Cratering: A Geologic Process, 245 pp. [3] Kieffer S. W. (1971) *JGR*, 76, 5449-5473. [4] Ahrens T. J. and Cole D. M. (1974) *Geochim. Cosmochim. Acta*, 3, 2333-2345. [5] Wünnemann K. and Collins G. S. (2007) *LPS XXXVII*, Abstract # 1514 . [6] Kieffer S. W. and Simonds C. H. (1980) *Rev. Geophys. Space Phys.*, 18, 143-181. [7] Grieve R. A. F. and Cintala M. J. (1992) *Meteoritics*, 27, 526-538. [8] Dressler B. O. and Reimold W. U. (2001) *Earth Sci. Rev.*, 56, 205-284. [9] Osinski G. R. et al. (2005) *Meteoritics & Planet. Sci.*, 40, 1789–1812. [10] Metzler A. et al. (1988) *Meteoritics*, 23, 197-207. [11] Redeker H. J. and Stöffler D. (1988) *Meteoritics*, 23, 185-196. [12] Stöffler D., Grieve R. A. F. (1994) *LPS XXV*, 1347. [13] Grieve R. A. F. (1975) *GSA Bull.*, 86, 1617-1629. [14] Ivanov B. A. and Deutsch A. (2002) *Phys. Earth Planet. Int.*, 129, 131-143. [15] Agrinier P. et al. (2001) *Geochim. Cosmochim. Acta*, 65, 2615-2632.

ENVIRONMENTAL EFFECTS ASSOCIATED WITH IMPACT EVENTS.

E. Pierazzo, Planetary Science Institute (1700 E. Ft. Lowell Rd., Suite 106, Tucson, AZ 85719, U.S.A.; betty@psi.edu).

Introduction: Impacts are among the most important mechanisms for the evolution, distribution and destruction of life in the solar system. They may have distributed primitive life forms in the solar system [1] and contributed directly to the evolution of life through extinction events [2], when they did not destroy it [3]. In particular, it was the wealth of studies of the Chicxulub (or KT) impact event and its connection to the end-Cretaceous mass extinction that brought to attention the important long-term consequences of large impacts on the climate.

Destructive effects of impact cratering: Environmental catastrophes occur when abrupt changes in the environment lead to extinction of living organisms. The event's abruptness is a crucial factor in producing an environmental catastrophe; large climate changes that develop over million of years do not seem to cause significant mass extinction events. Climate perturbations from large impacts would occur at most over few years, with the potential to trigger local or even global environmental catastrophes.

Most asteroid and comet impacts will result in localized effects, not global-scale extintions. The low energy end of impact events is based on comparison to nuclear blasts. Impacts with energies less than few thousands of Mt TNT equivalent (1 Mt = 4.184×10^{15} J) may cause at most a small to medium size crater. The airblast is likely the most destructive impact effect beyond crater formation and ejecta distribution. Using scaling from nuclear explosion data, Kring [6] estimated that the Meteor Crater impact event (20-40 Mt) would have cause total destruction 1 to 2 km away from the point of impact; trees would have been flattened by the blast wave over a radial distance of about 14 to 19 km, with up to 50%. casualty rates for human size mammals up to 9 to 14 km from the impact.

Several structures larger than 100 km in diameter are known on Earth today, but the only undisputed case of a large impact event that coincides with a mass extinction (KT) is the Chicxulub structure. Qualitative assessments of impact-related environmental and climatic effects abound, but a comprehensive quantitative investigation is still mostly lacking. The widespread effects caused by large impact events are usually divided into short term and long term [7].

Short-term effects extend up to few weeks after the impact, and are generally believed to have little influence on the long-term evolution of the climate. They include the localized direct effects of shock waves generated by the impact in the atmosphere, blast waves, and at the Earth's surface, such as earthquakes and tsunamis. More widespread effects include the production of toxic gases like NO_x, and HNO_3 by shock heating of the atmosphere from the entering projectile. Re-entering ejecta interacting with the atmosphere can cause intense frictional heating of the upper atmosphere. The resulting infrared heating could have been strong enough to ignite surface biomass [8]. This model is supported by evidence of soot at several KT boundary sites [9]. The fires, in turn, fill the lower atmosphere with smoke, dust and pyrotoxins in a scenario reminiscent of a nuclear winter [10].

Long-term effects extend over months to decades after the impact, and can have profound effects on the environment directly and indirectly by perturbing the overall climate. They include the radiative effects from stratospheric loading of small size dust [2,11] and climatically active gases. Release of climatically active gases is very dependent on the characteristics of the target: CO_2 and SO_x are released from sediments, while large amounts of water is released in oceanic impacts.

The effect of atmospheric dust-loading was first explored using simple numeric models of the atmosphere's radiative balance [12] for the KT impact. Results indicated that even a rapidly coagulating and settling dust layer may cause sub-freezing temperatures in continental interiors for few months after the impact and a global loss of photosynthesis for about half that time. A 3D atmospheric general circulation model simulation indicate a strong and "patchy" cooling on land, with temperature declining by up to ~12ºC, and a mild cooling over the oceans, accompanied by a collapse of the hydrologic cycle [11]. Later, it was realized that only the stratospheric portion of the fine (submicron) dust from an impact can affect the climate on a global scale for a significant period. The amount and size distribution of dust injected in the atmosphere by a large impact is still not well constrained [13].

Today, CO_2 is one of the main culprits of global warming. Impacts into terrains rich in carbonates could abruptly release large amounts of CO_2 in the atmosphere. Modeling studies of the KT impact [14,15] indicate that the impact does not release a significant amount of CO_2 when compared to the end-Cretaceous atmospheric inventory. However, a bigger contribution to the atmospheric CO_2 inventory may come from impact-related wildfires. Estimates from the identified soot layer at the KT boundary suggest the possibility of doubling the pre-impact CO_2 inventory [7]. This may cause a global warming of ~2ºC [15]. Lomax et al. investigated the global-scale response of terrestrial ecosystems to large increases in atmospheric CO_2 from the KT impact with a dynamic vegetationbiogeochemistry model [16,17]. Results suggest that a 4- to 10-fold increase of the atmospheric end-Cretaceous CO_2 inventory causes spatially heterogeneous increases in net primary productivity, and a biotic feedback mechanism that would ultimately help climate stabilization. They then artificially reduced the mean annual temperature by 6°C for 100 years, to addres the cooling effect of dust/sulfates, and added the effects of wildfires by burning 25% of the vegetation carbon (CO_2 concentration set to 10 times pre-impact levels) [17]. Model results indicate an initial collapse of the Earth's net primary productivity with total recovery within a decade. In their model, changes in productivity and vegetation biomass were larger at low latitudes, consistent with terrestrial paleobotanical data.

The release of SO_x and water vapor in the stratosphere results in the production of sulfate aerosols, as documented by volcanic eruptions. Sulfate aerosols scatter short-wave radiation, and can be strong absorbers of long-wave radiation (if >1 μm in diameter), causing a net cooling of the Earth's surface. The effect of injecting SO_x and H_2O in the stratosphere has been investigated with simple 1D atmospheric models combined with coagulation models. Using 2×10^{17}g (200 Gt) of SO_2 and water vapor, Pope et al. [18,19] found a significant reduction of solar transmission for about 8–13 years after the impact, causing a negative forcing about two orders of magnitude larger than CO_2 forcing. This would cause continental surface temperatures to approach freezing for several years [19]. Using a similar approach, Pierazzo et al. [20] obtained a slightly shorter duration of the sulfate effect, with a 50% reduction in solar transmission for 4 to 5 years after the impact, with a stronger overall forcing.

Oceans are a crucial component of the climate system. Their role in the long-term response of the radiative perturbation from a KT-type dust loading of the atmosphere were investigagted with a 2D, zonally averaged dynamic ocean circulation model [21]. Results indicate a sea surface temperature drop of several degrees in the first year post-impact, with strongest effects in equatorial regions. Deep-sea temperatures started to change only after ~100 years, and never exceeded few tenths of °C. Overall, the structure of the ocean circulation was not affected by the impact.

Constructive effects of impact cratering: Impact cratering can affect environments in a positive way, creating niches for life to florish. Modeling work on this aspect of impact cratering range from the potential delivery of complex organic molecules to planetary surfaces [22,23] to the creation of the conditions for a habitat more conducive to life [24,25].

The suggestion that a substantial fraction of the Earth's prebiotic inventory of organic molecule may have been delivered by infalling comets and asteroids is now about a century old [26]. Modeling studies have provided contrasting results. Recent modeling work using high resolution hydrocode simulations of impact cratering, indicate that at the time of the origin of life on Earth cometary impacts could have delivered large amounts of certain complex organic material, thus boosting the concentration of organic molecules crucial for the origin of life [22]. The same does not seem to have occurred on other planetary bodies, like Mars and the Moon, where most of cometary material and related surviving organics would reach escape [23].

Since the realization that hydrothermal systems are possible sites for the origin and early evolution of life on Earth (e.g., [24]) much attention has been directed to impact-related hydrothermal systems at the site of impact events. Evidence of hydrothermal circulation underneath terrestrial structures abound, as well as suggestions that hydrothermal systems could have formed underneath large Martian impact structures. Sophisticated computer models have been used to model the evolution of impact-related hydrothermal systems on Earth and on Mars [25,26], while modeling work is on its way to better characterize the early post-impact conditions that are conducive to the development of the hydrothermal system [27]. Modeling results suggest that heat generated in large impacts could drive substantial hydrothermal activity for hundreds of thousands of years, even under cold climatic conditions, supporting the idea that impact events may have played an important biological role on early Earth and on Mars [25,26].

This work is supported by NASA Grant NNG05GN57G.

References: [1] Melosh H.J. (1988) *Nature, 332*, 687. [2] Alvarez W. et al. (1980) *Science*, *208*, 1085. [3] Sleep N. et al. (1989) *Nature, 342*, 139. [4] Artemieva N., Shuvalov V. (2007) *LPSC, 38*, Abst. 1537. [6] Kring D.A. (1997) *MAPS, 32*, 517. [7] Toon O. et al. (1997) *Rev. Geophys.*, *35,* 41. [8] Melosh H.J. et al. (1990) *Nature, 373*, 399. [9] Wolbach W. et al. (2003) *Astrob., 3*, 91. [10] Turco R. et al., (1991) *AREPS., 19*, 383. [11] Covey C. et al. (1994). [12] Toon O.B. et al., (1982) *GSA Sp. Pap., 190*, 187. [13] Pope K.O. (2002) *Geol., 30*, 99.[14] Ivanov B. et al. (1996) *GSA Sp. Pap., 207*, 125. [15] Pierazzo E. et al. (1998) *JGR*, *103,* 28,607. [16] Lomax B.H. et al. (2000) *GRL*, *27*, 2149. [17] Lomax B.H. (2001) *EPSL*, *192*, 137. [18] Pope K.O. et al. (1994) *EPSL, 128*, 719. [19] Pope K.O. et al. (1997) *JGR*, *102*, 21,645. [20] Pierazzo E. et al. (2003) *Astrob.*, *3*, 99. [21] Luder T. et al. (2003) *JGR.*, *108*. CiteID 5074. [22] Pierazzo E., Chyba C.F. (1999) *MAPS, 34,* 909. [23] Pierazzo E., Chyba C.F. (2002) In *Comets and the origin and evolution of life* (Thomas-Hicks-Chyba-McKay Eds.), 137. [24] Farmer J. (2000) *GSA Today***,** *10*, 1. [25] Abramov O., Kring D.A. (2004) *JGR, 109*, CiteID E10007. [26] Abramov O., Kring D.A. (2005) *JGR, 110*, CiteID E12S09. [27] Pierazzo E. et al. (2005) *GSA Sp. Pap., 384*, 443.

THE IMPACT HYDROCODE BENCHMARK AND VALIDATION PROJECT: FIRST BENCHMARK AND VALIDATION TESTS.

E. Pierazzo[1], N. Artemieva[2], E. Asphaug[3], J. Cazamias[4], R. Coker[5], G.S. Collins[6], D.A. Crawford[7], G. Gisler[8], K.A. Holsapple[9], K.R. Housen[10], B. Ivanov[2], D.G. Korycansky[3], H.J. Melosh[11], E.A. Taylor[12], E.P. Turtle[13], K. Wünnemann[14], [1]Planetary Science Inst., 1700 E. Ft. Lowell Rd., Suite 106, Tucson, AZ 85719, USA (betty@psi.edu); [2]Inst. Dyn. Geospheres, Russian Acad. Sci, Moscow, 117979 Russia; [3]Univ. of Calif. Santa Cruz, S. Cruz, CA 95064, USA; [4]Univ. of Alabama at Birmingham, Birmingham, AL 35294; [5]Los Alamos Nat. Labs., Los Alamos, NM 87545, USA; [6]Imperial College London, London SW7 2AZ, UK; [7]Sandia Nat. Labs., P.O. Box 5800, Albuquerque, NM 87185, USA; [8]Univ. of Oslo, 0316 Oslo, Norway; [9]Univ. of Washington, Seattle, WA 98195, USA; [10]The Boeing Company, Seattle, WA 98124, USA; [11]Univ. of Arizona, Tucson, AZ 85721, USA; [12]The Open Univ., Milton Keynes MK7 6AA, UK; [13]APL, Johns Hopkins Univ., Laurel, MD 20723, USA; [14]Natural History Museum, Humboldt-Univ. , Berlin 10099, Germany.

Introduction: Over the last few decades, rapid improvement of computer capabilities has allowed impact cratering to be modeled with increasing complexity and realism, and have paved the way for a new era of hydrocode modeling of the impact process, dominated by full, three-dimensional (3D) simulations. When properly benchmarked and validated against observation, computer models offer a powerful tool for understanding the mechanics of impact crater formation. This work presents initial results of a collective validation and benchmarking effort from the impact cratering and explosion community. We are following our first benchmarking tests with a simple validation test of a Boeing impact experiment consisting of a glass sphere, 2 mm in diameter impacting water vertically.

The Validation and Benchmarking Project: The Validation and Benchmarking Project (VBP) brings together a collective expertise in numerical modeling of impact and explosion events, continuum mechanics and computational physics in an unprecedented effort to enhance, compare, validate and benchmark the computer models ("hydrocodes") used to model solar system impact events. The project involves at least 10 distinct codes and involves over 15 scientists, each with extensive experience in numerical modeling of impact and explosion events, from universities and research institutes worldwide as well as from national laboratories. The VBP identifies a two-part base of standards for comparing and validating hydrocodes. The benchmark component identifies a set of hypothetical explosive and impact events of varying complexity that must be run by the impact codes to compare the different numerical and physical models employed in the codes. The validation component defines a set of well-documented laboratory and field experiments over a wide range of event sizes, geological materials and problem types as type-cases that must be reproduced in detailed and systematic code simulations. All the simulations will test a range of physical mechanisms involved in impact events. This effort has not been undertaken before because it requires the coordination of many modelers that have specific experience with one or two computer codes, augmented by difficulties in accessing the extensive experimental data necessary for the code validation.

Identified standards, code simulations and results will be made widely available to the scientific community through a website dedicated to the project. By providing this information to the broad scientific community it will help prevent the incorrect and misinformed use of the codes and provide a set of rules and test cases to follow in order to properly benchmark and validate hydrocodes to come.

Impact Hydrocodes: hydrocodes currently enlisted for testing in the VBP include: ALE3D [1], AUTODYN [2], CTH [3], GEODYN [4], SAGE/RAGE [5], iSALE/SALEB [6,7], SOVA [8], SPH [9], ZEUSMP2 [10]. Some codes may work better for specific situations, although they all contain the fundamental physics needed to model high-energy impact/explosion events. Each code has been extensively tested individually, but no collective benchmarking and validation has ever been carried out.

Benchmark Testing involves the identification of impact standards, ideal tests to be run by the hydrocodes. It involves detailed comparisons of characteristic quantities that are not routinely measured in experiments. Simulations are divided into two classes:

Early-time simulations focus on the early stages of the dynamic explosion process, the propagation of a shock wave through the target and the projectile. These models focus on maximum shock pressure and its decay, internal energy, temperature, melting/vaporization and tracer particle histories during crater growth.

Late-time simulations focus on the late-time process, which involves the cessation of crater excavation and collapse of the impact crater. Here, a good strength model is important. Late-time model results will focus on the crater final morphology, tracer histories describing crater collapse, and stress/strain fields and their variations during crater collapse.

Initial results of our first benchmarking tests (Al into Al) were presented at the 38th Lunar and Planetary Science Conference last spring [11].

The Validation Testing: Validation testing involves the evaluation of hydrocodes through comparison of simulations with experiments that will provide stringent tests of the physical models used in the codes. The experimental test are drawn from laboratory studies of impact cratering and fragmentation and from large field tests of explosion cratering. Laboratory tests are useful because they are conducted under well-known conditions, although scale may influence the results. Field explosion tests are complementary in that they provide important data over a much larger range of sizes. It is important to consider as many aspects of the process as possible. A simulation must not only predict the correct final result, but also correctly reproduce the kinematics of the process, including material flow, ejection and stress levels. For this project experimental tests were selected to encompass as many observables as possible and to sample a wide a range of experimental conditions. They include tests in simple materials such as water and metal, and in more complex materials such as soil and rock.

Water tests are relatively simple. Simulations of impacts and explosions in water do not need a strength model and gravity only needs to be included to model the late stages of crater growth. Our first validation test consists in reproducing the Boeing quarter space laboratory experiment of a glass sphere, 2 mm in diameter, impacting water at 4.64 km/s [12]. This experiment used a quarter-space rectangular box made from 1-25 cm thick Al, 76cm×38cm×23cm in size (a thick plexiglass window was inserted close to the impact point for viewing purposes). The container was not affected by the test (no visible signs of deformation). Ambient chamber pressure was around 1-2×10^{-4} dyn/cm^2 (above the vapor pressure). Diagnostics measured during the experiment were: crater profile at given times (up to 83 msec), and ejection velocities of few small glass beads floating on the surface.

Preliminary Results: Simulations are carried out assuming a full impact simulation, i.e., the effects of the Al tank were not included. Fixed input conditions included the projectile size, impact velocity/angle, shape and material (glass), target material (water), and mesh size. Technical details (including resolution), material models and relative parameters for the materials were chosen by individual modelers. This is an important difference from the previous benchmark testing. Benchmark tests focus on comparing code performances given simple ideal tests. On the other hand, validation testing is also about testing the modelers identification and use of the proper models. One of our goals in this context is to verify how modelers' choices can affect the output results.

At this time there are several active simulations from different modelers. Codes for which we have some output results (currently most of them are still running the validation test) are: CTH, RAGE, iSALE, SOVA, ZEUSMP2.

In the early stages of impact codes appear to follow the experimental data quite closely, as shown in Fig. 1. A brief investigation of the early evolution of crater radius and depth with time shows a variability in results, compared to the experiments of less than 15%. CTH, iSALE and RAGE appear to follow the experimental data quite closely, with a maximum deviation of at most 8%. The SOVA simulation is still in a very early stage (with 2 diagnostic time steps covered so far). Simulations with ZEUSMP2 (heavily modified to model impact cratering) seem to develop instabilities beyond 2 msec. Suggested hypotheses for the problem are not optimal boundary conditions, problems at free surfaces or sharp material interfaces, problems with the Tillotson equation of state used.

Further results of our first validation test will be presented at the meeting.

This work is supported by NASA Grant NNX06AD65G.

References: [1] Sharp R. (2004) *UCRL-MA-152204 Rev.1*. [2] Century Dyn., Inc. (2003) *AUTODYN Theory Manual 4.3*. [3] McGlaun J.M. et al. (1990) *Int. J. Impact Eng., 10*, 351. [4] Lomov I., Rubin M.B. (2003) *J. Phys. IV, 110*, 281. [5] Gittings M.L. (1992) *Def. Nucl. Agency Num. Meth. Symp., 28-30 April 1992*. [6] Ivanov, B. A. et al. (1997) *Int. J. Imp. Eng., 17*, 375. [7] Wünnemann K. et al. (2006) *Icarus, 180*, 514. [8] Shuvalov V.V. (1999) *Shock Waves, 9*, 381. [9] Benz W., Asphaug E. (1994) *Icarus, 107*, 98. [10] Hayes et al. (2006) Astroph. J. Supp., 165, 188. [11] Pierazzo E. et al. (2007) *LPSC, 38*, Abs. #2015. [12] Schmidt R.M., Housen K.R. (1987) *Int. J. Imp. Eng., 5*, 543.

Figure 1: Crater profile for various codes at t=0.191 ms.

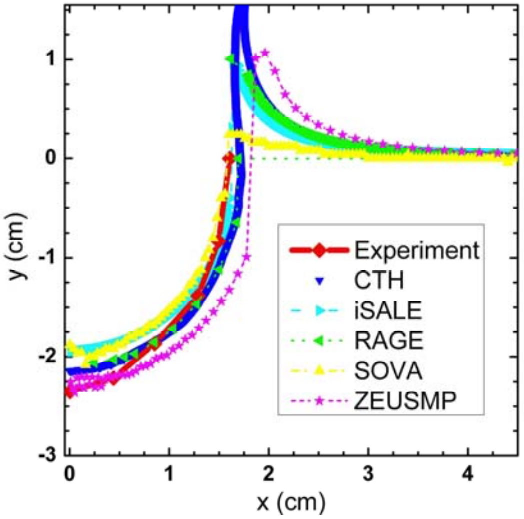

STRUCTURAL SIGNATURES OF OBLIQUE IMPACTS – INSIGHTS FROM FIELD OBSERVATIONS.

M. Poelchau, D. Elbeshausen, T. Kenkmann, K. Wünnemann. Museum für Naturkunde, Humboldt Universität Invalidenstr. 43, D-10115 Berlin, Germany. (michael.poelchau@museum.hu-berlin.de)

Introduction: It is well known that the majority of craters are formed by oblique impacts [1,2]. While vertical or near vertical impacts tend to show radial symmetry, it is expected that oblique impacts should exhibit deviations from radial symmetry in the form of asymmetric or bilateral patterns. For example, recent studies have shown that subsurface structures of the innermost crater interior do show preferential directions of folding and faulting that implicate a preferred transport direction and indicate the impact vector [3,4]. This is in agreement with 3D modeling of complex craters [5].

Ejecta blankets are even better indicators for impact angle and direction. The ejecta blankets of craters observed on other terrestrial bodies show a "forbidden zone" that develops uprange, and with increasing obliqueness also downrange, eventually resulting in a symmetrical "butterfly pattern".

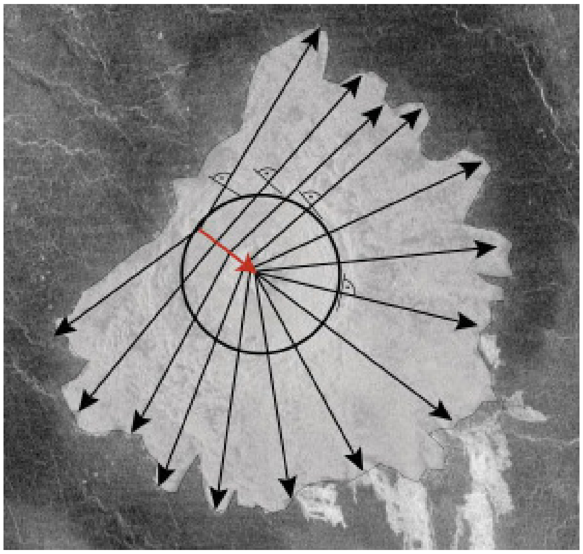

Fig. 1: Theoretical ejecta trajectories displayed in a modified Z-model, line source ejection, with resulting non-radial strike patterns. (Magellan Imaging Radar, Aurelia Crater, Venus.)

Trajectory model: We suggest that the ejecta trajectories that form these blankets deviate from radial symmetry and could probably be traced at the rim and overturned flap of simple craters, which represent the most proximal part of the ejecta. If we use a modified Z-model [6] to describe the mechanism of ejection with a line source that progresses from uprange to downrange during crater development, the resulting flow field should be bilaterally symmetric (Fig. 1). The strike of the folded strata should be orthogonal to the trajectories for originally horizontal bedding. Therefore the folded and uplifted bedding should show deviations from a concentrical alignment to the crater center and display bilateral patterns of strike.

Strike data was collected from Wolfe Creek Crater, Western Australia, a 0.3 Ma old simple crater with an average diameter of 880 m [7, 8]. Field data was compiled with previously published data [9] and translated from a geographic to an azimuthal reference scheme with the point of origin situated in the crater center. The strike of rock layers in the rim was examined for deviations from a hypothetical concentric orientation with regards to the crater center. The deviation is expressed as an angular value for each measurement and is displayed in a polar plot (Fig. 2).

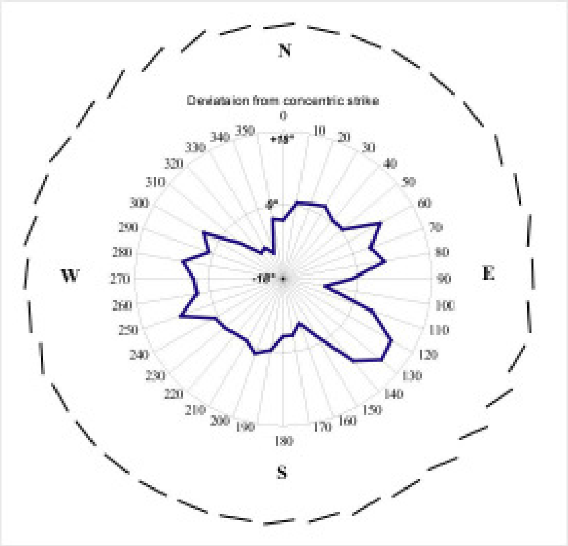

Fig. 2: Polar plot of proximal ejecta strike data displayed relative to crater center. Black lines surrounding the plot indicate average strike.

Strike data from the inner wall of the crater rim shows a strong connection to the rim morphology, whereas strike data of the proximal ejecta shows certain patterns that could indicate bilateral symmetry and might fit the model proposed above. In order to improve the interpretation of such data, 3D numerical models are needed. Currently, trajectories of tracer particles in oblique impacts are being modeled with a three-dimensional hydrocode [D. Elbeshausen et al., this volume]. We expect the results to greatly improve our understanding of the crater flow field, to show whether the modified Z-model is feasible, and to indicate if deviation from radial symmetry can be expected in the crater rim.

Dip in the crater rim: Dip data from Wolfe Creek was analyzed in a similar manner to the strike data. In an oblique impact more deformation is to be expected downrange due to downrange-directed particle motion [4, 10]. This could also have an effect on the amount of folding and uplift in different sectors of the crater wall and could be recognized in deeper dip values of originally horizontal layers. When converted to an azimuthal reference scheme, Wolfe Creek dip data shows a sector with relatively low dip angles, which could be interpreted as an uprange sector (Fig. 3).

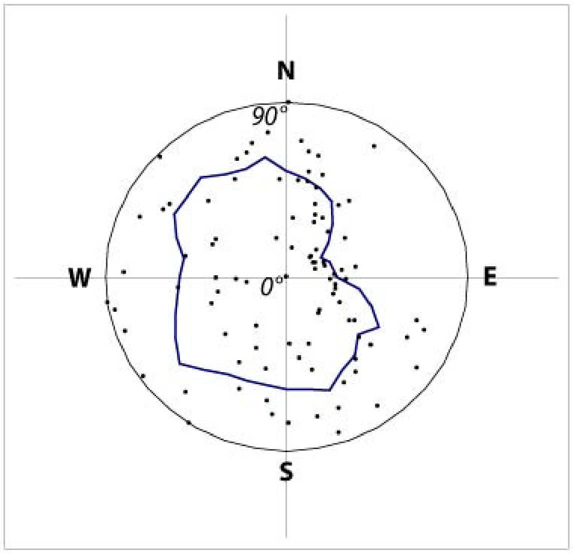

Fig. 3: Polar plot of dip data displayed relative to the crater center. Dip values are shallow in the ENE, which might indicate an impact direction.

Asymmetry in the central uplift: As stated in the introduction, central uplifts show asymmetric behavior and can be used to indicate an impact vector. We will continue research on central uplifts and have planned further fieldwork in Australia, which will focus on structural aspects in these features. One of our goals is to use our field results to enhance 3D numerical models [D. Elbeshausen et al., this volume], while at the same time utilizing these models to gain a better understanding of the formation processes involved in oblique impact cratering.

Conclusions: Through our method of analysis, we were able to display deviations from radial symmetry in field data collected at Wolfe Creek Crater. It is still uncertain to which degree these features are caused by a possible oblique impact. It may also be possible that pre-impact conditions like uneven bedding or joint sets, or post-impact processes like erosion have a strong effect on the symmetry of the final crater, and might even superimpose any structural signatures caused by the obliqueness of an impact. Thus 3D numerical models are of great importance for us. Modeling of particle trajectories could confirm or revise our current conception of the impact cratering flow field and in turn help improve our interpretation of field data, leading to a better estimation of the direction and angle of impact. We also hope to gain similar insights on the formation and structure of central uplifts.

Acknowledgements: We would like to thank the DFG for funding this project (KE 732-11/1).

References: [1] Gilbert, G. K. (1893) *Bull. Philos. Soc. Wash.,* 241-292. [2] Shoemaker, E. M. (1962) *Phys. And Astron. Of the Moon,* p. 283-359. [3] Scherler, D. et al. (2006) *Earth & Planet. Sci. Let.* 248, 43-53. [4] Schultz, P. H. & Anderson, R. R. (1996) *Geol. Soc. of Amer. Spec. Paper* 302, 397-417. [5] Shuvalov, V. V. et al., (2004) *MAPS* 39, 467-479. [6] Anderson, J. L. et al. (2004) *MAPS* 39, 303-320. [7] Hawke, P. J. (2003) *Geological Survey of Western Australia Record* 10, 1–9. [8] Shoemaker, E. M. (1990) *53rd Annual Meeting of the Meteoritical Society, Abstracts*, p. 409. Meteoritics 25. [9] Shoemaker, E. M. et al. (2005) *Australian Journal of Earth Sciences* 52, 529-544. [10] Gault D. E. and Wedekind J. A. (1978) *Proc. Lunar Planet. Sci. Conf.* 9: 3843-75.

Elbeshausen, D. et al. (2007) *Bridging the Gap II* (this volume).

PSEUDOTACHYLITIC BRECCIA DEVELOPMENT IN IMPACT STRUCTURES – STATUS OF RESEARCH IN THE VREDEFORT DOME (SOUTH AFRICA) AND BASIS FOR PROCESS MODELING.

W.U. Reimold[1] and R.L. Gibson[2], [1]Museum for Natural History, Humboldt University Berlin, Invalidenstr. 43, 10115 Berlin, Germany (uwe.reimold@museum.hu-berlin.de), [2]Impact Cratering Research Group, School of Geosciences, University of the Witwatersrand, Private Bag 3, P.O. Wits 2050, Johannesburg, South Africa (roger.gibson@wits.ac.za).

Introduction: "Pseudotachylite" is a volumetrically minor but relatively widespread clast-laden melt rock that most commonly occurs in cm-wide and dm-long veins in fault and shear zones. Its presence in these environments is attributed to cataclasis and frictional melting during high strain rate ($>10^{-1}s^{-1}$) coseismic slip. Together with the Sudbury area in Canada, the Vredefort region of South Africa is one of only two great "pseudotachylitic breccia" provinces in the world. It lies in the central parts of the geological Witwatersrand Basin, centered on the Vredefort Dome. Both the Sudbury and Vredefort-Witwatersrand breccia occurrences dwarf the individual and total volumes of melt breccia found at all occurrences of pseudotachylite around the world. This, and geological and geochronological evidence that, in both cases, links the formation of these breccias to major impact events, and the clear absence of any spatial links to faults and shear zones capable of generating such large melt volumes, has raised questions about the processes by which these breccias were formed. The Vredefort Dome itself was declared the type locality for *pseudotachylite* (i.e., friction melt *only*)[1]. These authors have challenged such a simplistic definition for the Vredefort breccias, pointing out that several different types of breccias can form during impact or be part of the target (impact melt, friction melt, cataclasite, ultramylonite). Consequently, they favor the non-genetic term *pseudotachylitic breccia*.

Witwatersrand pseudotachylitic breccias: Breccias exposed in the goldfields around the NW and W margin of the Witwatersrand basin range from decimeters to meters in thickness and are associated with wide cataclastic zones that display a more or less bedding-parallel orientation dipping towards the Vredefort Dome at shallow angles, or that are associated with subvertical faults generally radial to the dome. Although some evidence exists for the presence of some pre-impact pseudotachylite [2], the bulk of the breccias appear to be associated with the Vredefort impact event [3]. The inward-dipping faults appear to have been generated during normal dip-slip movement, and their scale and geometry are consistent with faults having formed during collapse of the transient crater by inward slumping of blocks off the crater wall. The radial faults appear to be, at least in part, older structures that were reactivated by impact-related block movement. In both cases, slip magnitude of hundreds of meters to perhaps as much as several kilometers, over at most a few minutes, provide the reasonable mechanism for the generation of such large breccia volumes by cataclasis and local friction melting. This far from the center of the impact structure no shock deformation effects have been observed and shock melting for the breccias can be precluded.

Melt breccias in the Vredefort Dome: Whilst the breccias in the Witwatersrand goldfields dwarf all known fault-related pseudotachylite occurrences in the world, they are, in turn, dwarfed both in terms of volume and abundance by the melt breccias in the Vredefort Dome. Within a 25 km radius of the center of the 90 km wide dome, few rocks are found that do not contain at least a small breccia vein, and veins remain common into the Ventersdorp Supergroup at 30-35 km from the center of the dome. Veins and lenses in the submillimeter to centimeter width range are associated with extensive, outcrop-scale fracture networks that sometimes display offsets (mostly mm to perhaps a few cm). Distinct relationships to fault or shear zones could only be rarely established. Relatively voluminous network breccias are found in a small number of roughly radial faults in the dome; however, similar "network breccia" outcrops are also observed entirely dissociated from faults. In addition, relatively voluminous breccia occurrences are found in the hinge zones of large radial folds. It is, thus, necessary to consider the possibility that the breccias in radial faults and folds were derived elsewhere and could have ponded in dilational sites. Wieland [4] speculated that, given the right degrees of superheating and shock-enhanced wallrock temperatures, mm- and cm-thick veinlets formed in either quartzite or shale host rock could have remained fluid for minutes, whereas thicker melt veins could have remained above their solidus T for up to several hours.

In the Archean gneiss core of the dome, several breccias reach widths of tens of meters and lengths of many hundreds of meters, and show no obvious links to shear zones commensurate with their size [5]. Petrographic analysis of thin veins in these rocks has shown that, whilst some evidence exists for cataclasis and displacement of mineral grains, the grains in the immediate walls of the veins are commonly marked by textures that are consistent with elevated shock pressures relative to the rest of the sample. Although recrystallization is strong owing to post-impact heating effects, the textures indicate transient fluidization of grains, either through the formation of mineral glasses or melts. We have shown that the rocks of the dome experienced background shock pressures between <10 GPa at r > 20 km to >30 GPa at r < 5 km, consistent with their proximity to the original point of impact. The textures along breccia veins are also clear evidence for the extreme heterogeneity of shock pressure at a local scale, and even at a scale of single grain diameters.

A similar scenario was proposed by Martini [6] who observed coesite and stishovite within and adjacent to thin melt veinlets in Witwatersrand quartzite in the outer dome. He speculated that thin melt breccia veins in the dome could be shock-induced melts resulting from explosive collapse of pre-impact joints during passage of the shock wave, or due to their activation as slip surfaces under shock compression owing to differential acceleration of their wall rocks. However, the existence of an intense joint set in all rock types of the dome, including those buried at mid-crustal depths prior to impact, appears unlikely.

Discussion: Several recent experimental and numerical modeling studies [7-9] of shock wave passage through heterogeneous materials have emphasized the heterogeneous nature of the shock wave, with large fluctuations of shock pressure caused by refraction- and reflection-induced interference. Kenkmann et al. [7] noted enhanced melt volumes along lithological interfaces, even where these were orthogonal to the shock propagation direction. Heider & Kenkmann [9] predicted that *in situ* veins would also form oblique to a plane of heterogeneity due to refraction of shock waves. Whilst slip is also possible as a result of differential acceleration of the wallrocks on either side of the plane of heterogeneity, an alternative explanation for at least some of the slip observed along Vredefort vein-fracture networks is that the fractures related to shock melting acted as slip surfaces for the brief period before crystallization or quenching of the melt. We believe that (many of) the most voluminous veins and dikes in the Vredefort dome could represent melts ponded in dilational sites that opened as the result of the structural disturbance accompanying central uplift formation immediately after passage of the shock wave and, more specifically, the late-stage collapse of the central uplift. Generation of the melts could involve either (or both of) decompression melting upon uplift or shock melting immediately after shock passage. Naturally, the rapid acceleration of large rock volumes does allow for the formation of a friction melt component, too, although the absence of suitably large faults in the dome remains problematic for such a mechanism..

Our model of shock melting with or without a friction melting component not only removes one of the biggest problems of pseudotachylitic breccia formation in an impact structure setting, namely how a slip zone can continue to generate melt once the first melt has formed and lubricates the slip surface. It also explains the staggering volume of melt found in the Vredefort Dome rocks in the absence of evidence for large-slip magnitude structures in the central uplift. The current studies of Lieger et al. and Mohr et al. [both this volume] attempt to further improve the meso-scale to microscopic data base on volumetry and geometry of pseudotachylitic breccias in different lithologies and their relationship to other parameters, including lithological contrasts (shock impedance), fracture density, relative timing of fracturing and breccia formations related to the impact.

Conclusion: With the detailed field and petrographic analysis of recent years and the current reinvestigations by Lieger et al. and Mohr et al. a basis will soon be available for comprehensive numerical modeling of the formation of pseudotachylitic breccias under shock compression and/or as a result of shock and friction melting. Once the likely processes upon breccia formation are fully understood, the cooling behavior of such impact-generated melts can also be refined through consideration of additional parameters such as clast content in different ambient environments (greenschist and amphibolite facies).

References: [1] Reimold W.U. and Gibson R.L. (2005) Impact Tectonics, Springer Publ., 1-53. [2] Reimold W.U. and Colliston W.P. (1994) GSA SP 293, 177-196. [3] Reimold W.U. and Gibson R.L. (2006) Chemie der Erde 66, 1-35. [4] Wieland F. (2006) PhD Thesis, Univ. of the Witwatersrand, Johannesburg, RSA. [5] Dressler B.O. and Reimold W.U. (2004) Earth-Sci. Rev. 67, 1-54. [6] Martini J.E.J. (1991) EPSL 103, 285-300. [7] Kenkmann T. et al. (2000) MAPS 35, 1275-1290. [8] Langenhorst F. et al. (2002) MAPS 37, 1541-1553. [9] Heider N. and Kenkmann T. (2003) MAPS 38, 1451-1460.

A MODEL TO DETERMINE COMETARY PROPERTIES FROM THE EJECTA PLUME BEHAVIOR RESULTING FROM DEEP IMPACT.

J. E. Richardson[1] and H. J. Melosh[2], [1]Center for Radiophysics and Space Research, 310 Space Sciences Building, Cornell University, Ithaca, NY 14853, richardson@astro.cornell.edu; [2]Lunar and Planetary Lab, University of Arizona, Tucson, AZ 85721. jmelosh@lpl.arizona.edu.

Introduction: On July 4, 2005, the Deep Impact mission successfully collided a 366 kg impactor with the surface of 6 km diameter Comet 9P/Tempel 1, at an oblique angle of about 56^o from the regional surface normal and a collision speed of 10.2 km sec^{-1} [1]. This impact produced a cratering event which was directly observed by a flyby-spacecraft which passed within 500 km of the comet, in two viewing windows: an approach phase of observations, made from 0 to 800 seconds following the time of impact; and a look-back phase of observations, made from 45 to 75 minutes following the time of impact [2]. The solid-particle ejecta plume produced by this cratering event rapidly emerged from the impact site and expanded to form a highly visible, cone-shaped cloud of launched particles, which dominates many of the subsequent images. This prominent plume remained visibly attached to the comet's surface as it rapidly extended longitudinally (away from the comet's surface) and expanded laterally (along the comet's surface) over the course of the observations made by the flyby-spacecraft.

Project Goal: During the first 800 seconds following the impact, the hollow interior of the ejecta plume was viewed as the flyby-spacecraft approached the comet. During the look-back phase of observations, 45-75 minutes following the impact, the conical exterior of the ejecta plume was viewed as the spacecraft departed the comet [2]. These later, look-back images permit measurements of the ejecta plume's lateral expansion rate over a time span of nearly half an hour, and thus provide a quantitative means for estimating the magnitude of Tempel 1's gravity field. This is because the observed ejecta plume consisted of billions of tiny ejecta particles, each one following its own ballistic trajectory under the influence of Tempel 1's gravity field, and as such, the lateral expansion rate of the collective ejecta plume is also a function of the comet's gravity field [3]. When coupled with a shape model for comet Tempel 1 [4], a reasonable gravity estimate also permits an estimate of the comet's mass and bulk density.

The Model: This gravity estimate for Tempel 1 is made by developing a first-order, three-dimensional, forward model of the cratering event's ejecta plume behavior [5], and then adjusting the parameters of this model (over many iterations) to match the spacecraft observations of the actual plume behavior, image by image (Figs. 1 & 2). This forward model is, in turn, based upon the Maxwell Z-model [6] and Pi-Group scaling relationships [7,8,9] for cratering events. In addition to gravity and density estimates for comet Tempel 1, this model also permits us to estimate the particle velocity distribution and total mass ejected by the impact, and obtain a rough estimate of the comet surface's effective strength at the impact site.

Results: This modeling exercise reveals that Deep Impact produced a reasonably "well-behaved" oblique-impact cratering event: one in which the impactor-spacecraft apparently struck a small, westward-facing slope of roughly 1/3-1/2 the size of the final crater produced (determined from initial ejecta plume geometry), and possessing an effective yield strength of not more than Y = 1-10 kPa (estimated via two different methods). The resulting ejecta plume followed well-established scaling relationships for cratering in a medium-to-high porosity target material, consistent with a transient crater of not more than 85-140 m diameter, formed in 250-550 sec, for the case of $Y = 0$ Pa (gravity-dominated cratering), and not less than 22-26 m diameter, formed in 1-3 sec, for the case of $Y = 10$ kPa (strength-dominated cratering). At $Y = 0$ Pa, an upper limit to the total ejected mass of 1.8×10^7 kg ($1.5\text{-}2.2 \times 10^7$ kg) is consistent with measurements made via long-range remote sensing, after taking into account that 90% of this mass would have stayed close to the surface and then landed within 45 minutes after the time of impact. However, at $Y = 10$ kPa, a lower limit to the total ejected mass of 2.3×10^5 kg ($1.5\text{-}2.9 \times 10^5$ kg) is also consistent with the remote sensing measurements: making this result somewhat ambiguous. The expansion rate of the ejecta plume imaged during the look-back phase of observations leads to an estimate of the comet's mean surface gravity of $g = 0.34$ mm sec^{-2} (0.17-0.90 mm sec^{-2}), which corresponds to a comet mass of $m_t = 4.5 \times 10^{13}$ kg ($2.3\text{-}12.0 \times 10^{13}$ kg) and a bulk density of $\rho_t = 400$ kg m^{-3} (200-1000 kg m^{-3}), consistent with the bulk densities estimated for other cometary nuclei, and where the high-end error is due to uncertainties in the magnitude of coma gas pressure effects on the impact ejecta particles in flight.

References: [1] A'Hearn, et al (2005). *Science*, **310**, 258-264. [2] A'Hearn, et al (2005). *Space Science Rev.*, **117**, 1-21. [3] Melosh, J.H. (2001). *32nd Lunar & Planetary Sci. Conf.*, 2135. [4] Thomas, P.C., et al (2007). *Icarus*, **187**, 4-15. [5] Richardson, J.E., et al (2005). *Space Science Rev.*, **117**, 241-267. [6] Maxwell D. & Seifert K. (1974) *Report DNA 3628F, Defense Nuclear Agency*, Washington, D.C. [7] Holsapple, K.A. (1993). *Annual Rev. Earth and Planetary Sci.*, **21**, 333-373. [8] Housen, K.R., et al (1983). *J. Geophys. Res.*, **88**, 2485-2499. [9] Richardson, J.E. (2007). *38th Lunar & Planetary Sci. Conf*, 1345. [10] Lisse, C.M. et al (2006). *Science*, **313**, 635-640.

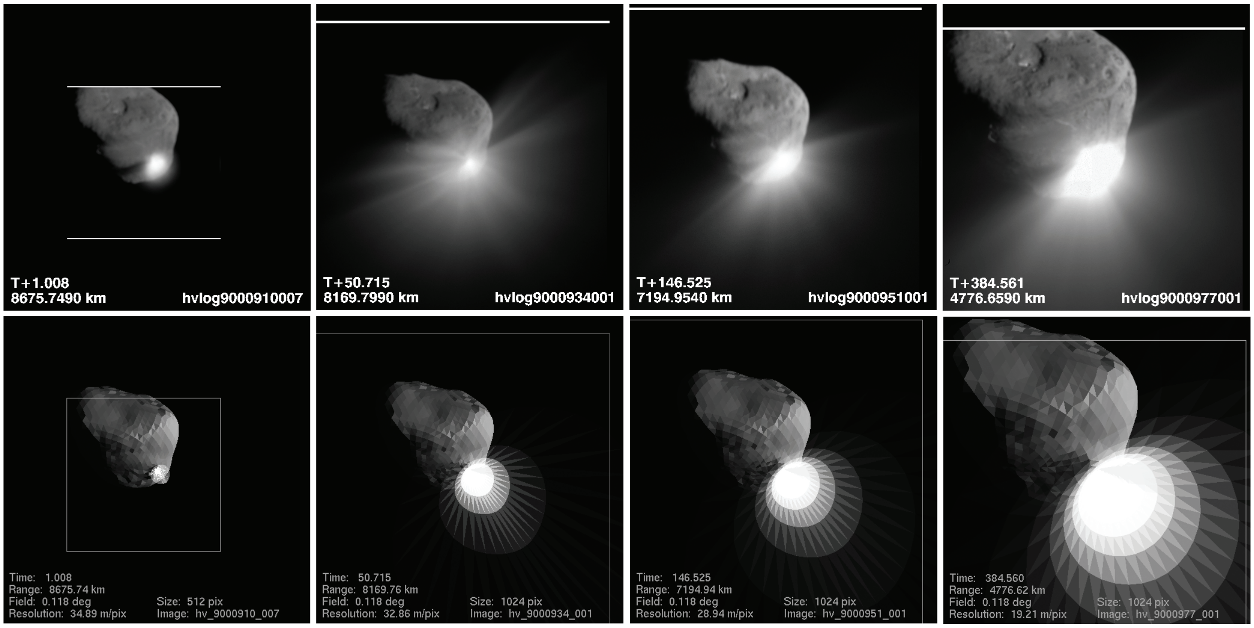

Figure 1: Deep Impact image sequence, part 1: a comparison between the actual HRI image sequence (*Upper Images*) and the best-fit modeled image sequence (*Lower Images*), using a Spitzer-based particle size distribution [10]. The two pairs of images on the left show the early interior view of the ejecta plume (phase 1), while the two pairs of images on the right show a near edge-on view of the plume's west (upper left) side (phase 2).

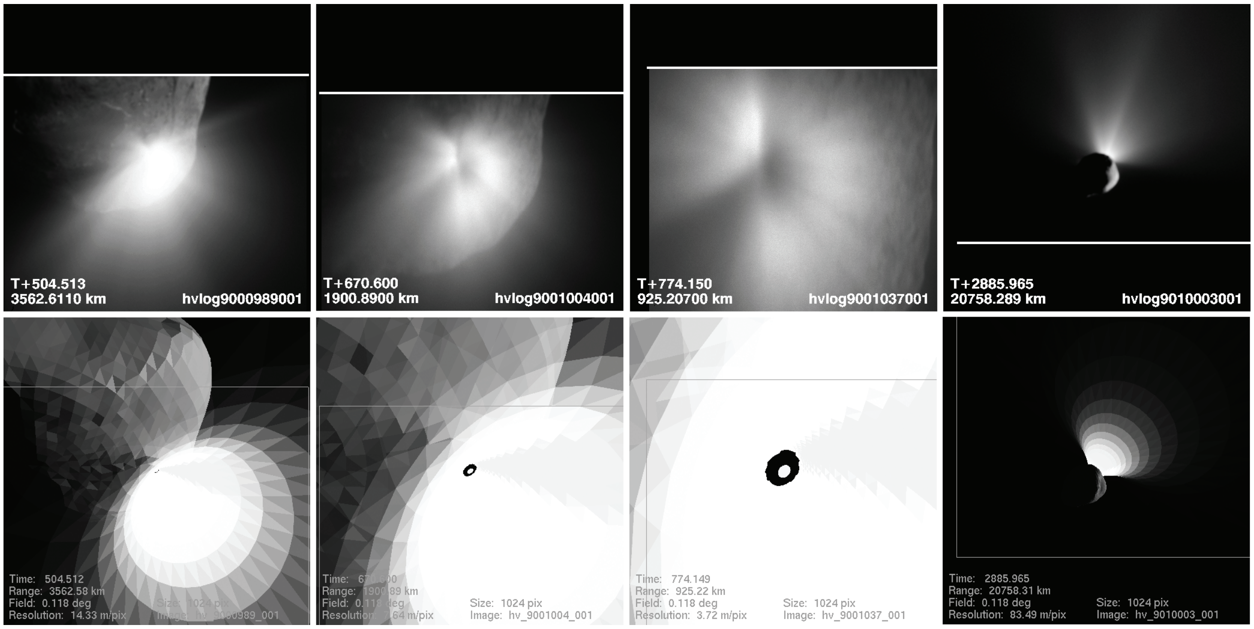

Figure 2: Deep Impact image sequence, part 2: a comparison between the actual HRI image sequence {*Upper Images*) and the best-fit modeled image sequence (*Lower Images*). The first pair of images on the left show the beginning of the transition from an edge-on view of the plume's west side (phase 2) to the late interior view of the plume's dark, oval base (phase 3), shown in the middle two pairs of images. The small grey circle near the center of the middle two synthetic images marks the impact crater, which the actual (upper) images failed to resolve due to obscuring dust. The final pair of images on the right show the beginning of the look-back phase of observations (phase 4).

KINEMATIC EVOLUTION OF THE SUDBURY BASIN INFERRED FROM SCALED ANALOGUE MODELLING AND STRUCTURAL GROUND TRUTH.

U. Riller[1], D. Boutelier[2], A.R. Cruden[2] and C. Schrank[2], [1]Museum für Naturkunde, Invalidenstrasse 43, Germany, ulrich.riller@museum.hu-berlin.de, [2]University of Toronto, Department of Geology, 22 Russell St., Toronto M5S 3B1, Canada.

Objectives: Crustal-scale domes and basins are ubiquitous, yet kinematically poorly understood structural elements in orogenic belts of all ages. This pertains also to the Paleoproterozoic Eastern Penokean Orogen of the southern Canadian Shield hosting the Sudbury impact structure, the central portion of which is the 60 km x 26 km Sudbury Basin. The Basin is delineated by the deformed, synformal Sudbury Igneous Complex (SIC), the relic of an impact melt sheet that is overlain by impact melt breccia, the Onaping Formation, and post-impact sedimentary rocks. In order to assess the distribution and orientation of imact-induced structures and lithologies in terms of the cratering process, the kinematics of post-impact deformation and mechanism of large-amplitude, non-cylindrical folding of the SIC needs to be understood [1]. Therefore, we conducted a series of scaled analogue experiments using viscous and granular materials, which are compared with structural ground truth of the Sudbury Basin.

Method: The experimental set-up of analogue models consists of a rectangular tank filled with layers of corn syrup, polydimethylsiloxane (PDMS), PDMS blended with plasticene and various fillers, and granular materials with Mohr-Coulomb rheology. These layers represent respectively the lithospheric mantle, lower crust, middle crust and sedimentary cover rocks. Bulk horizontal shortening of the layers is imposed by a piston moving at a constant rate.

Observations: Analogue modelling shows that deformation style depends strongly on the distribution and thickness of sedimentary cover rocks, the mechanically strongest layer in the system. More specifically, the wavelength and amplitude of folds in the middle crust increase with decreasing thickness of the sedimentary cover. Thicknesses of cover rocks exceeding 10 km in nature significantly inhibit the formation of mid-crustal folds. Moreover, reverse faults and thrusts in the sedimentary cover generally nucleate in the hinge zones of mid-crustal model synforms.

The importance of sedimentary cover rocks in controlling the style of mid-crustal folds and the localization of thrust faults is well evident in the Sudbury area. Here, the impact removed a 10 km thick sequence of Huronian cover rocks, thereby exhuming mid-crustal granitoid basement rocks in a circular area ~ 130 km in diameter. Omission of granular material in an equivalent area in the model induced a pronounced mechanical inhomogeneity of the model crust.

Analogue modelling of post-impact deformation of the model impact structure and its environs generated remarkable geometric and kinematic similarities with the natural prototype. These include the formation of a non-cylindrical basin consisting of a larger, shallowly dipping flank, on the opposite side of the piston, and a smaller, steeply dipping flank of the free surface of the model basement rocks. The flanks correspond respectively to the North Range and the South Range of the SIC in nature. Furthermore, a prominent reverse fault nucleated in the hinge zone of the deformed model impact structure and displaced the steeper flank over the shallowly dipping one. This zone corresponds spatially and kinematically to the South Range Shear Zone, well known from the surface structure of rocks and geophysical imaging. Finally, the geometry of higher-order discontinuities outside the model impact structure corresponds well with mineral fabric and fault patterns in equivalent positions of the natural prototype.

Results: Analogue modelling indicates that the geometry of the South Range Shear Zone and mineral fabric patterns in the Sudbury Basin are due to the crustal-scale mechanical inhomogeneity created by impact. More specifically, the shear zone formed as a consequence of deformation of the SIC and does not seem to have accomplished displacements larger than a few kilometres in nature. This places significant limits as to the estimated volume of the Onaping Formation contained within the Sudbury Basin. Moreover, the North Range was affected largely by rigid rotation indicating that impact-induced structures such as pseudotachylitic breccia zones, faults and shock-metamorphic features, although locally rotated up to 40°, were not distorted by post-impact deformation. Collectively, these kinematic characteristics of post-impact deformation are critical for estimating the original size of the Sudbury impact structure.

Scaled analogue experiments using viscous and granular materials provide a significant step forward in understanding the dynamic evolution of crustal structures such as the Sudbury Basin.

References: [1] Riller U. (2005) *Meteoritics & Planet. Sci., 40,* 1723-1740.

ICE-PENETRATING IMPACTS: INSIGHTS FROM HYPERVELOCITY IMPACT EXPERIMENTS AND GALILEO IMAGE MAPPING OF EUROPA

Kate C. Scheider and Rónadh Cox, Department of Geosciences, Williams College, Williamstown MA 01267; *rcox@williams.edu*

Introduction: Where an ice crust overlies water, as it seems to on Europa, some impactors may breach it completely. Chaos areas may provide a record of such events. Hypervelocity impact experiments at the NASA Ames Vertical Gun Range (AVGR) reveal some of the mechanics of ice-penetrating impacts; and combined with crater-count data from high-resolution images (<50 m/pixel) surrounding the large chaos area Thera Macula, provide an initial model for the geomorphologic expression of penetrating impacts.

Impact experiments: We report the results of two AVGR experiments. Impact velocities were 5.5 and 5 km/sec, and the targets consisted of ice plates (70 cm^2, 2.3 and 1.5 cm-thick respectively) overlying 25 cm of water in a tank 81 cm^2 x 40 cm deep. Both shots overwhelmed the target container and therefore edge effects are a problem: the design of future experiments will be modified to address this. But the data—from 1000 frame/sec imagery of the impacts—provide useful initial information about the ejecta dynamics.

Immediately on impact, an inverted ejecta cone formed at 60° to the target surface. Simultaneously, radial and concentric fractures propagated through the ice. The base of the ejecta cone was displaced upward by growth of a cupola [1] of water and spalled ice, which thereafter dominated the event sequence. Smaller fragments at the top of the cupola traveled at 80-90° up through the ejecta cone. As the cupola expanded, bulging water pushed the ice up and outward from beneath. The breaking ice hinged along concentric fractures, creating plates of successively larger sizes as the hinging progressed outward. Radial fractures were so widely spaced at distance from the impact site that the outermost spall plates were too large to be ejected; instead, they fell back, fracturing into smaller plates on impact with the water. The sides of the cupola evolved to form an ejecta curtain with angles 60-90° before collapsing. As the cupola disintegrated, a water spout (the central peak [2]) formed, and reached ≈0.75 m height before collapsing, generating gravity waves on the water surface.

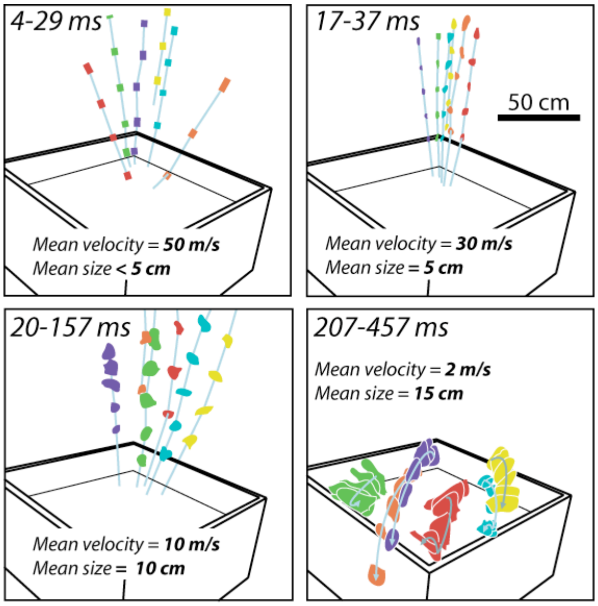

Fig. 1: Trajectories, average velocities, and average sizes for representative ejecta. Time range in each panel is in milliseconds post-impact, and the average velocity and average size (maximum dimension) for the measured population is given in each case. The ejection velocity decreased and the ejecta size increased with time. The maximum ejection velocity, in the earliest stages, was only ≈1% of the impact velocity; and the lowest ejection angles were ≈60°.

Ejecta velocities were low: the fastest moving fragments traveled at ≈50 m/sec, only 1% of the impact velocity (Fig. 1). In contrast, ejecta from hypervelocity crater-forming impacts into solid ice targets travel at 66-90% of the impact velocity [3], and those into porous ice or ice-silicate travel at 20-50% [4]. The maximum ejection angle $V_{e\ max}$ was almost 90° for the fastest-moving and smallest fragments, and even the lowest angles were close to 60° (for the late, slow-moving spall plates). Again, these contrast strongly with both solid ice ($V_{e\ max}$ 14-68° [3]) and porous ice targets ($V_{e\ max}$ 30-50° [4]). These results are consistent with hydrocode modeling, which predicts slower-moving ejecta for ice-penetrating impacts [5]. Ejecta landed both on the exposed water surface and outside the impact zone. Fragments landing on the water were tossed by waves, reoriented, and in some cases tilted.

Implications for planetary impacts: If ice-penetrating impacts puncture the crust and expose an underlying ocean, then the impact site will look nothing like a crater. Rather, it may resemble a jagged-edged hole, with ejecta fragments sitting in a matrix of refrozen liquid [6, 7]. The hole will be surrounded by a secondary impact field; but because V_e is so much lower than from impacts into solid ice, the secondary craters will be much smaller than those associated with non-penetrating impacts of the same energy. And because the ejection trajectories are so much steeper, (a) a large proportion of the ejecta will land within the impact site, potentially forming rafts in the exposed liquid; and (b) the radius of the secondary field will be smaller than for a comparable solid-target impact.

Chaos areas on Europa are candidates for ice-penetrating impact sites: Chaos areas are sites where the ice crust has been destroyed, and where liquid was exposed and mixed with pieces of the fragmented ice crust before freezing. Most chaos areas approximately equidimensional, with abrupt edges; and low-velocity impact experiments show that penetrating impacts produce morphologic outcomes with many of the features of chaos terrain [6, 7]. If chaos areas do represent impact sites, then they should have secondary crater fields associated with them.

Resolving secondary crater fields for ice-penetrating impacts: Although the secondary fields about large impact sites such as Pwyll and Tyre are clearly visible in the regional images of resolution 150-300 m/pixel, this is because the median crater size in these fields is of order ≈1 km [8, 9]. Reliable feature recognition drops off rapidly below 4 pixels diameter; and secondary-crater fields are not resolvable around smaller impact craters on Europa for this reason. Likewise—because of the order of magnitude difference in ejection velocity and factor of 2-3 difference in ejection angle—the much smaller secondary craters from penetrating impacts are therefore unlikely to be evident at regional imaging scales. Mapping such fields requires high-resolution images (<100 m/pixel).

Mapping secondary craters around Thera Macula: No large chaos areas (with the exception of Conamara Chaos, which lies within the Pwyll secondary crater field) are imaged at better than 250 m/pixel; but as luck would have it, there are three high-resolution mosaics distributed evenly around Thera Macula (Fig. 2) which—while they are not sufficiently extensive to allow us to fully map a secondary crater field—allow us to test whether small craters are distributed preferentially with respect to the chaos area [7].

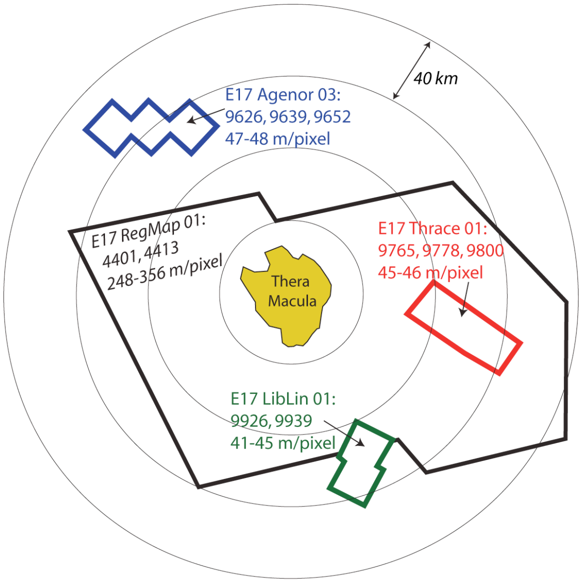

Fig. 2. Distribution of Galileo images in the Thera Macula region. Circles show distance from Thera's centre in 1-radius increments. The outlines of the regional images and of the high-resolution image mosaics are shown. The data in Fig. 3 were derived only from the three high-resolution mosaics. Colours keyed to Fig. 3.

Small-crater densities decrease exponentially as a function of distance from the centre of Thera (Fig. 3), suggesting that Thera is the source of the impactors. We do note, however, that because of the restricted high-resolution coverage, these data represent only ≈8% of the area between 3 and 7.5 Thera radii.

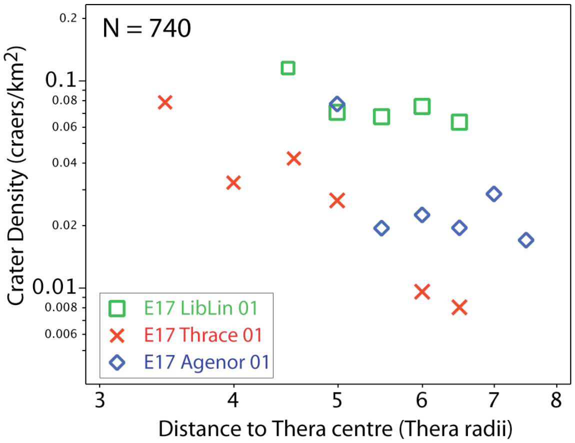

Fig.3. Crater densities mapped from high-resolution (41-48 m/pixel) image mosaics in the vicinity of Thera macula, as a function of distance from the chaos area centre. The decrease in small-crater density away from Thera's centre suggests that Thera is the source of the crater-forming debris.

If chaos areas do represent impact sites, their secondary crater fields will not be mappable on the current image database. Thera, at ≈80 km equivalent circle diameter, is more one of the largest chaos areas on Europa, more than 3 times larger than Pwyll and twice the size of Tyre. But the median size of small craters on the high-resolution images is only 400 m: less than half the size of the Pwyll and Tyre secondary craters. Impact experiments will continue to expand our understanding of impacts into layered ice-water systems, but resolving these features on Europa needs better image coverage than we presently have.

References: [1] Ormo J. et al. (2006) *Meteoritics and Planet. Sci. 41*, 1605-1612. [2] Gault D. E. and Sonett C. P. (1982) *Geol. Soc. Amer. Spec. Pap. 190*, 69-92. [3] Arakawa M. (1999) *Icarus 142*, 34-45. [4] Arakawa M. et al. (2002) *Icarus 158*, 516-531. [5] Moore J. M. et al. (1998) *Icarus 135*, 127-145 [6] Cox R. et al. 2005 *LPS XXXVI, Abstr. # 2101*. [7] Cox R. et al. (in press) *Icarus*. [8] Bierhaus B. 2006 *Workshop on Surface Ages and Histories: Abstr. #. 6028*. [9] Bierhaus B. et al. 2005 *LPS XXXVI, Abstr. #. 2386*.

IMPACT CRATERING IN SOFT SEDIMENT LAYERS.

P. H. Schultz, Brown University, Box 1846, Providence, RI 02912, peter_schultz@brown.edu

Introduction: Soft sediments cover much of the Earth and Mars, ranging from a few meters to 1km in thickness. While soft sediment impacts are widely studied in laboratory-scale experiments, there are few preserved examples on the Earth that allow direct comparison at large scales. One exception is the vast depositional loess deposits in Argentina that date back to the Miocene [1, 2]. Detailed petrologic studies reveal enhanced melting yet shocked minerals similar to crystalline basement rocks but at a scale of tens of microns [3,4].

The present contribution addresses the effect of unconsolidated sedimentary layers on the morphology of eroded impact structures, buffering of shock effects, and comparisons with relict structures to estimate the amount of missing sequences. Hypervelocity impact experiments were used to asess the effect of low-impedance surface layers on crater diameter, substrate damage, and soft-sediment compression. The resulting craters are compared with much larger structures on Mars with possible implications for larger terrestrial craters formed in easily eroded target materials.

Experimental Studies: Hypervelocity impact experiments at the NASA Ames Vertical Gun Range used porous sand and plasticene layers of different thicknesses over an aluminum plate for impacts at different angles. In addition, craters into pumice targets with layers at different depths were differentially eroded in order to assess the sensitivity to and expression of relict features.

Vertical impacts (90°) into the sand-over-aluminum target easily penetrated the low-impedance surface layer. Even though the crater bottomed-out at the substrate surface to form a diameter:depth ratio of 15:1, crater diameter in the surface layer remained unaffected until the layer depth (h) was reduced to less than three times the projectile diameter (a) as shown in Fig. 1. In this case, crater diameter and depth for gravity-controlled growth are not simply related but are decoupled, except for extremely thin layers. This appears to be the result of isolated shear (within a plane due to decreased coefficient of friction).

Decoupling crater diameter and depth reflects different processes controlling each dimension. While shock rarefaction off the free surface of the target controls crater diameter in loose particulates, projectile penetration affects crater depth. Penetration is limited by shock rarefactions in the projectile (both from the top and laterally) that decelerate and disrupt it until dynamic resistance (yield strength) limit further travel [e.g., 5]. Consequently, lateral crater growth in a low-impedance (low strength) surface layer can be limited by gravity while penetration is limited by both the shock transferred from the low-impedance veneer to the substrate and the residual momentum of this impactor (and compressed target material).

High-speed imaging and 3D-PIV techniques demonstrate that ejection angles and velocities of particulates from the veneer are not significantly different from values for impacts into a target composed of just the veneer. For example, ejection angles for sand over aluminum remained close to 48° (from the horizontal), comparable to the nominal 45° for a half-space experiment using just sand. Most collisions on planetary surfaces, however, are not vertical. Oblique impact experiments reveal that crater diameters for impacts at an angle of 45° are unaffected as h/a approaches 1. Impact angles less than 15° push h/a to less than 0.5 when the projectile fails and couples most of its energy to the target by ricocheting debris before significant penetration [6].

A low-impedance surface layer also can significantly reduce damage to the underlying competent substrate. Vertical hypervelocity impacts (90°) penetrate low-impedance layers and excavate the substrate until the depth of the final crater in the layer approaches the excavation depth, which is about 50% of the final crater depth.

Surface layers more effectively shield the subsurface during oblique impacts. Shielding is a corollary to the increased coupling to the surface layer, as indicated by reduced effects on crater diameter with smaller values of h/a (Fig. 1). Three processes contribute to reduced damage in the substrate. First, peak pressures directed downward in the target below the impact point are reduced by the vertical velocity component, as expressed by crater scaling [7], target damage [8], and peak shock pressures [9-11]. Second, the substrate is shielded from damage due to the reduced transmission of the shock from a low-impedance to a high-impedance material. Third, reflection of oblique shocks from interfaces reduce the peak pressures transmitted below. These three processes can decouple diameter and depth, provided that the surface layer does not have such a low impedance that the projectile penetrates through it unabated. The first two processes combined predict that a 5 km/sec at 30° into a layer of sand over an aluminum plate would cause damage to the plate as if it were an impacted directly at a velocity of less than 1 km/s.

Experiments with impacts into compressible particulates (such as pumice dust or loess) produce highly compacted materials beneath the floor. These compressed floor "plugs" can be removed intact following the impact experiments. When nearly completely eroded away, only small mounds of compressed dust (and melt) remain.

Implications and Tests: On Earth, impacts into thick deposits of loess or ice would be effectively destroyed. Impact craters on Mars, however, provide large-scale tests for the resulting expressions in eroded sedimentary sequences. Fluvial and eolian processes have produced thick, layered, unconformable sequences with significant accumulations around both poles, Arabia, and Medusa Fossae Formations [12]. Extremes in orbital forcing currently result in the cyclic redistribution of volatile-rich deposits. As a result, unusual crater relicts remain, including “pedestal craters” and inverted crater (circular mesas and knobs). “Pedestal craters” here refer to impact structures situated on a plateau with outward facing scarps.

Mechanisms proposed to account for pedestal craters at high latitudes include ejecta covering volatile-rich substrate [12], impact-generated winds [13], and an impact-heated atmosphere that results in melting and cementation of the ejccta [14]. These are not mutually exclusive models; rather, they apply in different environments and at different scales.

An outward-facing scarp develops as the underlying soft (volaitel-rich) sediment back-wastes the ejecta toward the crater rim. In extreme cases, only the crater floor (or exposed subfloor) remains, thereby leaving an inverted crater, i.e., the floor (rather than the rim) stands in relief above the deflated surroundings. In some regions, cycles of deposition filled the central crater and form resistant layers.

Secondary craters also can form inverted topography. For example, secondary chains from the crater Lyot extend into the northern plains but remain as inverted topography (elongated, rimless mounds or chains of hummocky material) [15]; similar inverted secondaries are well documented around the crater Mie near the Viking 2 landing site [16]. Regions that exhibit such crater relicts also exhibit anomalous crater size-frequency distributions: extremely young ages (Amazonian) based on small craters but very old (Noachian) based on large craters. They also typically have numerous small mounds superimposed across nearly all but the youngest large craters. The number density of these small mounds is consistent with the number of missing craters inferred from crater statistics. Consequently, very young surface ages for some regions on Mars may reflect exhumation ages (rather than unit ages) similar to the terrestrial record.

References: [1] Schultz P. H., et al. (2004), *Earth and Planet. Sci. Letts, vol. 219,* 221-238; [2] Schultz P. H. et al. (2006), *Meteoritics and Planetary Science,* 41, 749-771; [3] Harris R.S., Schultz P.H., and Bunch T.E. (2005), *Lunar Planet. Sci. Conf., XXXVI*, Abstract 1966; [4] Harris R.S. and Schultz P.H. (2005) in *SEPM Research Conference: The Sedimentary Record of Meteorite Impacts*, pp. 18-19; [5] Anderson Jr., C.E. and Orphal D.L. (2003), *Int. Jrnl. Impact Eng.* 29, nos. 1-10: 69-80; [6] Schultz P.H. and Gault D.E. (1990), In *Geol. Soc. of Amer. Special Paper 247*, 239-261; [7] Gault D.E., and Wedekind J.A. (1978), *Proceedings Lunar Planet. Sci. Conf. 9th*, 3843-3843-3875; [8] Schultz P.H. and Anderson R.A. (1996) *Geol. Soc. of Amer. Special Paper* 302, Boulder, CO.; [9] Dahl J.M. and Schultz P.H. (1998) *Lunar Planet. Sci. XXIX*, LPI, Houston, TX, 1958; [10] Dahl J. M. and Schultz P. H. (2001), *Int. Jrnl. Impact Eng.26,* 145-155; [11] Pierazzo E. and Melosh H. J., (2000), *Meteoritics and Planetary Science 35*, 117-130;[12] Schultz P.H. and Lutz A.B. (1988), *Icarus 73*, pp. 91-141; [13] Schultz P.H. (1992), *J. Geophys. Res.*, *97*, E7, 11,623-11,662; [14] Wrobel K., Schultz P. H., Crawford D. (2006), *Meteoritics & Planetary Science*, vol. 41, 1539-1550; [15] Schultz P. H. and Mustard J. F. (2004), *J. Geophys. Res.*, *vol.109*, E01001, doi: 10.1029/2002JE002025; [16] Thomson B. J. and Schultz P. H. (2007), *Icarus* (in press).

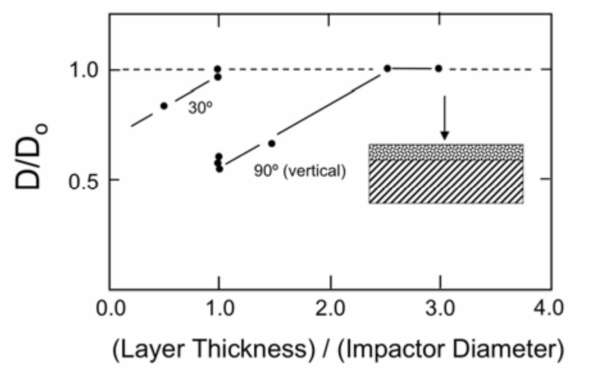

Figure 1: Effect of surface layer of loose sand (No. 24 represented by granular pattern) over 2024 aluminum (diagonals) on crater diameter (D) scaled to the diameter formed totally in sand. All impact speeds are 5 to 5.5 km/s (0.318 cm to 0.635 cm Pyrex). Surface layer has little effect on crater diameter for oblique impacts (30°) until the layer approaches the diameter of the projectile, even though the crater depth is reduced to a projectile diameter with minimal damage to the substrate. Such experiments suggest that oblique impacts into soft sediments may be efficiently eroded, leaving little trace except perhaps a shock-lithified floor.

COMPARING LABORATORY AND HYDROCODE EXPERIMENTS FOR OBLIQUE IMPACTS INTO SPHERICAL TARGETS.

P. H. Schultz[1] and D. A. Crawford[2], [1]Department of Geological Sciences Brown University, Box 1846, Providence, RI 02912; [2]Sandia National Laboratories, MS 0836, P. O. Box 5800, Albuquerque, NM 87185 (dacrawf@sandia.gov)

Introduction: In spherical targets, intersecting shocks and rarefactions off the free surface result in multiple failure planes deep inside the opposite side (antipodal). With increasing specific energy (well below catastrophic disruption), antipodal convergence can result in spallation off the opposite side of the sphere (see Figure 1). While PMMA is not a natural material, it does allow watching the consequences in three dimensions. Here we test the observations from the laboratory experiments by comparisons with preliminary CTH hydrocode results using a layered Moon with self-gravity.

Background: The South-Pole-Aitken (SPA) Basin represents one of the extreme examples of a major collision.The diameter of SPA (~2000-2500km) actually exceeds the radius of the Moon [1,2]. At such extremes, the size of the impactor approaches 500-800 km, particularly for an oblique trajectory. The first contact induces the initial strong shock. In an oblique impact, the impactor continues to penetrate and achieves maximum coupling downrange (and deeper), but still resides within the transient crater. For SPA, the offset between first contact and transient crater center should exceed 500-800 km. This means that any asymmetry due to the initial coupling may be expressed on the surface.

In 1976, it was proposed that the convergence of shock waves at the antipode of a spherical body could induce significant surface and subsurface disruption [3]. Possible surface expressions on the Moon (opposite to Imbrium and Orientale) and Mercury (opposite to Caloris) included disrupted (hilly and lineated) terrains. Subsequent efforts [4] tested this suggestion with an early hydrocode and concluded that the initial estimates were too conservative. Since then, various studies have continued to examine the consequences of convergent antipodal shock and seismic waves for the Moon [5, 6] and icy bodies [6], among other objects. While the relative role of convergent ejecta versus shock/seismic waves will continue to be debated, one test for the possible antipodal effects is to assess the consequences at the largest scales, i.e., the SPA Basin

Comparisons: Oblique impacts into spherical targets result in a series multiple sets of convergence corresponding to the asymmetry in the initial shock. Internal failure appears to be antipodal to the first point of contact, rather than the final crater (Fig. 1). In addition, there is a "haze" in the PMMA offset from the antipode (expressed as micro-cracks). High-speed imaging indicates that these are the first pattern of failure to emerge.

A preliminary 3D hydrocode computation used an improved version of CTH, including self-gravity and a molten core. For the model, an undifferentiated dunite body 800 km in diameter collided with the Moon at 10 km/s at an angle of 30° (from the impact tangent plane at first contact). The calculation used a simple MGRUN equations-of-state with a core radius of 350 km. In this case, the impact kinetic energy (KE) represents about 0.3% of the total gravitational potential energy of the Moon. Due to the oblique impact, however, some of this initial KE is decoupled as the impactor decapitates and continues downrange [7]. A second calculation used a faster (20 km/s) and smaller impactor (500 km) and yielded very similar results.

As shown in Figure 2, both the hydrocode and the laboratory experiments exhibit the same basic phenomena: the focus of tensile stresses is near the antipode to the point of first contact but with most extensive damage is offset toward the incoming trajectory. This should be expected because of the 3D geometry and the shock asymmetry. The hydrocode further demonstrates, however, that the duration of extension at the antipode evolves over more than 15 minutes and approaches the core, in spite of inclusion of self-gravity. Future one-to-one comparison between hydrocode and experiments will provide a better understanding the actual damage done, its possible depth, stresses on the surface, and combinations of scales and speeds. This approach is distinct from some other efforts [8], who focused on just the basin. Both the code and high-speed imaging of the experiment reveal that different styles of failure evolve and overlap.

Implications: In 1980, Whitaker [9] proposed an ancient Procellarum impact basin helps to account for the nearside maria and a pattern radial and concetric system of ridges and graben. While this hypothesis could help to account for the localization of the high-Th and KREEP [10, 11], preserved geophysical evidence for such a large impact, however, is lacking [12-14]. The basic observations made by Whitaker are not in question. Rather, it is suggested that the pattern of concentric and radial ridges and graben should be called the "Procellarum System." While subtle, this is an important distinction. The term "basin" on the Moon implicitly connotes an impact structure. With such a distinction, there could be several working hypotheses to explain Whitaker's System. One hypothesis is that it is indeed an ancient impact that has been completely overprinted. Another is that it represents a long-lasting expression of the SPA Basin on the opposite side of the Moon [15]. The problem is that the center of the Procellarum System (PS) is not antipodal to the SPA. A simple way to account for the offset between the SPA antipode and PS is if SPA was formed by an oblique trajectory, thereby accounting for the offset of the maximum antipodal effects from the SPA center as illustrated above.

The lunar interior antipodal to SPA may have developed deep pathways for deep-seated magma. At this point, there are no claims for melting induced by the convergent shocks; nor is it proposed that the magma immediately erupted over the surface following the impact. Rather it is suggested that the early internal plumbing on the nearside may have been created by SPA. Conversely, the absence of pathways on the lunar farside is due to the absence of deep-seated failure, not to mention the absence of any farside effects from a comparable-size Procellarum impact on the nearside. Subsequent excavation of nearside intrusions by the Imbrium impact to the north of the SPA offset antipode could then help explain the localization of high Th and KREEP across the nearside.

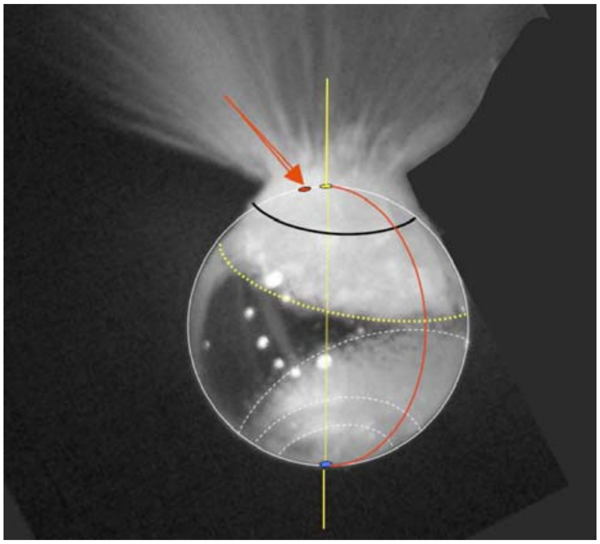

Figure 1: Oblique impact into acrylic sphere at 45º (0.64cm Pyrex sphere, right) at ~ 5.4km/s. Oblique trajectory (red) resulted in higher peak pressures downrange with antipodal failure opposite to the point of first contact, offset from the center of excavation.

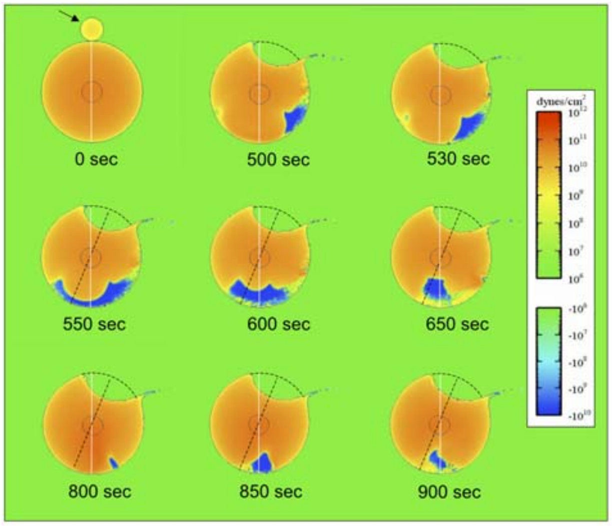

Figure 2: Results of CTH hydrocode simulation of an 800km diameter dunite body colliding with the Moon at an angle of 30°. Hydrocode reveals a pattern of offset antipodal failure that is similar to the experimental results.

References: [1] Stuart-Alexander, Stuart-Alexander, D. E., (1978) *U.S. Geol. Survey Misc. Geol. Inv. Map I-1047*; [2] Wilhelms D. E. (1984) *Geologic History of the Moon*, US Geological Survey Professional Paper 1348; [3] Schultz P.H. and Gault D.E. (1975), *The Moon*, *12*, pp. 159-177; [4] Hughes H.G., et al. (1977), *Phys. Earth Planet. Inter*. *15*, 251–263; [5] Bruesch L. S. and Asphaug E. (2004) *Icarus 168*, 457-466; [6] Hood L. L., Artemieva N. A. 2006. LPSC-37, abstr.#2137; [7] Schultz P.H. and Gault D.E. (1990), *Geol. Soc. of Amer. Sp. Paper 247*, 239-261; [8] Collins G. S. and Melosh H. J. (2004), *Lunar Planet. Sci. 35*, abstr. # 1375; [9] Whitaker, E. A. (1981), In *Multi-ring basins: Formation and evolution; Proceedings of the Lunar and Planetary Science Conference*, Houston, TX, November 10-12, 1980. New York and Oxford, Pergamon Press, 1981, p. 105-111; [10] Haskin L. A. (1998), *J. Geophys. Res.* 103, 1679–1689; [11] Korotev, R.L. (2000), *Jour. Geophys. Res. 105*, E5, 4317-4345; [12] Zuber et al. (1995), *Science 266* 1839-1843; [13] Neumann G. et al., J.Geophys.Res.101,16,841-16,843; [14] Wieczorek M. A. and Zuber M.T. (2004), *J. Geophys. Res.*, *109*, E01009; [15] Garrick-Bethel, I. and Zuber, M. T. (2005), *Lunar Planet. Sci. 36*, abstr. # 2372.

DIAGNOSTIC FEATURES FROM MODELING IMPACT CRATERING IN ICY LAYERED TERRAINS.

L. E. Senft and S. T. Stewart, Dept. Earth & Planetary Sci., Harvard U., 20 Oxford St., Cambridge, MA 02138 (lsenft@fas.harvard.edu).

Introduction. Icy and layered surfaces are seen throughout the solar system. In this work, we use numerical simulations to describe and quantify the effects of icy surface and subsurface layers on crater formation. We focus on understanding Martian crater forms because observations of Martian ice-related features and theoretical work on the dynamical history of Mars have illuminated how obliquity variations led to the deposition of ice-rich layers, ranging from 10 m to 1 km thick, on the surface [1, 2]. The impact crater record provides a powerful tool to investigate these layers' properties. Furthermore, icy layers may be a contributing factor to the layered ejecta structures found around the majority of Martian impact craters [e.g. 3].

Method. Cratering simulations are conducted using the shock physics code CTH [4]. We use the rock strength model of Collins et al. [5], which we have implemented into CTH [6]. The equations of state for basalt [7] and H_2O are gridded in Sesame tables. We constructed a new Sesame table for H_2O. This table includes three solid phases (ice Ih, VI, and VII), liquid, and vapor. The EOS of the phases and phase boundaries are determined experimentally [8, 9, 10, 11].

Results. A range of effects from icy layers are seen. Here we illustrate the effects using examples from a single layer of ice. Fig. 1 presents time series from simulations of a 200-m diameter projectile impact onto the Martian surface for different target configurations. In Fig. 1a, the target is homogenous basalt. Crater formation proceeds as expected, with the ejecta curtain forming a smooth inverted cone that sweeps outward (20 s) and the formation of a bowl shaped transient cavity whose walls collapse slightly ("end"). In Fig. 1b, a 100 m surface layer of ice is added. Crater formation proceeds as before, but when the basalt ejecta is laid down near the rim, it compresses the ice layer underneath. This leads to horizontal, non-ballistic motion of the near-surface ice, which thins the icy layer near the rim and thickens it at greater distances.

When the thickness of the surface ice layer is increased to 200 m (Fig. 1d), the proportion of ice relative to basalt in the ejecta blanket increases. The ejection of ice at higher angles than basalt creates a curved profile to the ejecta curtain. If the thickness of the surface ice layer is large enough (400 m, Fig. 1f), than the ice separates from the basalt in the ejecta curtain (2 s). This ejecta curtain structure has also been observed in simulations of marine targets [12]. Also, the icy rim appears to be unstable, flowing into the crater at late times ("end").

Burying the ice layer under a basalt layer produces further morphological variations. Figs. 1c and 1e show a 100 and 200 m ice layer, respectively, buried under a 200 m thick basalt layer. In both cases, the top basalt layer tears away from the underlying surface at early times (2 s). The ejecta trajectories are modified by wave reflections between the layers. The high ejection angles result in a hinge-like evolution of the ejecta curtain. The hinge area then collapses back towards the crater cavity (20 s). Finally, as the hinge slumps, it squeezes the ice layer, resulting in a late-stage icy extrusion into the crater. This ice behaves in a fluid manner because it is warm, however it is largely unmelted.

If the thickness of a buried icy layer becomes large enough (Fig. 1g; a 400 m thick ice layer buried under a 100 m basalt layer), then the actual crater (in the underlying basalt layer) becomes very small and the amount of ice being extruded into the crater at late times becomes very large. As the ice being extruded from all sides of the crater meets, it creates a central uplift which collapses back down in on itself and flows outward at temperatures near the melting point.

Comparison with Observations. Our simulations suggest that several of the features associated with Martian impact craters may be a result of surface or near subsurface icy layers, including:

"Dewatering" Features: Tornabene et al. [13] has recently documented flow features associated with young impact craters of a large size range (~3 to 60 km) and suggest that they are a result of the flow of water into the crater cavity. Our simulations (Figs. 1c, 1e, 1f, and 1g) show warm, thermally weakened ice flowing away from the crater rim and into the crater (as late-stage icy extrusions).

Rim Moats: Our simulations show non-ballistic, horizontal flow of ice away from the crater rim, which may produce observed circum-rim moats (Figs. 1b and 1d) [14].

Layered Ejecta Structures: Non-ballistic trajectories modify the radial distribution of ejecta from a simple power law. Terminal ramparts cannot be directly observed in the simulations because the scale is too small and the physics of debris flows are different from the physics of large-scale impact cratering events. However, simulations can provide the initial conditions for debris flow models.

Lack of Secondary Craters: Boyce and Mouginis-Mark [14] observe a lack of secondary craters around some double layer ejecta craters. Our simulations show that when there is a buried ice layer (Figs. 1c, 1f, and 1g), the ejecta flow can be somewhat impeded, leading to most of the ejecta being deposited close to the crater rim.

Paleolakes: A number of possible paleolakes in Martian craters have been identified [e.g. 15]. Our simulations show warm ice ponded on crater floors (Figs. 1c, 1e, and 1g).

Central Pit Formation: The thermal evolution of liquid water and ice deposits in the crater floor can be used to study the possible formation of central pits by dewatering [16].

Natural Variations: Martian impact craters display large variations in depths, rim heights, and amounts of ejected and uplifted material versus crater diameter [e.g. 17]. Our simulations produce a large range of these measures.

Conclusions. We have performed simulations of impact cratering events into layered icy terrains in order to understand the effect that such layers can have on the impact cratering process and the final crater morphology. The effects can be significant and may explain differences in crater morphologies between planetary surfaces and many of the features seen around Martian impact craters. Finally, note that dry, weak layers may produce some (but not all) of the same morphologies as icy layers, and we are investigating ways to differentiate between the two cases.

References. [1] Head J.W. et al. (2003) Nature 426, 797-802. [2] Laskar J. et. al. (2004) Icarus 170, 343-364. [3] Carr M.H. et al. (1977) JGR 82(28), 4,055 [4] McGlaun J.M. & Thompson S.L. (1990) J. Imp. Eng. 10, 352. [5] Collins G.S. & Melosh H.J. (2004) MAPS 39, 217-231. [6] Senft L.E. & Stewart S.T. (2007) JGR, accepted. [7] Kerley G. (1999) Kerley Technical Services Report, KPS99-4. [8] Wagner W. & Pruss A. (1993) JPCRD 22, 783. [9] Feistel R. & Wagner W. (2005) JPCRD 35, 1,021. [10] Stewart S.T. & Ahrens T.J. (2005) JGR 110, 2004JE002305. [11] Frank M.R. et al. (2004) GCA 68, 2,781. [12] Ormo J. et al. (2002) JGR 107, 2002JE001865. [13] Tornabene L. (2007) LPSC XXVIII, 2215. [14] Boyce J.M. & Mouginis-Mark P.J. (2006) JGR, 111, E10005. [15] Cabrol N.A. & Grin E.A. (1999) Icarus 142, 160. [16] Barlow, N.G. (2006) MAPS 41, 1425. [17] Stewart S.T. & Valiant G.J. (2006) MAPS 41, 1432.

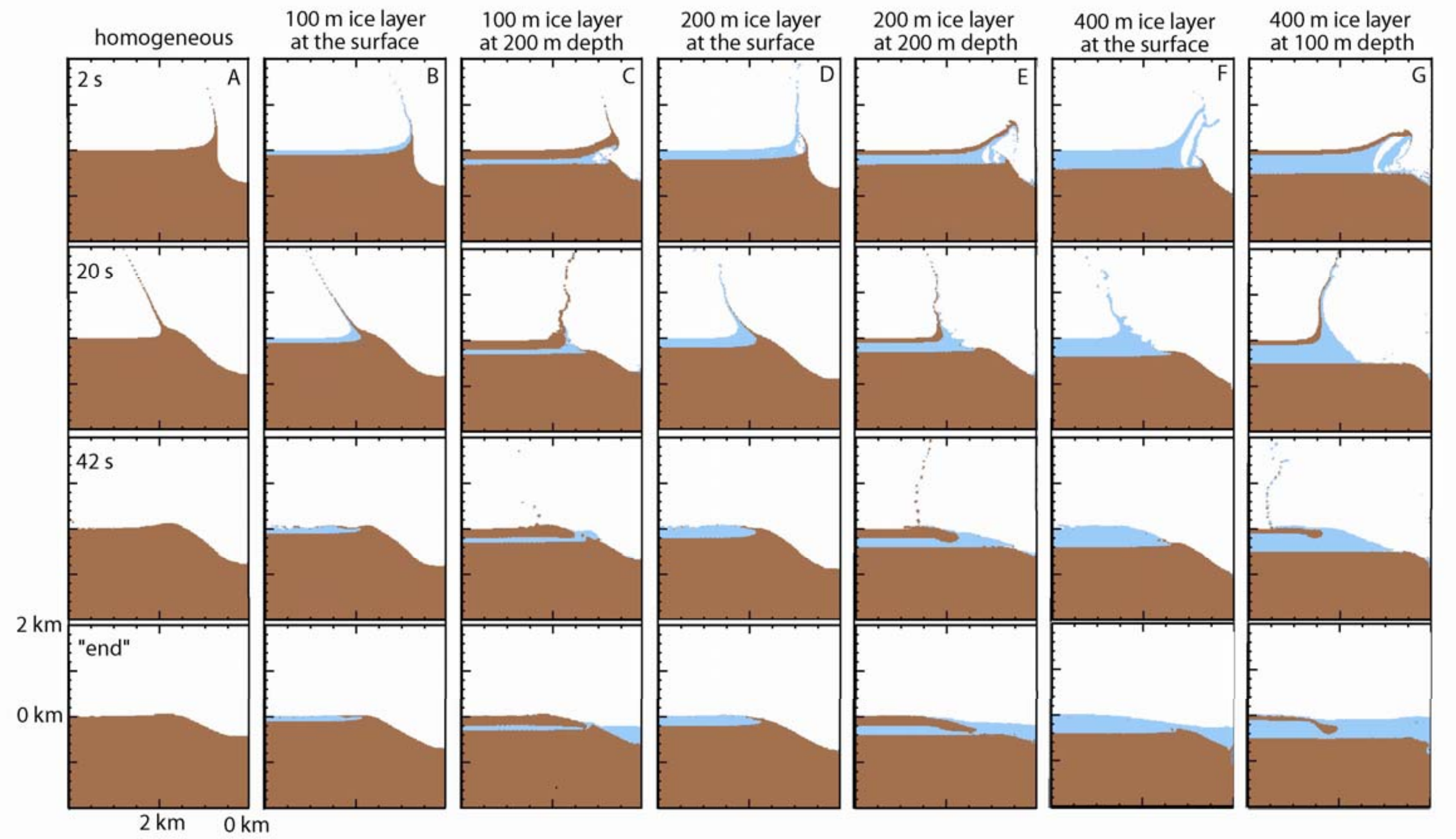

Figure 1. 200-m diameter projectile impact at 10 km/s for different target configurations under Martian gravity (nominal 4.9 km final rim diameter). Cross sections of cylindrically symmetric calculations are shown, where brown represents basalt and blue represents H_2O. Time increases downwards and the scale is the same in all panels. The "end" refers to the time when material has stopped moving appreciably.

ENVIRONMENTAL EFFECTS OF LARGE IMPACTS: WAS THE END-CRETACEOUS EVENT TYPICAL?

B. Simonson[1], S. Hassler[2], [1]Oberlin College (Oberlin, OH 44074 USA; Bruce.Simonson@oberlin.edu), [2]JFK University (Pleasant Hill, CA 94523 USA).

Introduction: Over 25 years of intense study of the Cretaceous-Tertiary (KT) or Cretaceous-Paleogene (KP) boundary layer has yielded a rich harvest of ideas about the global catastrophic effects of impacts by large extraterrestrial bodies, be they asteroids or comets. Effects that have been proposed include 1) the generation of large tsunami-like waves that ravaged coastal and shelf areas throughout the region adjoining today's Gulf of Mexico; 2) rapid heating of the upper atmosphere by the re-entry of ejecta (primarily spherules), leading to global wildfires; 3) the injection of enough fine dust and/or sulfate aerosol into the atmosphere to cause global cooling over a longer time span; and 4) one of the greatest mass extinctions in Earth history. These conclusions have come almost entirely from the study of the ejecta layer formed during the end-Cretaceous event and the sedimentary strata that host it [1 and references therein]. It is tacitly assumed by many researchers that impacts by objects comparable in size to the end-Cretaceous impactor had similar environmental effects throughout Earth history. The best way to test this assumption is to examine ejecta layers from other comparably large impacts and see if they are similar in nature.

KT versus other impacts. The first clue that the end-Cretaceous event may be atypical is the fact that no other ejecta layer of comparable size or complexity has been linked to a mass extinction, despite years of intensive searching. The problem is not a lack of ejecta layers - a dozen or more formed by impacts roughly comparable in size to the end-Cretaceous event have been discovered in the last few decades, most of which share a profusion of millimeter-scale spherules of former silicate melt [2,3]. Since most of these impacts happened in the Precambrian, the lack of Metazoan fossils makes it difficult to determine whether they did serious damage to the biosphere, but it can be done. For example, the ejecta layer formed by the Neoproterozoic Acraman impact appears to coincide stratigraphically with a marked increase in the diversity of acritarchs [4], the opposite of a mass extinction.

In addition to biotic changes, the nature of the ejecta and the relationship of the layers to surrounding strata can be compared to the KT boundary layer to assess whether they were comparable in other respects. In fact, it appears that most of the Precambrian layers differ from the end-Cretaceous layer in significant ways. For example, differences in the spherules suggest the Precambrian impactors struck target rocks with different compositions. Specifically, many of the Precambrian spherules show internal textures that are a close match for those of natural and artificial basalts [5,6]. Crystallized KT boundary layer spherules rarely show such textures; they typically contain dendritic clinopyroxene (CPX) crystals instead [1]. Since 90% or more of the mass of impact spherules is thought to be terrestrial in origin, this suggests the Precambrian impacts hit basaltic target rocks, whereas we know the end-Cretaceous impactor hit a combination of carbonates, sulfate evaporites, and continental basement rocks. The crystallization of CPX has been attributed to the formation of a hybrid melt relatively rich in Ca and low in silica. The only impact spherules that show comparable textures belong to the Eocene "CPX layer" [7]. It was probably generated by the Popigai impact, which also happened in carbonates overlying continental basement rocks. Interestingly, the Eocene CPX layer does not coincide with a major mass extinction, nor have long-lasting environmental effects been attributed to it. In addition, there is also controversy as to whether the Precambrian spherules originated as ballistic melt droplets or condensed from rock vapor [5,6].

Precambrian impacts. Finally, the features of many of the Precambrian ejecta layers suggest their regional environmental effects were similar to those of the end-Cretaceous event, but that may had little in the way of long-lasting environmental effects. Most of the Precambrian layers per se contain sedimentary structures indicating they were deposited during unusually high-energy events involving impact-induced waves and/or currents [5,8]; in this, they are very similar to the KT boundary layer in the Gulf region. Had the impacts caused large-scale, longer term changes in Earth's surface environments, one would expect the ejecta layers to coincide with major lithologic shifts in the stratigraphic record. A few of the Precambrian layers are close to such shifts, e.g., the 2.63 billion year-old spherule layer near the top of the Neoarchean Jeerinah Formation in the Hamersley Basin of Western Australia is 2 meters below the base of what is arguably the first large banded iron formation on Earth [9]. However, other Precambrian ejecta layers occur in the midst of continuous successions with no apparent difference between strata above and below the layers, e.g., in the Wittenoom Formation and Dales Gorge banded iron formation in the Hamersley Basin [9] or the Monteville Formation in the roughly contemporaneous Griqualand West Basin of South Africa [10].

In summary, the end-Cretaceous event has been a fascinating topic for study, but comparisons with other ejecta layers in the stratigraphic record raise the possibility that it was a "one-off" whose environmental effects may have been different from other impacts, even those comparable in size and Phanerozoic in age. At a minimum, inferences about the environmental effects of large impacts should not be extrapolated uncritically solely on the basis of the end-Cretaceous event. Equally intensive study and modeling of distal ejecta layers from a number of other large impacts are needed before we can adequately assess how "typical" the end-Cretaceous event really was.

References: [1] Smit J. (1999) *Ann. Rev. Earth Plan Sci., 27*, 75-113. [2] Lowe D. R. and Byerly G. R. (1986) *Geology, 14,* 599-602. [3] Simonson B. M. and Glass B. P. (2004) *Ann. Rev. Earth Plan Sci., 32*, 329-361. [4] Grey K. et al. (2003) *Geology, 31*, 459-462. [5] Lowe D. R. et al. (2003) *Astrobiology, 3,* 7-48. [6] Simonson B. M. (2003) *Astrobiology, 3,* 49-65. [7] Glass B. P. (2002) *Chem. Erde, 62,* 173-196. [8] Hassler S. W. and Simonson B. M. (2001) *J. Geol., 109,* 1-19. [9] Hassler S. W. et al. (2005) *Austral. J. Earth Sci., 52*, 759-771. [10] Simonson B. M. et al. (1999) *Geol. Soc. Amer. Spec. Paper, 339*, 249-261.

FRICTION MELTING MECHANICS: EXPERIMENTAL EVIDENCE RELEVANT TO IMPACT CRATERING

John Spray, Planetary and Space Science Centre, Department of Geology, University of New Brunswick, 2 Bailey Drive, Fredericton, New Brunswick E3B 5A3, Canada. Email: jgs@unb.ca

Introduction: Over the last decade or so, there has been a growing awareness that the impact process includes the localization of target deformation into fault systems of various widths and displacements. This is particularly the case during the modification stage of the formation of complex craters, where collapse and rebound features result in the displacement of enormous volumes of rock. In impact structures, the discretization of deformation is manifest in different arrays of slip systems from the microscopic (sub-mm) to megascopic (km-size) scales. If strain rates are sufficiently high, frictional melting of the fault walls will occur. The common development of friction melt-clast suspensions (pseudotachylytes) in fault zones (typically 1 cm thick for endogenic systems), including those associated with meteorite impact (typically up to 1 m thick), testify to the ability of such natural slip systems to frictionally melt fault walls (e.g., 1, 2).

Frictional melting hierarchy: Friction experiments using high-speed slip apparatus have enabled us to explore the mechanics of the melting process. These experiments reveal that the fracture toughnesses and shear yield strengths of the constituent minerals are critical to the melting path. These strengths are found to be dependent on mineral crystal structure and bond energy. A hierarchy of comminution and melting susceptibilities is apparent within the major rock-forming minerals, with, in order of decreasing melting susceptibility: phyllosilicates > inosilicates > tectosilicates > orthosilicates. The pre-melting condition is controlled by the elasticity of a given mineral species and its thermal conductivity. At a critical grain size, typically <1 micron, the volume of elastic-plastic deformation during grinding exceeds the fragment's ability to remove heat from the deforming outer zones and so the temperature rises to the melting point. Once this occurs, the melted species contributes to lowering the friction until a critical volume of melt is generated.

Friction Experiments: In this presentation, we report on a series of rotary friction experiments performed on Westerly granite at start velocities of 2.0-4.0 m s^{-1}, under a loads of 250-500 N until the system stalls (up to ~4 s). A typical sample configuration is shown right (Fig. 1). Interface temperature, velocity and force have been measured at intervals of 0.2 milliseconds. The results show that kinetic friction increases in direct proportion to temperature up to a critical value T_{cr}, whereupon the system changes from boundary lubrication (slip strengthening) to hydrodynamic lubrication (slip weakening) with an associated decrease in friction and temperature. For Westerly granite T_{cr} is ~1150 EC. This corresponds to the melting point of feldspar, which constitutes ~50% of the rock. If T_{cr} is exceeded in natural slip systems, which will depend on rock type, this can result in the generation of friction melt. T_{cr} tends to be easily exceeded in impact events, because collapse structures involve large (km-size), single-slip displacements (e.g., side wall slumping). This is in contrast to endogenic earthquake faults, where constrained fault terminations act to limit the slip distance.

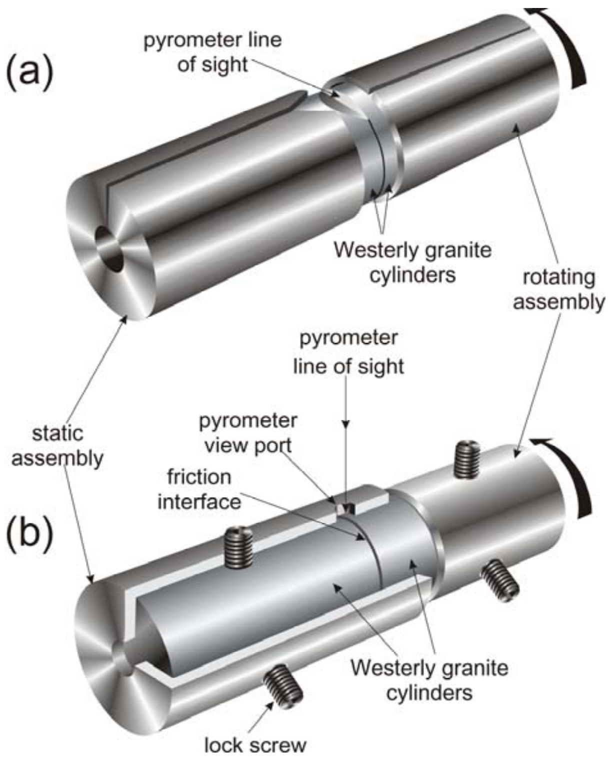

Figure 1. Sample holder design for (a) open runs and (b) closed runs (with cutaway for clarity). Rock cylinder diameter 37 mm

Mega-friction melts in impact structures: We explore the development of mega-pseudotachylyte systems (km-size) in impact structures in terms of collapse features. A prime example is the Frood-Stobie ore belt at Sudbury, which is currently the largest known example in the world. This is a pseudotachylyte breccia that is up to 1 km wide and 45 km length and hosts one of the largest known Cu-Ni sulfide orebodies. In this case, the acceleration of the fault mitigates decreasing friction due to lubrication because violent wall rock interactions introduce a continuous feed of clasts into the slip system. This is distinct from the smaller, pinned, endogenic slip systems, where lubrication feedback is prevalent.

References: [1] Sibson, R.H. (1975) *Geophys. J. R. Astron. Soc. 43*, 775-794. [2] Spray, J.G. (1997) *Geology 25*, 579-582.

FRICTIONAL MELTING AND COMPLEX CRATER COLLAPSE.

S. T. Stewart and L. E. Senft, Dept. of Earth & Planetary Sciences, Harvard University, 20 Oxford St., Cambridge, MA 02138 (sstewart@eps.harvard.edu).

Introduction: The formation of complex craters requires a mechanism(s) to cause transient weakening of the target material to reproduce observed morphologies and structural deformation. Several processes have been suggested for the dominant weakening mechanism [1, 2, 3], with the most widely tested model to date being the block model approximation of acoustic fluidization [2, 4, 5, 6]. Here we investigate the possible role of frictional melting in the collapse of complex craters.

Frictional Melting in the Lab: It has long been recognized that slip at high velocities and high displacements may produce melt; recent experiments illuminate how frictional melt forms and affects the strength along a fault [7, 8, 9]. For example, Hirose and Shimamoto [7] demonstrate that frictional melting has a very strong influence on the coefficient of friction. Two stages of weakening are observed with increasing slip. The first stage is thought to be due to small amounts of frictional melting along asperities (also known as flash heating; melting occurs along a very small surface area of the fault). As melting continues, the friction increases (to a level lower than the initial dry friction), because melt patches tend to 'stick' as they form. Eventually, a continuous melt layer forms, and as this layer grows, a second weakening event is observed. Note that although the melt viscosity tends to increase during layer growth, the shear strain rate decreases sharply, leading to an overall weakening. Finally, widening of the layer due to melting is balanced by loss of melt from the system (in experiments, melt is squeezed out the sides of the sample; in the field, melt may be squeezed into surrounding fractures), leading to a steady state friction. The friction at steady state depends strongly on (1) the melt viscosity, and (2) the shear strain rate across the melt layer, which is determined by the thickness of the melt layer and, hence, the rate of melt loss.

Frictional Melting in the Field: Frictional melting may be an important process in reducing friction along high strain rate, large displacements faults. The total effect, however, is difficult to quantify. Rice [10] suggests that flash heating of asperities, along with pore fluid pressure effects, may explain the strengths observed along large crustal faults during seismic slip events. The drastic loss of strength associated with flash heating may halt the onset of large-scale melting for many faults, inhibiting the formation of pseudotachylites [10]. If the displacement and strain rates are large enough, melting will nonetheless proceed and the second weakening event discussed above may become relevant. However, it is difficult to say what the degree of weakening will be because the steady state friction (if it is reached) will depend strongly on the melt viscosity and the rate of melt loss.

Frictional Melting and Complex Crater Collapse: Field studies of complex craters suggest that collapse occurs largely by brittle deformation, as the crater walls collapse inward along faults [e.g. 11, 12]. Additionally, pseudotachylites (μm to km scale) have been observed around complex craters [13, 14]. Spray [15] estimated the viscosity of these melts to be very low; additionally, because pseudotachylites are not bulk melt but clast-melt suspensions, they may exhibit pseudoplastic behavior. Thus it is likely that both flash heating and large-scale melting contribute to reducing the coefficient of friction along faults during impact crater collapse. Note also that the presence of large-scale pseudotachylites is not a requirement for frictional heating effects (if the weakening is from flash heating of asperities).

The resolution of cratering simulations is much coarser than individual faults that are formed and/or are active during planetary-scale impact crater formation. In a continuum model, discrete deformation (fractures) is approximated by a nondimensional damage variable, where zero represents completely intact material and one represents completely fractured material. We use the strength-damage material model of Collins et al. [16], which we have implemented into CTH [17]. In this model, yield strength, Y_d, of the fractured rock is assumed to follow a friction law, $Y_d = \mu_d P$. When frictional melting occurs, the coefficient of friction, μ, is reduced. As a simplified approximation, when both the velocity and damage in a cell are above certain values (v_{cut}, d_{cut}), then the coefficient of friction is decreased to a new value (μ'). This is based on the assumption that the strength in these cells is being determined by slip along faults undergoing some form of frictional melting. In actuality μ' is some complex function involving a number of factors, including velocity, rock type, fault geometry, and slip distance, but we approximate it as a single value here for exploratory purposes.

Fig. 1 shows results for impacts of a 1-km diameter asteroid at 17 km/s on Earth (nominal final rim-to-rim diameter of ~24 km). Three different cases are shown: crater formation (1) with no additional weakening mechanism, (2) with acoustic fluidization using parameters from [4], and (3) with frictional melting using v_{cut}=0.2 m/s, d_{cut}=0.9, and μ'=0.2 (higher values of v_{cut} and d_{cut} did not produce enough collapse and lowering d_{cut} did not have any significant effects). Note that a μ' of 0.2 is well within the range of friction coefficients determined experimentally.

The light and dark layers are the same material with the same strength properties; the layers are shown to illustrate the deformation. Similar final crater morphologies are observed in both cases, but the collapse processes are different. With acoustic fluidization, collapse appears to be driven by the uplift of the crater floor (and the walls slump in as a response), while with frictional heating, collapse appears to be driven by slumping from the walls (and the central peak forms as the wall collide). This results in different stratigraphy beneath the craters. In larger impact events, e.g., Chicxulub-scale, the central uplift is formed primarily by uplift of the crater floor using both acoustic fluidization and frictional heating, although some stratigraphic differences are apparent.

A simplified schematic of the similarly sized Haughton crater is shown for comparison [Fig. 2, from 20]. The maximum observable stratigraphic uplift is ~1450 m. This amount of uplift is more consistent with the frictional heating results; however, modifying the acoustic fluidization parameters can change the amount of uplift. Varying the frictional heating parameters produces a smaller range of possible structures compared to acoustic fluidization.

The central uplift at Haughton extends to about 5-6.5 km radially (Fig. 2); this is seen in both the acoustic fluidization and frictional heating simulations. Note that none of the simulations reach the predicted transient crater surface diameter from π-scaling (11.2 km predicted versus ~9 km in the simulations) [18]. According to complex crater scaling laws, a 9 km transient crater should collapse to a 16.3-20 km final rim to rim diameter crater [19], in agreement with both the acoustic fluidization and frictional heating cases.

Conclusions: Frictional melting may be an important mechanism in determining the strength during the collapse of complex craters. Simple numerical simulations show differences in the stratigraphy beneath simulations utilizing acoustic fluidization and frictional melting. Such differences may help to discriminate between collapse mechanisms.

References: [1] H.J. Melosh (1989) Impact Cratering, Oxford UP. [2] H.J. Melosh & B.A. Ivanov (1999) AREPS 27, 385. [3] J.D. O'Keefe & T.J. Ahrens (1999) JGR 104, 27,091. [4] G.S. Collins (2002) PhD Thesis, U. London. [5] B.A. Ivanov & V.N. Kostuchenko (1997) LPSC, abs. 1655. [6] K. Wunnemann & B.A. Ivanov (2003) Pl. Space Sci. 51, 831. [7] T. Hirose & T. Shimamoto (2005) JGR 110, B05202. [8] J.G. Spray (1995) Geo. 23, 1119. [9] T.E. Tullis & D.L. Goldsby (2003) AGU, abs. S51B-05. [10] J. Rice (2006) JGR 111, B05311. [11] G.R. Osiniski & J.G. Spray (2005) MAPS 40, 1813. [12] B.J. Kriens, et al. (1999) JGR 104, 18,867. [13] L.M. Thompson & J.G. Spray (1994) GSA Sp. Paper 293, 275. [14] J.G. Spray (1998) GSA Sp. Pub. 140, 195. [15] J.G. Spray (1993) JGR 98, 8053. [16] G.S. Collins & H.J. Melosh (2004) MAPS 39, 217. [17] L.E. Senft and S.T. Stewart (2007) JGR, accepted. [18] K.A. Holsapple (1993) AREPS 21, 333. [19] W.B. McKinnon (2003) Bridging the Gap, abs. 8047 [20] G.R. Osinski et al. (2005) MAPS 40, 1759.

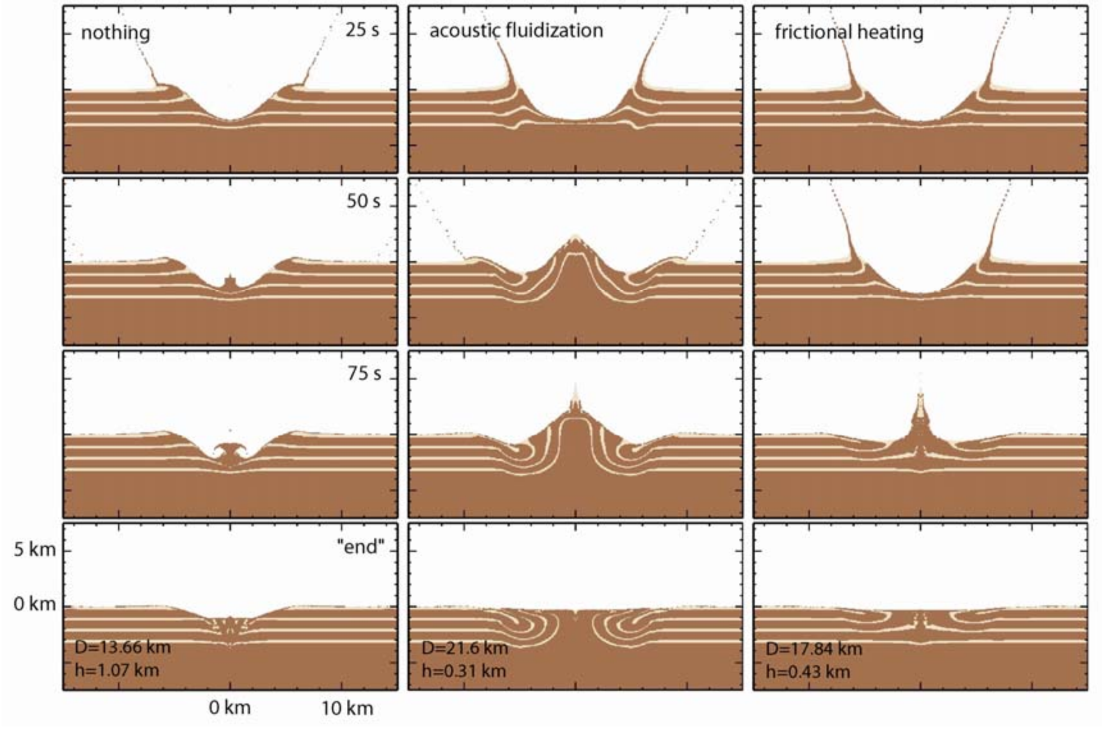

Figure 1. Crater formation from D=1 km asteroids impacts at 17 km/s on Earth for three different collapse scenarios. 2D cylindrically symmetric calculations. Final rim diameters and depths from the original surfaces are noted.

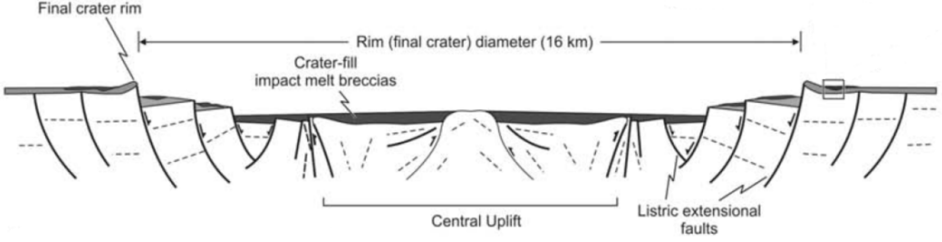

Figure 2. Simplified schematic of the Haughton impact structure, Devon Island, Canadian High Arctic [from 20].

FURTHER DEVELOPMENT OF A HUGONIOT FOR YORKSHIRE SANDSTONE.

E. A. Taylor[1], K. Tsembelis[1, 2*], A. T. Kearsley[2] and K. Miljkovic[1], [1]Department of Physics and Astronomy, Centre for Earth Planetary Space and Astronomical Research, The Open University, Walton Hall, Milton Keynes, MK7 6AA, U. K. (e.a.taylor@open.ac.uk; kostas@tsembelis.com; k.miljkovic@open.ac.uk). [2]Physics and Chemistry of Solids, Cavendish Laboratory, Madingley Road, Cambridge CB3 0HE, U.K. [3]Department of Mineralogy, Natural History Museum, London SW7 5BD, U.K.(a.kearsley@nhm.ac.uk).

Introduction: In order to improve our understanding of the shock response of Yorkshire sandstone, particle impact tests were carried out using the Open University's All Axis Light Gas Gun [1, 2], and 1-D plate impact shock studies implemented using the University of Cambridge's Plate Impact Facility [3]. Preliminary measurements of the crater depth and diameter have been carried out, using a range of techniques. Prediction of the pressures generated on impact requires appropriate material data, preferably measured for the material (particularly relevant for geological materials where there can be material variability). This paper reports on the development of a Hugoniot for Yorkshire sandstone, building on previous work [4, 5, 6]. A range of hydrocodes and analytical techniques were used [7, 8], supported by published data on sandstones and related rocks and minerals [9, 10, 11, 12]. Techniques to estimate the shock-driven heating of the target were applied [13]. This work is a precursor to investigating the possibility of shock-driven DNA modification of microbial organisms in sandstone targets, which could occur at lower pressures than those previously established to cause extinction [14, 15]. Future studies may also look at impact-driven changes to subsurface habitats, noting that shock processing of rocks may make them more colonisable [16]. Before any conclusions can be drawn for these large structures, the different responses for the strength and gravity dominated regimes must be established.

Sandstone Properties: The measured Hugoniot values are reported in Ref. 4. The bulk density was measured to be 2.24 g/cm^3. The composition of the sandstone was established using low vacuum backscattered electron images to obtain modal mineral analyses (i.e. % of whole rock by area ~ volume) for five representative areas of a polished section taken from the edge of the target (example shown in Figure 1). All areas were very similar in their major mineral contents (quartz ca. 60%), and porosity (10-16%), but variable in the minor mineral contents. The results are reported in Table 1. Noting that the ratio of chlorite to K feldspar is estimated to be 5:1, and that the ratio of SiO_2 to albite is estimated to be 9:1, we set the composition of the Yorkshire sandstone (for the purposes of developing a "composite" synthetic Hugoniot) to be: quartz (59%), pore space (14%), chlorite (9%), kaolinite (8%), albite (7%), Fe and Ti oxides (3%) and K feldspar (2%).

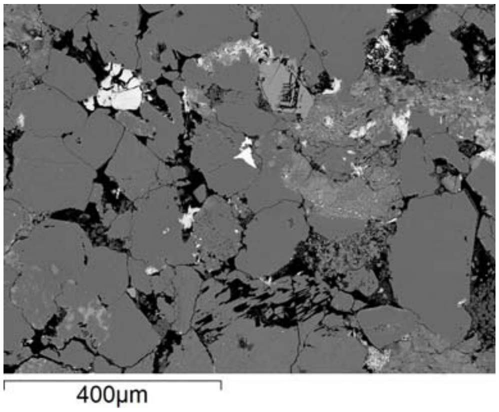

Figure 1. Backscattered electron image of the Yorkshire sandstone sample.

Table 1. Composition of Yorkshire sandstone sample

Material	*Proportion (%)*	*Error (st.dev.)*
"Bright" (metal oxides)	2.90	1.98
Chlorite and K feldspar	10.52	2.99
Silica and albite	65.28	2.85
Kaolinite	8.02	1.81
Pore space	13.60	2.18
TOTAL	100.32	N/A

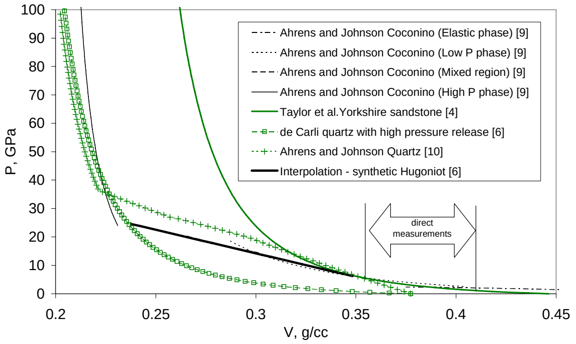

Figure 2. P-V curve for Yorkshire sandstone. A trilinear Hugoniot was derived from these data [6].

---

[*] Now at Atomic Energy of Canada Ltd, Chalk River Labs, ON, Canada.

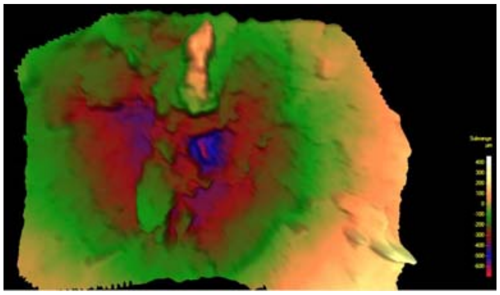

Figure 3. Profile of central region of the impact crater, produced by 1 mm spherical particle stainless steel projectile, impacting at 4.8 km/s at 30° to the horizontal.

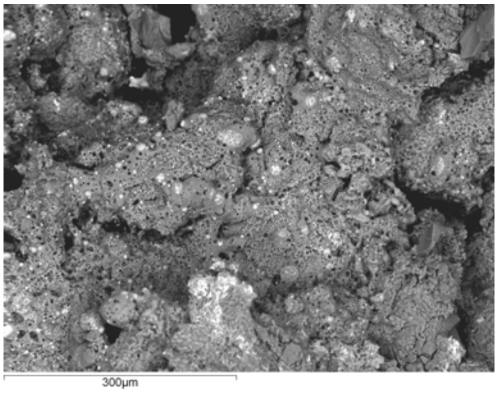

Figure 4. Distribution of impact residue

Further Development of a Sandstone Hugoniot: Based on previous work, as shown in Figure 2, where the P-V curve was based on an interpolation between experimentally measured data for Yorkshire Sandstone and a high pressure quartz data set., we now construct a "composite" synthetic Hugoniot from mineral data. Shock data for serpentine are used as the closest available analogue for K feldspar. All other data are from published experimental tests. A simple pressure-dependent crush-up model, following the approach of Ref. 13, is also developed.

Hydrocode Simulations and Analytical Calculations: A series of 1-D, 2-D and 3-D simulations are presented. The tri-linear (and a bi-linear, with a range fits reflecting the data in this intermediate regime) Hugoniot, as defined in U_s-u_p space, are used in two hydrocodes (AUTODYN and CAV_KO). A new composite Hugoniot, based on data for the constituent minerals is also used as input to the hydrocode simulations. Both sets of results are compared with analytical results based on the planar impact approximation (CAV_SHOCK).

Further Work: Strength and failure models for sandstone will be need to be implemented before a better understanding of the cratering processes. We plan to explore application of the Johnson-Holmquist 2 damage model, as previously used by the two of the authors to explore cratering and penetration in soda lime glass [17]. The objective is to characterise more fully the pressures generated on impact, and to draw broad conclusions on the pressure bounds for any changes observed in the microbial specimens. A constraint on the modeling will be provided by crater profile data, as shown in Figure 3. Plate data for water saturated sandstone are needed, noting recently reported results on survivability of microbial life differing between dry, and saturated, sandstone [18]. Modelling of larger scale impacts – a longer term aim – must consider gravity-driven effects, and other aspects, before any conclusions can be drawn about pressures experienced by any microbial life and changes in habitability driven by shock effects. The derived Hugoniot will be used to estimate release temperatures via analytical calculations of waste heat generated [13]. Initial observations suggest that material may have been emplaced downrange, possibly both from ejecta, and also down fracture systems (Figure 4). A detailed map of the impactor-bearing residue will need to be produced.

References: [1] Taylor, E. A. et al. (2006), Proc. 57th ARA Meeting, Italy, Sept. 2006. [2] McDonnell, J. A. M. (2006), *Int. J. Impact Engng., 33,* 410-418. [3] Bourne, N. K. et al. (1995), *Meas. Sci. Technol., 6,* 1462-1470. [4] Taylor, E. A. et al. (2005), *Proc. Shock Compression Condensed Matter 2005,* 1488-1491. [5] Taylor, E. A. et al., Presented at 1st Conf. Impact Cratering Solar System, Netherlands, May 2006. [6] Milković, K. et al. (2007), submitted to *Proc. Shock Compression Condensed Matter 2007.* [7] Tsembelis, K., CAV_SHOCK software and CAV_KO software, obtained via http://www.shockphysics.com. [8] Century Dynamics Inc. (2003) AUTODYN Theory Manual.. [9] Ahrens, T. J., and Johnson, M. L (1995), Shock Wave Data for Rocks, *AGU Ref. Shelf 3.* [10] Ahrens, T. J., and Johnson, M. L. (1995), Shock Wave Data for Minerals, *AGU Ref. Shelf 2.* [11] Anderson, W. W. et al (1995), DNA-TR-95-32. [12] Ahrens, T. J. et al (1995), AFOSR-TR-95-0493. [13] Sharp, T. G. and deCarli, P. S. (2006), *Meteorites Early Solar System II*, Univ. Arizona Press, 653-677. [14] Stöffler, D. (2007) et al, *Icarus, 186 (2),* 585-588. [15] Burchell, M. J. et al (2004), *Mon. Not R. Astron. Soc., 352,* 1273-1278. [16] Cockell, C.S. et al. (2002), *MAPS, 37,* 1287-1298. [17] Taylor, E. A. et al (1999), *Int. J. Impact Engng., 23 (10),* 895-904. [18] Migaiski, M. et al. (2007), LPSC XXXVIII #1286.

Differences in the subsurface block distributions across the Moon's Southern Highlands.

Thomas. W. Thompson[1], Bruce A. Campbell[2], Rebecca R. Ghent[3], and B. Ray Hawke[4]

[1] JPL, Pasadena, CA 91109: Thomas.W.Thompson@jpl.nasa.gov; Ph: +1 818 354-3881, Fax: +1 818 393-5285; [2]Center for Earth and Planetary Studies, Smithsonian Inst., MRC 315, Washington, D.C 20013, [3]Dept. of Geology, University of Toronto, Toronto, ON, Canada, M5S 3B1 [4]Hawaii Inst. of Geophysics and Planetology, University of Hawaii, Honolulu, HI 96822.

Introduction. The distribution of small (1-16 km diameter) craters with radar-bright ejecta is not uniform across the southeastern nearside lunar highlands. The region north of a line between Tycho and Janssen (~45° S), a region associated with Imbrian-aged basin deposits, has more radar-bright craters than the highlands south of this line. The abundance of these small radar-bright craters likely reflects a difference in the distribution of the larger (100 m to 1 km) blocks in the Imbrian-aged basin ejecta to the north as compared with older pre-Nectarian- and Nectarian aged ejecta deposits to the south. Thus, this difference in the populations of these small radar bright craters provides insights into the nature of the highlands "mega-regolith".

Radar Data. Dual-polarization radar image data at 70-cm wavelength were collected for the southern highlands in 2002-2006 by transmitting from the Arecibo (1000 foot) telescope and receiving the echoes at the Green Bank (300 foot) radio telescope [1]. The image data are focused to maintain the optimum achievable spatial resolution of a few hundred meters over the illuminated area. Fig. 1 shows same-sense (SC, depolarized) radar echoes for the southern highlands. The SC echoes are dominated by diffuse scattering associated with meter-sized blocks/rocks on the surface or in the upper 10-50 m of the subsurface. Thus, high 70-cm SC returns result from an abundance of blocks, whereas low returns signify a paucity of wavelength-scale scatterers in the upper 10-50 m of regolith.

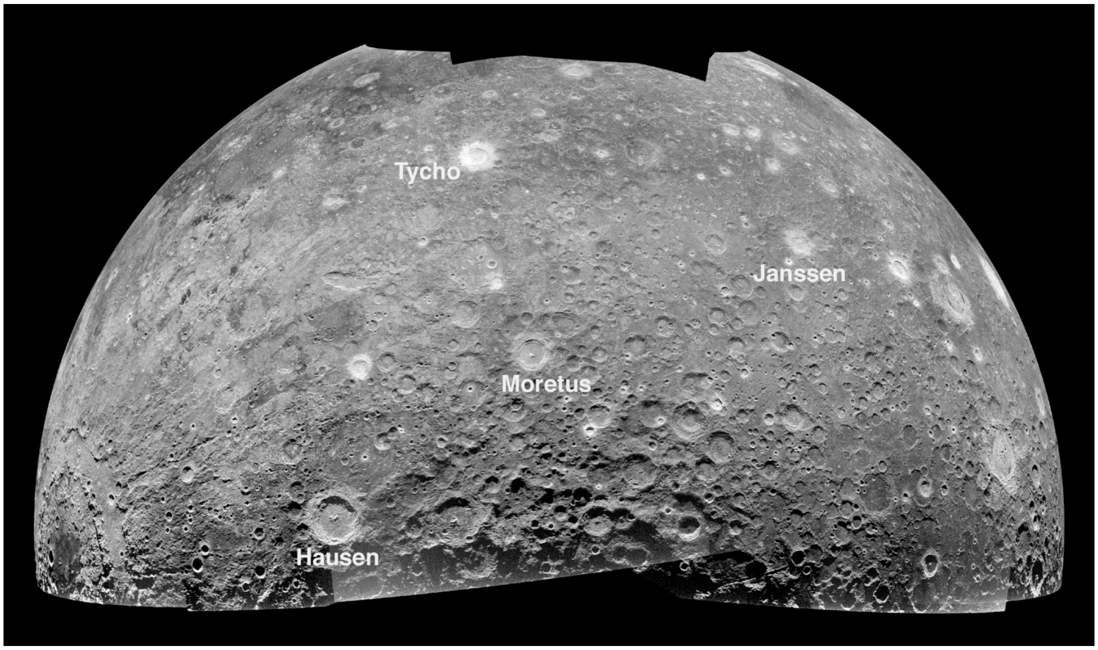

Fig. 1. 70-cm same-sense (SC, depolarized) radar echoes for the southern lunar highlands (orthographic projection centered on the south pole). Bright radar echoes due to blocky ejecta surround Eratosthenian- and Copernican-period craters. There are few small (1-16 km) radar bright craters in the area of the southeastern highlands below a line from Tycho to Janssen, while above this line in an area of younger basin ejecta there are significantly more radar-bright craters.

Observations.

The Moon's southern highlands are a complex, overlapping sequence of materials deposited by the major basins, going back to the South-Pole-Aitken event. The line defined approximately by Tycho and Janssen craters at about 45^o S marks the transition between units mapped as younger Imbrian-aged basin materials to the north and older pre-Nectarian and Nectarian deposits to the south [2]. Our radar data offer new insights into differences between these two general areas.

Craters with Radar-bright Ejecta. To the north of the Tycho-Janssen line, there are more craters, 1-16 km in diameter, with radar-bright ejecta than are present in the highlands extending south toward the pole (Table 1). This change in crater density approximately follows the shift from Imbrian-aged deposits to older basin deposits to the south. The density of small radar-bright craters across the entire southern highlands is significantly less than in the maria (represented here by Mare Humorum).

Area	**1-2 km Diam**	**2-4 km Diam**	**4-8 km Diam**	**8-16 km Diam**
Mare Humorum	138+/-44	166+/-48	97+/-37	28+/-20
North of Tycho-Janssen Line	8+/-2.3	11+/-2.7	13+/-2.9	18+/-3.4
South of Tycho-Janssen Line	5+/-2.7	8+/-3.3	12+4.1	10+/-3.6

Table 1. Density of small radar bright craters, per 10^6 km^2, for the floor of Mare Humorum as well as the northern and southern portions of the south-eastern lunar highlands. Density of 4-8 km mare craters is close to a production curve with a decrease in the 1-4 km diameter range due either to loss of detection from resolution or from shorter radar-bright lifetimes of these smaller craters.

Interpretation. The 70-cm radar characteristics of small (1-16 km diameter) craters depend upon the abundance of blocks ~1m and larger in diameter excavated by the impact. Small impacts excavate ejecta to depths of ~1/10 of their diameter (i.e., depths from 100 m to 1.6 km), which coincides with the approximate depths of the mega-regolith. The availability of blocks in turn depends upon the target material. Mare targets are characterized by competent lavas overlain by relatively thin regolith, and thus provide a ready source of blocks. For small craters in the maria, meter-sized competent blocks in the ejecta should survive to ages commensurate with a few meters of meteoritic gardening (approximately Eratosthenian-period age). The radar-bright ejecta disappear when gardening depths reach several meters (about late Nectarian age) [3]. By contrast, highland megaregolith is much thicker, and small craters in the highland megaregolith will have ejecta that are a mixture of already-comminuted material and "fresh" meter-sized blocks. Distinct highland terrains differ from one another in megaregolith thickness as well as in the relative densities of large (100 m - 1 km) blocks, depending on their ages and proximities to basin centers and their relative ages [4-5].

Our preliminary analysis of the small radar-bright crater distribution across the southern highlands suggests an increase in the depth of well-comminuted material as we move south across the approximate Tycho-Janssen boundary. Craters north of this line as small as a few km have on average impacted more 100 m-1 km sized blocks in the megaregolith than those to the south, providing more blocky debris to form radar-bright ejecta. Most craters south of this line have impacted an older, more comminuted megaregolith with significantly fewer km-size blocks.

References: [1] Campbell, B.A., et al., *IEEE Trans. Geosci. Rem. Sensing, submitted*, 2007; [2] Wilhelms, D., Geologic History of the Moon, USGS #1348, 1987; [3] Thompson, T.W., et al. proc. *Proc. Highlands Crust Conference*, 1980; [4] Moore, H., et al., *Proc. Lun. Plan. Sci. Conf. 5*, 71-100, 1974.; [5] Petro, N., and C.M. Pieters, LPSC XXXVII, abs. 1868, 2006.

HIGH STRAIN-RATE DEFORMATION EXPERIMENTS ON CARBONATE-SILICATE ROCKS: IMPLICATIONS FOR IMPACT CRATERING PROCESSES.

C. H. van der Bogert[1], P. H. Schultz[2], and J. G. Spray[3]; [1]Institut für Planetologie, Westfälische Wilhelms-Universität, Wilhelm-Klemm-Str. 10, 48149 Münster, Germany, Email: vanderbogert@uni-muenster.de; [2]Department of Geological Sciences, Brown University, Providence, RI 02912, USA; [3]Planetary and Space Centre, Department of Geology, University of New Brunswick, Fredericton, NB E3B 5A3, Canada.

Introduction: The response of carbonates to shock experiments has raised considerable interest and controversy. Carbonates do not respond to experimental shock deformation as predicted by theoretical calculations [e.g., 1, 2, 3]. Specifically, devolatilization is expected to occur at pressures exceeding 40 GPa [1,3], with vaporization taking place upon decompression from 37 GPa for calcite and 14 GPa for dolomite [3]. Instead, incipient CO_2 loss begins at about 10 GPa for calcite [4]. Indeed, Lange and Ahrens (1986) note that the formation of shear bands within their samples caused heating which led to devolatilization, but that this was not clearly related to experimental shock pressures [4]. Oblique impact experiments with dolomitic marble targets show increasing devolatilization with decreasing impact angle [5], which implies that shear heating plays an important role in vaporization and decarbonation processes [6].

Previous investigations of carbonate target materials have involved both shock and impact experiments. The benefit of performing frictional melting experiments is that they allow us to investigate target material behavior independently from shock deformation and for longer duration than impact experiments. This allows the independent investigation of conditions analogous to high strain-rate deformation during impact events, which occurs either in response to shock deformation, just after it (i. e. modification stage processes), or due to downrange material motion associated with oblique impact. Similar studies have been conducted with ordinary chondrite meteorites [7].

Samples and Techniques: A frictional melting experiment was performed using separate dolomitic marble and quartzite samples to simulate conditions during an impact into carbonate-silicate target rocks. The experiment followed the method of Spray (1995)[8]. The samples, one cube of quartzite (~99.5% quartz with trace magnetite) and one cube of dolomitic marble (~99% dolomite, ~1% calcite and phlogopite), 1.5 cm on each side, were mounted onto separate steel cylinders with epoxy. Using a computer-controlled Blacks FWH-3 axial friction-welding rig, the samples were brought into contact at room temperature and under dry conditions with ~5 MPa applied pressure. Contact was maintained for two seconds at 750 rpm for a sustained strain-rate of 10^2 to 10^3 s^{-1}.

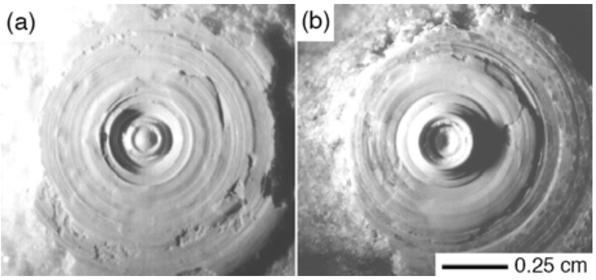

Figure 1. Dolomitic marble (a) and quartzite (b) contact faces after axial friction-welding at a strain-rate of 10^2 to 10^3 s^{-1} for two seconds.

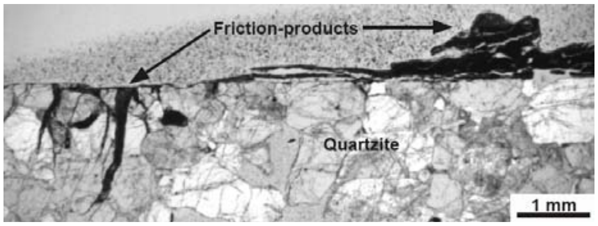

Figure 2. Thin section of the quartzite sample perpendicular to the rotation axis (right edge) showing opaque friction products adhered to the sample surface and injected into fractures that formed in the sample.

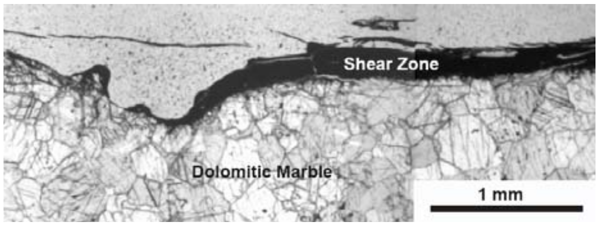

Figure 3. Thin section of the dolomitic marble sample perpendicular to the rotation axis (left edge). Only minor fracturing and infiltration of material into the sample occurred. Besides the shear zone, mechanical twinning was the dominant effect.

Results: Vapor or fine dust escaped from the interface during the experiment. Immediately after sample separation, the interfaces were incandescent. Once cooled, opaque white material adhered to the quartzite sample (Fig. 1, 2), particularly around the axis of rotation, leaving a complementary depression in the carbonate sample (Fig. 1, 3).

Quartzite sample. Material was injected into cracks that formed in the quartzite sample. Cooling and crystallization of the friction products resulted in the formation of minerals such as periclase and calcium-magnesium-silicates. No pure lime was observed to be present. Elemental mapping and EMP analyses reveal segregation of MgO and CaO (Fig. 4). While pure MgO was observed, CaO combined with SiO to form Ca-silicates and with CO_2 to form new carbonate phases. The formation of vesicles and the greater abundance of MgO in the friction products, versus the original marble, implies that ≥ 5 wt % CO_2 was lost during the experiment.

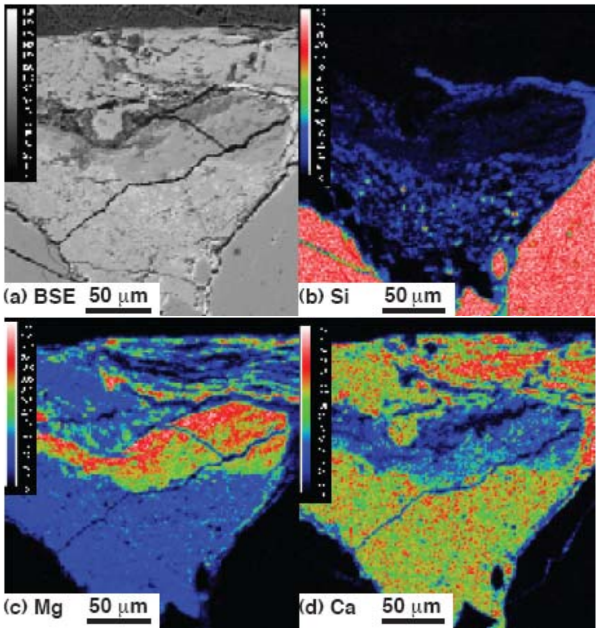

Figure 4. BSE image and Si, Mg and Ca maps for an indented area of the quartzite sample face that retained friction products. Note the segregation of Mg and Ca.

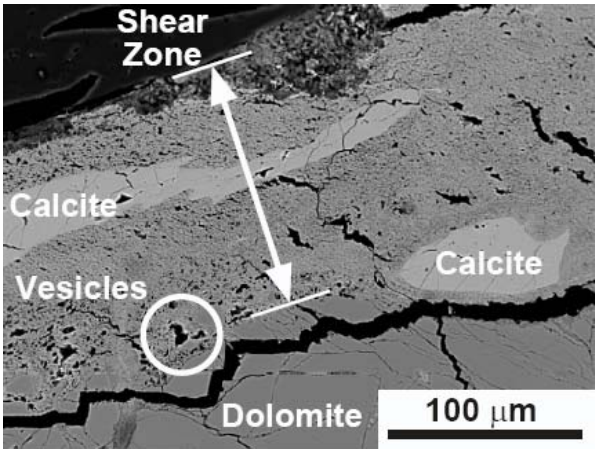

Figure 5. BSE image of the dolomitic marble sample showing the experimental shear zone. Note the pervasive small vesicles and new calcite grains.

Dolomitic marble sample. The dolomitic marble section exhibited thinner and shorter fractures than the quartzite sample. Mechanical twinning was induced by the deformation, in particular around the axis of rotation. The adhered friction products exhibit very fine-grained material with larger, freshly crystallized calcitie and possible huntite, in addition to pervasive micron-scale vesicles (Fig. 5).

Discussion: Because one of the most important factors for the decarbonation of target materials is the confining pressure [10], it has been proposed that decarbonation of carbonate target rocks only occurs upon decompression, thus limiting the overall volume of CO_2 gas released [11]. In addition, back-reactions between trapped CO_2 and highly reactive CaO also reduce the overall volume of CO_2 gas thought to be released during an impact [12]. These factors limit the amount of CO_2 released as a result of shock.

However, the results of this and other studies [6] indicate that high strain-rate deformation can cause significant devolatilization of carbonate target rocks. The presence of akermanite indicates temperatures in excess of 700° C were generated by the experiment [9]. Thus, the temperature conditions are similar to those caused by the post-shock temperature increase following a 55-60 GPa shock alone [3]. When this temperature increase is coupled with fracturing, comminution and subsequent melting associated with high strain-rate deformation and the effects of shock deformation, the loss of CO_2 is enhanced.

Especially during oblique impacts, high strain-rate deformation continues after shock decompression and creates pathways for CO_2 gas to escape by further fracturing target rocks. In addition, high strain-rate deformation affects a greater volume of the target than shock deformation alone, thus increasing the overall volume of material subject to decarbonation. High strain-rate deformation is thus an important impact process, leading to enhanced vaporization, decarbonation, melting and deformation of the target rocks.

References: [1] Boslough M. B. et al. (1982) *EPSL 61*, 166-170. [2] Grady D. E. et al. (1976) *JGR 81*, 889-893. [3] Martinez I. et al. (1995) *JGR 100*, 15456-15476. [4] Lange M. A. and Ahrens T. J. (1984) *EPSL 77*, 409-418. [5] Schultz P. H. (1996) *JGR 101*, 21117-21136. [6] Schultz P. H. et al. (2006) *Internat. Jour. Impact Eng. 33,* 771-780. [7] van der Bogert et al. (2003) *MAPS 38*, 1521-1531. [8] Spray J. G. (1995) *Geology 23*, 1119-1122. [9] Edgar (1965) *Can. Journ. Earth Sci. 2*, 596-621. [10] Ivanov and Deutsch (2002) *Phys. Earth Planet. Int. 129*, 131-143. [11] Kenkmann et al. (1999) *LPSC XXX*, Abstract #1521. [12] Agrinier et al. (2001) *GCA 65*, 2615-2632.

SHIYLI DOME, KAZAKHSTAN: ORIGIN OF CENTRAL UPLIFT BY ELASTIC RESPONSE.

S. A. Vishnevsky[1], [1]Inst. of Geology & Mineralogy, 3 Koptug pr., Novosibirsk-90, 630090, RUSSIA (svish@uiggm.nsc.ru).

Introduction: Origin of central uplifts in complex astroblemes is still debatable [1-3], and a whole rank of hypotheses was proposed in this connection. Among the most important among them there are the hypothesis of elastic response, still proposed by Baldwin [4] and the hypothesis of crater's gravity collapse under the action of acoustic dilution, which is developing by Melosh [1]. Shiyli Dome in Western Kazakhstan is a unique model object for the studies on the problem and for the development of the elastic response hypothesis. Well-known regional stratigraphy and geologic history as well as detailed geophysical and boring data provide favorable testing support for the conclusion.

Description: The Shiyli Dome is a heavily eroded impact structure represented by a central uplift of 1.2 km in diameter, with center co-ordinates 49°10' N and 57°51' E **(Figs. 1,2).** Its target is made up of dense Paleozoic basement (strongly dislocated Devonian+Carboniferous sequence) and loose Mesozoic+Cenozoic cover rocks (marine E$_{1-2}$ clays, Ꝑ$_2$-E$_1$ sandstones+opoka, K$_2$c gypsum-bearing clays, K$_2$s clays, sands and sandstones, K$_1$alb clays+sands, K$_1$apt clays+sands, K$_1$h clays). We have to note that the members of the cover are very monotonous in thickness and have sub horizontal bedding. Earlier, the Dome was considered to be a salt diapir with oil and gas potential. Geophysical and boring prospecting found that there are no salt bodies in the basement but the Dome itself, surrounded by the ring of Paleogene rocks, is a non-root structure localized in the cover rocks only. For a long time, the Dome was considered as a non-explained geological phenomenon, until the macroscopic (shatter cones, "gries" breccias, shock slickensides) and microscopic (PDFs in quartz) evidences of weak shock metamorphism were found in its rocks [5]. Regional geologic history and impact cratering theory allow obtaining the useful reconstructions of the Shiyli impact event. Following to them, it was the marine impact event equal to explosive crater of ~3.2 km in diameter in energy equivalent. It took place in shallow, ~350 m deep, Eocene marine basin **(Fig. 3).** Upper horizons of the sedimentary cover, preserved both in the Dome and the ring subsidence around it, indicate that the underwater crater was either very shallow, <50 m in depth, or was absent at all. In the last case, one can suppose that except for the central uplift, the excavation was limited by centrifugal near-bottom turbid flows only. Following to presence of upper horizons of the sedimentary cover in the Dome, and the marine basin at the time of impact, the age of the Shiyli astrobleme is estimated to be from Early to Middle Eocene (39-53 Ma).

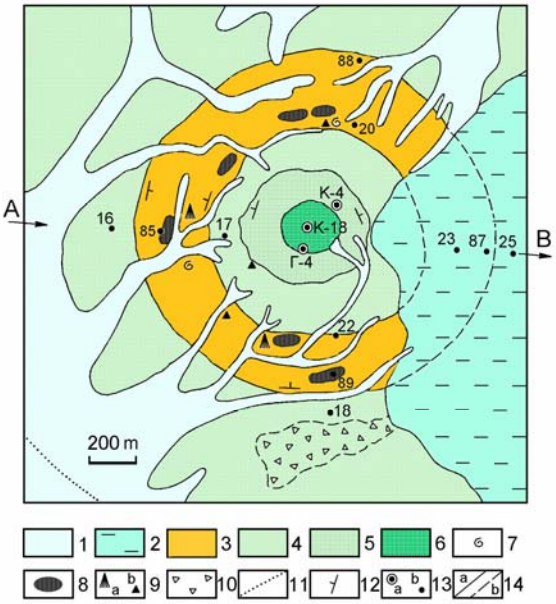

Fig. 1. Geologic map of the Shiyli Dome. Legend. *Sedimentary members:* 1 – Holocene, Q$_{IV}$; 2 – Pliocenian-Quarternary, N$_2$-Q$_1$; 3 – Paleocenian-Early Eocenian, Ꝑ$_2$-E$_1$; 4 – Campanian, K$_2$c; 5 – Santonian, K$_2$s; 6 – Albian, K$_1$alb; *Other units:* 7 – fauna; 8 – "gries" brecciation; 9 – shatter cones (a) and PDFs in quartz (b); 10 – brecciation zones; 11 – supposed limit of impact dislocations; 12 – strike and dipping of rocks; 13 – deep (a) and shallow (b) boring holes; 14 – observed (a) and supposed (b) geological boundaries.

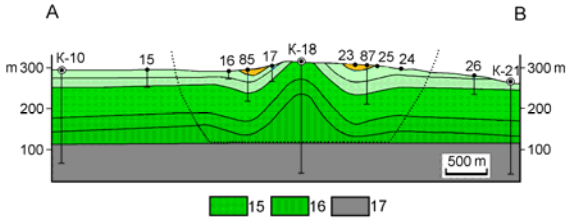

Fig. 2. Geologic cross-section of the Shiyli Dome from A to B (see Fig. 1). Legend. *Sedinebtary members:* 15 – Aptian, K$_1$apt; 16 – Hauterivian, K$_1$h; 17 – Paleozoic basement. Other units see on Fig. 1.

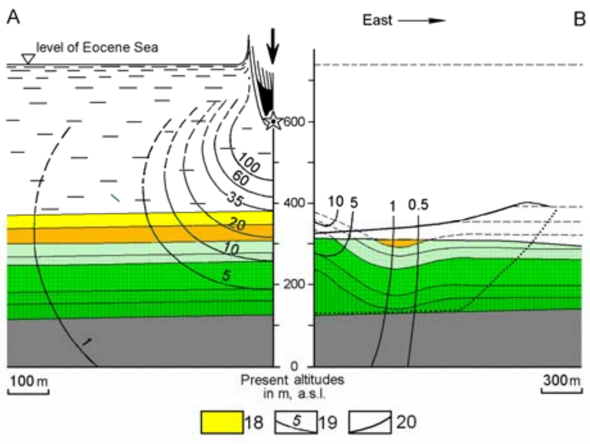

Fig. 3. Reconstruction of the Shiyli impact event (variant of shallow crater). A – pre-impact state of target; B – present state of astrobleme.
Legend: 18 – Low-Middle Eocenian, $E_{1\text{-}2}$; 19 – shock wave isobars, in GPa, in target (A) and their traces in present structure of Dome (B); 20 – supposed line of crater bottom. Other units see on Figs. 1 and 2.

Origin of the Shiyli central uplift: Following to geological data, the Shiyli Dome originated as a result of centripetal movement of the sedimentary cover rocks. The traces of the movement are evident both from the axial symmetry of the Dome **(Fig. 2)** and rock slickensides met in the boring cores. Layers of plastic Hauterivian clays in the base of the sedimentary cover were subjected to a maximal shift. Their thickness on the axis of the structure increased up to 120 m vs. 20-30 m in the frame of the Dome. Axial centripetal shift of Hoterivian clays provided compensating subsidence of uppermost layers with the origin of annual trough around the Dome **(Figs. 2,3).** However, more hard rocks of the target basement did not react on the excavation force. Since the Shiyli crater was either very shallow or was absent at all, its gravity collapse as a course of central uplift origin has to be ruled out. Hypothesis of elastic response is the only possible alternative here. Within the frames of this hypothesis and based upon cratering mechanics after [6], the uplift-forming centripetal shift of the disturbed ground is supposed to take place within any spherical segment under the center of the impact, where the shock and the release wave isobars were parallel to each other. Resulting ground motion within the segment was summarized from the particle velocity behind the shock front (centrifugal vector) and velocity of quasi-elastic expansion in release waves (centripetal vector). Similar ground motion takes place in deep seated underground explosions, where the influence of a free surface is ruled out. Schematic ground motion for the Shiyli impact event is shown on **Fig. 4.** Wide enough, ~120°, the spatial angle of the spherical segment where the centripetal ground motion took place, is attractive. Probably, it is due to relatively deep penetration of the projectile into the water part of the target.

Conclusion: The example of the Shiyli Dome shows that the elastic response is one of the real causes for the origin of central uplifts in terrestrial impact structures, and it should not be ignored. In this aspect, the Shiyli is interesting model object for testing the hypothesis of elastic response. One can add also, that there is another one impact structure - the Upheaval Dome – which is very similar to Shiyli in geological aspect, and for which authors [7] also suppose similar to our mechanism of the origin of the central uplift.

References: [1] Melosh H. J. (1989) Impact Cratering: A Geologic Process. Oxford Univ. Press, 245 pp. [2] Spudis P. D. (1993) The Geology of Multi-Ring Basins. The Moon and Other Planets. Ibiddem, 263 pp. [3] French B. M. (1998) Traces of Catastrophe. LPI Contr. No. 954, 120 pp. [4] Baldwin R. B. (1963) The Measure of the Moon. Univ. of Chicago Press, 488 pp. [5] Vishnevsky S. & Korobkov V. (2004) *Uralskii Geologicheskii Zhurnal, 1,* 3-36 (in Russian). [6] Gault D. E. et al. (1968) In Shock Metamorphism of Natural Materials, Mono Book Corp., pp. 87-99. [7] Kriens B. J. et al. (1997) *LPI Contr. No. 922,* pp. 29-30.

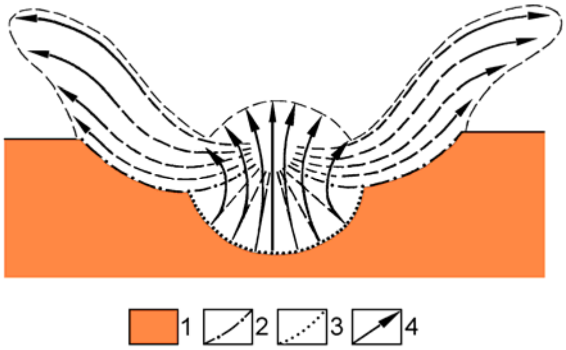

Fig. 4. Schematic ground motion at the Shiyli impact event, with the origin of central uplift by elastic response of target rocks. Legend: 1 – target rocks; 2 – limit of lateral centrifugal flow; 3 – limint of any spherical segment in compression zone of target, where shock wave and rarefaction wave isobars were parallel to each other; 4 – trajectories of ground motion.

POPIGAI IMPACT FLUIDIZITES DERIVED FROM THE “WET” UNITS OF TARGET: INJECTIONS OF HOT & MOBILE MELT+H_2O MIXTURES WITH LONG-LIVING RESIDUAL SHOCK PRESSURES.

S. A. Vishnevsky[1], J. Raitala[2], [1]Inst. of Geology & Mineralogy, 3 Koptug pr., Novosibirsk-90, 630090, RUSSIA <svish@uiggm.nsc.ru>; [2]University of Oulu, Oulu, P.O. Box 3000, FI-90014, FINLAND, <jouko.raitala@oulu.fi>.

Introduction: “Dry” model is common in various impact studies. However, such an approach is an incomplete and very simplified scheme, because the presence of H_2O principally changes all the impact processes, from the shock melting [1], origin of high-pressure polymorphs [2], excavation [3], etc., to post-shock evolution of impact melts [4] and alteration. Below, there are some specific features of impact processes, provided by H_2O, and considered on the example of Popigai impact fluidizites (PIFs).

Description: PIFs (see for details in [5-8]) form dykes and veins in low-shocked host gneiss (HG) lumps from the megabreccia. Macroscopically, they look like as psammitic tuffs with impact glass particles. Fluidal schlieren, “welded” with other parts of the rock, dominate among the particles. “Swirled” and stream-like particles are often present, indicating turbulent mixing of the material during injection **(Fig. 1).**

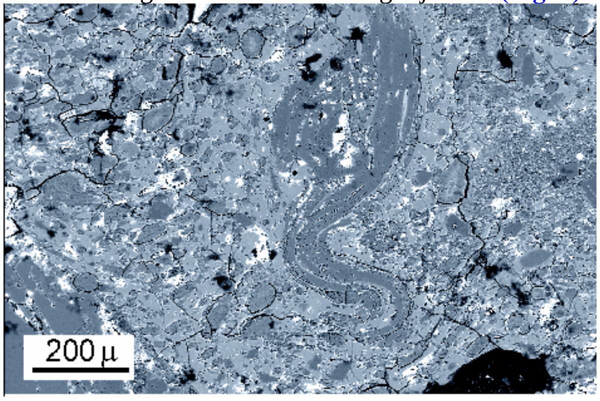

Fig. 1. Heterogeneous glass schlieren from PIFs, made up of convoluted homogeneous (light-gray) and K-Na-Ca feldspar (dark-grey) glasses. SEM image.

Much of the glasses are mixed homogeneous ones derived from the target gneisses; however, some of glasses are rather heterogeneous **(Fig. 1),** or made up of pure monomineral (SiO_2 and K-Na-feldspar compositions) species. Gas chromatographic and ion probe data show [6] that PIF glasses contain essential amount of H_2O (from 1.1 wt. % in lechatelierite up to 9 wt. % in K-Na feldspar glasses). A great number of co-genetic fluid inclusions of various densities are present in lechatelierite schlieren (LSs) **(Fig. 2).** Following to cryometry and thermometry [5,9], the fluid phase of the inclusions is made up of H_2O with low salinity (from 0.5 to 8 wt. % of salts in NaCl-equivalent).

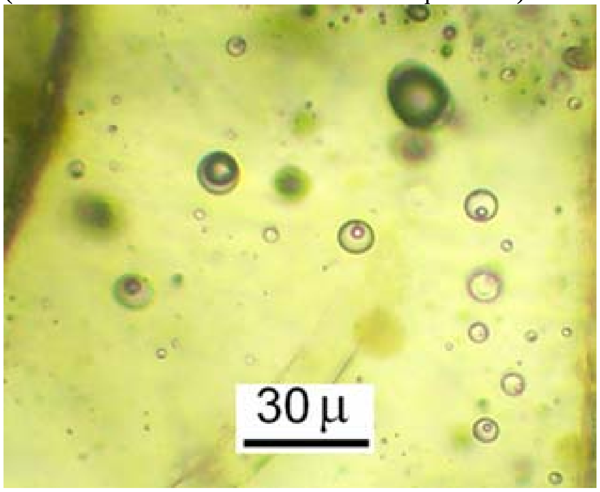

Fig. 2. Co-genetic water fluid inclusions of various densities in lechatelierite schlieren from PIFs (at 20°C). Micro photo in plane polarized light.

In some cases the rock glasses contain co-genetic immiscible calcite globules (CGs) and montmorillonite globules (MGs) **(Fig. 3)** [5,8]. MGs in LSs are of a special interest **(Fig. 4).** They are of Ca-type, rich in Fe and Mg and low in Na (average of 12 analyses of individual MGs, in wt. %: SiO_2 50.43; TiO_2 0.36; Al_2O_3 13.52; FeO 12.85; MnO 0.03; MgO 5.92; CaO 1.49; Na_2O 0.07; K_2O 0.42; BaO 0.08; total 85.17).

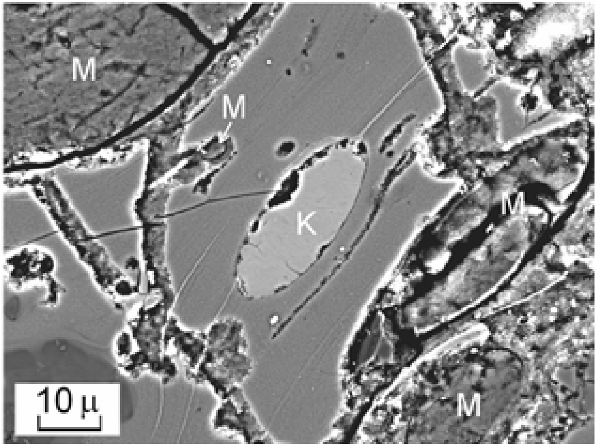

Fig. 3. Co-genetic globules of calcite (K) and montmorillonite (M) in mixed PIF glass. SEM image.

Fig. 4. Co-genetic MGs (indicated by arrows) together with water fluid inclusions in LS from PIFs (at 20°C). Micro photo in plane polarized light.

Interpretation: Heterogeneity of PIF glasses indicates their origin from the marginal part of the Popigai impact melting zone (P~50-60 GPa, R ~14-15 km). Large amount of H_2O and data on REE and trace elements show [10,11] that the glasses were derived not from the "dry" granulites, but from the "wet" Archean diaphtorites. The HGs with PIF dykes and veins, exhibit no petrographic traces of shock affect and were derived from principally another zone of shock metamorphism (P<8-10 GPa, R>25-30 km). So, the melt+H_2O mixtures were able to travel up to ~12-15 km distance from their birthplace to the point of dynamic contact with the HG during the excavation **(Fig. 5).** The simplest estimations based upon impact cratering theory show that the time of such a travel was ~10-12 s [7].

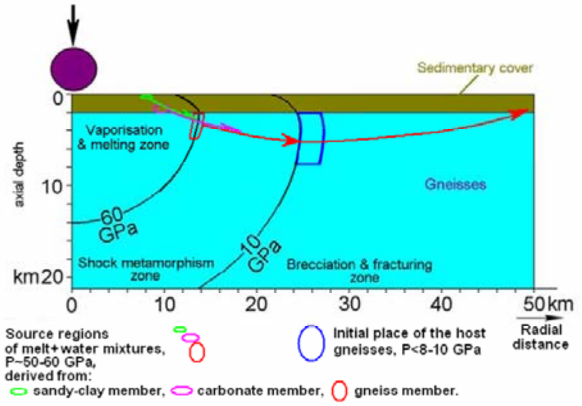

Fig. 5. Principal spatial sources and excavation transport of PIF material from the birthplace to the point of dynamic contact with the HGs.

LSs in PIFs show that the mixtures were hot, >1700°C, during the injection. Dense (0.5-1 g/cm^3) H_2O inclusions in LSs are of particular petrologic concern, indicating their high, ~0.8 to 3.3. GPa, trapping pressures. Such pressures could not be lithostatic ones. So, the mixtures preserved the residual shock pressures during the time of ~10-12 s until the contact with the HGs. These pressures are explained by buffer action of H_2O [9]. The conclusion meets an agreement with the experimental data by [3], namely: since any moment, the pressure release of "wet" compressed materials is controlled by H_2O behavior. CGs disseminated in PIF glasses, are the result of shock melting of Cambrian carbonate members of the target [5,8]. MGs most probably were derived from shock-molten maturated Paleozoic and Mesozoic members of sedimentary cover [8]. Spatially-different sources of CGs, MGs and gneiss-derived PIF glasses are the evidence of very mobile state for melt+H_2O mixtures during the Popigai impact event. The contact interaction of the products was a result of turbulent centrifugal excavation flow. MGs from LSs and other PIF glasses, are rather similar to the montmorillonites known in the Ries [12] and can serve as a good supporting argument for the hypothesis by [1,3,12,13] about the origin of supercritical H_2O+silicate fluids and hydrous silicate melts with the unlimited solubility, derived from some "wet" target lithologies as a result of shock metamorphism.

Conclusion: Hydrous and very mobile impact melt mixtures were derived from various "wet" target units (Archean diaphtorites, Cambrian carbonate and Paleozoic+Mesozoic sandy-clay(?) rocks) during the Popigai impact event. Due to the action of H_2O buffer the mixtures could keep relatively high (up to 3.3 GPa) residual shock pressures for a long (up to 10-12 s) time. The data may be of comparative interest for study of both the terrestrial and other planet (Mars, etc.) astroblemes originated on the water-bearing targets.

Acknowledgement: This study was supported by the RFBR grant #04-05-64127 and by the Finnish Academy of Sciences grant #207759.

References: [1] Kieffer S. W. et al. (1976) *Contributions to Mineralogy and Petrology, 59,* 41-93. [2] Valter A. A. et al. (1982) *Mineralogicheskii Zhurnal, 5,* 21-28 (in Russian). [3] Kieffer S. W. and Simmonds C. H. (1980) *Reviews of Geophysics and Space Physics, 18,* 143-181. [4] Vishnevsky S. A. and Montanari A. (1999) In Large Meteorite Impacts and Planetary Evolution II. *GSA Special Paper 339,* p.p. 19-59. [5] Vishnevsky S. A. et al. (2005a) *LPSC XXXVI,* Abs. #1145. [6] Vishnevsky S. A. et al. (2005b) *MAPS, 40,* Supplement, A162. [7] Vishnevsky S. A. et al. (2006a) *LPSC XXXVII,* Abs. #1268. [8] Vishnevsky S. A. et al. (2006b) *Russian Geology & Geophysics, 47,* 711-730.
[9] Gibsher N. A., Vishnevsky S. A. (2006) *LPSC XXXVII,* Abs. #1234. [10] Vishnevsky S. A., Simakin S. G. (2006a) *MAPS, 41,* Supplement, A182. [11] Vishnevsky S. A., Simakin S. G. (2006b) *MAPS, 41,* Supplement, A183. [12] Osinski G. R. (2003) *MAPS, 38,* 1641-1667. [13] Bureau H., Keppler H. (1999) *EPSL, 165,* 187-196.

INDICATIONS FOR FLUIDIZATION OF THE RIES CRATER'S EJECTA BLANKET.

A. Wittmann[1a] and T. Kenkmann[1b], [1]Humboldt-Universität zu Berlin, Museum für Naturkunde, Mineralogie, Invalidenstrasse 43, 10115 Berlin, Germany, [a]axel.wittmann@museum.hu-berlin.de, [b]thomas.kenkmann@museum.hu-berlin.de.

Introduction: The Ries crater formed ~14.3 Ma ago as a ~24 km diameter impact structure in a layered target of Permian to Miocene sedimentary rocks on top of a Precambrian to Paleozoic crystalline basement. A continuous ejecta blanket is composed of the Bunte Breccia, a lithic clastic matrix breccia that is mainly composed of sedimentary target clasts, and reworked surficial sediments. This unit is locally overlain by Suevite, an impact melt bearing breccia, which indicates far higher temperatures and degrees of shock metamorphism and is apparently composed predominantly of clasts and melt particles derived from the crystalline basement. The Ries crater's ejecta blanket is tested for the hypothesis of fluidization during emplacement.

Observations: Outcrops in variable distances from the center of the structure were examined for indicators of fluidzation and emplacement mechanisms (Table 1).

Table 1 Outcrop locations at the Ries crater and their lithological settings.

Location	Distance & direction from center	Setting (S=Suevite, BB=Bunte Breccia)
Unterwilfingen	8 km WNW'	S - BB melange
Aumühle	9 km NE'	S - BB contact
Altenbürg	11 km SW'	Limestone blocks in S
Ronheim	13 km SE'	BB - cover rocks contact
Mauren	15 km SE'	BB
Otting	15 km E'	S - BB contact
Seelbronn	17 km SW'	S - BB contact
Bollstadt	17 km SSW'	S - BB contact
Oberringingen	17 km S'	BB
Iggenhausen	20 km SW'	BB megablocks
Gundelsheim	20 km E'	BB - cover rocks contact
Binsberg	22 km SE'	BB

Bunte Breccia sedimentological features. Flow textures in the sandy, silty and clayey matrix [1] occur occasionally and some sub-horizontal planes that may indicate internal gliding or shearing processes were found in Mauren (Fig. 1). The overall chaotic nature and lack of alignment of component clasts within the Bunte Breccia suggest that the matrix behaved thixotropic: It was viscuous under confining stresses and froze upon pressure release before gradations could develop. Moreover, ramps and shear planes accomodated the stacking of blocks (Oberringingen).

Fig. 1 Bunte Breccia outcrop in Mauren-Bräulesberg quarry. Arrow indicates subhorizontal, stepped plane between ejecta sublayers. Outcrop height is ca. 10 m.

Frequently, larger blocks are coated with rims of clays in which smaller clastic debris exhibits alignment. This may indicate the presence of water saturated clays that accreted around the blocks during gliding transport. Injections of clay in deformed allochthonous limestone blocks were found in Iggenhausen.

Contact Bunte Breccia-autochthonous cover rocks. In Gundelsheim, layered limestones exhibit striations that show strict orientation towards the crater's center. However, in hummocky reef facies limestones in Ronheim, striations indicate variable orientations [2]. This suggests that obstacles diverted the erosive ejecta flow already at a distance of ~1 km past the crater rim.

Contact Suevite-Bunte Breccia. This contact is marked by a ~decimeter to cm thick, poorly consolidated transition zone [2]. This transition zone is characterized by fine grained debris and sometimes shows rounding and comminution of clasts. Also, clast size reduction occurs in this zone. It contains a larger content of sedimentary rock clasts compared to the suevites and towards the Bunte Breccia, silty layering is sometimes developed. Microscopic analyses of this transitional layer revealed that it is composed of variable amounts of impact melt particles, some of which indicate welding, while towards the overlying suevites vesicular melt shards occur that are indicative of airborne transport. It grades into a polymict breccia, which becomes size-sorted towards the Bunte Breccia. Diaplectic quartz glass with coesite is frequently preserved in this transition zone, which suggests very rapid quenching from post-shock temperatures. At the contact zone of the Bunte Breccia with Suevite, vertical vent pipes formed locally that transect the suevite (Fig. 2) [3]. At their inside, the pipes are matrix deficient and some show hydrothermal precipitates. These pipes likely vented steam from water saturated Bunte Breccia that was covered with hot suevite.

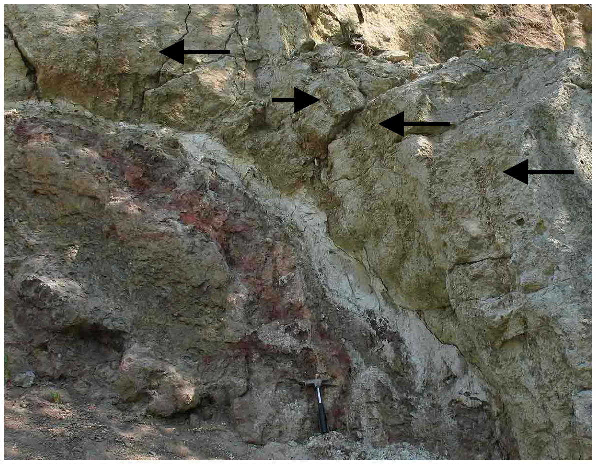

Fig. 2 Bunte Breccia contact with Suevite in Aumühle quarry. Arrows indicate vertical venting pipes in Suevite that originate at contact with Bunte Breccia.

Model: Previous interpretations of the emplacement of the Bunte Breccia assumed analogies to the Moon: (I) as a ballistic emplacement that triggered a ground hugging debris surge [4], or (II) as a rolling and gliding emplacement under high localized confining pressures [5]. These models did not regard the potential role of water saturation in the target sequence. This was previously suggested by [6] from analyses of displacements in the bedrock below the Bunte Breccia. These authors suggested that the Ries may more likely have formed analogous to Martian rampart craters. Some sedimentological evidence from the ejecta blanket was found in support of this hypothesis. A variably thick cover of poorly consolidated Tertiary sediments and underlying sedimentary rocks have to be considered for the formation of a fluidized ejecta blanket. The apparent lack of surficial water in the target area at the time of impact may be comparable to conditions on Mars, where liberated volatiles from near surface sources in the ground supposedly led to the formation of fluidized ejecta blankets [7]. Upon loading with ejecta, the surficial sediments assumed a thixotropic character above a critical yield stress, which accomodated the gliding surge of the Bunte Breccia. Upon loss of momentum, confining pressures dropped and basal portions of the fluidized ejecta blanket froze. This led to the formation of sub-horizontal glideplanes. The glideplanes might have accomodated stacking of ejecta layers within the Bunte Breccia, which was observed by [6] as a possible mechanism in the ejecta blanket of the Chicxulub crater. However, such glideplanes were only found close to the crater rim of the Ries crater and no such features could be found in greater distance.

A complex transition zone between the Bunte Breccia and overlying suevites likely formed during the touchdown of the collapsing fireball. Indications for scouring and turbulence were recorded with the interface between Bunte Breccia and Suevite. These sedimentological features of the poorly consolidated quench zone, and formation of venting pipes support the presence of water at the Bunte Breccia's surface during the emplacement of Suevites.

Outlook: For the emplacement of the Bunte Breccia, a combination of ballistic sedimentation, rolling and gliding, and low viscous flowing has to be regarded. A quantification of Tertiary sediments in the vicinity of the Ries crater at the time of impact is required to provide estimates for their potential contribution to a fluidized ejecta blanket. This could resolve whether fluidization has merely been a localized phenomenon of the ejecta blanket.

Was the suevite predominantly formed from the crystalline basement or did sedimentary rock components decompose due to porosity and water content? The apparent separation of hot, highly shocked crystalline basement dominated ejecta from cool ejecta formed from sedimentary target components of low shock degrees may be testable with a detailed analysis of the Bunte Breccia-Suevite transition zone.

Acknowledgments: This study was made possible by a Barringer Family Fund For Meteorite Impact Research grant. Dr. Sabine Heuschkel and Märker Zementwerk GmbH are thanked for quarry access. Gisela Pösges (Rieskratermuseum Nördlingen), Ralf Barfeld, and the Zentrum für Rieskraterforschung Nördlingen (ZERIN) are thanked for their substantial support.

References: [1] Hüttner R. 1977 Geologica Bavarica 76, 117-122. [2] Hüttner R. & Schmidt-Kaler H. (1999) Wanderungen in der Erdgeschichte Band 10: Meteoritenkrater Nördlinger Ries, Verlag Dr. Friedrich Pfeil, 144 p. [3] Newsom H. E. et al. (1986) *JGR 91, B13*, E239-E251. [4] Hörz, F. et al. (1983) *Rev. Geophys. & Space Phys. 21*, 1667-1725. [5] Chao E. C. T. et al. (1992) Aufschlüsse im Ries-Meteoriten-Krater, *Bay. Geol. Landesamt*, 84 p. [6] Kenkmann T. & Schönian F. (2006) *MAPS 41*, 1587-1603. [7] Reiss D. et al. (2006) *MAPS 41*, 1437-1453.

EJECTA LOCALITIES OF INTERMEDIATELY SHOCKED AND SHOCK MELTED IMPACTITES IN TERRESTRIAL CRATER EJECTA AND MODELING CONSTRAINTS ON THEIR FORMATION AND DEPOSITION

Shawn Wright, School of Earth and Space Exploration, Arizona State University, Tempe, AZ 85287-6305, **Shawn.P.Wright@asu.edu**

Introduction: Fieldwork at two well-preserved, simple, bowl-shaped impact craters reveals a double-layer ejecta (DLE) structure consistent with observations at larger impact structures such as Ries [1] and perhaps an analog for DLE craters observed on Mars [2,3]. Field observations at Lonar Crater, India are described here and related to Shoemaker's well-known descriptions of the Meteor Crater, Arizona ejecta blanket [4]. Constraints on the process(es) responsible for the deposition of the upper suevite ejecta layer are discussed and suggestions for modeling communities are given.

Lonar Crater ejecta structure and comparsions to Meteor Crater: Whereas field data of any preserved terrestrial ejecta blanket is relevant to understanding the impact process and products, studies of Lonar Crater have implications for Mars [5-8]. The target Deccan basalt provides an opportunity to examine terrestrial shocked basalt similar to shergottites from Mars [8,9]. Further, Deccan basalt has been labeled as an excellent analog for Surface Type 1, a thermal infrared spectral type identified from orbital and Rover observations [10]. Field geology at Lonar Crater (diameter = 1.8 km) reveals a DLE structure with two distinct layers of ejecta [5,11] (**Figure 1**). The lower unit is lithic breccia extending to the limits of the continuous ejecta blanket (CEB), or 1.4 km (~1 ½ crater radii) from the crater rim and measuring ~8 m at maximum thickness. The clasts in the lithic breccia are angular, highly fractured, and either unshocked (mineralogically) or Class 1 shocked basalt (0-20 GPa) [5], which consists of fractured grains but no melting or mineral phase changes [5]. As shock pressures are typically 1-2 GPa near the crater rim, no intense shock metamorphism has occurred. From comparisons to basalt flows exposed in the crater walls, the clasts originated from both the oldest flows that have more secondary mineralization of groundmass and from the youngest flows that lack this feature. This is attributed to the level of the pre-impact water table of the ~65 Ma Deccan basalts [11]. The matrix consists of finely pulverized basalt. In theory, this unit grades into what would be overturned or inverted strata near the crater rim, but the crater has degraded since its initial diameter (1.7 km, based on gravity surveys [6]), meaning that ~50 m of the original crater rim has eroded to contribute to the post-crater fill. The upper ejecta unit is a suevite breccia containing clasts shocked to all degrees of shock pressure from unshocked up to Class 5 (> 80 GPa) of Kieffer *et al.* [5]. The suevite layer measures ~1 m in thickness and extends to ~0.5 km (~½ crater radii) from the rim. The matrix is finely pulverized basalt but with the addition of local glass spherules, beads, and dumbbells [5,6] reportedly not found in the lithic breccia unit.

This DLE structure described for Lonar Crater is similar, if not identical, to the "throw out" and "fall out" layers observed at Meteor Crater [4] or the Bunte Breccia and Suevite at Ries Crater [1], and suggests that two processes are responsible [3] for the ballistic emplacement of the lithic breccia moments before the "falling out" of the fall-out suevite layer. Shoemaker [4] identified a suevite layer within Meteor Crater, then later surmised that this unit likely used to be thicker in near-rim regions of the CEB, but has eroded, as the fine matrix of this unit is easily transported by the SW winds of the Colorado Plateau to leave behind the clasts of the suevite layer as a lag [4].

Whereas the lower, more weathered basalt flows have not been identified as protoliths for Classes 2 through 5 in the suevite breccia, heavily fractured basalt corresponding to these basalt flows is observed that are either unshocked or Class 1, implying that these deeper strata are incorporated into the suevite layer. At Meteor Crater, the Coconino Sandstone serves as a lithologic tracer, as highly shocked lechatlerite is distributed in the Meteor Crater fall-out layer [4], suggesting material deep in the target sequence is incorporated into this unit. This provides data to "ground truth" modeling of Lonar Crater, Meteor Crater, and similar small (1-2 km diameter) craters.

Modeling: The potential ground-hugging flow of the lithic breccia unit at Lonar Crater [7] and other craters needs to be understood, but a model that explains the emplacement of both ejecta units should be the goal of impact modeling. Several objectives can be placed on the modeling based on observations at Lonar Crater:

1.) Because the shock wave weakens as it expands, the disparity in the shock levels of the clasts in the two ejecta layers tell us their location in the transient crater. It is obvious that the clasts in the lithic breccia were ballistically emplaced and are from the "curtain" or "flap" [7] and originate towards the outer edges of the expanding sphere. Some of the clasts currently in the suevite ejecta layer must have been located further towards the center of the sphere, although it cannot be said that all of the suevite layer is from this region.

2.) It has been noted that the number of cells and variables in modeling is limited [12], but perhaps more

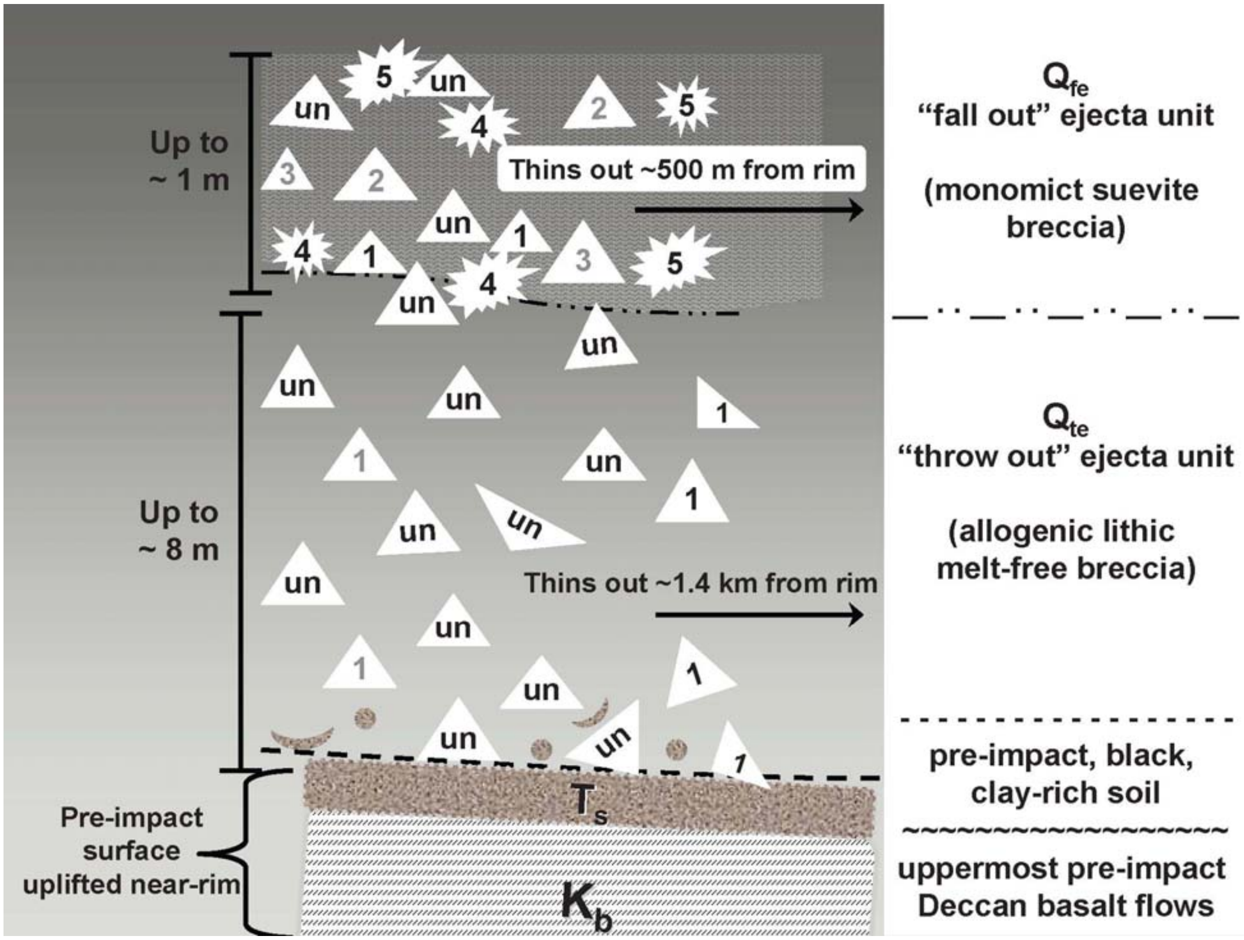

Figure 1. Structure of the Lonar Crater, India ejecta blanket. The figure represent a stratigraphic cross section viewed as a slice through the Lonar ejecta. The number on the clasts represents the class of shocked basalt, and thus the shock level, with “un” representing unshocked basalt. It is suggested that early modeling attempts to duplicate the overall structure seen here.

emphasis should be directed at understanding the deposition of the suevite layer. One problem is that the volume of the lithic breccia comprises roughly ~96% of the total Lonar ejecta. Further, as discussed at Meteor Crater and seen at Lonar, the ~4% of ejecta volume that is the upper suevite unit, with its location and friability, is likely amongst the 1st materials to be eroded/transported after crater formation. However, whereas the process, although not the details, responsible for the deposition of the lithic breccia is constrained, little is known about the deposition and formation of the suevite layer. It is hypothesized that a portion of the target is thrown to high heights in a plume and emplaced is a base surge-like process [13].

3.) Whereas a complete geologic map, including the exact thicknesses and distances of both units in all directions, may provide for an accurate model of various parameters such as impact angle, it suggested that early models of Lonar attempt to reproduce the general thicknesses, distances, and shock levels of both units circum around the crater.

Acknowledgements: H.E. Newsom is thanked for discussions that led to our recent paper on Lonar ejecta [11]. P.R. Christensen has provided financial support and guidance for Lonar efforts. M.S. Ramsey and V. Peet are thanked for assistance during fieldwork at Meteor Crater and K. Louzada, A.C. Maloof, S.T. Stewart-Mukhopadhyay, and B.P. Weiss for collaborative fieldwork at Lonar.

References: [1] Hörz *et al*. (1983) *Rev. Geophys. Space Phys. 21*, 1667-1725 [2] Barlow *et al.* (2000) *J. Geophys. Res. 105*, 26733-26738 [3] Komatsu *et al*. (2007) *J. Geophys. Res. 112*, 10.1029/2006JE002787 [4] Shoemaker (1963) *Moon, Meteorites, & Comets 4,* 301-335 [5] Kieffer *et al*. (1976) *Lun. Plan Sci. Conf. VII*, 1391-1412 [6] Fudali *et al*. (1980) *Moon & Planets 23,* 493-515 [7] Stewart *et al*. (2005) *Rol. Vol. Atm. Martian Impact Crater.*, #3045 [8] Wright *et al.* (2006) *LPSC XXXV*, #1786 [9] Wright (2007) *7th Int. Conf. Mars*, #3399 [10] Bandfield *et al*. (2000) *Science 287*, 1626-1630 [11] Wright and Newsom (2007) *Geology*, in press [12] Melosh (2003) Bridging the Gap I, #8053 [13] Gault *et al*. (1968) *Shock Metamorphsim of Natural Materials*, 87-99

EJECTA LOCALITIES OF INTERMEDIATELY SHOCKED AND SHOCK MELTED IMPACTITES IN TERRESTRIAL CRATER EJECTA AND MODELING CONSTRAINTS ON THEIR FORMATION AND DEPOSITION

Shawn Wright, School of Earth and Space Exploration, Arizona State University, Tempe, AZ 85287-6305, **Shawn.P.Wright@asu.edu**

Introduction: Fieldwork at two well-preserved, simple, bowl-shaped impact craters reveals a double-layer ejecta (DLE) structure consistent with observations at larger impact structures such as Ries [1] and perhaps an analog for DLE craters observed on Mars [2,3]. Field observations at Lonar Crater, India are described here and related to Shoemaker's well-known descriptions of the Meteor Crater, Arizona ejecta blanket [4]. Constraints on the process(es) responsible for the deposition of the upper suevite ejecta layer are discussed and suggestions for modeling communities are given.

Lonar Crater ejecta structure and comparsions to Meteor Crater: Whereas field data of any preserved terrestrial ejecta blanket is relevant to understanding the impact process and products, studies of Lonar Crater have implications for Mars [5-8]. The target Deccan basalt provides an opportunity to examine terrestrial shocked basalt similar to shergottites from Mars [8,9]. Further, Deccan basalt has been labeled as an excellent analog for Surface Type 1, a thermal infrared spectral type identified from orbital and Rover observations [10]. Field geology at Lonar Crater (diameter = 1.8 km) reveals a DLE structure with two distinct layers of ejecta [5,11] (**Figure 1**). The lower unit is lithic breccia extending to the limits of the continuous ejecta blanket (CEB), or 1.4 km (~1 ½ crater radii) from the crater rim and measuring ~8 m at maximum thickness. The clasts in the lithic breccia are angular, highly fractured, and either unshocked (mineralogically) or Class 1 shocked basalt (0-20 GPa) [5], which consists of fractured grains but no melting or mineral phase changes [5]. As shock pressures are typically 1-2 GPa near the crater rim, no intense shock metamorphism has occurred. From comparisons to basalt flows exposed in the crater walls, the clasts originated from both the oldest flows that have more secondary mineralization of groundmass and from the youngest flows that lack this feature. This is attributed to the level of the pre-impact water table of the ~65 Ma Deccan basalts [11]. The matrix consists of finely pulverized basalt. In theory, this unit grades into what would be overturned or inverted strata near the crater rim, but the crater has degraded since its initial diameter (1.7 km, based on gravity surveys [6]), meaning that ~50 m of the original crater rim has eroded to contribute to the post-crater fill. The upper ejecta unit is a suevite breccia containing clasts shocked to all degrees of shock pressure from unshocked up to Class 5 (> 80 GPa) of Kieffer *et al.* [5]. The suevite layer measures ~1 m in thickness and extends to ~0.5 km (~½ crater radii) from the rim. The matrix is finely pulverized basalt but with the addition of local glass spherules, beads, and dumbbells [5,6] reportedly not found in the lithic breccia unit.

This DLE structure described for Lonar Crater is similar, if not identical, to the "throw out" and "fall out" layers observed at Meteor Crater [4] or the Bunte Breccia and Suevite at Ries Crater [1], and suggests that two processes are responsible [3] for the ballistic emplacement of the lithic breccia moments before the "falling out" of the fall-out suevite layer. Shoemaker [4] identified a suevite layer within Meteor Crater, then later surmised that this unit likely used to be thicker in near-rim regions of the CEB, but has eroded, as the fine matrix of this unit is easily transported by the SW winds of the Colorado Plateau to leave behind the clasts of the suevite layer as a lag [4].

Whereas the lower, more weathered basalt flows have not been identified as protoliths for Classes 2 through 5 in the suevite breccia, heavily fractured basalt corresponding to these basalt flows is observed that are either unshocked or Class 1, implying that these deeper strata are incorporated into the suevite layer. At Meteor Crater, the Coconino Sandstone serves as a lithologic tracer, as highly shocked lechatlerite is distributed in the Meteor Crater fall-out layer [4], suggesting material deep in the target sequence is incorporated into this unit. This provides data to "ground truth" modeling of Lonar Crater, Meteor Crater, and similar small (1-2 km diameter) craters.

Modeling: The potential ground-hugging flow of the lithic breccia unit at Lonar Crater [7] and other craters needs to be understood, but a model that explains the emplacement of both ejecta units should be the goal of impact modeling. Several objectives can be placed on the modeling based on observations at Lonar Crater:

1.) Because the shock wave weakens as it expands, the disparity in the shock levels of the clasts in the two ejecta layers tell us their location in the transient crater. It is obvious that the clasts in the lithic breccia were ballistically emplaced and are from the "curtain" or "flap" [7] and originate towards the outer edges of the expanding sphere. Some of the clasts currently in the suevite ejecta layer must have been located further towards the center of the sphere, although it cannot be said that all of the suevite layer is from this region.

2.) It has been noted that the number of cells and variables in modeling is limited [12], but perhaps more some shock features occur at lower shock pressures in porous materials than in competent rock [9,10].

The common approach to record the thermodynamic history of materials in numerical models is the usage of massless tracer particles. In this method, a tracer is placed into computational cells or along certain profiles of interest. While the tracers move through the computational grid, their thermodynamic path is recorded. The tracer's final position and the recorded peak shock pressure can then be compared with field observations, summarized as shock barometry on impact structures [1]. This approach is one of the most valuable linkages between nature and numerical modeling.

Melting and vaporization occur during or after release from shock wave compression when a certain material-dependent threshold pressure is exceeded (50 to >100 GPa in crystalline rocks, for whole melting [1]). As projectile velocity in impact experiments is insufficient to yield significant amounts of melt, the melt production in impact craters can only be investigated by hydrocode modeling. The generated melt volume is closely related to the understanding of shock wave decay or distribution of peak shock pressure in the target. Therefore, the above described tracer method can be used to derive the volume of impact melt. In earlier studies [7] lines of tracer particles were used to determine shape and size of the area where shock pressures exceed the critical pressure for melting. The volume of this area then corresponds to the melt volume produced in an impact event. It was found that melt and vapor production scales with the energy of the impactor [7] and that the region of melting is roughly spherical. This finding is in agreement with more recent studies, where a tracer was located in each computational cell [11]. The melt volume is then determined by summing up the corresponding volume of tracers (the volume of the cell that the tracer was initially located in) that experienced shock pressures in excess of the critical melt pressure [11]. For oblique impacts the shape of the melting region is assymmetric and the volume decreases by 20% for impacts from 90° to 45° [12]. In general, modeled melt volumes agree well with estimates based on observations at crater structures in crystalline targets [7]. But predictions have failed for craters in sedimentary or mixed targets [10]. Whether this is due to inappropriate treatment of porous and water saturated rocks in numerical models or whether there is actually much more melt present than detected so far [13] has remained unsolved. The recent drilling at Lake Bosumtwi revealed much less melt than predicted [14]. Yet in fact, craters in porous target materials should contain more melt due to the extra heat that is generated by the crushing of pores [10].

Damage: When the shock decays, with increasing distance from ground zero, below the HEL (Hugoniot elstic limit), only brittle fracturing and cataclasis occur in the rocks. In numerical models brittle deformation of the rocks is quantified by a damage parameter. Damage is a state variable included in many codes that describes the degree of fracturing; but as a scalar quantity it does not provide any information of fracture size, length, or direction. Damage covers micro-cracks as well as large fractures. Damage is accumulated due to tensile and shear failure, and both processes can be separated in numerical models [15]. Size and shape of the zone damaged by brittle fracturing are responsible for most geophysical anomalies observed at impact structures (gravity, seismics) [16]. However, models cannot provide any information about the increase of open pore space that is introduced by the opening of fractures (shear bulking or dilatancy). Quantification of this process would allow direct comparison of gravity anomalies with numerical models of crater structures.

Discussion: The progressive development of sophisticated codes has resulted in increasingly more realistic models of real collisions. Nevertheless the major shortcoming that will remain for the future is resolution: a km-scale impact model can not provide detailed information on the micro-scale but gives the thermodynamic conditions that larger rock units were exposed to. So, there will always be a distinction between meso/micro-scale models and studies that are aiming at crater formation as a whole. Other shortcomings include insufficiently accurate EOS, although. better constitutive models of geological materials can in principle be developed to result in major improvements in modeling.

Acknowledgments: We thank Boris Ivanov and Jay Melosh for their valuable contribution and continous support in hydrocde development. This work was funded by DFG grants Wu 355/5-1 and De 401/15.

References: [1] Stöffler D. and Langenhorst F. (1994) *Meteoritics 29*, 155-181. [2] Grieve R.A.F. et al. (1996) *MAPS 31*, 6-35. [3]. Baratoux D. and Melosh H.J. (2003) *EPSL 216*, 43-54. [4] Hertzsch J.M. et al. (2002) in Impact Tectonism, Springer. [5] Heider N. and Kenkmann T. (2003) *MAPS 38*, 1451-1460. [6] Schade S. and Wünnemann K. (2007) *LPSC XXXVIII*, #1338. [7] Pierazzo B. et al. (1997) *Icarus 127*, 408-423. [8] Wünnemann K. et al. (2006) *Icarus 180*, 514-527. [9] Kieffer S. W. et al. (1976) *CMP. 59*, 41-93. [10] Wünnemann K. and Collins G. (2007) *LPSC XXXVIII*, #1514. [11] Artemieva N.A. (2007) *MAPS 42*, 883-894. [12] Pierazzo B. and Melosh H. J. (2000) *Icarus 145*, 252-261. [13] Osinski G.R. et al. (2002) LPSC #1078. [14] Deutsch A. et al. (2007) *MAPS 42*, 635-654 [15] Collins G.S. (2004) *MAPS 39*, 217-231. [16] Pilkington M. and Grieve R.A.F. (1992) *Rev. Geophys. 30*, 161-181.

NOTES

NOTES